



HAL
open science

Milieux granulaires vibrés proches du Jamming: Des liquides figés aux solides mous

Corentin Coulais

► **To cite this version:**

Corentin Coulais. Milieux granulaires vibrés proches du Jamming: Des liquides figés aux solides mous. Soft Condensed Matter [cond-mat.soft]. Université Pierre et Marie Curie - Paris VI, 2012. English. NNT: . tel-00764093v1

HAL Id: tel-00764093

<https://theses.hal.science/tel-00764093v1>

Submitted on 12 Dec 2012 (v1), last revised 14 Jan 2013 (v2)

HAL is a multi-disciplinary open access archive for the deposit and dissemination of scientific research documents, whether they are published or not. The documents may come from teaching and research institutions in France or abroad, or from public or private research centers.

L'archive ouverte pluridisciplinaire **HAL**, est destinée au dépôt et à la diffusion de documents scientifiques de niveau recherche, publiés ou non, émanant des établissements d'enseignement et de recherche français ou étrangers, des laboratoires publics ou privés.

THÈSE DE DOCTORAT
DE L'UNIVERSITÉ PIERRE ET MARIE CURIE

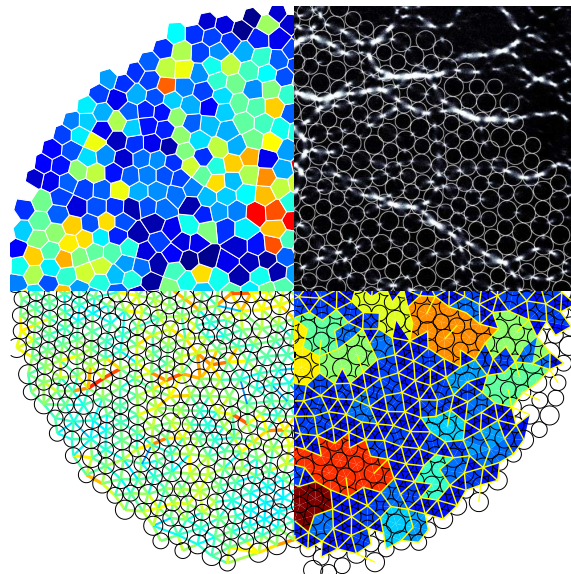
Spécialité : PHYSIQUE
École doctorale 107 : Physique de la Région Parisienne

présentée par
Corentin COULAIS

pour obtenir le grade de
DOCTEUR DE L'UNIVERSITÉ PIERRE ET MARIE CURIE



**Milieux granulaires vibrés proches du Jamming:
Des liquides figés aux solides mous**



Thèse soutenue le 5 octobre 2012 devant le jury composé de :

M. Robert. P. BEHRINGER	Invité
M. Ludovic BERTHIER	Invité
M. Olivier DAUCHOT	Directeur de thèse
M. Jean-Christophe GÉMINARD	Rapporteur
M. Martin VAN HECKE	Examineur
M. Gilles TARJUS	Président du Jury
M. Hajime YOSHINO	Rapporteur

Université Pierre & Marie Curie - Paris 6
Accueil, inscription des doctorants et base de données
Esc G, 2ème étage
15 rue de l'école de médecine
75270-PARIS CEDEX 06

Tél. Secrétariat : 01 42 34 68 35
Fax : 01 42 34 68 40
Tél. étudiants de A à EL : 01 42 34 69 54
Tél. étudiants de EM à ME : 01 42 34 68 41
Tél. étudiants de MF à Z : 01 42 34 68 51
E-mail : scolarite.doctorat@upmc.fr

Résumé

Un ensemble de particules avec interactions répulsives, dans un empilement dense, se bloquent dans un état rigide: sous cisaillement, ces systèmes ont une contrainte seuil avant de céder. Pour des particules sans friction et à température nulle, l'empilement, à la transition de Jamming, est isostatique. Les propriétés mécaniques et géométriques présentent de nombreuses lois d'échelles avec la distance au Jamming qui peut alors être vu comme un point critique. La généralisation de ce concept en présence de température et son lien avec la transition vitreuse ont fait récemment l'objet de nombreux travaux et laissent encore de nombreuses questions ouvertes.

Nous tentons d'apporter des éléments de réponse à celles-ci en étudiant expérimentalement la dynamique des particules et du réseau de force d'un empilement désordonné de disques bi-disperses photo-élastiques vibrés horizontalement, dont nous varions la fraction surfacique pour plusieurs amplitudes de vibrations γ .

Au delà d'un lent mouvement convectif d'ensemble, la dynamique des grains présente principalement une dynamique complexe —intermittente et hétérogène— à une échelle bien plus petite que la taille typique d'un grain. Ces hétérogénéités dynamiques sont d'amplitude maximale à une densité intermédiaire $\phi^*(\gamma)$.

Au niveau du réseau de contacts, nous observons deux signatures franches et distinctes—statique et dynamique— analogues à la phénoménologie de la transition vitreuse. À l'instar du maximum d'hétérogénéités dynamiques des déplacements, la signature dynamique du réseau de contacts a lieu à $\phi^*(\gamma)$, si bien que dynamiques des déplacements et des contacts sont liées. En revanche, c'est à une densité plus élevée $\phi_J(\gamma)$ que l'on identifie la signature statique de la transition de Jamming.

Lorsque l'on diminue l'amplitude de vibration vers la limite d'excitation mécanique nulle, $\gamma \rightarrow 0$, $\phi^*(\gamma)$ et $\phi_J(\gamma)$ se confondent, et l'échelle de longueur des corrélations dynamiques augmente. Nous comparons ces résultats aux propriétés des sphères molles au voisinage du Jamming.

Abstract

At large packing fraction, disordered packings of particles with repulsive contact interactions jam into a rigid state where they withstand finite shear stresses before yielding. For frictionless particles at zero temperature, the Jamming transition coincides with the onset of iso-staticity. Various geometrical and mechanical properties exhibit critical behavior with the distance to Jamming. What vestiges of Jamming remain at finite temperature and how Jamming impacts the thermodynamics of glasses remain open issues.

We address these questions experimentally by investigating the dynamics of both the density field and the force network of an horizontally shaken bi-disperse packing of photo-elastic disks while varying the packing fraction, ϕ , at several vibration amplitudes γ . Although disks displacements reveal a slow global convective dynamics, strongly collective and intermittent motions take place on length scale much smaller than the grain diameter. These so-called dynamical heterogeneities are maximum at an intermediate packing fraction $\phi^*(\gamma)$.

The statics and dynamics of the contact network display, respectively, two distinct sharp signatures, which are reminiscent of the glass transition phenomenology, albeit occurring at the contact scale. A dynamical signature occurs at $\phi^*(\gamma)$, and we relate it to the dynamical heterogeneities of the displacements. The static signature occurs at a larger packing fraction $\phi_J(\gamma)$.

We show further that $\phi^*(\gamma)$ and $\phi_J(\gamma)$ merge in the $\gamma \rightarrow 0$ limit and that the dynamical signature strongly increases as the vibration amplitude is reduced. These results are discussed in light of thermal soft-sphere properties close to Jamming.

Remerciements

Les trois années qui se sont écoulées ont été de belles années, et c'est sans doute grâce aux personnes qui m'ont entourées.

Mes premiers remerciements vont d'abord à Olivier Dauchot, non seulement pour m'avoir appris l'humilité au baby-foot, mais surtout pour m'avoir initié à l'univers et au métier dans lesquels j'ai mordu peu à peu. Au cours de cette aventure scientifique, outre le soutien inconditionnel qu'il m'a apporté, il m'a transmis, je pense, le sérieux comme l'enthousiasme, le scepticisme comme l'optimisme, l'attente de l'établi comme l'acceptation de l'inattendu.

Bien sûr, tout cela n'aurait jamais pu prendre corps sans l'environnement humain et scientifique exceptionnels du GIT, devenu SPHYNX, où, en dépit des changements, la légèreté de l'ambiance et la qualité de la science resteront une référence pour moi, une "griffe". En particulier, je dois beaucoup à Cécile Gasquet, devenue Wiertel, qui, non contente de posséder de réelles facultés pour faire parler moteurs et machines, m'en a transmises quelques-unes, toujours avec le mot pour rire, le conseil adéquat et une complicité certaine. Moins certaines, mais tout aussi complices, sont les joutes verbales, auxquels Vincent Padilla et moi-même nous sommes adonnés à tour de rôle. En revanche, son rôle au tour, à la fraiseuse, et surtout à la conception a été essentiel dès lors qu'il s'agissait de faire évoluer la manip, depuis sa naissance en 2006 lors de la thèse de Frédéric Lechenault. Ça a finalement été le destin de cette manip de passer de mains en mains et d'évoluer continuellement, mais il faut préciser que sans l'apport essentiel de Cécile Wiertel et Vincent Padilla, elle ne serait restée qu'à l'état de Pokémon débutant. Je tiens aussi à remercier mes prédécesseurs, grands-frères de thèse, Raphaël Candelier et Julien Deseigne, qui m'ont transmis le savoir occulte de la "granulanguie", consistant à parler avec les grains sans devenir fou, ça a presque marché. Un grand merci aussi à Sébastien Aumaitre, dont j'ai partagé le bureau pendant ces trois ans, et à qui je suis gré de l'humour grinçant, de la patience et des nombreuses discussions que nous avons pu avoir ensemble. Je remercie vivement François Daviaud, qui, par son soutien continu, a permis que cette thèse s'achève dans d'excellentes conditions.

Je tiens aussi à remercier tous les membres du GIT/SPHYNX, où personne n'est avare d'un conseil ou d'un coup de main, et où tout le monde sait maintenir une joyeuse ambiance: Marco Bonetti, Élisabeth Bouchaud, Arnaud Chiffaudel, François Daviaud, Bérengère Dubrulle, Sébastien Léonard, Simon Thalabard, Brice Saint-Michel, Baudouin Saint-Yves, Cécile Wiertel, Vincent Padilla, Jean Boisson, Éric Herbert, Sébastien Aumaitre, Olivier Dauchot, Pablo Gutierrez-Matus, Julien Deseigne.

Je tiens à remercier Ludovic Berthier, avec qui j'ai peu interagi, mais toujours à des moments clés. Ses questions précises et ses suggestions pertinentes ont largement influencé le contenu de cette thèse et ma compréhension

du sujet. Enfin, un grand merci à Bob Behringer, auprès de qui ça a été un vrai plaisir d'apprendre certaines subtilités de la physique expérimentale comme de la langue anglaise, lors des quelques mois qu'il est venu passer au Laboratoire. Je le remercie aussi vivement pour sa relecture patiente et avisée.

Contents

1	Introduction	1
1.1	Jamming	2
1.1.1	Structure & packing issues	
1.1.2	Mechanical rigidity	
1.1.3	Slowness issue	
1.2	The glass transition	18
1.2.1	Liquids	
1.2.2	Hard Sphere glass transition	
1.2.3	Glassy dynamics in colloids and granular media	
1.2.4	Intermezzo	
1.3	Bridging the gap: Going soft	36
1.3.1	Glass transition of soft spheres	
1.3.2	Thermal vestiges of Jamming	
1.3.3	Getting them together	
1.3.4	Open questions	
1.3.5	This work	
2	Experimental Setup	41
2.1	Existing setup	41
2.1.1	Hardware	
2.1.2	Software	
2.2	Miscellanies on Photo-elasticity	47
2.2.1	Definition of Photo-elasticity	
2.2.2	The case of disks	
2.2.3	The G^2 measurement	
2.3	Photo-elasticity at high frequency	50
2.3.1	Lens	
2.3.2	Light	
2.3.3	Commuting photo-elastic and position information	
2.3.4	Polariscope	
2.3.5	Final experimental setup	
2.4	Protocol and Calibration	57
2.4.1	Protocol	
2.4.2	How to tune the ϕ_{JS} ?	

2.4.3	Calibration of Photo-elasticity	
2.5	Image Processing & Data Analysis	63
2.5.1	Position Detection	
2.5.2	G^2 measurements	
2.5.3	Summary of the data	
3	From a stuck liquid to a soft solid	73
3.1	Convection	74
3.1.1	Solid Rotation	
3.1.2	Shear	
3.1.3	Aftermath : convection thwarts long time observations	
3.2	Structural Relaxation	82
3.2.1	About granular glasses	
3.2.2	Neighbors	
3.3	Mechanical Rigidity	84
3.3.1	Wall pressure	
3.3.2	Bulk force properties	
3.3.3	Geometry of the force network	
3.3.4	Spatial Correlations	
3.4	Dynamics	95
3.4.1	Rattlers	
3.4.2	Root mean square displacement	
3.4.3	More details on displacements statistics	
3.4.4	Dynamical Heterogeneities	
3.4.5	Summary	
3.5	Force dynamics	109
3.5.1	Instantaneous Pressure and Heterogeneity fluctuations	
3.5.2	“Volatility” of the pressure inside grains	
3.5.3	Summary	
3.6	Conclusion and open questions	114
4	“Glassy” Dynamics of Contacts	117
4.1	Extracting the contacts	118
4.1.1	Normal force	
4.1.2	Inter-particle distance	
4.1.3	Contact criteria	
4.1.4	Test: average number of contacts	
4.1.5	Robustness vs. quench and vibration phase of the picture trigger	
4.1.6	Conclusion on contacts	
4.2	Spatial Correlations of the contacts	129
4.2.1	Direct Spatial Correlations	
4.2.2	Gaussian temporal distribution	
4.2.3	Spatial correlations through temporal fluctuations	
4.2.4	Loops	

4.3	Dynamics of the contacts	133
4.3.1	State of the art	
4.3.2	The Contact overlap function	
4.3.3	Average	
4.3.4	Details of the contact dynamics	
4.4	Conclusion and comparison with the brass disks experiment .	142
5	Route towards zero temperature Jamming	145
5.1	Measuring the “zero temperature”	146
5.1.1	Experiment	
5.1.2	Simulation	
5.1.3	Protocol	
5.2	The effect of vibration on the absolute values of ϕ_J and ϕ^* .	152
5.3	Merging crossovers and the Increasing fluctuations	154
5.3.1	Finite size effects	
5.4	The Widom lines for Jamming	157
5.4.1	Widom lines for the liquid gas critical point	
5.5	Conclusion and comparison with related work	158
6	Conclusion and perspectives	161
6.1	A dynamical transition of contacts at ϕ^*	161
6.1.1	Spatial origin of dynamical heterogeneities	
6.1.2	Link with the vibrational modes	
6.1.3	Exploring the glass phase	
6.2	A spin glass transition of contacts at ϕ_J ?	163
6.2.1	Our observations	
6.2.2	Spin-glasses phenomenology	
6.2.3	The analogy	
6.3	The route towards a-thermal Jamming	165
6.4	Active matter	166
6.5	Towards rheology	166
A	Letter on the Widom lines	169
B	Recipes	177
B.1	Dynamical Recipes	178
B.1.1	Indirect method : temporal variance	
B.1.2	Link with dynamical heterogeneities	
B.2	Modelling the motion of one grain	180
C	Side studies	183
C.1	More on rattlers	184
C.1.1	“Non force-bearing” particles	
C.1.2	Comparison with “rattling” particles	

C.2	Another contact overlap function	187
C.2.1	The average magnetization	
C.2.2	The contact overlap function	
C.2.3	The dynamical susceptibility	
	Bibliography	191

List of Figures

1.1	Portrait of T. Graham.	2
1.2	Manifestations of frustration for tetrahedral-icosahedral order	3
1.3	Portrait of J. Kepler and his conjecture.	3
1.4	Portrait of S. Hales and his iron pot experiment.	4
1.5	Random packings.	5
1.6	M&M's packing	7
1.7	random Constraint Satisfaction Problems (rCSP).	9
1.8	From unjammed to jammed solid.	10
1.9	Soft spheres potential.	10
1.10	Excess number of contacts close to Jamming.	11
1.11	Scalings with the excess number of contacts.	12
1.12	Scaling of mechanical moduli with density.	14
1.13	Departing from soft frictionless sphere Jamming.	15
1.14	Low frequency modes close to Jamming.	17
1.15	Aging in granular media under compaction.	18
1.16	Angell plot.	19
1.17	“A pedestrian map of supercooled liquids.”	21
1.18	Schematic mean-field phase diagram of hard spheres in \mathbb{R}^3 . .	25
1.19	(m, φ) diagram.	26
1.20	Two steps relaxations in Colloids.	27
1.21	Dynamic Heterogeneities.	29
1.22	Dynamical Susceptibility.	31
1.23	Glasses and Jamming.	32
1.24	Glass transition for soft spheres.	36
1.25	Thermal vestiges of the Jamming transition.	37
1.26	Thermodynamics and structure close to Jamming.	39
2.1	Brass disks experimental setup.	41
2.2	Pictures of the setup.	42
2.3	Ensemble view of the brass disk experimental setup.	44
2.4	Calibration of the force sensor.	45
2.5	Control and acquisition software.	46
2.6	Photograph of D. Brewster and Kaleidoscope.	47
2.7	Birefringence	48
2.8	Photo-elastic pattern of a disk	49

2.9	Pictures of photo-elastic disks.	52
2.10	Polariscope.	54
2.11	Pictures of the polarized setup.	55
2.12	Experimental Setup.	56
2.13	Compaction and decompaction protocol.	57
2.14	Compaction-Decompaction protocol.	59
2.15	Compaction protocol for different compaction rates.	60
2.16	Compaction protocol for different compaction rates.	61
2.17	Calibration of photo-elasticity.	62
2.18	Interface of the LABView program.	64
2.19	Scheme of the image processing program.	65
2.21	Zoom on one grain.	66
2.20	Position detection algorithm.	66
2.22	G^2 measurement on disks algorithm.	68
2.23	G^2 measurement on “Camemberts”.	70
3.1	Solid rotation.	75
3.2	Removing convection.	76
3.3	Temporal rotation magnitude	77
3.4	Rotation magnitude.	78
3.5	Removing shear.	79
3.6	Shear magnitude.	80
3.7	Convection magnitude.	81
3.8	Convection validity criteria.	82
3.9	Obtaining a granular glass.	83
3.10	Wall pressure.	84
3.11	Instantaneous Pressure.	86
3.12	Instantaneous microscopic pressures.	87
3.13	Force chains.	88
3.14	2D autocorrelation for the “annealed” system.	91
3.15	2D autocorrelation decay	92
3.16	Force chains orientation.	93
3.17	Sketch of pressure vs. density.	94
3.18	Rattlers.	96
3.19	Rattlers properties.	97
3.20	Rattlers properties.	98
3.21	Root mean square displacements.	99
3.22	Structure factors.	101
3.23	Rescaled structure factors $Q(\tau, a)$	102
3.24	Displacements.	104
3.25	Distribution of displacements	105
3.26	Dynamical Heterogeneities.	107
3.27	Sketch of dynamics.	108
3.28	Forces fluctuations.	109

3.29	Statics and Dynamics of the microscopic pressures.	110
3.30	Volatility of grains pressure.	111
3.31	Forces Dynamics.	113
3.32	Quench dependence and plateau value of MSD.	114
3.33	Pressure and mean square plateau.	116
4.1	Measuring contact forces.	118
4.2	Normal forces distributions.	119
4.3	Interparticle distance.	120
4.4	Inter-particle gap distributions.	121
4.5	Joint distributions on inter-particle gaps and forces.	122
4.6	Average number of contacts.	124
4.7	Robustness of contact number.	127
4.8	Spatial correlations of the contacts.	129
4.9	Temporal fluctuations of contact number.	130
4.10	Contacts temporal fluctuations.	131
4.11	Force loops.	133
4.12	Contact dynamics.	135
4.13	Comparing the overlap functions.	136
4.14	Contact overlap function vs. time.	138
4.15	Variances of contact overlap functions.	139
4.16	Contact overlap susceptibility.	140
4.17	Maximal dynamical contact susceptibility.	141
4.18	Glassy dynamic of the contacts.	142
4.19	Two possible scenarios when decreasing the “Temperature”.	144
5.1	Grain Diffusion properties.	147
5.2	Forces on a grain.	148
5.3	Motion of a simulated grain.	149
5.4	Simulated grain diffusion properties.	150
5.5	Experimental Protocol.	151
5.6	Shift of ϕ_J and ϕ^*	152
5.7	Approaching the zero vibration.	154
5.8	Approaching the zero vibration.	155
5.9	Finite size effects.	156
5.10	Widom lines for Liquid-gas critical point.	157
5.11	Approaching the zero vibration.	158
5.12	Different lines.	159
6.1	Spin glass order parameter.	164
6.2	Mapping granular packing with a spin system.	165
6.3	Snapshot of a pulling intruder.	167
C.1	Rattlers	185
C.2	Rattlers	186

C.3	Spin magnetization.	187
C.4	Spin overlap function.	188
C.5	Spin overlap dynamical susceptibility.	189

List of Tables

1.1	Glass transition and Jamming packing fractions.	35
2.1	All the data.	72
3.1	Packing fraction color code	74
4.1	Experimental Jamming packing fractions.	126

Chapter 1

Introduction

We introduce this work by giving examples of systems that can undergo a Jamming phenomenon : grains, foams, emulsions, colloids, networks, optimization problems. We then turn towards the definition of a more precise system : a-thermal soft-spheres. This system undergoes a well defined Jamming transition, which we discuss in detail. In particular, we show that the Jamming transition is associated with the appearance of mechanical rigidity but that depends on the microscopic interactions. Also, disorder plays a crucial role in this transition. Despite those points, the Jamming transition displays numerous features of a critical point.

Much less is known when we depart from the ideal a-thermal case: (i) Shearing close to Jamming involves strongly non-affine displacements and non-linear response. The link between yield stress and Jamming is neither clear nor universal. (ii) Temperature: whether the Jamming transition remains critical, and the existence of finite temperature Jamming are matters of debate.


In 1998, Liu and Nagel [1998] attempted to generalize the Jamming transition to a Jamming scenario that would explain the slowing down of viscous liquids at the glass transition and the emergence of a Yield Stress in sheared complex suspensions was proposed. This picture engendered enormous efforts, and many works support or disagree with this scenario.

In this work, we will focus on the temperature issue. After a brief review of the glass transition phenomenology, we will review here some theoretical work aiming at encompassing the glass and Jamming transition of hard spheres in the same theoretical framework. Surprisingly, we will see that some optimization problems based on random graphs can be fully addressed theoretically and provide fruitful insights on the glass and the Jamming transitions.

We then discuss experimental and numerical results that address the problem of soft spheres. We finally draw a list of questions that remain to be tackled and explain why a granular experiment is appropriate to do so.

1.1 Jamming

Getting jammed is something everybody has experienced: crowd. And that's something people usually dislike; for three main reasons : (i) one is surrounded, (ii) one is compressed and (iii) one is slow. Although we—mankind—dislike to be jammed, we like to jam a lot of things for our practical purposes: granular materials, for food, construction and toys; smaller grains, called colloids (see box below), for painting, chemistry, food and toys; foams, for cosmetics, firemen and toys.

<p>Thomas Graham, born in Glasgow in 1805, was a chemist. Well known for having worked on the diffusion of gases (Graham's law) and phosphates components. He also worked on aurora borealis and on ... colloids! He indeed was the first who used the words <i>colloid</i> and <i>gel</i> [Graham, 1864]. He invented a method to separate colloids which is known to be the precursor of dialysis (See gra for further details on Graham's biography). Note that he had already observed the slowing down of a colloidal glass: <i>"The flow of liquid colloids through a capillary tube is always slow compared with the flow of crystalloid solutions, so that a liquid-transpiration tube may be employed as a colloidoscope. With a colloidal liquid alterable in viscosity, such as silicic acid, the increased resistance to passage through the colloidoscope is obvious from day to day. Just before gelatinizing, silicic acid flows like an oil."</i></p>	 <p>THOMAS GRAHAM (from a recent Photograph)</p> <p>Figure 1.1: Portrait of T. Graham. From Williamson [1864].</p>
--	---

Jamming is a general phenomenon where (i) dense packings, (ii) rigidity issues and (iii) slow dynamics are at stake. In the following, we will describe examples related to these three points.

1.1.1 Structure & packing issues

Packing is an old problem that dates back to Kepler, who had stated the so-called Kepler conjecture, that in Euclidean 3 dimensional space, no packing of mono-disperse spheres tiles the space with an average density greater than the cubic close packing [Torquato and Stillinger, 2010]. A proof of this conjecture has been recently provided by Hales [2005]. However, in three dimensions, the locally preferred structure is not close cubic packing but isocahedron [Tarjus et al., 2005] (see figure 1.2). As a result, when aiming at increasing the packing fraction of an assembly of hard spheres, one easily ends up in dense random configurations. Note that this is true in three

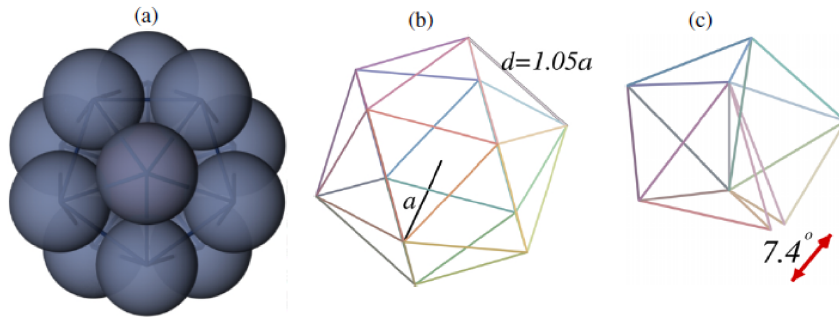


Figure 1.2: “Manifestations of frustration for tetrahedral-icosahedral order in 3D atomic systems: (a) the fivefold rotational symmetry of the icosahedron shown here is not compatible with translational periodicity. (b) The distance d between the atoms of the first shell is slightly larger than the distance a between the central atom and its neighbors: $d = 1.05 \dots a$. (c) The dihedral angle of the tetrahedron, $\cos^{-1}(1/3)$, is not commensurate with 2π so that five tetrahedra packed along a bond leave a defect angle of about 7.4° .” Extracted from Tarjus et al. [2005].

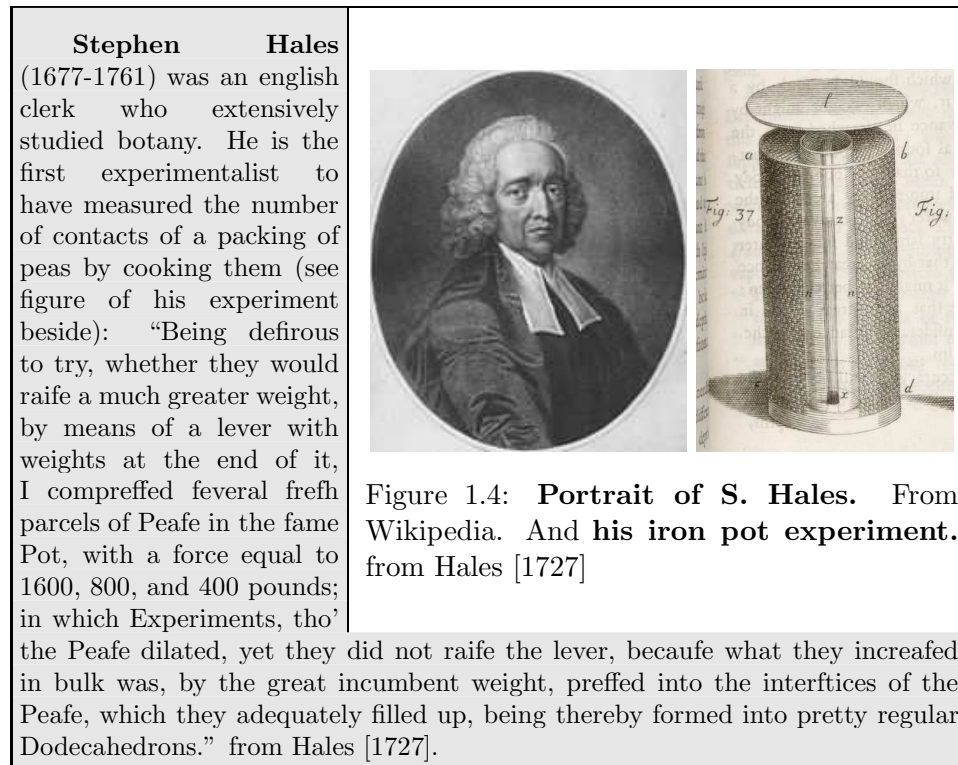
dimensions and above, but not in two dimensions, where the hexagonal order is favored both locally and globally.

<p>In his book <i>De nive sexangula</i> (‘On the six-sided snowflake’) of 1611 Jonathan Kepler formulated his conjecture. The picture is one image from photographs taken of the copy of the original edition of Kepler’s pamphlet, now located at the Thomas L. Fisher Library at the University of Toronto.</p>	
--	--

Figure 1.3: Portrait of J. Kepler and his conjecture. From Wikipedia.

To the best of our knowledge, no mathematical evidence of the existence of a random close packing has been given [Parisi and Zamponi, 2010, Torquato et al., 2000]. In three dimensions, the densest random packing achieved experimentally reaches a packing fraction of 0.64. Since the early works of Stephen Hales (see box), physicists have tried to characterize the properties of randomly packed grains. Of particular interest are the works of

Bernal and Mason [1960], who poured ink through a packing of beads and counted the number of spots without ink per grains (see picture in figure 1.5 (a)). They thus constructed histogram that we reproduce in figure 1.5 (b), of the coordination number, and found an average contact number of 6.4. They then further attempted to investigate the radial distribution function [Bernal et al., 1962]. At this time, both the average number of contacts per grain and the pair correlation function were investigated.



Recently, Donev et al. [2005] ran more modern computer simulations to extensively investigate these quantities for large systems. We plot in figure 1.5 (c) the pair distribution function of a 10 000 hard spheres packing from such a work. We see that there is a divergence at a radius corresponding to particles diameter d , because a majority of the particles are in touch with each other. Also note that two discontinuities occurs at $r = d\sqrt{3}$ and $r = 2d$. The number of contact can also be computed by counting all the particles that are closer than a distance $d(1 + \tau)$, where τ is an arbitrary threshold, and we reproduce the histogram of contact number for various values of τ in figure 1.5 (d). The authors find an average number of contacts equal to 6.0. Same properties arise in different systems such as emulsions: we plot in figure 1.5 (e) a three dimensional snapshot of an emulsion by a confocal microscope [Jorjadze et al., 2011]. The number of contacts is then extracted

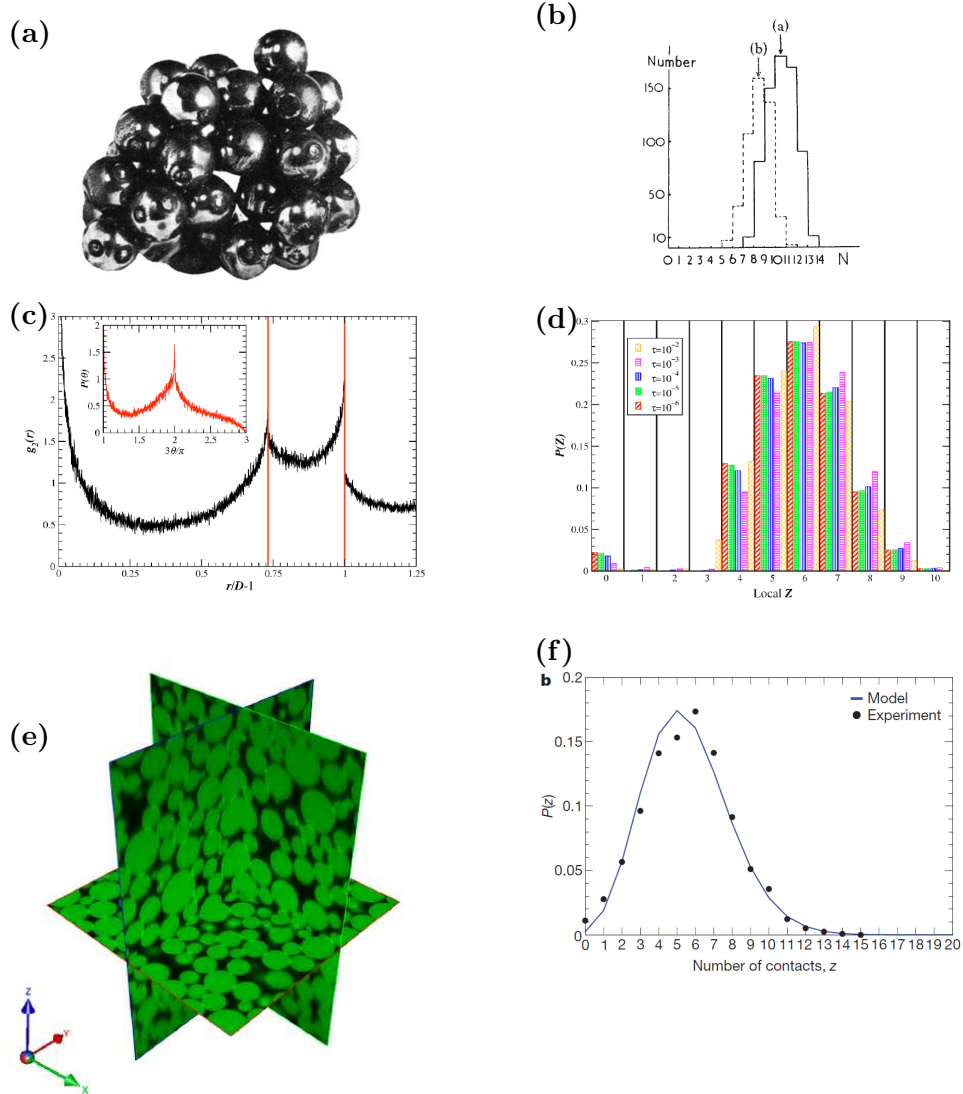


Figure 1.5: **Random packings.** (a): Randomly packed beads (Extracted from Bernal and Mason [1960]). (b): Histograms of contact numbers derived (a) from calculated random model and (b) from assembly of spheres. Extracted from Bernal and Mason [1960]. (c): Pair correlation function averaged over five packings of 10 000 simulated hard spheres. (c)-Inset: Probability distribution of bond pair angles. Extracted from Donev et al. [2005]. (d): Histograms of contact numbers from a packing of 10 000 simulated hard spheres for different thresholds τ used to define contacts. Extracted from Donev et al. [2005]. (e): A snapshot of an emulsion imaged by a confocal microscope. From Jorjadze et al. [2011]. (f): Distribution of contact number for the same emulsion. From Clusel et al. [2009].

from position detection combined together with a fluorescent marker that is activated whenever the droplets are in contact. We represent in figure 1.5 (f) a histogram of the number of contacts per particle.

1.1.1.1 Maxwell criteria

Although random packings geometry have no clear mathematical description yet, the Jamming transition can be rigorously addressed in term of iso-staticity and mechanical stability: lower and upper bounds of the number of contacts at Jamming can be computed. This is the so-called Maxwell counting argument. Very nice explanations can be found in Tkachenko and Witten [1999], van Hecke [2010]. We recall here the basic argument. Let's consider a generic packing made of N particles with a certain number of contacts, $N_c = zN/2$, where z is the average number of contacts per particles.


Torque and Force Balance: requiring the mechanical equilibrium of the packing involves that there is force and torque balance on each grain, this is F_{const} constraining equations. The total number of degrees of freedom in the forces is F_{dof} . Ensuring the forces not to be overdetermined requires

$$F_{dof} \geq F_{const}. \quad (1.1)$$

Touching condition: the condition that particles are just touching implies that their geometrical degrees of freedoms N_{dof} must not be overdetermined by the number of geometrical constraints N_{const} . This yields

$$N_{dof} \geq N_{const} \quad (1.2)$$

1. In the case of N spherical frictionless particles in the euclidean space in d dimension with N_c contacts, there is one force to determine per contact, $F_{dof} = N_c$, and there is d force balance equations per particle so that $F_{const} = Nd$. Hence equation 1.1 becomes $z_{iso} = 2d \leq z$. In addition, there are d geometric degrees of freedom per grain, $N_{dof} = Nd$, and there is one geometric condition per contact which is $N_{const} = N_c$, so that $z \leq 2d$. As a result, the two bounds are equal and this yields $z = 2d$.
2. In the case of frictional particles, there are d forces to determine per contact, $F_{dof} = dN_c$, and there is $d(d+1)/2$ force and torque balance equations per particle $F_{const} = Nd(d+1)/2$. We then obtain $z_{iso} = d+1 \leq z$. The geometric degrees of freedom remain unchanged: there is d geometric degrees of freedom per grain, $N_{dof} = Nd$ and one geometric condition per contact, $N_{const} = N_c$, so that $z \leq 2d$. Hence, $d+1 \leq z \leq 2d$.

<p>Ellipsoids: As a third example, we can check out the case of frictionless ellipsoids, that have been recently studied in a few works [Mailman et al., 2009, Zeravcic et al., 2009, Donev et al., 2007, 2004]. There is 1 force to determine per contact, $F_{dof} = N_c$, but rotation comes into plays and there is $d(d+1)/2$ force and torque balance equation per particle $F_{const} = Nd(d+1)/2$. Thus, equation 1.1 yields $z_{iso} = d(d+1) \leq z$. We have to take rotation into account in the geometric degrees of freedom: there are $d(d+1)/2$ geometric degrees of freedom per grain, $N_{dof} = Nd(d+1)/2$ and one geometric condition per contact, $N_{const} = N_c$, so that $z \leq d(d+1)$. Hence, $z = d(d+1)$. We see that there are more contacts number between ellipsoids, therefore, as discussed by Donev et al. [2004]; M&M's pack more efficiently than spheres.</p>	 <p>Figure 1.6: M&M's packing. From Donev et al. [2004].</p>
--	---

1.1.1.2 An analogy with random Constraint Satisfactory Problems (rCSP)

Constraint Satisfactory Problems (CSP) can be summarized as follows: given a number N of variables constrained by a number of constraints M , what are the configurations which satisfy all the constraints? A powerful tool to represent CSP is a graph representation. An example of a CSP graph is pictured in figure 1.7 (a): there are $N = 7$ variables (circles) and $M = 3$ constraints (black squares). CSP are of practical interest for computer sciences, and progress in CSP have improved, for instance, in algorithms used in telecommunications.

As a matter of fact, one can think of the packing issue as a CSP and the two approaches can actually be matched [Krzakala and Kurchan, 2007, Berthier et al., 2011a, Semerjian, 2012]. We will attempt here to provide physical insights into this analogy:

- a packing problem can be summarized as follows: Is it possible to obtain a geometric configuration ensuring that all the grains can be arranged in a box without any overlap between them?
- Similarly, a optimization problem can be presented the following way: Given a number N of variables and a number M of constraints between these variables, it is possible to satisfy all the constraints?

In general, finding the actual satisfactory solutions of CSP is a very difficult task. Therefore, a first step to address these problems is to ask whether, they are *SATisfiable* (all the constraints are satisfied) or *UNSATisfiable* (at least one constraint is not satisfied). In other words, one would like to find

the threshold value of $\alpha = M/N$ below which the problem is SAT. One also may further wonder about the structure of the ensemble of solutions.

Recently, tools of spin glasses statistical physics —quenched disorder and the thermodynamic limit— have become useful to address a random version of CSP [Mézard et al., 2002]: random Constraint Satisfactory Problems (rCSP). The questions can be reformulated as follows: in a typical realization of disorder, at the thermodynamic limit ($N \rightarrow \infty$ and $M \rightarrow \infty$), what is the bound α_s between *SAT* and *UNSAT*? What about the structure of the ensemble of solutions for $\alpha < \alpha_s$? These questions can be tackled analytically for the following reasons:

- the randomness of the constraints gives a “mean-field” smell to these problems;
- at the thermodynamic limit, graph loops are sub-extensive: locally, the problem has the structure of a tree;
- the tree structure allows one to define distances, which is necessary for the study of the structure of the solutions.

The number of constraints in which the variables are involved is called the degree of the variable. Starting from one arbitrary variable of the tree, one can process a *leaf removal* that consists of removing recursively the variables of degree one. One can show that there is a value α_d such that for $\alpha < \alpha_d$, the remaining of the *leaf removal* is empty, and for $\alpha > \alpha_d$, the remaining is not empty and is called the *core*.

One can further show that, among the solutions of the core, there is a number, $\exp N\Sigma_*(\alpha)$ of them, which are far apart. They are called clusters, and the complexity, $\Sigma_*(\alpha)$, becomes zero at α_c , when the number of clusters turns sub-exponential. We represent in figure 1.7 (b), a scheme extracted from Krzakala et al. [2007], where the authors draw the configuration space of two models, called k-SAT and q-color. Black regions represent clusters of solutions. We see that below α_d , there is only one big cluster, and all the solutions are connected. For $\alpha_d < \alpha < \alpha_c$, an exponential number of clusters appears; it becomes sub-exponential for $\alpha_c < \alpha < \alpha_s$, and for $\alpha > \alpha_s$, there are no more solutions.

If we now return to the packing problem, the packing fraction can intuitively be compared to α : the larger ϕ , the larger the number of constraints. Hence, random close packing, if it exists, would correspond to the satisfiability threshold α_s . Now imagine that we prepare a packing by slowly increasing the packing fraction. Once the packing fraction has reached the value “ ϕ_d ” (equivalent to α_d), the system is trapped in one of the clusters, whose distance is far away from the other clusters. This means that there is no way to escape this cluster without major change in the packing. Therefore, the packing configuration will stay trapped in one of the clusters, and

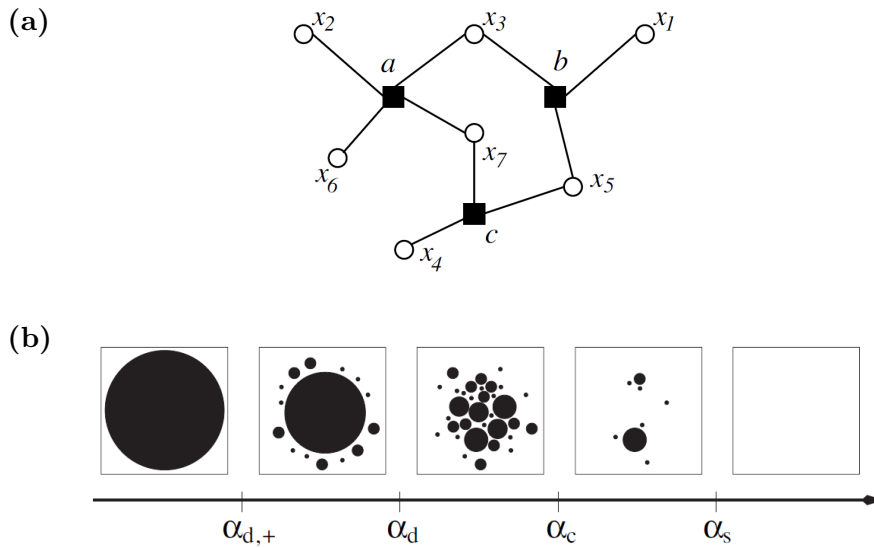


Figure 1.7: **random Constraint Satisfaction Problems (rCSP).**

(a) : Small CSP: filled squares are constraints and empty circles variables.

(b) : “Pictorial representation of the different phase transitions in the set of solutions of a rCSP. At α_d^+ , some clusters appear, but for $\alpha_d^+ < \alpha < \alpha_d$ they comprise only an exponentially small fraction of solutions. For $\alpha_d < \alpha < \alpha_c$ the solutions are split among $\sim \exp(N\Sigma_*)$ clusters of size $\exp(Ns_*)$ but the clusters “cover” phase space. If $\alpha_c < \alpha < \alpha_s$ the set of solutions is dominated by a few large clusters (with strongly fluctuating weights), and above α_s the problem does not admit solutions any more.” Extracted from Krzakala et al. [2007].

the size of this cluster will be reduced as the packing fraction is increased, until... it is empty. At this point, there is no more close solution, the grains start to overlap: this is Jamming. Hence, we see that the packing can be jammed at a lower density than the random close packing density, and that the Jamming point is not unique; it depends on the cluster the packing ends up in when it crosses α_d , which, in turn depends both on the initial condition and the compression protocol.

1.1.2 Mechanical rigidity

Hard spheres packings cannot be compressed above the Jamming transition because the pressure diverges. On the contrary, soft particles can overlap each other, and soft spheres packing can be compressed above the Jamming transition. The Jamming transition for soft disks is schematically represented in figure 1.8: we see three packings below (left), at (middle) and above (right) the jamming transition. We will show in the following that the mechanical properties of jammed packing have peculiar properties: above

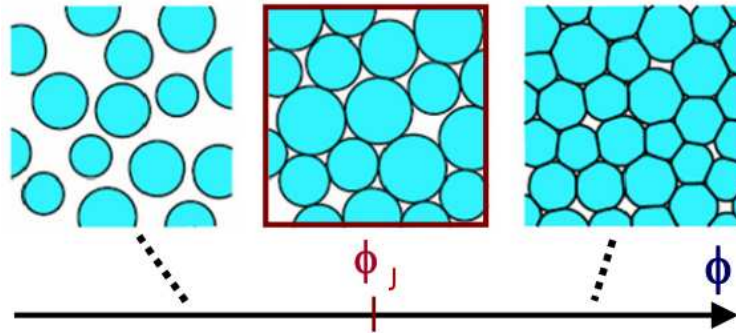


Figure 1.8: **From unjammed to jammed solid.** Sketch of soft disks at different densities. Adapted from van Hecke [2010].

the Jamming threshold (for soft particles), the particles overlap, the average number of contacts has increased and the packing has acquired rigidity: these properties scale with the distance to the transition.

<p>Soft Spheres: In this section, we will often refer to soft spheres. Let's make precise here what we precisely mean by soft spheres. The widely spread model of soft spheres assume a pair potential between particles and is represented on figure 1.9. For two particles i and j, it is defined as follows:</p> $V_{ij} = \begin{cases} \frac{\epsilon_{ij}}{\alpha} \delta_{ij}^\alpha & \text{for } \delta_{ij} \leq 0 \\ 0 & \text{for } \delta_{ij} > 0 \end{cases}, \quad (1.3)$ <p>where $\delta_{ij} = 1 - \frac{r_{ij}}{\sigma_{ij}}$, σ_{ij} is the sum of the radii of particles i and j, r_{ij} is the distance between their center, and ϵ_{ij} is the characteristic energy scale of the interaction. α is the stiffness of the potential and is often taken equal to 2 (Harmonic potential) or to 5/2 (Hertzian potential).</p>	<p>Figure 1.9: Soft spheres potential.</p>
--	---

In the following, we define ϕ_J to be the jamming packing fraction, and z_J its associated number of contacts. Above the Jamming onset, the measured density is ϕ and its associated number of contacts is z . The density can be related to the inter-particle distance δ . At Jamming, most particles are just touching, $\delta = 0$. For a small isotropic increase in density, at first order, the average inter-particle distance δ scales with $\phi - \phi_J$.

1.1.2.1 The number of contacts

As seen previously in section 1.1.1.1, the number of contacts of a stable packing of frictionless spheres is larger than $z_{iso} = 2d$. In practice, var-

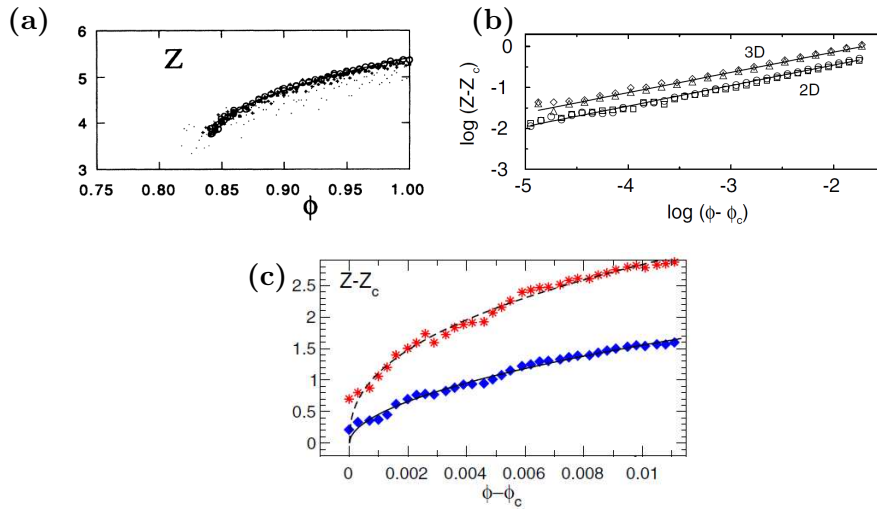


Figure 1.10: **Excess number of contacts close to Jamming.** average contact number versus packing fraction: (a) in a simulation of foam [Durian, 1995]; (b) in a simulation of soft harmonic and hertzian spheres in 2D and in 3D [O’Hern et al., 2002]; (c) in an experiment of 2D photoelastic grains [Majmudar et al., 2007].

ious studies in simulated foams [Bolton and Weaire, 1990, Durian, 1995], in simulated soft spheres [O’Hern et al., 2002], and in experiments of two dimensional granular systems [Majmudar et al., 2007] have shown that the average number of contacts jumps to a finite value z_J ($z_J = z_{iso}$ for frictionless systems) at the Jamming density ϕ_J . Once compressed further, the number of contacts increases with a particular dependence on packing fraction:

$$z - z_J \sim (\phi - \phi_J)^\beta, \quad (1.4)$$

where $\beta \sim 0.50$ in most systems. We represent in figure 1.10 the average number of contacts versus packing fraction for simulated foams [Durian, 1995] (a), simulated soft spheres [O’Hern et al., 2002] (b) and for a granular experiment [Majmudar et al., 2007]. Although the square root scaling has been observed in many systems, there is no simple argument to understand this power law: this is a non-trivial exponent that takes its root in the disorder and the marginality of the Jamming transition.

1.1.2.2 Diverging length-scale

From simple arguments, one can justify a diverging length-scale at the isotropic point [Wyart et al., 2005b]. This can be done thanks to the following thought experiment: imagine a packing with an average excess number of contacts Δz . We now consider a subsystem, a box of size L containing N particles. The size of the box thus scales with N^d , where d is the dimension of space. In the box, the excess number of contacts scale thus with $N\Delta z$.

We now cut the contacts at the boundary of the box, so that the number of contacts we cut scales as L^{d-1} . In this box, the excess number of contacts thus becomes $AN\Delta z/2 - BL^{d-1}$, where A and B are arbitrary constants. Therefore, the size L^* of the box at which the packing become isostatic scales like

$$L^* \sim \frac{1}{\Delta z}. \quad (1.5)$$

This gives a diverging length scale as the packing tends to isostaticity.

1.1.2.3 Link with mechanical response

Vibrational response The density of states $D(\omega)$ (see box below) is the spectrum of vibrational frequencies of solids. We plot in figure 1.11, left, $D(\omega)$ versus ω for a numerical packing of soft spheres for differently jammed packings. We see that they have a plateau for low frequencies with a lower limit, ω^* . We plot in figure 1.11, right, the frequency ω^* defined above versus the excess number of contacts Δz : it scales like $\omega^* \sim \Delta z$. The spatial structure of the modes can be studied through the dispersion relation [Silbert et al., 2005]. This yields a wavelength that scales with $1/\sqrt{\omega^*} \sim 1/\sqrt{\Delta z}$ for transverse waves and with $1/\omega^* \sim 1/\Delta z$ for longitudinal waves. Thus the longitudinal diverging wave-length directly scales as L^* and also diverges at the Jamming transition.

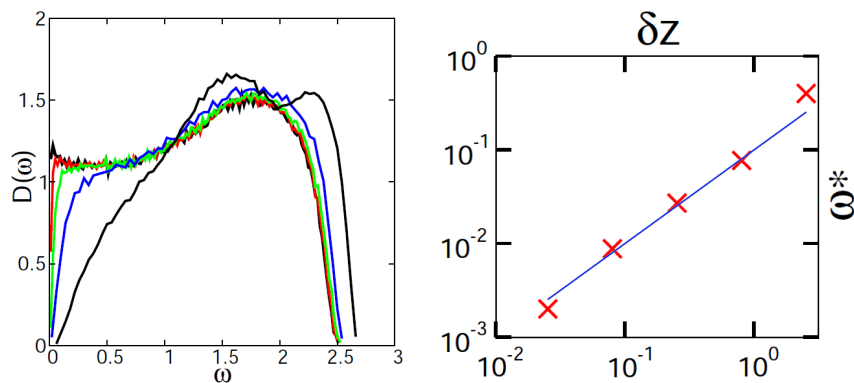


Figure 1.11: **Scalings with the excess number of contacts.** (Left): 1024 spheres interacting with repulsive harmonic potentials were compressed in a periodic cubic box to volume fraction ϕ , slightly above the jamming threshold ϕ_c . Then the energy for arbitrary small displacements was calculated, and the dynamical matrix inferred. The black curve at the extreme right is at a relative volume fraction $\phi - \phi_c = 0.1$. Proceeding to the left the curves have relative volume fractions 10^{-2} , 10^{-3} , 10^{-4} , 10^{-8} , respectively. (Right): cutoff frequency ω^* versus excess number of contacts δz . Adapted from Wyart et al. [2005a], which was already adapted from O'Hern et al. [2003].

Vibrational Density Of States (DOS): A common tool to study vibrational properties of solids is the vibrational density of states. Let's consider a solid made of N equal masses m at positions $\vec{r}_i(t)$ coupled together. By definition of a solid, all the positions have a well defined equilibrium position \vec{r}_i^0 . We suppose that $\vec{r}_i(t)$ vibrate harmonically around \vec{r}_i^0 . Thus, going to temporal Fourier space, the mechanical equilibrium of the solid writes

$$-\omega^2 m \delta \vec{r}_i(\omega) = \sum_j K_{ij} (\delta \vec{r}_i(\omega) - \delta \vec{r}_j(\omega)) \quad (1.6)$$

where $\delta \vec{r}_i(\omega)$ is the Fourier transform of $\delta \vec{r}_i(t) = \vec{r}_i(t) - \vec{r}_i^0$, m_i is the mass of particle i and K_{ij} is the coupling spring constant between i and j . Equation 1.6 can be rewritten

$$\omega^2 \delta \vec{r}_i(\omega) = \kappa_{ij} \delta \vec{r}_i(\omega), \quad (1.7)$$

where $\kappa_{ii} = -\frac{1}{m} \sum_j K_{ij}$ and $\kappa_{ij} = K_{ij}/m$ is real and symmetric. Therefore, it is diagonalizable with real eigenvalues. The probability density function of the square root of its eigenvalues is the vibrational density of states of the solid, $D(\omega)$.

N.B. As pointed out when defining the Density Of States (DOS), this spectral decomposition assumes that the vibrations are harmonic around well defined positions. For packings close to the marginal Jamming point, that are on the verge of mechanical stability, the oscillations that are induced to probe the DOS will strongly affect the system. As a matter of fact, several studies have shown a strong anharmonicity close to the Jamming threshold [Schreck et al., 2011, Xu et al., 2010, Brito et al., 2010] and extreme dependence on the vibration frequency for similar elastic network systems [Tighe, 2012].

Mechanical Moduli After the early work of Durian [1995] on foams, the first intensive studies of the mechanical properties of Jammed soft spheres were performed by O'Hern et al. [2002, 2003]. We plot in figure 1.12 the bulk (**left**) and shear (**right**) moduli versus the distance to Jamming packing fraction $\Delta\phi = \phi - \phi_J$ for both harmonic ($\alpha = 2$, α is defined in eq. 1.3) and Hertz Potential ($\alpha = 5/2$). Indeed, the shear modulus G and the bulk modulus K are found to scale like

$$K \sim \Delta\phi^{\alpha-2} \quad \text{and} \quad G \sim \Delta\phi^{\alpha-\frac{3}{2}}, \quad (1.8)$$

These scalings can be rewritten independently of the potential : the repulsive part of the potential of equation 1.3 averaged over the system can be rewritten $V \sim k\delta^2$, where $k \sim \delta^{\alpha-2}$ is the stiffness of the potential and δ is the average overlap between particles. Since $\delta \sim \Delta\phi$, and $\delta z \sim \Delta\phi^{0.5}$,

$$\frac{G}{k} \sim \Delta z \quad \text{and} \quad \frac{K}{k} \sim \Delta z^0. \quad (1.9)$$

These scalings are represented in figure 1.13 (b). The fact that G/k and K/k scale differently has to do with the fact that non-affine displacements play a crucial role under shear and are not involved under compression [Ellenbroek et al., 2009b, van Hecke, 2010]. In the case of compression, K scales trivially with the stiffness, because the dominant effect is affine deformation: particle overlap matters. Note, also, that for random elastic networks [Ellenbroek et al., 2009a, Wyart et al., 2008], both bulk and shear moduli vanish as the system reaches the isostatic point, as represented in figure 1.13 (c) and (d). This points out that jammed packings of soft spheres are very peculiar, since the mechanical behavior depends on the forcing. Soft spheres close to Jamming resist compression but do not resist shear, they have a very unusual mechanical behavior.

1.1.2.4 Is Jamming critical in general?

Friction As explained in 1.1.1.1, iso-staticity and stability do not coincide as soon as friction comes into play, and the average number of contacts at Jamming, z_J , lies between $z_{iso} = d + 1$ and $2d$. Therefore, packings for $z_J > z_{iso}$ are hyperstatic: the contact forces are not uniquely determined at Jamming. The consequence is that mechanical moduli K/k and G/k and DOS cutoff frequency ω^* do not scale with Jamming z_J but with the isostatic point z_{iso} [van Hecke, 2010, Somfai et al., 2007]. We illustrate this by sketching in figure 1.13 the packing pressure (e) and mechanical moduli (f) versus the average number of contacts. Since K/k , G/k and ω^* do not scale with respect to Jamming, frictional Jamming is not critical.

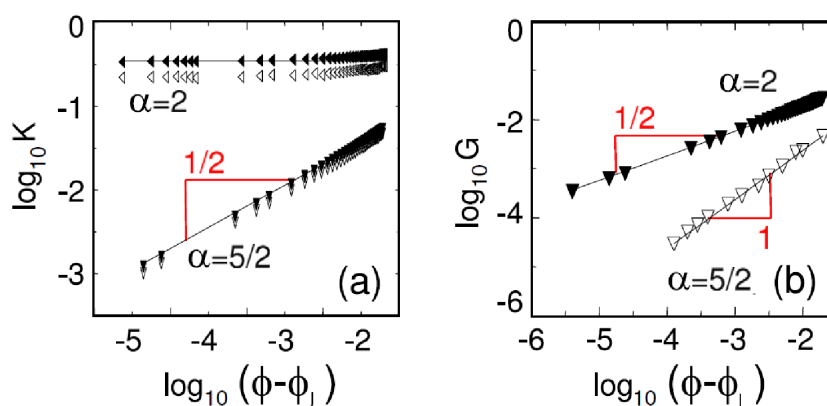


Figure 1.12: **Scalings of mechanical moduli with density.** Scaling of the Bulk and Shear Moduli K (left) and G (right) versus distance to Jamming packing fraction $\phi - \phi_J$. Adapted from van Hecke [2010], which was already adapted from O’Hern et al. [2003].

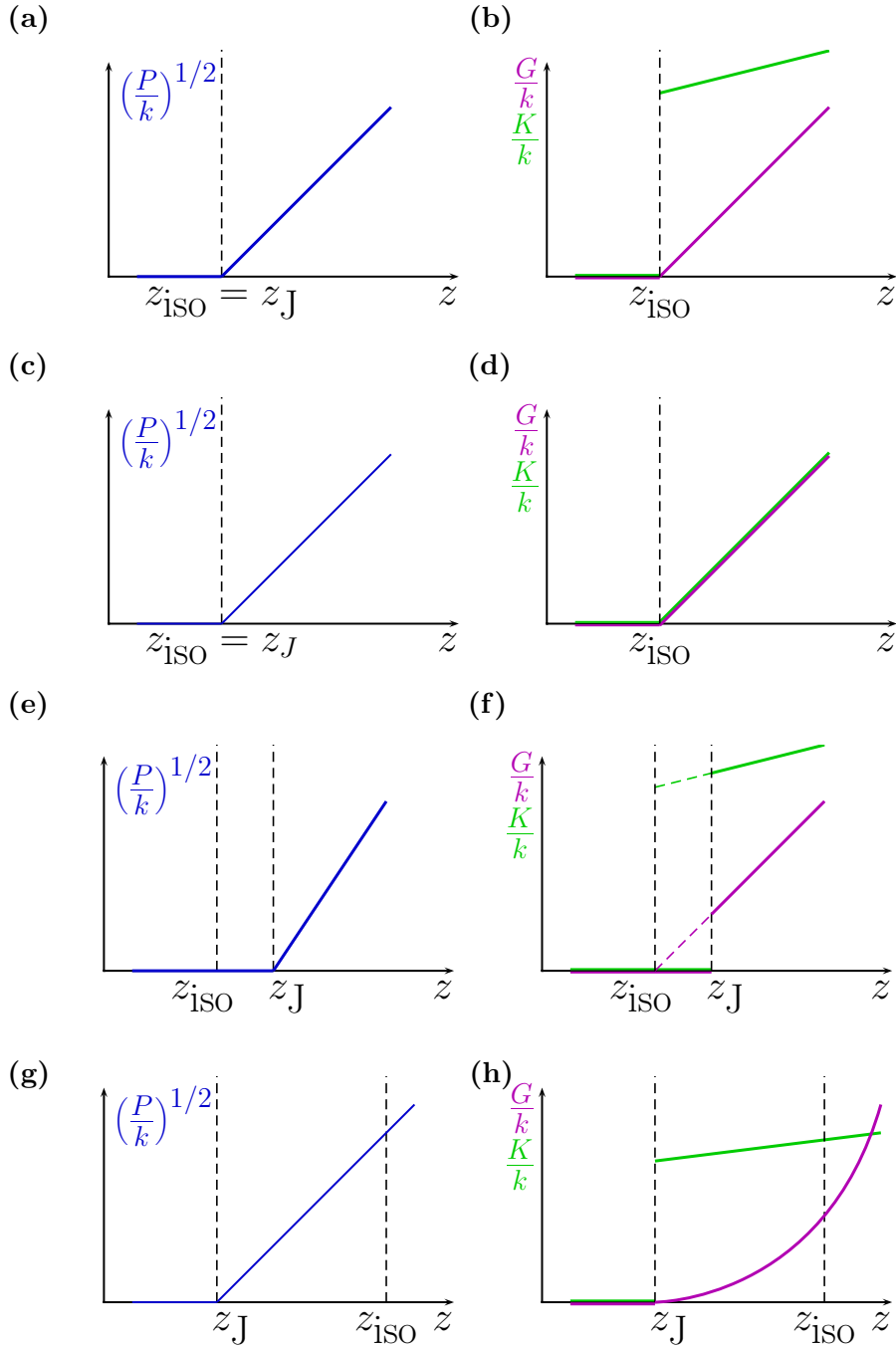


Figure 1.13: **Departing from soft frictionless sphere Jamming.** Pressure over stiffness (**left row**) and Bulk and Shear moduli over stiffness (**right row**) vs. number of contacts for : frictionless spheres **(a) and (b)**, random spring network **(c) and (d)**, frictional spheres **(e) and (f)**, and frictionless ellipsoids **(g) and (h)**.

Ellipsoids An other way to depart from the ideal soft spheres Jamming transition is to study ellipsoids. The simplest ellipsoids we can think of still have a symmetry axis and can either be *oblate* (M&M's) or *prolate* (cigars). They have been experimentally [Donev et al., 2004] and numerically studied recently [Mailman et al., 2009, Schreck et al., 2012, Donev et al., 2004, Zeravcic et al., 2009]. As stressed in section 1.1.1.1, $z_{iso} = d(d + 1) = 12$ in 3D and 6 in 2D. We represent in figure 1.13 (g) a sketch of the pressure over stiffness versus the average number of contacts, the pressure increases from z_J , which is smaller than z_{iso} : packings of ellipsoids are hypostatic. We then turn to the study of the mechanics: we plot in figure 1.13 (h) the shear modulus over stiffness G/k and bulk modulus over stiffness K/k versus number of contacts. Although the exponent for the shear modulus differs from the spheres case —which suggests subtle coupling effects between rotations and translations of particles, G scales with distance to Jamming, whereas K doesn't, as in the sphere case. Therefore, jammed ellipsoids display critical behavior, not related to isostaticity.

To conclude, the Jamming transition for frictionless system is a critical point in some special cases, and the properties of the critical point seem to strongly depend on the microscopic details.

1.1.2.5 Jamming as a marginal critical point

Jamming shares common properties with usual critical points: at least on the jammed side, there is a diverging length and time scales, and proper scaling invariance of mechanical properties can be expressed with respect to an order parameter: the excess number of contacts. Yet, Δz is only a good order parameter on the jammed side of the transition, for negative Δz , the system is in a mechanical vacuum state, and neither scaling invariance nor power law dependence can be expressed so easily with respect to jamming: no clear scaling law or diverging length scale has ever been observed. Before entering the discussion about the glass transition, increases of time-scale above and below Jamming will be discussed in the next section.

1.1.3 Slowness issue

We show in this section that when Jamming is approached, from above or from below, time scales increase.

1.1.3.1 Increase of timescales above Jamming

As already mentioned in section 1.1.2.3, investigations of the vibrational properties of elastic solids [Wyart, 2008, Wyart et al., 2005b, Chen et al., 2010, Silbert et al., 2005] reveal an increase of low frequency vibrational modes as the Jamming density is approached. We plot the vibrational density of states versus frequency in figure 1.14, top left, from Silbert et al.

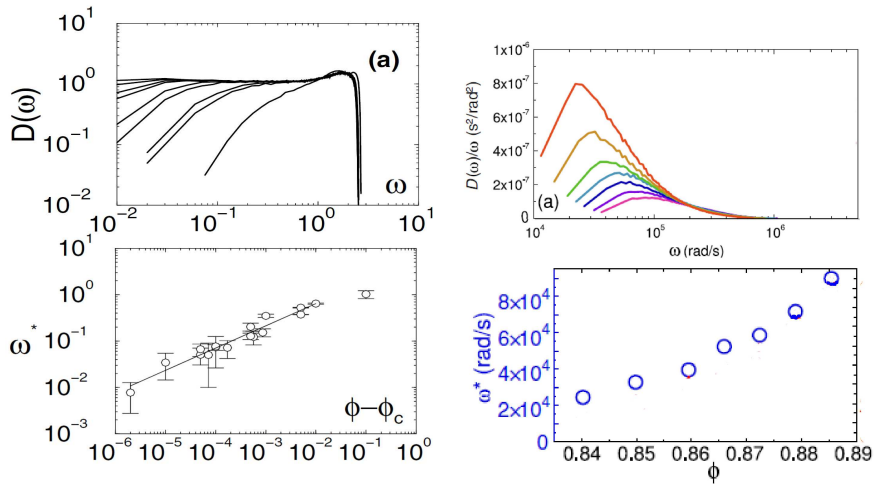


Figure 1.14: **Low frequency modes close to Jamming.** **Top Left:** Density of states for $N=1024$ for different values of $\phi - \phi_c$ in the soft harmonic spheres system. ϕ_c is the Jamming packing fraction. **Bottom Left:** Corresponding cutoff frequency ω^* versus $\phi - \phi_c$. Adapted from Silbert et al. [2005]. **Top Right:** Density of modes over frequency $D(\omega)/\omega$ vs. frequency ω as a function of packing fraction. **Bottom Right:** Corresponding cutoff frequency ω^* versus packing fraction ϕ . Adapted from Chen et al. [2010].

[2005]. We indeed see that more and more low frequency modes are populated as the distance to the Jamming packing fraction is reduced. The cutoff frequency, ω^* , can thus be extracted and it scales with the distance to Jamming. The very same observation has been performed in two dimensional jammed colloids [Chen et al., 2010]. We plot in figure 1.14, top right, $D(\omega)/\omega$ versus ω , and we see that indeed, low frequency modes grow as the packing fraction is reduced towards the Jamming packing fraction. This is further illustrated by figure 1.14, bottom right, where the cutoff frequency ω^* is plotted versus packing fraction. Therefore, the timescales tend to increase significantly as the packings approach the Jamming point from above.

1.1.3.2 Increase of timescale below Jamming

We commonly observe an increase of timescales near Jamming in our kitchen. As we want to put more coffee, wheat or what ever in a pot, we first pour it into the recipient, and we give a few tap. A direct consequence is that the grains occupy less volume, the density increases. Should we tap further, the grains continue to compact —they jam into denser states, but by tinier and tinier amounts. In other words, we need more taps to increase the density. This is a direct evidence that, as the packing gets denser (closer to random close packing), the time scales increase.

Such an aging effect has been reported in vibrated [Jaeger et al., 1989,

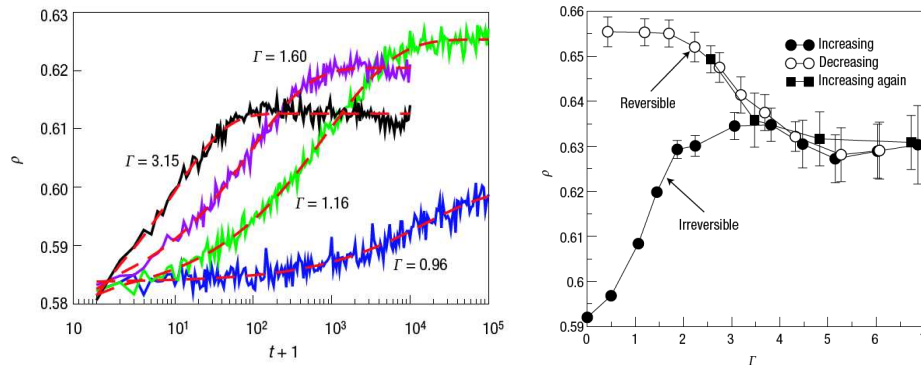


Figure 1.15: **Aging in granular media under compaction. Left:** Density versus number of taps in vertically tapped granular packing. Adapted from Richard et al. [2005]. **Right:** Density versus acceleration in vertically tapped granular column. Adapted from Richard et al. [2005], Knight et al. [1995].

Knight et al., 1995, D’Anna and Gremaud, 2001, Philippe and Bideau, 2003, 2002, Richard et al., 2005] cyclically expanded [Divoux et al., 2008] or sheared [Pouliquen et al., 2003, Dauchot et al., 2005] granular packings. We plot in figure 1.15, left, the density of a vertically tapped packing of grains versus the number of taps: the compaction becomes logarithmically slow. This is a long time dynamics, and all ever longer as the packing fraction grows. As highlighted by figure 1.15, right, where we plot density versus strength of the taps in a similar experiment, packings undergo a strong history dependence.

Therefore, a direct consequence is that the Jamming transition deals with diverging time scales. Hence, the sampling of jammed packings is a non-equilibrium game and it is always very difficult to disentangle the Jamming onset and glassy dynamics. This calls for a more precise definition of the glass transition, and an investigation of its consequences on compacted granular materials. This will be the subject of the next section.

1.2 The glass transition

Needless to say, the zero temperature Jamming is an ideal picture. We now would like to investigate the effect of temperature or, as an analogy, of vibration (in granular systems). In other words, we would like to understand the link between athermal ($T = 0$) and thermal ($T > 0$) systems. To this end, two types of issues will be considered:

- Thermal agitation is a way to “visit” the possible configurations. Especially for systems in hard sphere systems, there is no relevant energy scale: only timescales are modified by temperature.
- In systems where there is a relevant energy scale, for instance in soft

spheres systems, the free energy landscape depends on particles softness: temperature matters.

After a brief review of the glass transition of atomic and molecular liquids, we shall present theoretical results on the thermodynamics of hard sphere systems as the system density is increased toward the Jamming packing fraction. We then discuss experimental and numerical investigations of the dynamics of hard sphere systems: we will see that because of a drastic slowing down of the dynamics, namely *the glass transition*, the Jamming point is unreachable by equilibrium investigation. Rather, a complex glassy behavior arises.

1.2.1 Liquids

1.2.1.1 Phenomenology

As they are cooled down, many liquids can actually avoid crystallization and enter a metastable “supercooled phase”. In this supercooled phase, decreasing the temperature further leads to an increase of the structural relaxation time, or equivalently, of the viscosity by orders of magnitude. As the system relaxation time gets longer and longer, the time for the system to reach equilibrium becomes longer than what can be obtained experimentally. The glass transition temperature T_g is then defined when the relaxation time τ_α exceeds the conventional experimental time of 100 s, or equivalently, when the viscosity of the liquid reaches 10^{12} Pa.s. T_g is, therefore, a completely empirical quantity, that depends on the glass formation protocol. *This is*

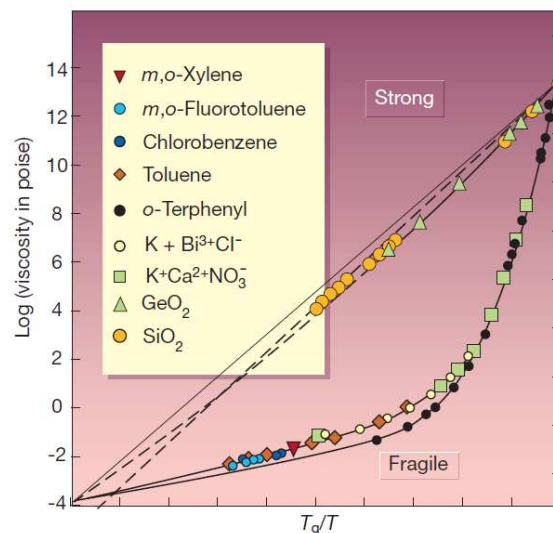


Figure 1.16: **Angell plot.** Viscosity versus inverse of the temperature for various glassforming liquids. Extracted from Debenedetti and Stillinger [2001].

*one of the main issues of the glass transition: the equilibrium physics of supercooled liquids for low temperatures cannot be experimentally visited, and we are doomed to study non-equilibrium supercooled liquids. Still, the evolution of the viscosity with respect to T/T_g —the so-called *Angell-plot* displayed in figure 1.16— exhibits some generic —material independent— features. First, and this is one of the most striking aspects of glasses, the same phenomenon spans 16 order of magnitude. Second, we see that there are two typical classes of glass-forming liquids: (i) strong: their viscosity η obeys an Arrhenius behavior $\eta \sim \exp -E/k_B T$. This behavior can be understood by a thermal activation picture (Eyring’s model). (ii) fragile: their viscosity obeys a super-Arrhenius behavior. Within the picture of thermally activated dynamics, this would correspond to energy barriers, whose heights depend on temperature. A good fit for these fragile glass formers is the Vögel-Fucher-Tamman (VFT) fit, $\eta \sim \exp -DT/(T_0 - T)$. An extrapolation of this fit below T_g leads to a divergence of the viscosity at a finite temperature. Note that some models (Adam-Gibbs) predict a VFT behavior, and provide a thermodynamical interpretation for T_0 . Note that this fit is not unique, and a Bässler expression, $\eta \sim \exp K(T_*/T)^2$ fits the data as well. An extrapolation of this fit would thus lead to a divergence of the viscosity at zero temperature. Some models, such as Kinetically Constrained Models (KCM) [Chandler and Garrahan, 2010] predict a Bässler expression.*

While huge changes occur in the dynamics, only weak changes occur in the statics: there is hardly a difference between the structure of the liquid and the structure of the glass. This is the third striking fact about the glass transition.

1.2.1.2 Thermodynamics

A basic picture of the thermodynamics of the glass transition is given in a very nice review by Cavagna [2009]. This is summarized in figure 1.17, where we plot a schematic representation of the entropy as a function of temperature in a liquid. Starting from a high temperature, in the liquid phase, and going down into the supercooled phase, we describe the various temperatures crossovers and compare with to rCSP we have described in figure 1.7.

- T_m : Melting of the crystal, where a first order transition occurs. There is no equivalent in rCSP.
- T_c : Dynamic transition temperature. This corresponds to the temperature at which the Mode Coupling Theory (an introduction to MCT can be found in Reichman and Charbonneau [2005]) predicts a divergence of the structural relaxation of the liquid [Szamel, 2012,

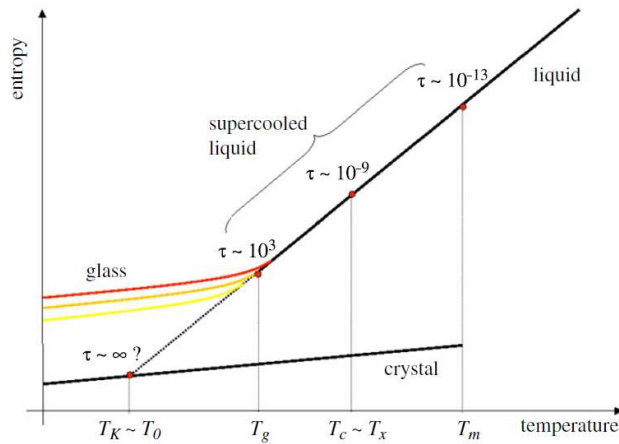


Figure 1.17: “A pedestrian map of supercooled liquids.” The black plain line represents the experimental equilibrium lines. The dotted line represents the extrapolated equilibrium line of the supercooled liquid. The colored lines represent non-equilibrium glass phase. Extracted from Cavagna [2009].

Szamel and Löwen, 1991]. This divergence is never observed in experiments because of the mean-field character of MCT.

Mode Coupling Theory(MCT): For a simple atomic liquid, MCT consists in deriving a differential equation for the dynamical structure factor $F(k, t)$, where k is the wave vector. This equation involves a so-called Memory term, whose expression can be derived through a hierarchy of equations. The MCT approximations consist in truncating this hierarchy, assuming that there is separation of scales between low k conserved quantities and high k random quantities.

In its first derivation, MCT indeed fails to describe any cooperativity and collective dynamics, although recent developments used Fluctuation-Dissipation Theorem together with MCT to predict a dynamical susceptibility [Biroli et al., 2006] and hence collective phenomena. In rCSP, the analog is α_d , which corresponds to the temperature at which the accessible phase-space clusterizes, and gives rise to an activated dynamics between configuration that are “far apart”. The p -spin model (see Castellani and Cavagna [2005] for an introduction), which is a fully connected spin model with quenched disorder also places a similar pure dynamic transition at this temperature. Actually, there is an intimate connection between MCT and the p -spin model: the schematic version of MCT (without wave vector dependence) is considered to be a mean-field version of p -spin.

- T_X : Goldstein’s Crossover from non-activated to activated dynamics: in the picture of energy landscapes, for temperature $T > T_X$, the dynamics is dominated by the saddle points, whereas for $T < T_X$, the system is made of an exponentially large number of metastable states or “basins”; the dynamics of which is dominated by hopping between these states. Although T_X and T_c come from different models, they share a common physical picture.
- T_g : T_g is the dynamic glass transition, where the relaxation time exceeds the conventional experimental time of 100 s: the experimentalist is not patient enough to let the system reach equilibrium.
- T_K is called the Kauzmann’s Entropy crisis temperature: the extrapolated liquid entropy reaches the entropy of the crystal, in other words, the configurational entropy of the liquid attains zero: the system is in an ideal glass phase. In rCSPs, the analog of the configurational entropy is the complexity, and the equivalent of T_K is α_c .
- T_0 is the temperature where the Vogel-Fulcher-Tamman fit locates a divergence of the relaxation time. It is found to be close to the Kauzmann temperature.

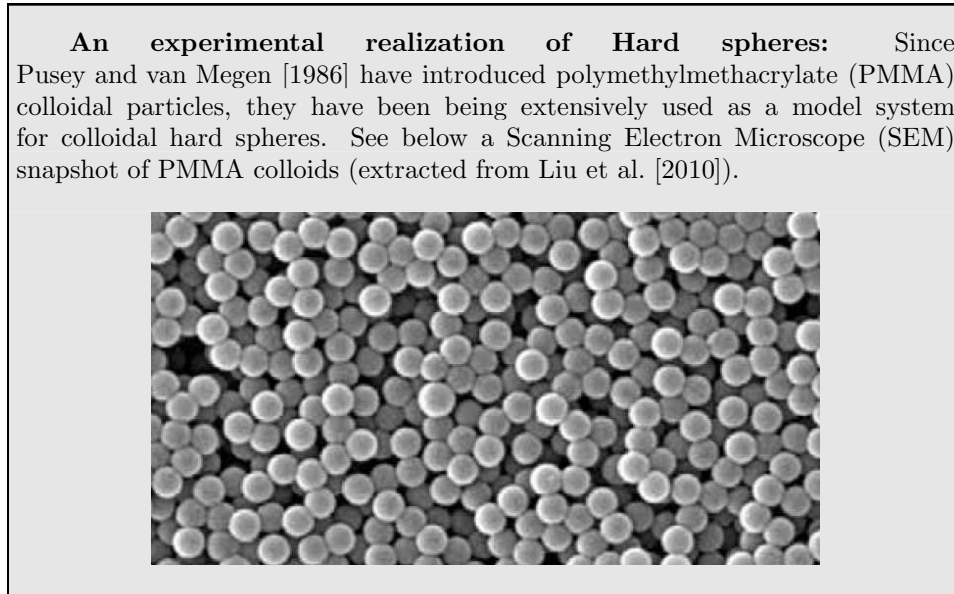
1.2.2 Hard Sphere glass transition

1.2.2.1 The glass transition

Unlike liquids, hard spheres do not have attractive potential, but they have been a good minimal model to understand the properties of liquids [Bernal, 1964]. The analogy goes further, because hard sphere systems can actually undergo a glass transition, where the temperature is replaced by the density. In three dimensions, above the glass transition density $\phi_g \sim 0.58$, the structural relaxation time exceeds the experimental window. In this dense regime, since only the repulsive part of the potential is considered to be at stake [Chandler et al., 1983, Weeks et al., 1971], and the analogy with liquids is thus salient. As a side remark, the MCT equations for atomic liquids and for Brownian particles strictly match [Szamel and Löwen, 1991, Szamel, 2012]. Note however, that a recent work stresses that truncating the liquid interaction potential may be too crude to quantitatively describe the increase of the relaxation time [Berthier and Tarjus, 2009].

In addition, a sole experimental realization of the thermalized hard spheres is colloidal hard PMMA particles [Pusey and van Megen, 1986], [van Megen and Underwood, 1994], [Cipelletti and Weeks, 2011]. Unlike molecular liquids, the great advantage of colloids is that they are actually visible through modern microscopy techniques, such as Dynamic Light Scattering (DLS), or direct visualization [van Megen and Underwood, 1994, Pusey and van Megen, 1987, Cipelletti and Weeks, 2011]. The microscopic

mechanisms associated with the glass transition thus have been closely investigated in these systems [Weeks and Weitz, 2002].



Still, a major difference between molecular and colloidal supercooled liquids is the breadth of timescales, that spans 16 decades for molecular supercooled liquids, but is limited to 6 orders of magnitude in simulations [Berthier and Biroli, 2011] and to 5 orders of magnitude in experiments [Brambilla et al., 2009] on colloids. Because colloids are much larger, thermal motion is less significant—the microscopic relaxation time of the liquid is of the order of 10^{-2} s. Since the largest experimental windows can hardly exceed 10^4 s, the dynamic range is limited to 6 decades.

Therefore, it is not clear whether colloidal systems can fully describe the molecular glass transition. Still, the colloidal glass transition can be considered as a model system, and is also a problem of interest in itself.

1.2.2.2 Thermodynamics of dense hard spheres

As stressed in the first part, timescales increase by orders of magnitude when Jamming is approached from below. Yet, this tremendous increase lies within the picture of the glass transition. In this section, we legitimately question the interplay between the Jamming and the glass transitions. This picture has been suggested in Liu and Nagel [1998], O’Hern et al. [2003], where it was proposed that the critical nature of the Jamming point could dominate the features of the glass transition and even the yield stress properties of shear complex fluids. This has driven a lot of work and debate [Berthier et al., 2011a]. Still, recent experimental [Brambilla et al., 2009],

numerical [Berthier and Witten, 2009b] and theoretical [Parisi and Zamponi, 2010] studies of the glass transition in hard sphere three dimensional systems find that the glass transition has nothing to do with the appearance of rigidity in the system, that would correspond to Jamming.

Let's describe first the theory: in the context of the Random First Order Theory (RFOT), a mean field thermodynamic description of both the glass and the Jamming transition using replicas for hard spheres has been proposed [Parisi and Zamponi, 2010].

Replicas: the initial use of replicas computation on liquids dates back to Monasson [1995]. The idea is to couple the liquid to a “replica”, which is a given equilibrated liquid configuration, and define an overlap function which quantifies a “distance” between the 2 configurations. Making the difference between the “replicated” coupled liquid and the normal one allows one to estimate the logarithm of the number of metastable states: *the complexity*. This trick can be generalized to an arbitrary number of replicas m . Surprisingly, m can be tuned as a non-integer and even taken lower than 1. Thus, studying a “molecule” of m components at a fictive temperature T gives the thermodynamic properties of the system at mT . This computation has been performed to investigate the thermodynamics of glasses [Mézard and Parisi, 1999]. Studying a hard sphere liquid, Parisi and Zamponi [2010] performed different approximations describing the glass transition and the approach to Jamming from below. But, close to Jamming, the hard sphere limit appears to be a singular limit and they could not extend the validity of the approximation through the Jamming point.

The resulting physical picture is summarized in figure 1.18. This diagram represents a schematic evolution of the pressure versus the density through the hard sphere glass transition. The plain line represents the equilibrium line: at low packing fractions, the system is liquid; it then undergoes a first order phase transition. The plateau thus corresponds to liquid-crystal coexistence. Beyond the plateau, the pressure increases again and diverges at the ordered close packed density. The red dashed line stands for the metastable branch of the supercooled liquid. Below the density ϕ_d , the configurations of the liquid are “linked” states represented by one black zone on the figure: it is easy for the system to go from one state to one another. Still, when ϕ_d is approached, the connections between the states become smaller. Above ϕ_d , there are many glassy states which are “far apart” from one another. In practice, the system falls out of equilibrium, trapped in one of the glassy states and follows one of the branches. When it is compressed further, the pressure diverges at one packing fraction, which, therefore, depends on the protocol. For a different protocol, the systems may stay longer on the red branch and the pressure diverges at a higher packing fraction. Thus, it is reasonable to define the Jamming packing fraction as the packing fraction at which the pressure diverges. The green line represents

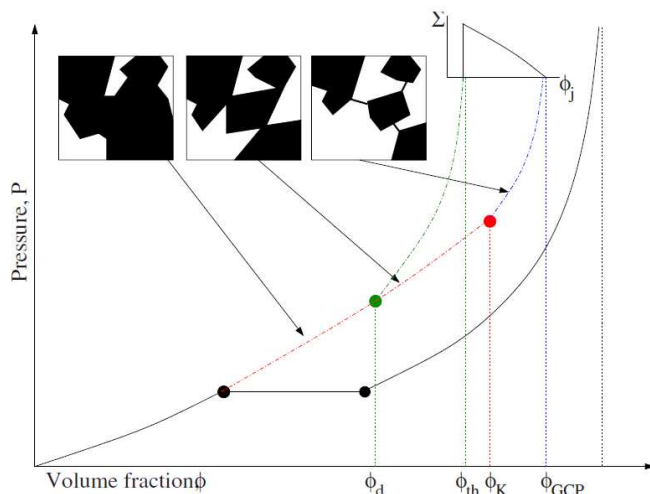


Figure 1.18: **Schematic mean-field phase diagram of hard spheres in \mathbb{R}^3 .** (P, ϕ) diagram: the full black line represents the equilibrium phase diagram with the liquid-solid transition. In the inset, the complexity, *i.e.*, the logarithm of the number of glassy states, is plotted as a function of the Jamming density ϕ_j . The boxes show a picture of the (dN) -dimensional phase space of the system: black configurations are allowed; white ones are forbidden by the hard-core constraint. Extracted from Parisi and Zamponi [2010].

the lowest density glass phase that leads to the lowest jamming density ϕ_{th} . At ϕ_K , the system reaches its densest equilibrated state, its glass branch diverges at the Random Close Packing (or Glass Close Packing). On the inset is represented the complexity, *i.e.* the logarithm of the number of glassy states versus their associated jamming packing fraction. The complexity is maximum at ϕ_{th} and decreases monotonically to zero at ϕ_{GCP} .

We plot in figure 1.19 a schematic representation of the m —density space. On the $m = 1$ line lies the thermodynamic transition for a liquid ($\phi < \phi_d$) to a supercooled liquid with many metastable states ($\phi_d < \phi < \phi_K$), where the complexity is finite, to the ideal glass, ($\phi = \phi_K$). Lower values of m allow one to study the thermodynamic of the glass, on approaching the jamming, for $m \rightarrow 0$. Thus, the various Jamming densities are the $m \rightarrow 0$ limit at finite complexity: $\phi_{th} < \phi < \phi_{GCP}$.

To conclude, there are as many glass transition packing fractions as Jamming packing fractions, but they are not the same. Indeed, while the glass transition of one configuration can be seen as a crossover from equilibrated supercooled liquid to a glass (leaving the red branch), the Jamming transition is the upper limit of the glass (end of green and blue branches).

This is of great importance when we investigate this issue with experiments or simulations, if we want to compare Jamming and glass transitions,

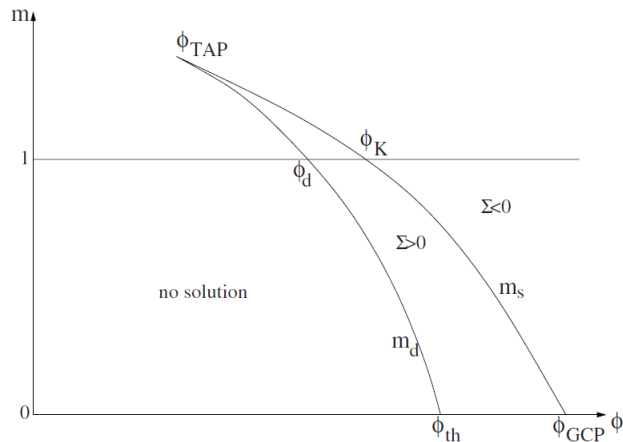


Figure 1.19: (m, φ) **diagram**. “Schematic (m, φ) diagram: above the clustering line $m_d(\varphi)$ a nontrivial solution for the inter-replica correlation is found. This solution gives a positive complexity in the region enclosed between the lines m_d and m_s ; therefore, in this region glassy states are present. The line $m_s(\varphi)$ is defined by the condition $\Sigma(m, \varphi) = 0$ and corresponds to the ideal glass state. The intersections of the line $m_d(\varphi)$ (respectively $m_s(\varphi)$) with $m = 1$ and 0 define φ_d (respectively φ_K) and φ_{th} (respectively φ_{GCP}).” Extracted from Parisi and Zamponi [2010].

one has to do this within the very same realization, and not between different experiments.

For the purpose of completeness, let us mention that the case of the ideal glass transition has been investigated in two dimensions in various models [Santen and Krauth, 2000, Torquato et al., 2000, Tarzia, 2007, Donev et al., 2006]. These works report no ideal glass transition in two dimensions.

1.2.3 Glassy dynamics in colloids and granular media

1.2.3.1 Two-step relaxation function

Upon approaching the glass and the Jamming transitions, a complex glassy dynamics sets in: first a two-step relaxation process is observed; second, the microscopic dynamics reveals strong correlated motions: *dynamic heterogeneities*. In order to study the relaxation of the density profile, a common tool is the dynamical structure factor [Berthier et al., 2011b]:

$$F(\vec{k}, t) = \frac{1}{N} \left\langle \sum_{i=1}^N \exp -i\vec{k} \cdot \vec{r}_i(t) \sum_{j=1}^N \exp i\vec{k} \cdot \vec{r}_j(0) \right\rangle, \quad (1.10)$$

where $r_i(t)$ is the position of the particle i at time t , k is a wave vector and $\langle \cdot \rangle$ is an ensemble average. Note that $F(\vec{k}, t)$ is also the time autocorrelation

of the Fourier transform of the density $\rho_{\vec{k}}(t)$:

$$F(\vec{k}, t) = \frac{1}{N} \left\langle \rho_{\vec{k}}(t) \rho_{-\vec{k}}(0) \right\rangle. \quad (1.11)$$

It can be shown that Dynamic Light Scattering (DLS) can probe the self part of quantity $F_s(\vec{k}, t)$ (*i.e.* summing only with $i = j$ in equation 1.10) [Cipelletti and Weeks, 2011]. In addition, note that in practice, the ensemble average is sampled over time. The phenomenology in question is quite general, as it can be found not only in various simulations of colloidal particles and of Lennard-Jones liquids, but also in molecular glasses. As a matter of fact, some features are even predicted by MCT [Reichman and Charbonneau, 2005]. We represent in figure 1.20 (a) $F_s(\vec{k}, t)$ versus t at one fixed $k = \|\vec{k}\|$ for different densities obtained from DLS in a PMMA colloidal experiments [Brambilla et al., 2009]. For low densities, it decreases continuously from 1 to 0 within three temporal decades. For high densities (above $\phi \sim 0.55$), the decrease can be decomposed in two steps: (i) a short time decorrelation

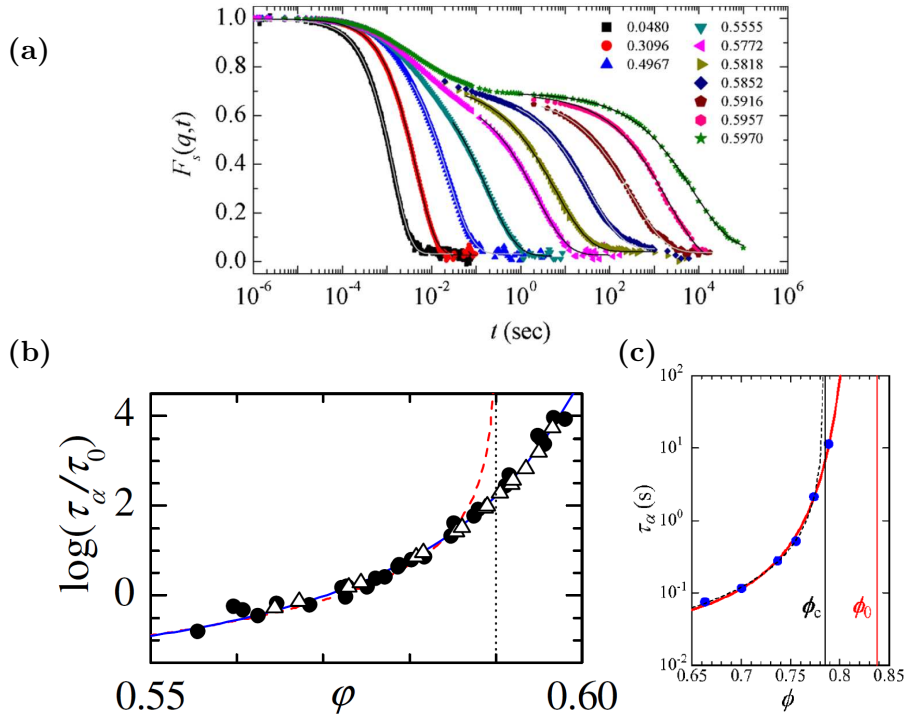


Figure 1.20: **Two steps relaxations in Colloids.** (a): Dynamical structure factor versus lag time for different densities in a colloidal suspension of PMMA at one fixed wave vector q . (b): corresponding decay time of the second relaxation τ_α versus packing fraction. Extracted from Brambilla et al. [2009]. (c): Decay time τ_α versus packing fraction in an experiment of 2D shaken grains. Extracted from Watanabe and Tanaka [2008].

(called β relaxation), and the dynamical structure factor drops down to 0.7. The typical decay time of this relaxation does not depend much on density; (ii) a long time decorrelation (called α relaxation) sets in afterwards, the dynamical structure factor drops down to 0. In contrast with the first relaxation, this decorrelation decay time depends strongly on density and tends to diverge as the packing fraction is increased. This decay can be fitted by a stretched exponential $\exp -(t/\tau_\alpha)^\beta$. τ_α can thus be plotted versus packing fraction in figure 1.20 **(b)**. τ_α seems to diverge at a packing fraction 0.637.

N.B.: Direct space analogs of the dynamical structure factor can also be used [Abate and Durian, 2007, 2006, Keys et al., 2007, Lechenault et al., 2010, 2008a,b, Dauchot et al., 2005]. This is of interest for direct imaging techniques, where the Fourier calculation of the dynamic structure factor is not necessary. The self part thus is

$$Q(a, t) = \frac{1}{N} \left\langle \sum_{i=1}^N W_a(\|\vec{r}_i(t) - \vec{r}_i(0)\|) \right\rangle, \quad (1.12)$$

where $W_a(\|\vec{r}_i(t) - \vec{r}_i(0)\|)$ can be for instance [Keys et al., 2007]:

$$W_a(\|\vec{r}_i(t) - \vec{r}_i(0)\|) = \begin{cases} 1 & \text{if } \|\vec{r}_i(t) - \vec{r}_i(0)\| \leq a \\ 0 & \text{if } \|\vec{r}_i(t) - \vec{r}_i(0)\| > a \end{cases}, \quad (1.13)$$

or [Dauchot et al., 2005]

$$W_a(\|\vec{r}_i(t) - \vec{r}_i(0)\|) = \exp -\frac{\|\vec{r}_i(t) - \vec{r}_i(0)\|^2}{2a^2}. \quad (1.14)$$

These different definitions are equivalent in principle. We see that the wave vector is replaced by a length a , that can be adjusted to probe the dynamics. This can be determinative when the scale at which the dynamics takes place changes, for instance close to the Jamming transition [Lechenault et al., 2008b, Haxton and Liu, 2010].

Among others, Abate and Durian [2006, 2007], Keys et al. [2007], Watanabe and Tanaka [2008] and Watanabe et al. [2011] have been performed similar measurements in two dimensional shaken granular media. The major advantage of grains is their size: their trajectories are directly accessible. Hence $F_s(k, t)$ is obtained directly from particle tracking. Similar procedure leads then to a measurement of τ_α , which is plotted versus packing fraction in figure 1.20 **(c)**. A Vögel-Fucher-Tamman fit leads to a divergence at $\phi = 0.838$.

1.2.3.2 Dynamical Heterogeneities

We have seen that, like molecular glasses, granular and colloidal glasses exhibit a drastic slowing down as the packing fraction is increased. One of the major interest of these materials is that we can actually image them, and hence understand the microscopic mechanisms associated with this slowing down. In order to study the microscopic details of the dynamics [Berthier et al., 2011b, Tarjus, 2012], one can define a single particle mobility

$$f_i(\vec{k}, t, 0) = \exp i\vec{k} \cdot (\vec{r}_i(t) - \vec{r}_i(0)), \quad (1.15)$$

or equivalently,

$$f_i(a, t, 0) = W_a(\|\vec{r}_i(t) - \vec{r}_i(0)\|). \quad (1.16)$$

As an example, we plot in figure 1.21 mobility maps extracted from shaken granular experiments. We see that the mobilities are heterogeneous; these are the so-called *dynamic heterogeneities*. The spatial correlations of the mobility field or maps can be extracted (see box): the size of these dynamic heterogeneities can be estimated directly through the decay of the spatial correlator $G_4(r, t)$, but this is a complicated task. Easier to compute is its integral, $\chi_4(t)$, which is directly related to $\xi_4(t)$.

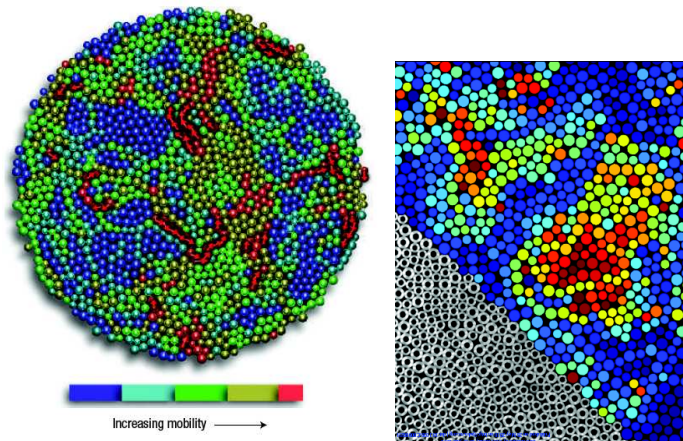


Figure 1.21: **Dynamic Heterogeneities.** Maps of Mobilities of driven granular materials (see text for definition). **(Left):** Mobile regions are indicated in red and immobile regions in blue. Extracted from Keys et al. [2007]. **(Right):** Mobile regions are indicated in blue and immobile regions in red. Extracted from Lechenault et al. [2010].

We can thus define a mobility field

$$f(\vec{r}, \vec{k}, t, 0) = \frac{V}{N} \sum_{i=1}^N \delta^{(d)}(\vec{r} - \vec{r}_i(t)) f_i(\vec{k}, t, 0), \quad (1.17)$$

where $\delta^{(d)}$ is the delta function in dimension d . Thus, the spatial autocorrelation of $f(\vec{r}, \vec{k}, t, 0)$ is given by

$$G_4(r, t) = \frac{N}{V^2} \int d^d r' \langle \delta f(\vec{r}, \vec{k}, t, 0) \delta f(\vec{r} - \vec{r}', \vec{k}, t, 0) \rangle, \quad (1.18)$$

where

$$\delta f(\vec{r}, \vec{k}, t, 0) = f(\vec{r}, \vec{k}, t, 0) - \langle f(\vec{r}, \vec{k}, t, 0) \rangle. \quad (1.19)$$

Analogy with critical phenomena can lead to the assumption that

$$G_4(r, t) \sim \frac{A(t)}{r^p} \exp -\frac{r}{\xi_4(t)}. \quad (1.20)$$

$\xi_4(t)$ is thus the typical decay length of the spatial mobility field. We can also consider $\chi_4(t) = \int d^d r G_4(r, t)$, which can also be written as

$$\chi_4(t) = N \left\langle \frac{1}{N} \left(\sum_{i=1}^N f(\vec{r}_i, \vec{k}, t, 0) - \langle f(\vec{r}, \vec{k}, t, 0) \rangle \right)^2 \right\rangle. \quad (1.21)$$

Therefore, if equation 1.20 is satisfied,

$$\chi_4(t) \sim \xi_4(t)^d. \quad (1.22)$$

The size of the dynamical heterogeneities has been reported to increase as the packing fraction is increased in several experimental study of bidimensional driven granular materials [Watanabe and Tanaka, 2008, Keys et al., 2007]. We plot in figure 1.22, top left, the dynamical susceptibility versus lag time for different packing fractions. The time location of the maximum gives the typical time at which the systems is the most heterogeneous: it increases with packing fraction. The magnitude of the maximum increases as the packing fraction is increased. To summarize, as the packing fraction is increased, the system becomes more and more heterogeneous on longer timescales. The magnitude of the dynamical heterogeneities is plotted for a similar experiment [Watanabe and Tanaka, 2008] in figure 1.22, top right. We see that it increases with packing fraction.

However, closer investigation of the dynamics when the system is in the vicinity of the Jamming point has revealed rather intriguing non-monotonic behavior of the dynamical susceptibility. (i) in PMMA (hard colloids) colloidal systems [Ballesta et al., 2008]. The maximal dynamic susceptibility is plotted versus packing fraction in figure 1.22, bottom left. A maximum is

located close to $\phi \sim 0.73$ whereas the Jamming packing fraction is identified as $\phi = 0.752$ (dotted line on the figure). (ii) In a vibrated granular experiment [Lechenault et al., 2008b]. The maximal dynamical susceptibility is plotted versus packing fraction, and it is maximum at $\phi = 0.8416$, whereas the Jamming packing fraction is identified at $\phi = 0.8436$. In these two experiments, a strong dynamical signature occurs at a slightly lower packing fraction than the Jamming packing fraction. Note that in both cases, the structural relaxation time scale has exceeded the experimental window, and the probing wave vector, \vec{k} , or length a , are in both cases close to a hundredth of particle diameter. The same mechanism seems to be at play in these two different experiments, and it seems it has something to do with the Jamming threshold.

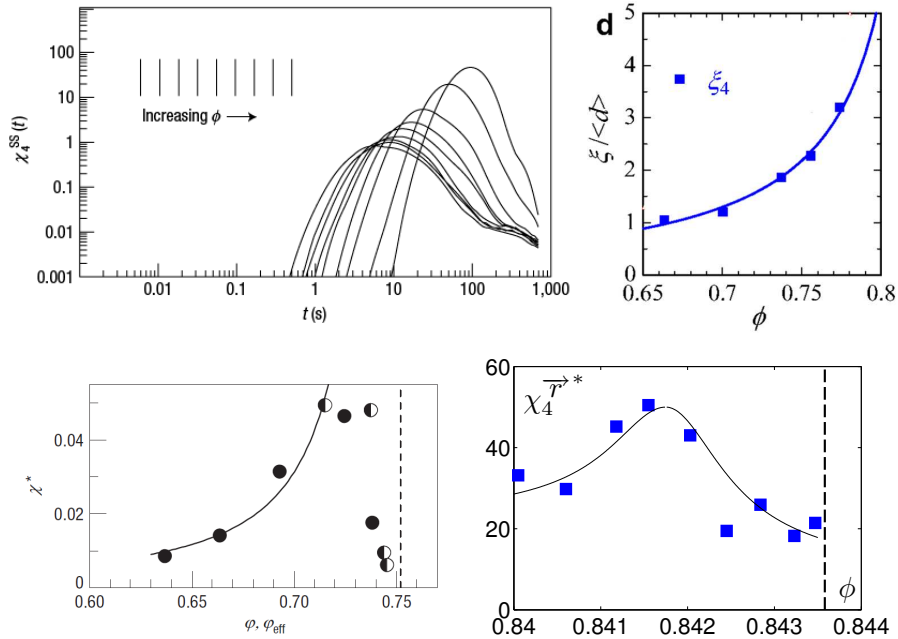


Figure 1.22: **Dynamical Susceptibility.** In 2D driven granular experiments. **(Top Left):** Dynamical susceptibility versus lag time for different packing fractions. Extracted from Keys et al. [2007]. **(Top Right):** Maximal dynamical susceptibility versus packing fraction. Extracted from Watanabe and Tanaka [2008]. **(Bottom Left):** Maximal dynamical susceptibility versus packing fraction for colloids. Extracted from Ballesta et al. [2008]. **(Bottom Right):** Maximal dynamical susceptibility versus packing fraction for shaken grains. Adapted from Lechenault [2007].

1.2.4 Intermezzo

1.2.4.1 Timescales

Let's now try to gather what we have learned in these two sections: we represent in figure 1.23, top, both (i) the glass transition side (blue part) for hard spheres at finite temperature and (ii) the jammed side (red part) for soft spheres at zero temperature. A tremendous increase of timescales happens on both sides: (i) the structural relaxation time scale τ_α increases as packing fraction is increased. Around ϕ_g , it exceeds τ_{exp} , the experimentalist patience time. τ_α can be extrapolated by a MCT fit, which diverges at ϕ_{MCT} . A better fit is given by a Vögel-Fucher-Tamman fit, which yields a divergence at a packing fraction ϕ_0 . Trying to connect with thermody-

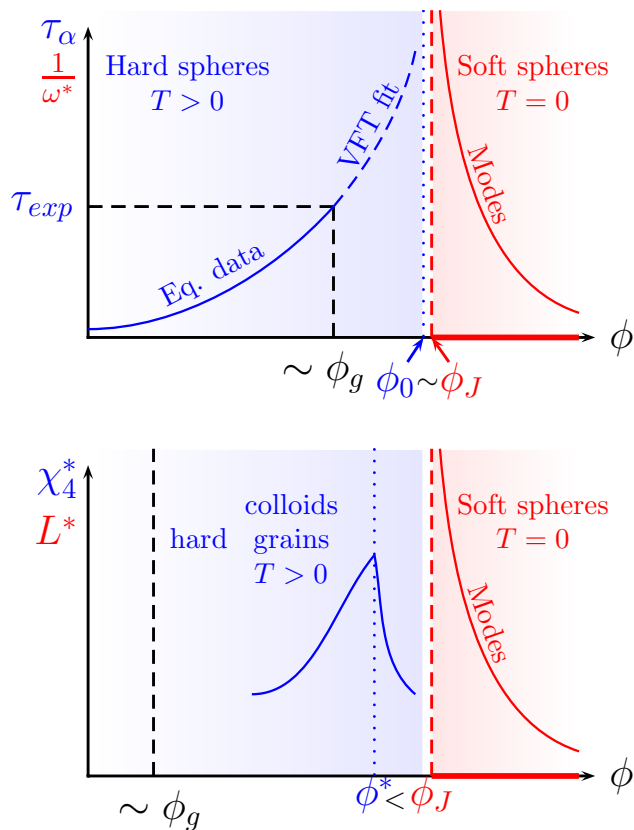


Figure 1.23: **Glasses and Jamming. Top: timescales.** Schematic picture of the hard spheres glass transition and diverging timescale at the unjamming transition of a-thermal soft spheres. **Bottom: length-scales.** Maximal dynamical susceptibility versus packing fraction for agitated hard spheres and diverging length-scale at the unjamming transition of a-thermal soft spheres.

namics, mode coupling transition ϕ_{MCT} is close to the dynamic transition at ϕ_d , and VFT divergence ϕ_0 is close to the ideal glass transition ϕ_K .

In practice, ϕ_0 is found to be close to the jamming onset, ϕ_J , *i.e.* where the pressure diverges (see table 1.1). Nevertheless, since the value of ϕ_0 is given by an extrapolation, it is difficult to claim it confidently.

(ii) On the other side, the typical frequency of vibrational modes scales with the distance to Jamming of soft jammed spheres. In other words, the timescales $1/\omega^*$ of the slowest vibrational modes diverge when ϕ_J is approached.

As proposed by Liu and Nagel [1998], one could be tempted to understand sides (i) and (ii) within a common framework, especially because the packing fractions ϕ_0 and ϕ_J are close. We display in table 1.1, the typical packing coming from either numerical, experimental or theoretical studies of the glass transition and Jamming.

1.2.4.2 Lengths

We gather now the evidence of diverging length scales on sides (i) and (ii). (i) As sketched in figure 1.23, bottom, recent work on hard colloids and vibrated grains [Ballesta et al., 2008, Lechenault et al., 2008a] have measured a non-monotonous dynamical susceptibility χ^* at a density ϕ^* , lower than the Jamming packing fraction ϕ_J . This dynamical susceptibility can be related to a dynamical length, which is therefore maximal at ϕ^* . (ii) On the other side, we have seen that the vibrational modes are associated to diverging length when approaching the unjamming transition.

1.2.4.3 Interm-end-zo

To conclude, we see that it is tempting to associate the Jamming and the glass transition because time and length scales diverge at similar packing fractions: the values of ϕ_0 of the divergence of the VFT fit and the values of ϕ_J of the Jamming transition displayed in table 1.1 seem close.

However, there is a conceptual difficulty when trying to bridge the athermal soft spheres unjamming transition and the thermal hard spheres glass transition. Indeed, because it is a non-equilibrium problem, we would like to stress that, to be addressed properly, the Jamming transition has to be studied along one experimental or numerical realization. In contrast, the study of the glass transition is an equilibrium game: it is the the equilibrium relaxation time that is fitted by the VFT fit.

Therefore, in order to compare the Jamming and glass transitions, one has to work in the same experimental realization. This is what has been done in [Ballesta et al., 2008, Lechenault et al., 2008a], and a dynamical signature of the Jamming transition has been observed just below the Jamming transition, but still remains to be understood.

Second, in order to be able to study both sides of the Jamming transition, one has to study a system of soft particles. A first attempt is then to study the glass and the Jamming transitions of thermal soft spheres.

Work	Reference	ϕ_g	ϕ_{MCT}	ϕ_d	ϕ_0	ϕ_K	ϕ_J	ϕ_{MRJ}	ϕ_{RCP}
3D Theory	Parisi and Zamponi [2010]			0.58		0.6165	0.64-0.68		0.6836
2D Theory						0.811-0.816			0.874
3D Numerics	Torquato et al. [2000]							0.64	
3D Exp. Colloids	Brambilla et al. [2009]	0.59	0.590		0.637				
	van Megen and Underwood [1994]	0.58	0.58						
3D Numerics	Berthier and Witten [2009b]		0.592		0.635		0.648		0.67
2D Exp. Grains	Keys et al. [2007]	0.79	0.79		0.84		0.84		
	Watanabe and Tanaka [2008]	0.80	0.789		0.838		0.84		

Table 1.1: Glass transition and Jamming packing fractions.

1.3 Bridging the gap: Going soft

We have described both sides of the Jamming transition: (i) above Jamming, we have described the properties of jammed solids; (ii) below Jamming, we have described the interplay of Jamming and glass transitions for hard sphere systems. In order to bridge the gap between these two sides, let's add a further ingredient : softness.

1.3.1 Glass transition of soft spheres

The glass transition of soft spheres has been studied recently, numerically in Berthier and Witten [2009b]. This study yields the picture drawn in figure 1.24, where we represent a $(T-\phi)$ phase diagram. Squares represent equilibrium simulations and dotted lines iso- τ_α lines. First, τ_α can be rescaled with respect to T and ϕ by a dynamic scaling law, very analogous to what is done in critical phenomena. This yields a “scaled glass line”, that corresponds to the divergence of τ_α . Note that the $T \rightarrow 0$ limit corresponds to the hard sphere limit, and data can be extrapolated with a VFT fit. No clear link with the Jamming transition could be established at that time.

1.3.2 Thermal vestiges of Jamming

Closer investigations of the Jamming transition at lower temperature in both numerics and colloids experiments [Zhang et al., 2009] have finally revealed a structural signature of the Jamming transition: the pair correlation function displays a maximum, whose amplitude decreases and whose location shifts as the temperature is increased. The experimental part of this paper

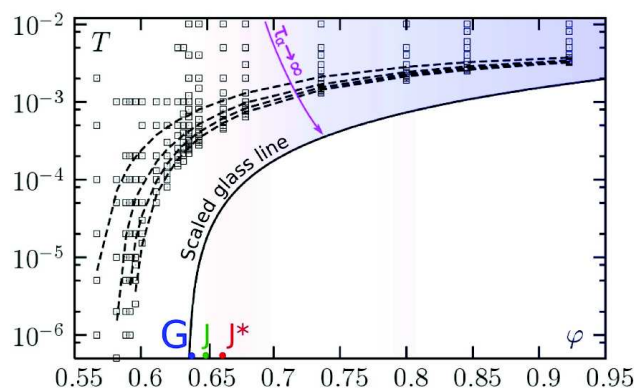


Figure 1.24: **Glass transition for soft spheres.** Phase diagram for soft spheres. Squares represent equilibrium simulations and dotted lines iso- τ_α lines. Point G is located at $T \rightarrow 0$ and $\phi_0 = 0.635$. Taken from Candelier [2009], which was extracted from Berthier and Witten [2009b].

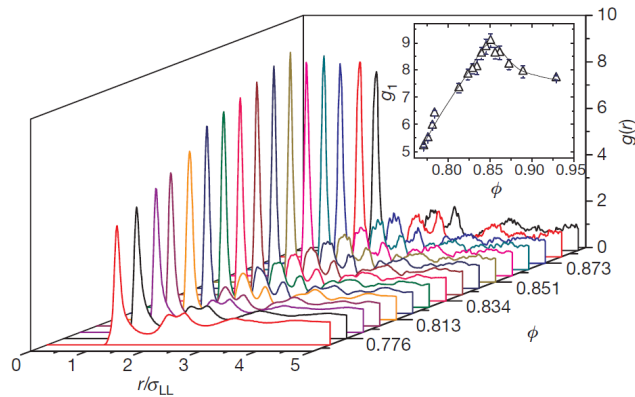


Figure 1.25: **Thermal vestiges of the Jamming transition.** Partial pair correlation function versus distance for various densities in NIPAM colloids. **Inset:** Maximum of the pair correlation function versus packing fraction. Extracted from Zhang et al. [2009].

only probes one temperature but also reports a finite maximum. We represent in figure 1.25, the partial pair correlation function—*i.e.* the radial distribution of large particles—for different densities. The first peak maximum g_1 is maximum at an intermediate packing fraction. Note, nonetheless, that Cheng [2010] measured the same effect in a-thermal tapioca pearls (of diameter 5 mm): the finiteness of the maximum is then certainly due to finite size effects so that it is not clear that they are not dominant also in colloids.

1.3.3 Getting them together

Recent theoretical developments drawn from the replica approach introduced in section 1.2.2.2 have extended it to the case of harmonic spheres [Berthier et al., 2011c, Jacquin et al., 2011]. The computation of the complexity has allowed one to locate both the thermodynamic glass transition and the Jamming transition in one unique theoretical description.

We plot in figure 1.26 their results. In panel (a), we represent the theoretical phase diagram. The red line represents the Kauzmann temperature—*i.e.* where complexity vanishes—with respect to packing fraction. The magenta dotted line represents the ground state energy, which originates in the overlap of particles. These lines are different. Of course, the sketch displays a caricature, where the system jams at ϕ_{GCP} , but any Jamming density $\phi_J < \phi_{GCP}$ would yield a similar scenario.

In panel (b), the optimal m parameter is plotted versus temperature for different packing fractions: the $m \rightarrow 0$ limit, which gives the zero temperature limit, can be investigated at various packing fractions. This allows

one to compute the thermodynamic of the glass through Jamming. In panel **(c)**, m^*/\sqrt{T} versus $|\phi - \phi_{GCP}|/\sqrt{T}$ shows scaling collapse, which is different on both sides of ϕ_{GCP} . From thermodynamics, the pair correlation function can be derived. Its maximum is reported versus packing fraction for different temperatures in panel **(d)**. At low temperatures, it has a huge maximum at ϕ_{GCP} . As the temperature is increased, the magnitude of this maximum decreases and its location is shifted towards higher packing fractions. Finally, the pair correlation function also allows one to compute the average number of contacts, which is plotted versus packing fraction for different densities in panel **(e)** for both theoretical and numerical results. In the regime $\phi > \phi_{GCP}$, theory and simulation clearly disagree. However, in the regime $\phi < \phi_{GCP}$, they seem to match in the low temperature limit.

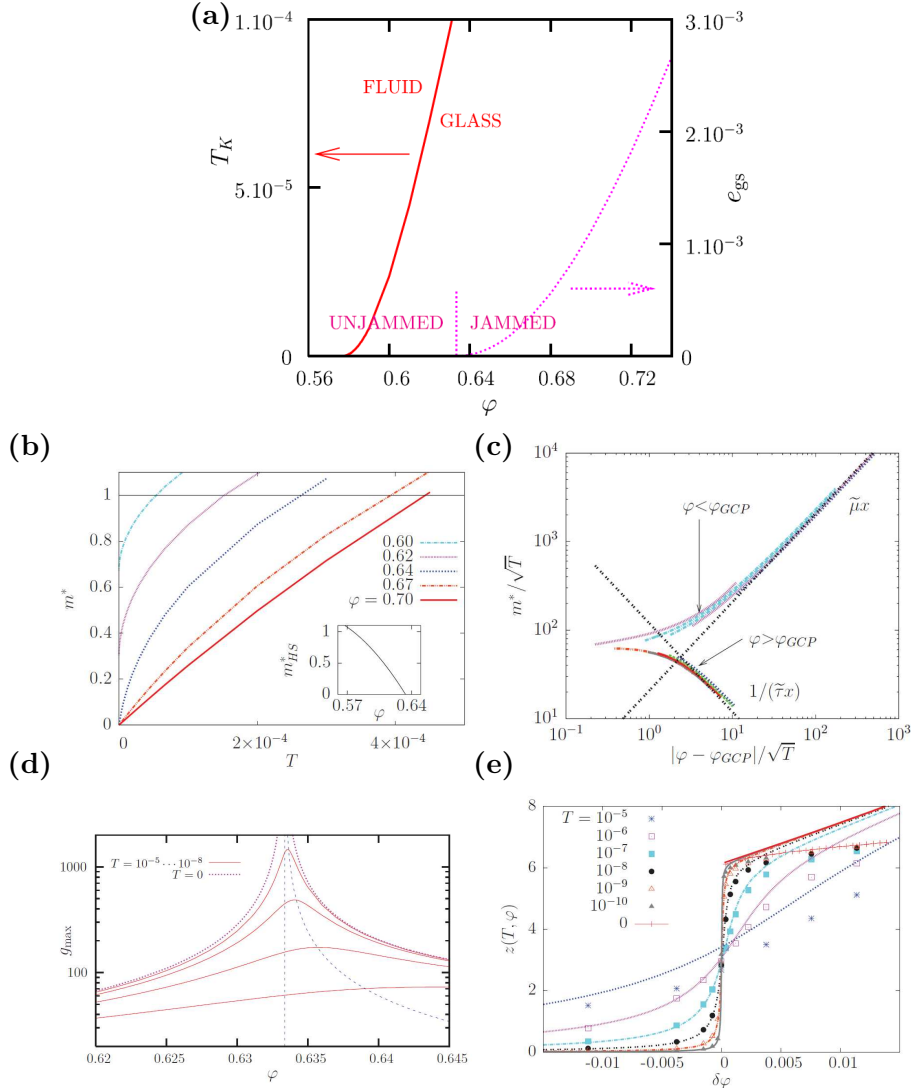


Figure 1.26: **Thermodynamics and structure close to Jamming.** (a): “Theoretical phase diagram of soft repulsive spheres. The glass transition temperature T_K separates the liquid and glass phases with $T_K \sim (\phi - \phi_K)^2$ near $\phi_K \sim 0.577$. At $T = 0$, the glass jams under compression across $\phi_{GCP} = 0.633$, above which no glass state with no particle overlap exists at $T = 0$. Thus, the ground state energy e_{gs} increases continuously from 0 as $e_{gs} \sim (\phi - \phi_{gcp})^2$.” Extracted from Jacquin et al. [2011]. (b): Replica parameter m^* versus temperature for different densities. (c): Scaling of Replica parameter m^* with respect to temperature and different densities. (d): First peak of the pair correlation function versus density for different temperatures. (e): Average contact number versus density for different temperatures. The lines indicate the theory and the markers indicate numerical simulations. Extracted from Berthier et al. [2011c].

1.3.4 Open questions

To conclude, despite some discrepancies, a unique theoretical framework of thermal soft spheres has allowed us to understand the differences between the Jamming and the Glass transition, and to recover experimental and numerical observations of structural thermal vestiges of Jamming. Altogether, the Jamming transition happens to lose its criticality in the presence of temperature.

However, neither this theoretical static mean-field approach—which has nothing to say about the dynamics, nor the experimental investigations of soft thermal spheres, have been able to explain the interplay between the maximal dynamical heterogeneities observed at ϕ^* in hard colloids or vibrated grains and the Jamming transition $\phi_J > \phi^*$. The question whether the mechanical vibration is similar to temperature, and how friction matters is also an open question in granular media.

Finally, the underlying mechanisms of such a dynamical signature are still unknown.

1.3.5 This work

We have seen in section 1.1.2.1 that the number of contacts is a good parameter to describe the vibrational and mechanical properties of the Jamming transition. We have also seen that using soft particles allows to cross the Jamming transition and to better understand the relationship between Jamming and unJamming.

Therefore, vibrated photo-elastic soft grains seem to be a good experimental model system to tackle those issues.

This work will address the vicinity of the Jamming transition in a vibrated layer of bi-disperse *soft disks*. We will modify the experiment used in F. Lechenault's PhD [Lechenault, 2007] in order to adapt to photo-elasticity techniques and study the dynamics and the statics of the contact network across the Jamming transition.

Chapter 2

Experimental Setup

2.1 Existing setup

2.1.1 Hardware

The original experimental setup was built during the Ph.D. of Frédéric Lechenault and used again during Raphaël Candelier's Ph.D. Many people contributed to this setup: Marco Bonetti, Raphaël Candelier, Olivier Dauchot, Frédéric Lechenault, Patrick Meininger, Vincent Padilla, Cécile

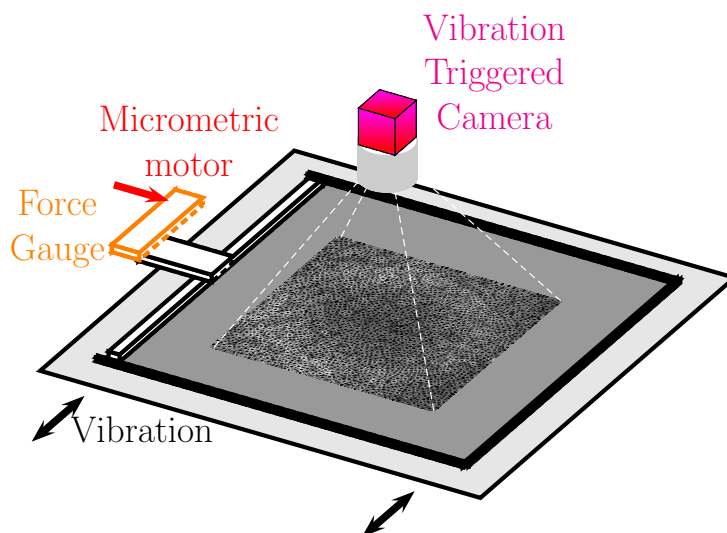


Figure 2.1: **Brass disks experimental setup.** See text for a description.

Wiertel-Gasquet. Lots of information about the experimental setup can be found in their Ph.D. manuscript [Candelier, 2009, Lechenault, 2007]. Before turning to photo-elasticity, we had further improved the setup, mainly by interfacing several motors with the acquisition program, and by reinforcing some mechanical parts. The following description takes account of these slight modifications, and is presented in figures 2.1, 2.2 and 2.3. A mixture of 8000 bi-disperse brass disks (a) —of diameter 4 and 5 mm— lies on a glass plate (b). In order to prevent them from buckling, a Plexiglas board lies upon them, with a clearance of 1 mm. They are confined in a rectangular cell (c): the width of the cell is fixed, and is equal to 400.00 mm, and its length can be tuned between 393.22 and 377.22 mm, thanks to a moving piston (d) on one side. The moving piston is attached to a slider¹ (e) and pushed by a force sensor² (f). Force measurements can thus be performed through an amplifier³ and acquisition board⁴, and then transformed into data files through interfacing program⁵. The force sensor is attached to a micrometric translation step motor⁶, which is driven by an external controller⁷. The controller can be interfaced to the computer by a USB port. The translation stage is fixed to an optical table⁸ (g) underneath. The

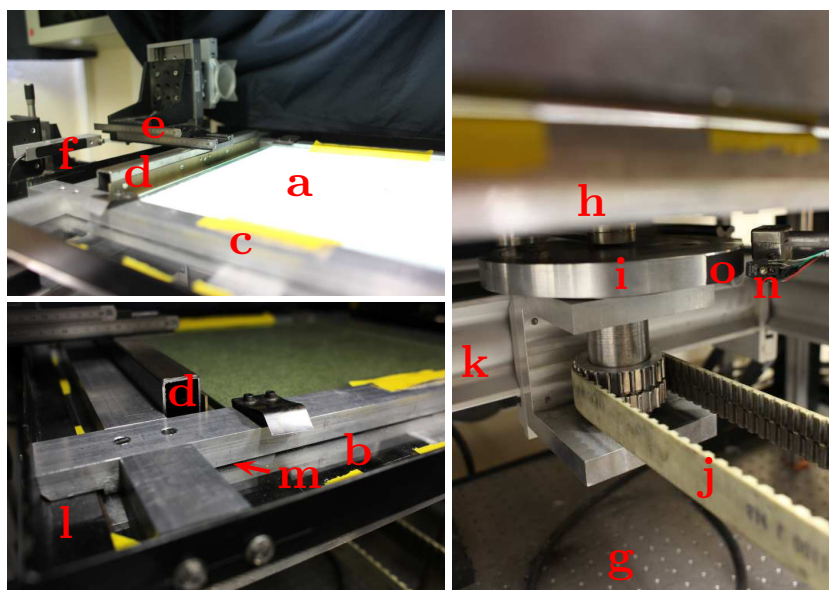


Figure 2.2: **Pictures of the setup.**

See text for description.

¹Microcontrôle

²Tedea Huntleigh, 1024, 7kg

³Tedea Huntleigh, Model 433 Bridgesensor

⁴National Instruments, DAQPad, 6020E

⁵National Instruments, LABView

⁶Microcontrôle, MT160PP

⁷Newport, Motion Controller ESP 301

glass plate (570 mm \times 570 mm) is embedded in a home made⁹ aluminum frame **(h)** (600 mm \times 600 mm). Under the glass plate is taped a black tissue to ensure optimum contrast of the pictures. A rubber gasket and tight taping ensure smooth contact and no slipping between the glass board and the aluminum frame. The frame is attached on three sliders¹⁰. One of the sliders is connected by a rod to an eccentric revolving shaft **(i)**, which is driven by a stepper motor¹¹ **(p)** through a notched belt **(j)**. The stepper motor is driven at constant speed by a controller¹², which is embedded in a switchgear cubicle, so that it is electronically isolated. The motor is fixed to a home made “bridge” **(k)** made of bars¹³. In order to prevent this bridge from vibrating, it is attached to the wall of the lab room **(u)** and to a box containing 300 kg of lead bricks. The lower part of the sliders—also attached to the bridge—allows one to fine-tune the leveling of the oscillating board to make it horizontal. All efforts have been made to mechanically separate the bridge from the confining cell. The cell is embedded in a bigger frame **(l)**, which is attached to four manual micrometric translation stages¹⁴ **(r)**. This allows one to ensure precise leveling of the confining cell with respect to the oscillating board: the gap **(m)** is fixed at 0.75 mm. The translation stage are attached to stainless steel bars¹⁵ **(t)**, which are screwed to the optical table. Also attached to the optical table is a trigger. The trigger is made of a reflection photo-transistor/photo-diode device¹⁶ **(n)**, together with a home made Schmitt trigger electronic circuit¹⁷. The device is set in front of the revolving shaft, where a piece of black tape **(o)** has been taped. As a result, when the sensor is in front of the tape, we obtain a 5 V signal and when the sensor is in front of the aluminum, we obtain a 0 V signal. Therefore, we can tune the Mark-to-Space ratio of the trigger signal by changing the length of the black tape, and we we can change the phase of the trigger by changing the position of the tape on the shaft.

The camera¹⁸ **(s)** is fixed on a shelf **(q)**. The shelf lies on the optical table, with rubber bands inserted in between: they are crucial to damp the vibrations in order to prevent vibration induced blur of pictures. We use a 28 mm focus lens¹⁹, which is at a distance 300 mm from the grains. This images the center of the disk assembly (165 mm \times 165 mm). The pictures

⁸Newport, RP Reliance™, Sealed Hole Table Top.

⁹V. Padilla Corp.

¹⁰Microcontrôle

¹¹Yaskawa, AC Servo Motor, SGM2H-15-AAA61D-OY.

¹²Omron, SGD7 15AE-S-OY

¹³Microcontrôle

¹⁴Microcontrôle

¹⁵Microcontrôle, X95

¹⁶Honeywell, HOA1405, DC Supply: Sodilec, 5V, 1A

¹⁷Texas Instruments, SN74HC14, DC Supply: Sodilec, 5V, 1A

¹⁸RedLake Megaplug II, Monochrome, 2048 \times 2048, 8 bits

¹⁹Nikon, 1.8, 28 mm

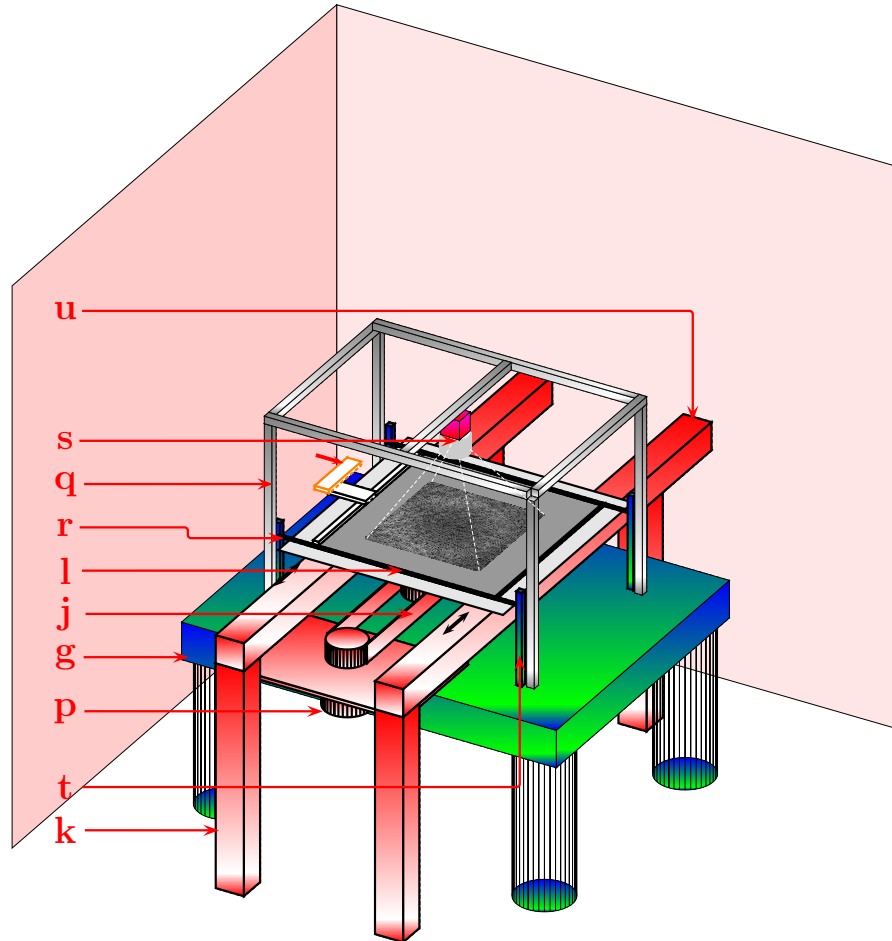


Figure 2.3: **Ensemble view of the brass disk experimental setup.** See text for a description.

are triggered with the phase of the vibration using the previously described trigger. This trigger is plugged into the Camera acquisition card²⁰, which is then transferred to the acquisition computer²¹. The external light is provided by 12 incandescent 100-Watt bulbs placed around the camera so that the light diffused by the disks is as homogeneous as possible and that there is no aliasing of light intensity.

²⁰Redlake Megaplus II, Camera Link protocol

²¹DELL, RAID-0 mounted 750 Go Hard drive.

2.1.1.1 Sensor Stiffness

The sensor has a finite stiffness. We perform a calibration of the sensor that consists of compressing two stainless steel bars²², which deform much less than the sensor as represented in figure 2.4, left. We thus measure the force F with respect to the translation stage position μ . We plot in figure 2.4, right, F versus μ . It increases linearly, with a slope $k_{sensor} = 5.73 \text{ kg/mm}$. Therefore, the position of the piston is $\mu_{piston} = \mu - F/k_{sensor}$.

2.1.2 Software

The major improvement we have brought to the acquisition and control software consists in building an all-in-one program. We can then choose between automatic or manual control over the following features:

- control and measurement of the position of the piston;
- control of the vibration frequency;
- synchronization between pictures and piston force measurement;

We display in figure 2.5 the interface of the software we have developed and its principle of operation.

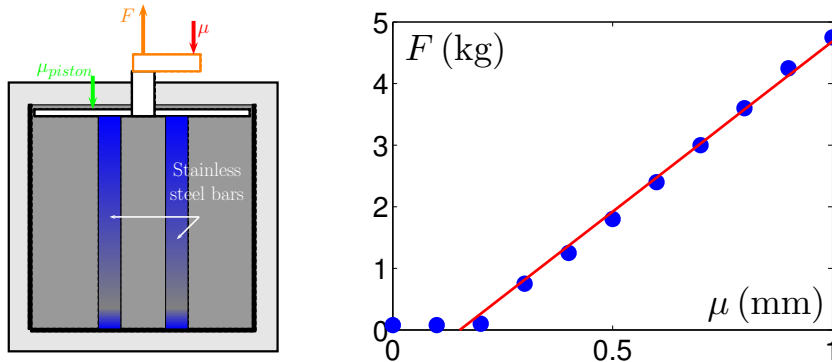
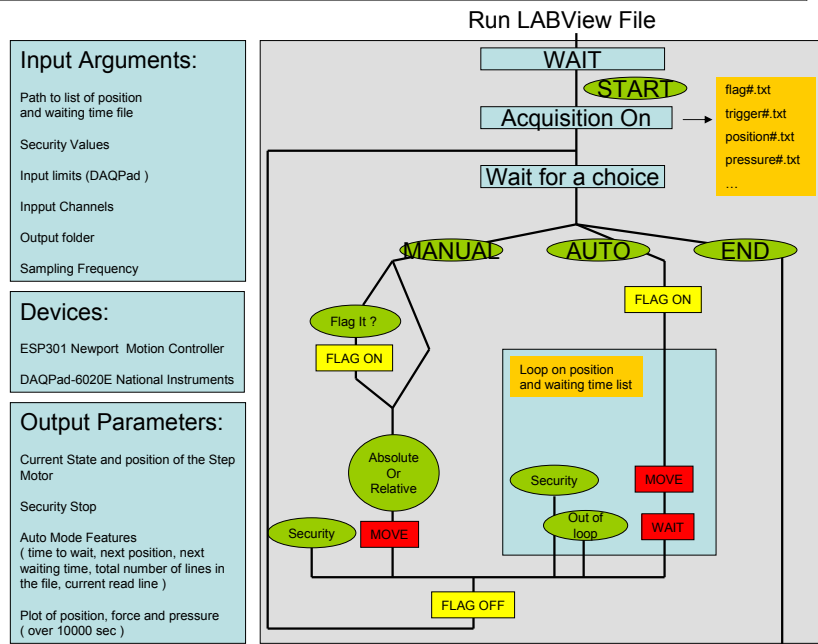
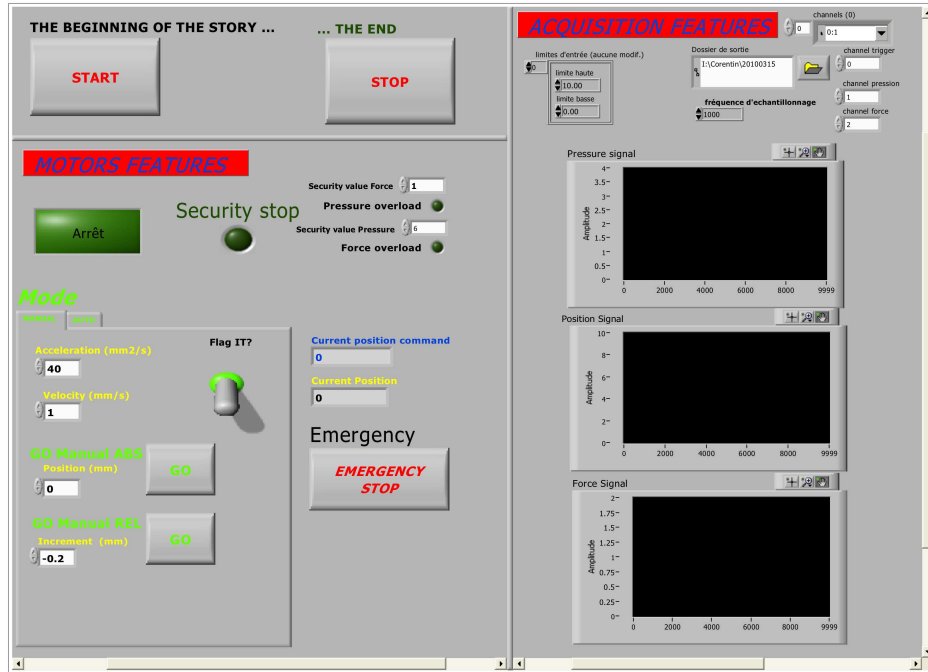


Figure 2.4: **Calibration of the force sensor.** **Left:** Sketch of the calibration experiment. F is the force measured by the sensor; μ is the position of the translation stage; μ_{piston} is the position of the piston. **Right:** piston force F versus translation stage position μ .

²²Microcontrôle, X95.

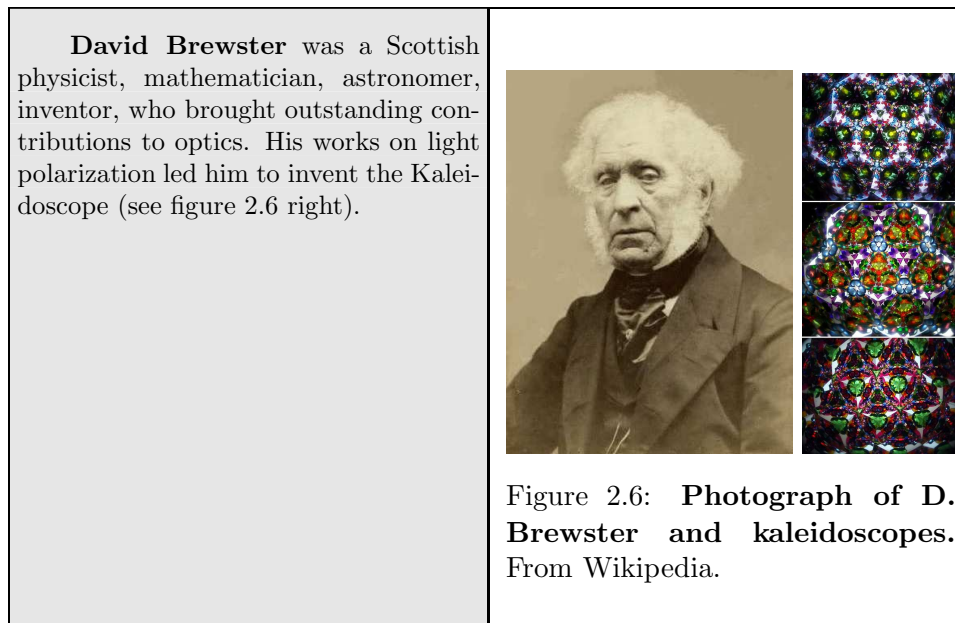


LABView File Stopped

Figure 2.5: Control and acquisition software. Top: Interface. Bottom: Schematic organigram.

2.2 Miscellanies on Photo-elasticity

Discovered in 1816 by Sir David Brewster (see box), photo-elasticity has now become a common technique to characterize stresses in structures [Vishay, 2010]. The interested reader may refer to Hecht [2005] for a very brief introduction and to the book by Sextant to design table top experiments. We will here briefly present the principle of photo-elastic measurements.



2.2.1 Definition of Photo-elasticity

Birefringent materials have an index of refraction that depends on light polarization. For crystalline solids such as quartz or anisotropic media, such as liquid crystals, this has to do with the symmetry of the microscopic structure : light propagates differently along the different symmetry axes. In contrast, amorphous materials such as glass or polymeric solids (plastic) have no microscopic order and the speed of light is independent of its polarization.

We present in figure 2.7 a schematic experimental setup aimed at observing birefringence: a parallel light beam is incident on a vertical polarizer, producing a vertical polarization. This polarized beam traverses the material and a second polarizer orientated horizontally. If the polarization has not been changed by the material, the initial light polarization is orthogonal to the second polarizer direction: no light comes out. However, if the material is birefringent, the light does not propagate at the same speed for different polarizations. We present in figure 2.7 the fate of a 45° polarized

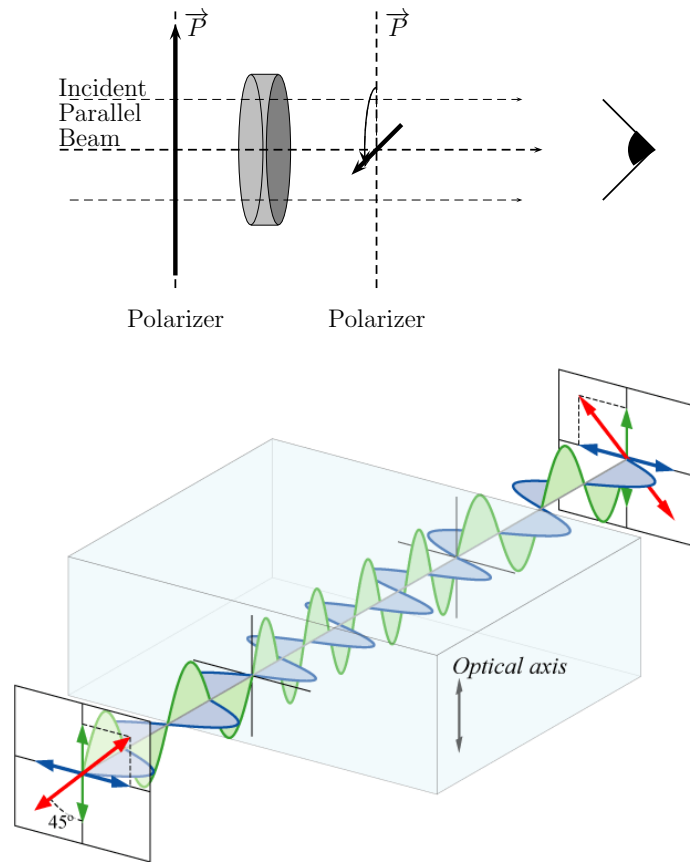


Figure 2.7: **Top** : Scheme of measuring birefringence setup. The material lighted by transmission between two crossed polarizers. **Bottom**: Fate of a polarized light (red) through a quarter wave plate with optical axes along vertical and horizontal axis. The vertical axis has a higher refraction index and the light along the vertical axis is faster. From Wikipedia.

light beam (red), as it passes through a quarter wave plate with optical axes along vertical and horizontal axis. The vertical axis has a higher refraction index and the light polarized along the vertical axis (green) is faster than the light polarized along the horizontal axis (blue). In this example, the phase shift at the exit of the material corresponds precisely to $\pi/2$, so that the polarization has rotated of an angle $\pi/2$. Note that it is necessary to use a polarizer afterwards, because the eye cannot see that the vertical and the horizontal oscillations have a specific phase delay. The last polarizer will decompose the two vibrations onto the same axis, where they interfere. Therefore, the resulting signal intensity depends on the optical phase difference.

Birefringent materials such as quartz have specific birefringence, which

is due to that peculiar crystalline structure. By contrast, amorphous plastic solids are made of randomly frozen polymer strands. Elastic deformations of such materials provoke alignment of polymeric chains according to the deformation direction, and thus induce birefringence, called *photo-elasticity*. Therefore, the birefringence of such materials is directly linked to the deformation field.

2.2.2 The case of disks

The deformation field of a disk to which several point forces are applied is strongly inhomogeneous [Landau and Lifshitz]. Therefore, a photo-elastic disk with several contact forces has a strongly inhomogeneous refraction index, and this induces a “fringe” pattern. Moreover, in order to study all directions, we will not use linear polarizers, but circular polarizers. In contrast with linearly polarized light, circularly polarized light probes all directions of the material isotropically. As an example, we represent in figure 2.8, left, an experimental picture of a disk undergoing three localized forces. The spatial variation of the optical index is so significant that the change of optical path becomes several times the wave length, thus explaining the “fringes” pattern. A crude way to measure the pressure inside a grain is thus to compute the number of “fringes”. To do so, the square of the spatial gradient is integrated over an area. This will be called the G^2 measurement in the following.

Therefore, in order to have a sensitive signal, one use soft grains, which are polyurethane (PSM-4) grains. They have a Young Modulus $E = 0.5$

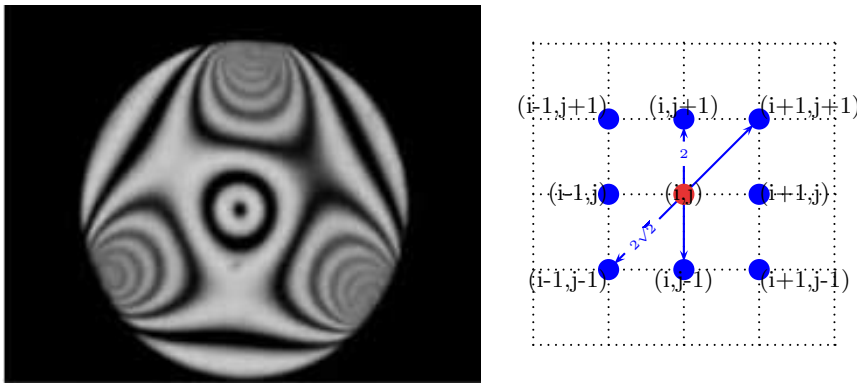


Figure 2.8: **Photo-elastic pattern of a disk.** **Left :** experimental picture of one photo-elastic grain undergoing three point forces between two circular polarizers lighted by transmission. Adapted from Majmudar and Behringer [2005]. **Right :** 2 dimensional discrete differentiation scheme. The spatial gradient can be computed by differentiating along vertical and horizontal axis or diagonal and anti-diagonal axis.

MPa [Micro-Measurements, 2010]. Assuming Hertz law [Landau and Lifshitz], the stiffness of two compressed 4 mm height cylinders is thus 1.5×10^3 N/m.

2.2.3 The G^2 measurement

The spatial gradient over a certain zone *area* is expressed as follows:

$$G^2 = \iint_{area} dXdY \|\nabla I(X, Y)\|^2. \quad (2.1)$$

However, we deal here with discrete arrays, and the gradient can be computed by finite differentiation. Therefore, G^2 can be re-expressed as follows:

$$G^2 = \sum_{i,j \in area} \|\nabla I(i, j)\|^2, \quad (2.2)$$

where $I(i, j)$ is the intensity of the photo-elastic picture at the location (i, j) and

$$\|\nabla I(i, j)\|^2 = \frac{1}{2} \left[\left(\frac{I(i+1, j) - I(i-1, j)}{2} \right)^2 \right. \quad (2.3)$$

$$\left. + \left(\frac{I(i, j+1) - I(i, j-1)}{2} \right)^2 \right] \quad (2.4)$$

$$+ \frac{1}{2} \left[\left(\frac{I(i+1, j+1) - I(i-1, j-1)}{2\sqrt{2}} \right)^2 \right. \quad (2.5)$$

$$\left. + \left(\frac{I(i-1, j+1) - I(i+1, j-1)}{2\sqrt{2}} \right)^2 \right]. \quad (2.6)$$

$$(2.7)$$

As schematically represented in figure 2.8, right, we choose to differentiate along both vertical—horizontal and diagonal—anti-diagonal axis, and we average the two measurements. This is one of the simplest ways to estimate the spatial gradient.

2.3 Photo-elasticity at high frequency

One goal of this experiment is to reproduce Frédéric Lechenault's experiments, together with the photo-elasticity technique. Therefore, we have to ensure the following constraints:

1. we would like to light the grains by transmission with a parallel polarized beam together with a homogeneous intensity field;
2. we would like to have the light device embedded in the existing vibrating table;

3. we would like to have a region of interest of about a thousand grains;
4. we would like to have —at least— a measurement of the local pressure within each grain;
5. we would like to be able to detect and to track the grains;
6. we would like the vibration frequency to be 10 Hz.

2.3.1 Lens

In order to tackle constraints 1 and 3, one has to use a narrow angle lens²³, and to place the camera as far as possible from the grains. Therefore, the camera has been placed just under the ceiling, and is now at a distance 1.2 m from the grains. The resulting field of view is a (165 mm × 165 mm) region, containing about 1 500 grains, whose diameters contains 50 to 60 pixels. However, as a direct consequence, the amount of detected light has diminished.

2.3.2 Light

In order to address constraints 1, 2 and 3, the key device is a LED panel²⁴, that is thin (8 mm thick), has a large area (400 mm × 400 mm), offers more than 95% intensity homogeneity, and is the most powerful light source we could find at that time. It is powered with an external controller²⁵. In order to have a circular polarized light, we tape a linear polarizer and a quarter wave sheet²⁶ between the back-light and the glass plate.

The light heats the grains a little bit: this provokes some thermal expansion. This increases the packing fraction significantly [Divoux et al., 2008]. Indeed, typical thermal expansion coefficients of polyurethane is $\sim 10^{-4} \text{ K}^{-1}$ (see [ENG]). Therefore, an increase of 1°C provokes an increase of packing fraction of $\Delta\phi \sim 10^{-4}$, which corresponds approximately to the experimental resolution on packing fraction. The first clue of this occurrence was the increase of the piston force on long time scales for jammed packings, after we had turned on the light, during preliminary experiments. The LED controller offers a trigger mode. Therefore, we turn on the light during 10 ms out of every 100 ms, which mitigates the heating effect.

²³Tamron, F2.8, 70 – 200 mm, Ø 77, A001, MACRO

²⁴PHLOX, PHL LEDW-BL-400X400-SLLUB

²⁵Smartek, Strobe Controller 6. DC Supply: Sodilec, Alimentation Stabilisée 24V 3.5A.

²⁶WF-OG4-WE Quarter-wave plate retarder film Extended Temperature (WF-OG4-WE) and PFA - Polarizer with or without adhesive, LCD-quality (PFA) Adhesive. Size NA_HS 50 × 62 cm (20 × 24 in) NO adhesive. Available on Polarization.com, we can buy them by meters!

In order to gain more light intensity, the Plexiglas board above the grains was replaced by a glass plate because light transmits better through glass than through Plexiglas.

2.3.3 Commuting photo-elastic and position information

Constraints 4 and 5 require that we are able to detect grains positions and to obtain photo-elastic information at the same time. We represent in figure 2.9, top-left, an example of a cross-polarized picture of photo-elastic disks. Since we can hardly locate the grains positions by eye, we can hardly imagine that they could be detected by image analysis. Two possibilities therefore remain: (i) add a non-polarized source of light (ii) remove the second polarizer.

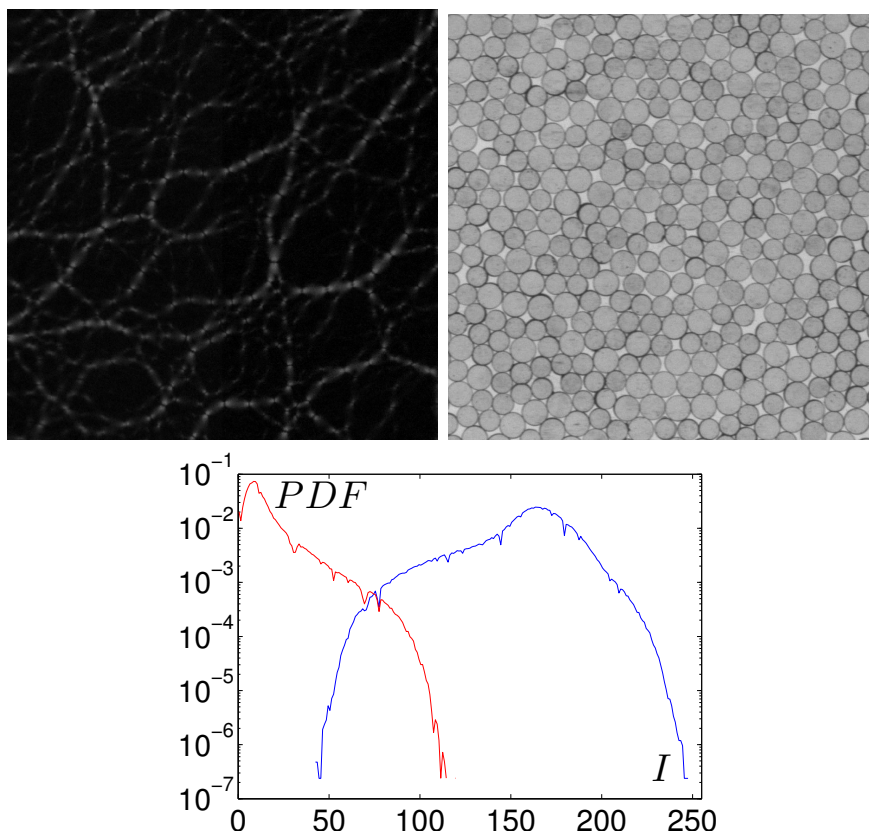


Figure 2.9: **Picture of photo-elastic disks. Top Left** : Cross-polarized picture of photo-elastic disks. **Top Right** : Picture of photo-elastic disks without second polarizer. **Bottom** : Probability density function of the gray level intensity I of cross-polarized (red) and non-cross-polarized (blue) pictures.

In order to maximize the contrast of photo-elastic cross-polarized images, we choose the second solution, that implies two types of images. We display in figure 2.9, top-right, a picture of grains, where the second polarizer has been removed. It seems like detecting grain positions is doable.

We now want to have the cross-polarized and the single-polarized pictures at the same time. The first solution we could think of was to have two cameras and to use a beam splitter. However, two major issues arise here: (i) a beam splitter divides the amount of light by 2. (ii) having two camera and two lenses and ensuring the data acquisition of twice the amount of data is expensive. Therefore, we choose to periodically insert one polarizer in front of the camera. Cross-polarized (respectively non-cross polarized) pictures will be taken every odd (respectively even) period. Assuming that grains have not moved significantly between two vibration cycles, we are able to associate grains positions and photo-elastic patterns. In the following, we will call $2P$ images the cross-polarized pictures and $1P$ images the non-cross-polarized pictures.

The setup of the camera is chosen so that: (i) the range of the camera is maximum; (ii) grain pictures are not blurred. In order to ensure (ii), we set the exposure time to 6 ms. In addition, one cannot change the features of the camera between the two types of images at a frequency of 10 Hz. Therefore, the settings have to be the same for $1P$ and $2P$ images. We then set the gain of the camera to +36 dB so that the intensity of both types of images cover the maximum intensity range. To illustrate this, we plot of figure 2.9, bottom, the distribution of gray level intensity for both a $1P$ (blue) and a $2P$ (red) picture. While the $2P$ covers half of the intensity range, $1P$ covers 4/5 of the intensity range. We are happy with this choice. In addition, to minimize blur, we choose the phase of the vibration to correspond to a phase such that the grain displacement is minimal during the exposure time.

2.3.4 Polariscope

The game now is to be able to build a device which is capable of precisely inserting the polarizer at the frequency of the vibration, which is typically 10 Hz. The appropriate device to do so is a rotating stepper motor²⁷ together with a controller²⁸, which is embedded in the switchgear cubicle. We want an object that can hold the polarizers and whose position can be synchronized accordingly to the trigger; let's call it the *polariscope*. The lens diameter is 77 mm wide: we use a 90 mm diameter polarizing filter. Since the stepper stop-and-go motion is performed at 10 Hz, we want the polariscope static and dynamic momenta to be balanced, in order to require minimal effort on the stepper axis. We therefore choose a six-holes disk: one polarizer is taped every two holes. In addition, both the camera lens

²⁷Yaskawa, AC Servo Motor, SGMAH-04AAF41D

²⁸Yaskawa, SGDH-04AE

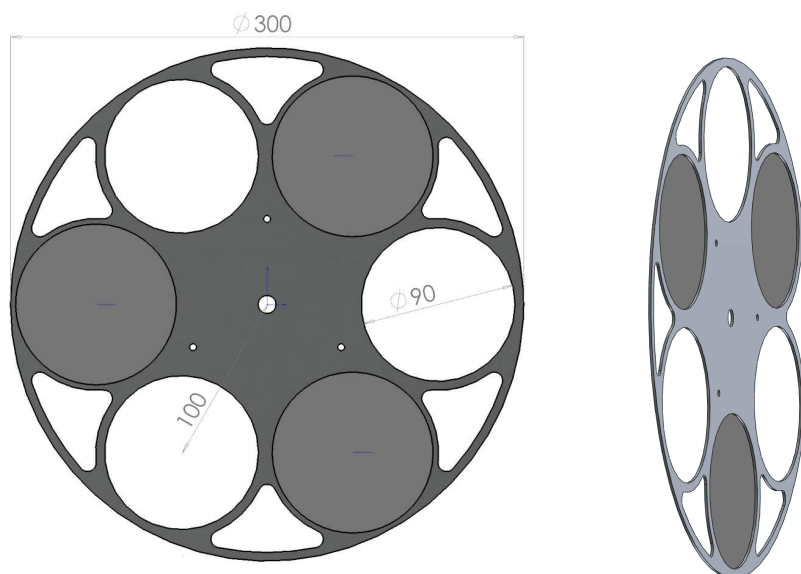


Figure 2.10: **Polariscope. Left: Top View. Right: Side View.**

and the stepper are 100 mm wide. Hence, the polariscope radius is chosen to be 150 mm. Furthermore, motor vibration directly induces blur on the pictures. Therefore, the stepper is separated from the shelf and attached to the ceiling.

We want the transient duration to be the shortest possible. Its duration is limited by the capabilities of the stepper and the inertia of the polariscope. Building the polariscope requires several steps, a numerical milling machine and a very clever technician—Vincent Padilla, who designed and machined the polariscope:

1. A first step prior to building the polariscope was to test the capabilities of the stepper with a disk of known inertia. This gives a limit for the moment of inertia of the polariscope and settings for the electrical features (PID loop) of the stepper. We estimated it to be $I_{max} = 2.4 \cdot 10^{-3} \text{ kg.m}^2$.
2. Then, a sketch, using a 3D design software²⁹, allows us to design the polariscope and to adapt its thickness and material to the inertia momenta limit.
3. Finally, turn the sketch into an esthetically appealing piece of work, which is displayed in figure 2.10. Note that unnecessary material was removed in order to limit the moment of inertia. We paint its lower part in black to avoid reflection effects.

²⁹Solidworks

2.3.5 Final experimental setup

We end up with a beautiful experiment, that is displayed in figures 2.12 and 2.11.

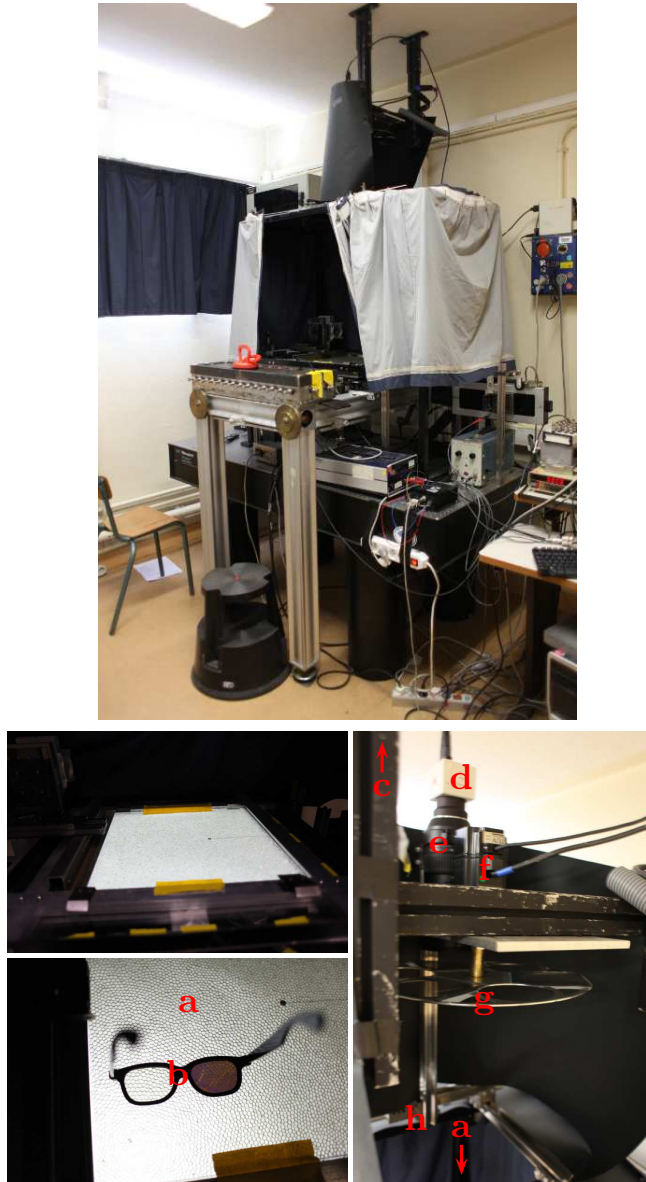


Figure 2.11: **Pictures of the polarized setup.** (a): photo-elastic grains lighted by transmission by a polarized backlight. (b): cheap version of the polariscope: 3D movie theater glasses. (c): ceiling. (d): camera. (e): lens. (f): stepper. (g): polariscope. (h): shelf.

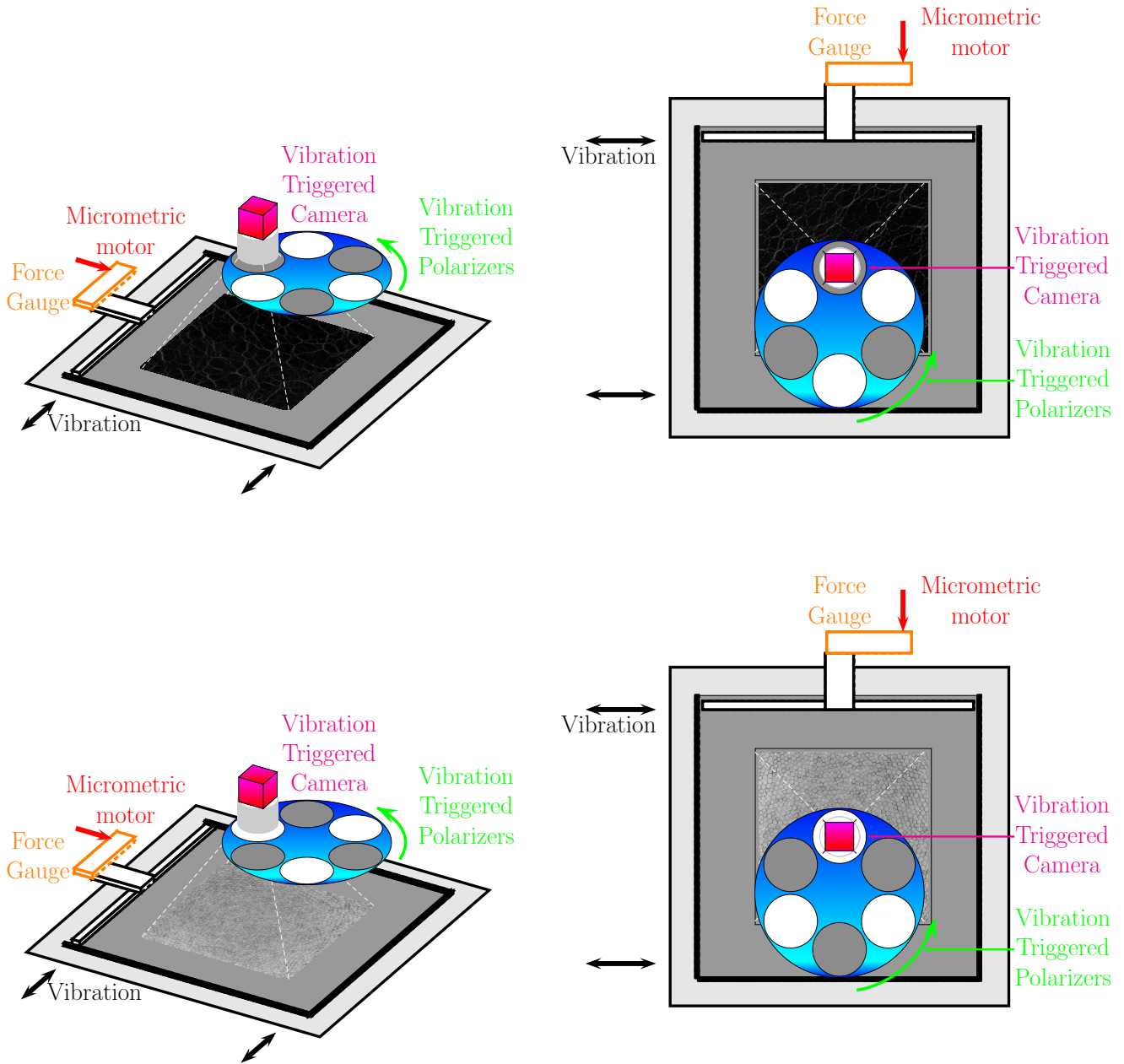


Figure 2.12: **Experimental Setup. Left: Side View. Right: Top View. Top : Cross-polarized configuration Bottom : Non Cross-polarized configuration**

2.4 Protocol and Calibration

2.4.1 Protocol

Vibrated granular packings compact logarithmically under constant loading force [Knight et al., 1995]. Thanks to the automation of the piston, we can mimic such a compaction effect. We can, indeed, perform automatic logarithmic compression of the packing at any desired rate by imposing constant steps, $d\mu_{piston}$, to the micro-metric piston, separated by pauses whose duration, t_w , increases exponentially at each step.

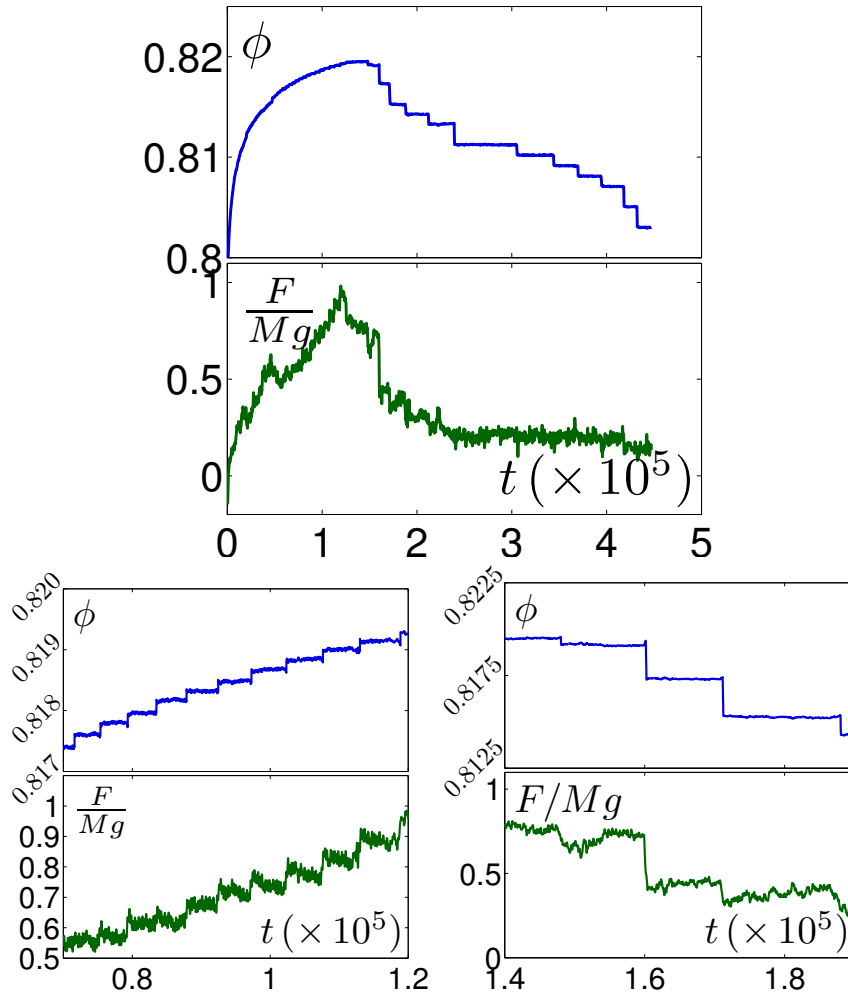


Figure 2.13: **Compaction and decompaction protocol.** **Top:** Packing fraction (upper panel) and normalized force at the piston (lower panel) versus time expressed in number of vibration cycles. **Bottom Left :** Zoom on compaction. **Bottom Right :** Zoom on decompaction.

In order to ensure that this protocol leads to reproducible packing properties and limited aging effects, we measure the “pressure”, *i.e.* the force sustained by the sensor at the piston. We thus plot the packing fraction and the pressure versus time for one experiment in figure 2.13, top. In the upper panel is displayed the packing fraction, and in the lower panel is displayed the piston force F/Mg . The first increasing part of the signal corresponds to the logarithmic compaction. This compaction is associated with an increase of the piston force. We present in figure 2.13, bottom left, a zoom of this compaction. We see that at each compaction step, the force jumps, and relaxes slowly: it is not stationary. We continue the compaction until the piston force corresponds to one or several times the weight Mg of all the grains. Because grains slip on the glass plate, the piston typically endures a force, $\mu_d Mg$, where μ_d is the dynamic grains-glass friction coefficient. Therefore, Mg is the relevant force scale at play. Then, successive decompaction steps follow. The measurements of the dynamics are done in between. We plot in figure 2.13, bottom right, a zoom of the packing fraction, and, the force versus time. At each step, the pressure drops. Then, long time temporal fluctuations occur, but not systematic relaxation. Therefore, the force signal indicates that the dynamics is nearly stationary.

2.4.2 How to tune the ϕ_{JS} ?

We perform here a preliminary study of the compaction rate on the final Jamming packing fraction. We want here to compact “logarithmically” the packing. This is motivated by the fact that shaken granular materials compact “logarithmically” under constant load, as we explained in section 1.1.3.2. In other words, we want to compact the material rather quickly when it is loose and rather slowly when it is dense.

2.4.2.1 Protocol

We explained in section 2.4, that the piston position μ_{piston} was increased by constant tiny amounts $d\mu_{piston} = 0.1$ mm with exponentially increasing time steps t_w . Thus, we impose

$$t_w = \exp \mu_{piston} B_1. \quad (2.8)$$

where B_1 is the compaction rate. And we stop the compaction process when the piston force has reached 2.5 times the total weight of the grains.

Besides,

$$\phi = \frac{A_{grains}}{W_{cell} \times (L_{cell} - (\mu_{piston} - \frac{F}{k}))}, \quad (2.9)$$

where A_{grains} is the total surface of grains, W_{cell} , the width of the cell, L_{cell} the length of the cell when the piston position is set to zero, F the piston

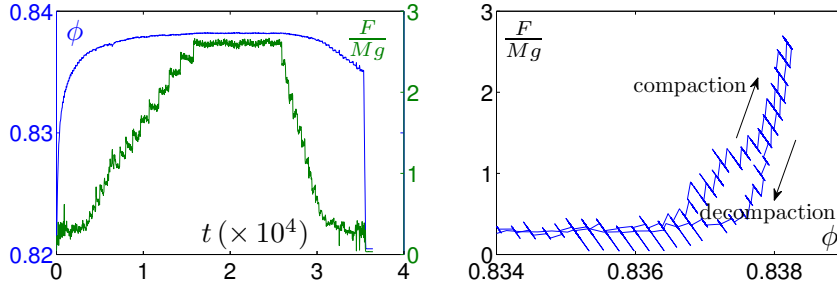


Figure 2.14: **Compaction-Decompaction protocol.** **Left:** Packing fraction ϕ (left axis) and piston force F/Mg (right axis) versus time for a compaction-decompaction experiment. **Right:** Piston force vs. packing fraction for a compaction-decompaction experiment.

force, and k the stiffness of the piston. Therefore, at each compression step, ϕ is increased by an amount,

$$d\phi \sim \phi_0 \frac{1}{L_{cell}} \left(d\mu_{piston} - \frac{1}{k} dF \right), \quad (2.10)$$

where $\phi_0 \sim \frac{A_{grains}}{W_{cell} \times L_{cell}}$, and dF is the jump of the piston force. Since an increase of the piston force will reduce the packing fraction, we don't totally master the increase of the packing fraction. In order to do this, a further improvement could be to control the position of the piston instead of the translation stage. But this would require to add a position sensor to the setup, which is already complicated. Therefore, we will, in the following section, try to estimate the compaction rate directly from the compaction curve.

We perform several experiments, consisting of compacting the packing at different compaction rates, and decompacting it at a constant rate. We display in figure 2.14, left, the packing fraction and the piston force normalized by the weight of the grains versus time for one experiment. As stressed in section 2.4, piston force relaxation time is longer and longer as the system is compacted. At the highest packing fraction, the piston force is stationary. We plot in figure 2.14, right, the piston force vs. the packing fraction. We see that there is a hysteresis cycle: the pressure is larger during the compaction than during the decompaction.

2.4.2.2 The compaction

We plot in figure 2.15 the packing fraction versus time for different compaction rates. We observe different curves depending on the imposed rate. Inspired by previous studies on granular compaction [Richard et al., 2005],

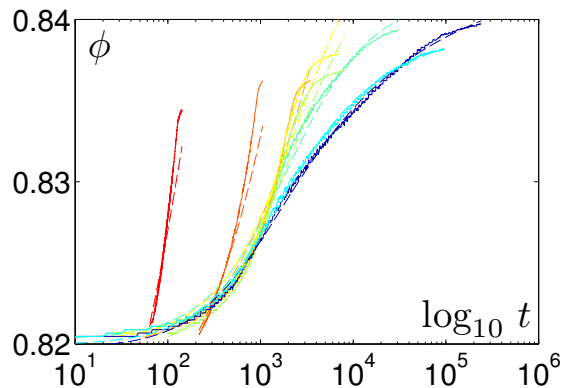


Figure 2.15: **Compaction protocol for different compaction rates.** Packing fraction versus time for different compaction protocols. The dashed lines indicate the fit by equation 2.11. Experiment performed for the brass disks.

we fit by

$$\phi = \phi_f - \frac{\phi_f - \phi_0}{1 + B \log \left(1 + \frac{t}{\tau} \right)}, \quad (2.11)$$

where ϕ_f is the final packing fraction, ϕ_0 is the initial packing fraction, τ is a time constant, and B can be seen as a compaction rate. We see that, apart from the two largest compaction rates, the fit quality is rather good. We will in the following focus on the parameter B to quantify the compaction rate.

2.4.2.3 The Jammed packing

Let's now try to see if there is any correlation between the compaction rate and the reached jammed state. To do so, we performed different experiments on the brass disks. We plot the piston force vs. packing fraction during decompaction for different compaction rates, B , in figure 2.16, top. B has been determined from the fit described in equation 2.11. We see that, the higher the compaction rate, the lower the Jamming packing fraction ϕ_J . Note, that the packing with the highest B curves has a negative slope: this is because the pressure is not stationary. Indeed, it has been quenched so fast, that the packing ages during the decompaction. We define ϕ_J as the highest packing fraction reached by the packing. We then plot ϕ_J vs B in figure 2.16, bottom left. We see a global decrease. This is consistent with previous studies on numerical systems [Silbert et al., 2002, Zhang and Makse, 2005, Shundyak et al., 2007]. We can further attempt to characterize the structure, by counting the fraction of rattling particles. Since the packing is densely packed, there is only a tiny motion and defining

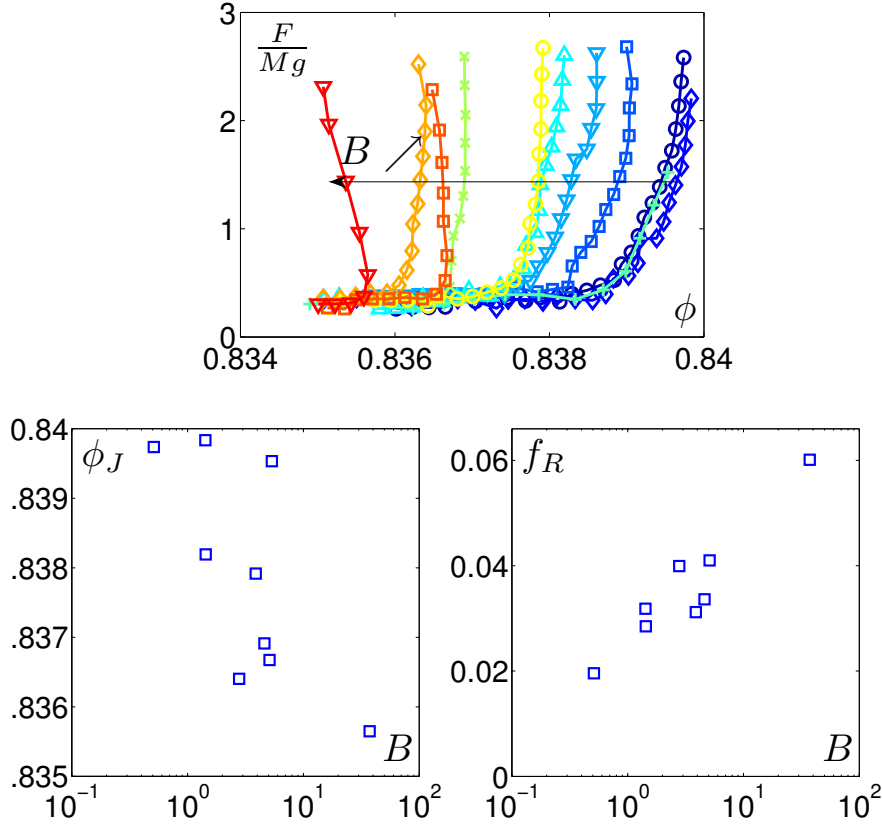


Figure 2.16: **Compaction protocol for different compaction rates.** **Top:** Piston force vs. packing fraction for different compaction rates B . **Bottom left:** Jamming packing fraction ϕ_J vs. compaction rate B . **Bottom right:** Fraction of rattlers f_R vs. compaction rate B .

rattlers is an easy task. It is done by thresholding the displacement: every particle that moves more than 1×10^{-3} grain diameter is selected as a rattler. We plot in figure 2.16, bottom right, the instantaneous fraction of rattlers versus the compaction rate B . We see that it increases: fast compacted packings have more rattling particles.

2.4.3 Calibration of Photo-elasticity

A further step is to compare the photo-elastic measurement to the piston force measurement. We plot in figure 2.17, left, time averages of the G^2 measurement over all the disks versus the time average of the wall pressure performed during decompaction steps. We see that, except for the two last points, the data are linear, with a coefficient $A_G = 8.78 \cdot 10^4$. We explain the high force discrepancy by the fact that the size of photo-elastic pattern—“fringes”—becomes smaller than the camera resolution. This is

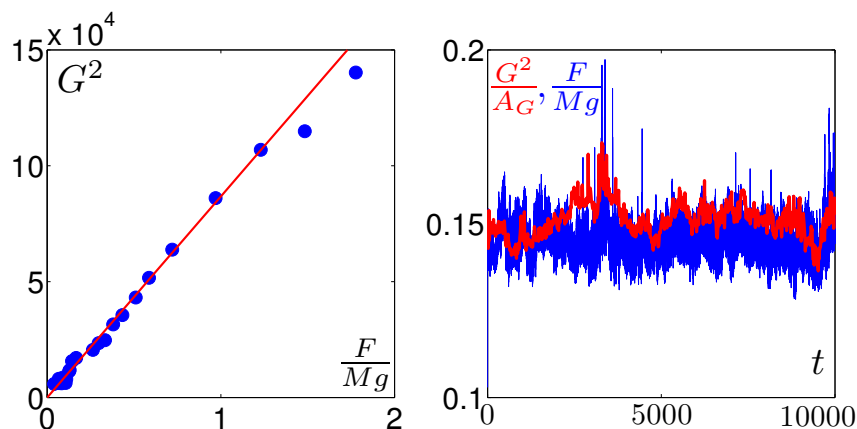


Figure 2.17: **Calibration of photo-elasticity.** **Left :** G^2 measurement over all the disks versus normalized piston force F/Mg . The red line is a linear fit that exclude the two last points. It has a slope $A_G = 8.78 \times 10^4$. **Right :** normalized G^2/A_G measurement over all the disks (red) and normalized piston force F/Mg (blue) versus time at a density $\phi = 0.8146$.

illustrated in figure 2.8, left, where a cross-polarized picture of a grain is shown. Close to the contact, the strain variation is so large that the optical path difference changes by several wave lengths over a small distance, which is close to the picture resolution.

Therefore, except for high forces measurements, the G^2 measurement and the piston force are equivalent. In the following, we shall use the calibration coefficient A_G to normalize G^2 measurements. Thus, G^2 measurements will be expressed in terms of force renormalized by the weight of the grains. Later on, when we compute G^2 over disks, the reader will have to keep in mind that 1 corresponds to the total weight of the grains.

In addition, we plot the time dependence of both G^2/A_G and F/Mg in figure 2.17, right. We see that they undergo similar fluctuations, and that there is less high frequency noise within the G^2 measurement. The significant noise of the piston force signal could be rooted in the mechanical vibrations.

2.5 Image Processing & Data Analysis

There are two types of image processing: (i) position detection; (ii) G^2 measurements. Moreover, prior to G^2 , several steps of data-mining and tessellation are necessary. In order to do this, we choose to separate image processing from data analysis. Image processing is done using LABView because there are a lot of built-in image processing tools, and because we have a very clever LABView programmer Cécile Wiertel-Gasquet working in the lab. The following project has been conceived together with her, and mostly written by her. Data analysis is performed using a standard programming language. In order that the data can be shared by the two languages, the data is stored on an external MySQL Database server, which can be accessed by the network. This storing technique was set up during the thesis of Raphaël Candelier and Julien Deseigne.

In order to have the image processing easily handleable and modifiable, and to loop over several tens of thousands pictures, we have written an all-in-one project, whose interface is displayed in figure 2.18. It is very easy to use, since all that we have to do is to feed data to the interface. Beneath this interface is an organigram, which is represented in figure 2.19. The steps that correspond to initialization of the program and to the Database protocol are sketched in orange. The rest consists of : (i) position detection steps (in blue), (ii) G^2 measurements in disks (in green); (iii) G^2 measurements in “Camemberts” (in magenta).

We will explain the details of these three steps in the following sections.

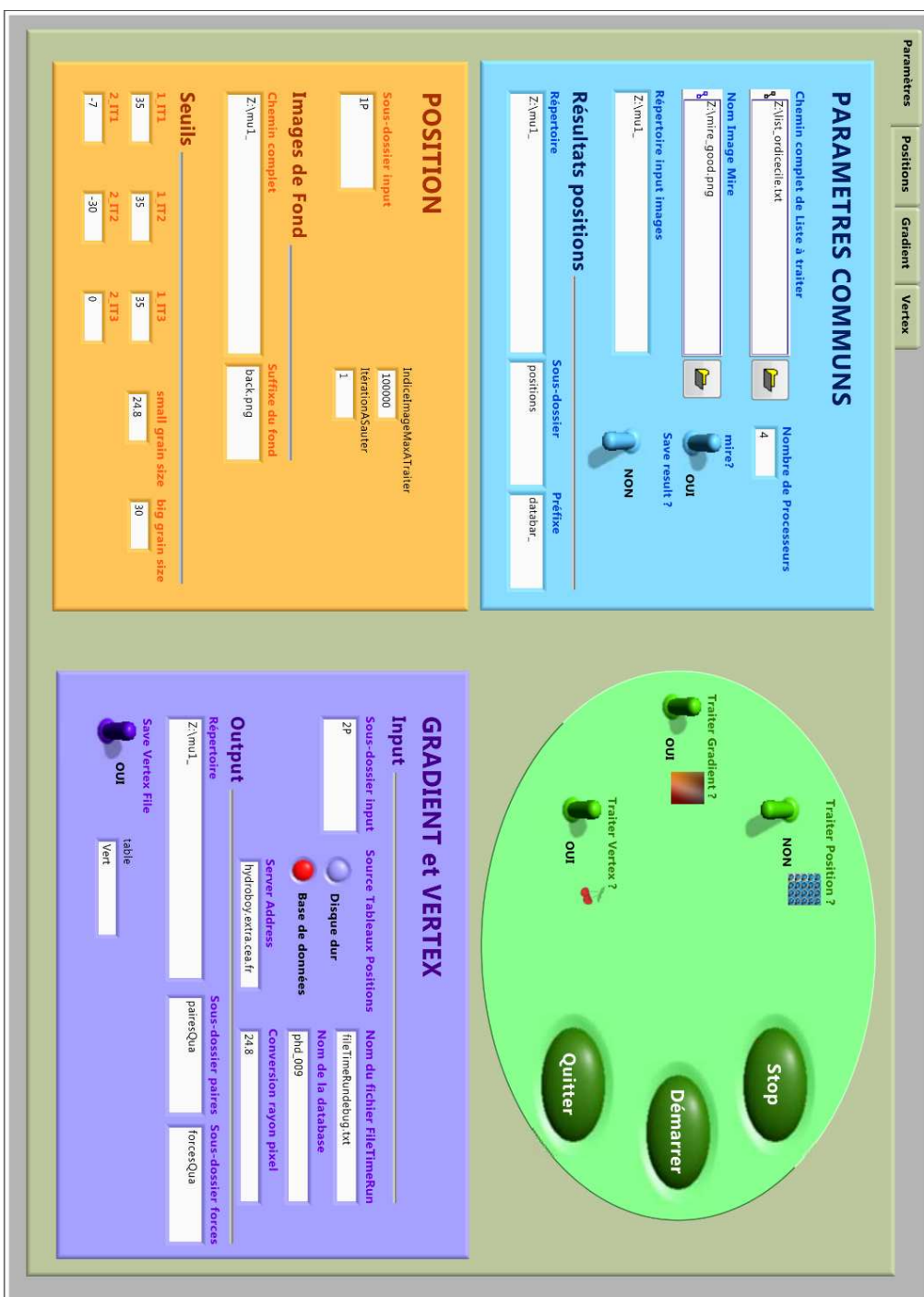


Figure 2.18: Interface of the LABVIEW program.

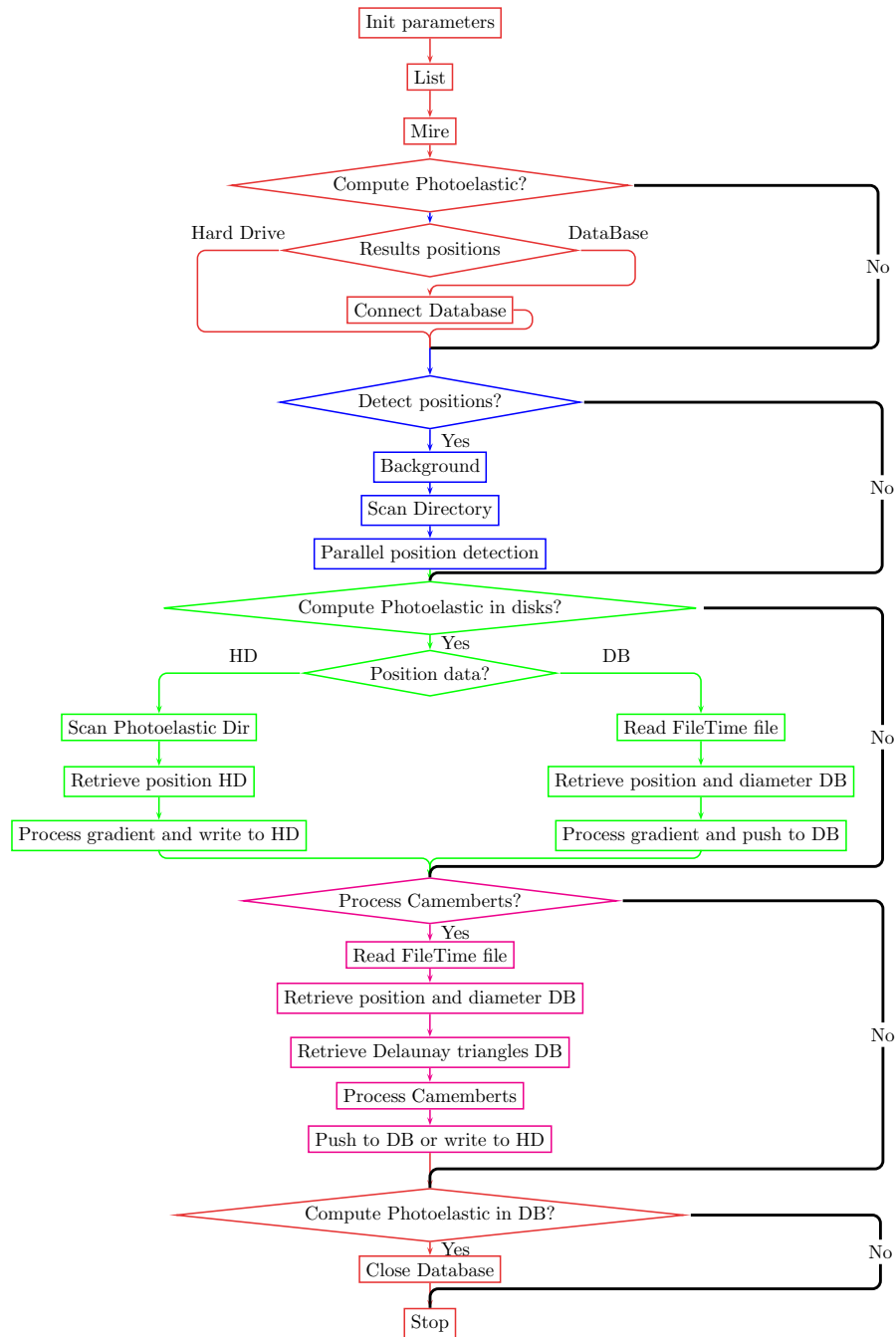


Figure 2.19: **Scheme of image processing program.** Orange steps represent initialization, files and Database properties. Blue steps represent the position detection steps. Green steps represent the G^2 measurement in disks. Magenta steps represent the G^2 measurement in “camemberts”.

2.5.1 Position Detection

We present here the idea of the position detection algorithm. We have seen in figure 2.9, top right, that the contrast of $1P$ images is rather poor. We see it also in figure 2.21, where a zoom of a $1P$ image is displayed. In particular the distribution of figure 2.9 bottom reveals no straightforward criteria (i) to distinguish between the grains and the background; (ii) to separate the grains. Furthermore, we see that some grains have escaped the close manual investigation that we have carefully performed prior to picture: some are darker than oth-

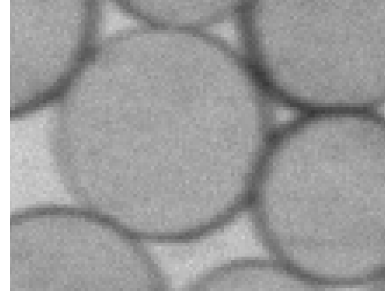


Figure 2.21: **Zoom on one grain.**

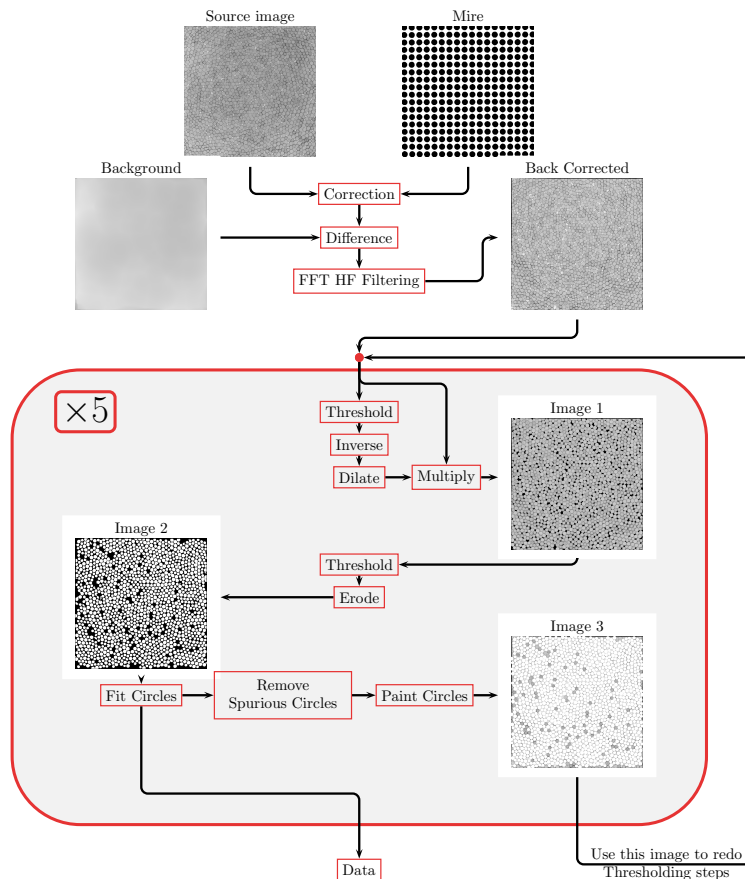


Figure 2.20: **Position detection algorithm.**

ers; some are stained. In order to tackle those issues, we have developed a multi-step algorithm, which we sketch in figure 2.20. A first main step consists in correcting the source image for optical distortion, light intensity gradient, and noise.

- To correct for distortion, we image a grid made of separate black disks. We then use a bilinear distortion correction.
- To correct for large scale intensity gradients, we apply a high-pass Fourier filter of cutoff length 500 pixels to an image. We then obtain a background that can be subtracted from the source image.
- We apply a gaussian low-pass filter cutoff length of 3 pixels on the pictures, which limits the noise.

We end up with a corrected image to which thresholds can be applied. The background is lighter than the grains, but the edges of the grains are darker.

- The first step consists in turning the light background into black and dilate it so that it merges with the edges of the disks (Image 1).
- The second step consists in thresholding again to separate the grains from the dark background. We obtain a binary image (Image 2) made of circular blobs.
- We then fit these blobs to ellipses. We then reject the blobs, whose diameter either does not match the diameter of small or big disks, or whose circularity is not equal to 1 ± 0.05 . For a perfectly well defined circle, the fit resolution is about 0.01 pixels. However, because of blur and noise, disks positions are not so well defined as it is depicted in figure 2.21. In practice, we reach a precision of 1/4 pixel. Since a grain diameter is 50, this gives an absolute resolution of $n_g = 5 \times 10^{-3}$ grain diameter.

As stressed above, disk transparency is not uniform: there is no hope for one unique threshold. Therefore, we perform 5 recursive steps with slightly different values of the threshold parameters. At each step, we fill the successfully detected disks so that they will not be spotted again by the algorithm. The first step gets 90% of the disks, and the second gets 90% of the remaining. Steps 3 to 5 detect very specific cases, and usually get 1 to 5 particles. Altogether, this algorithm ensures less than 1 undetected particle per frame. Still, if one consider 1 lost particle in 10 000 pictures, it is as though we had lost 10 000 particles. Therefore, before the data is stored into the database, it is semi-automatically data-mined: the lost particles are searched using the neighbors structure. The position detection algorithm takes about 10 s per frame, but it can be parallelized on several chips and computers. Altogether, position detection and semi-automatic

data-mining are very time consuming and limit the number of experiments that can be done.

2.5.2 G^2 measurements

2.5.2.1 In disks

The G^2 measurement in disks is also performed with the same program. Its principle is sketched in figure 2.22, top: spatial square gradient and particle coordinates are associated so that we obtain a measurement of the pressure in each grain.

In the following, for the sake of simplicity, we shall call $G_i(t)$ the G^2 measurement inside grain i at time t , normalized by the calibration constant A_G .

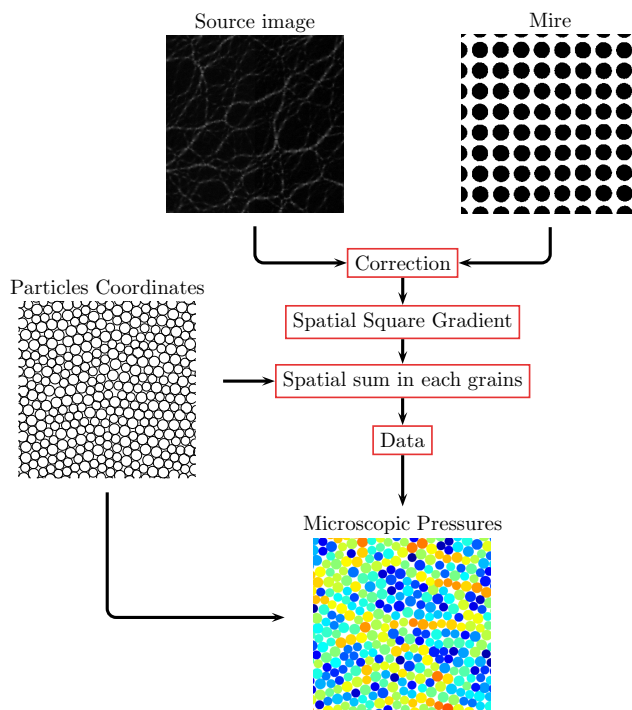


Figure 2.22: G^2 measurement on disks algorithms. **Top:** In disks. **Bottom:** In “Camemberts”.

2.5.2.2 In “Camemberts”

In order to measure contact forces between grains. We choose to use the tessellation structure because it is a well defined geometrical structure and because this is an efficient way to store the data. To do so, we split the Delaunay triangles into six “camemberts” by using the Voronoï vertices, as represented in figure 2.23 (a). Each “camembert” is defined by: (i) a vertex of the Delaunay triangle (point 1, 2 or 3 in fig. 2.23 (a)); (ii) the Voronoï vertex associated to this triangle (point V in fig. 2.23 (a)); (iii) the point at which the line separating two Voronoï vertices cross the adjacent Delaunay triangle edge (point L , M or N in fig. 2.23 (a)). Thus the six “camemberts” in figure 2.23 (a), are $1LV$, $2VL$, $2MV$, $3VM$, $3NV$ and $1VN$. A key point here is that each Voronoï vertex has 6 “Camemberts”: it is a robust data structure. We show in figure 2.23 (b) a zoom of a cross-polarized picture and its associated tessellation structure. In this figure, the link between grains 1 and 4 is associated with four “Camemberts” a , b , c and d . We show in figure 2.23 (c), the result of the G^2 measurement in all the “Camemberts”. We sketch in figure 2.23 (d), the algorithm used to perform the G^2 measurement in “Camemberts”. In order to obtain normal force measurements, we can sum the G^2 measurement over the four “camemberts” that lie along two neighbors. These ‘camemberts’, named, a , b , c and d are depicted in figures 2.23 (b) and (c). We estimate the normal force between grains 1 and 4,

$$F_N = G_a^2 + G_b^2 + G_c^2 + G_d^2, \quad (2.12)$$

where the G^2 have been normalized by the calibration constant A_G , defined in section 2.4.3. Similarly, we also estimate the tangential force,

$$F_T = |G_a^2 - G_b^2| + |G_c^2 - G_d^2|. \quad (2.13)$$

We will discuss in further detail the measurement of normal forces in section 4.1.1.

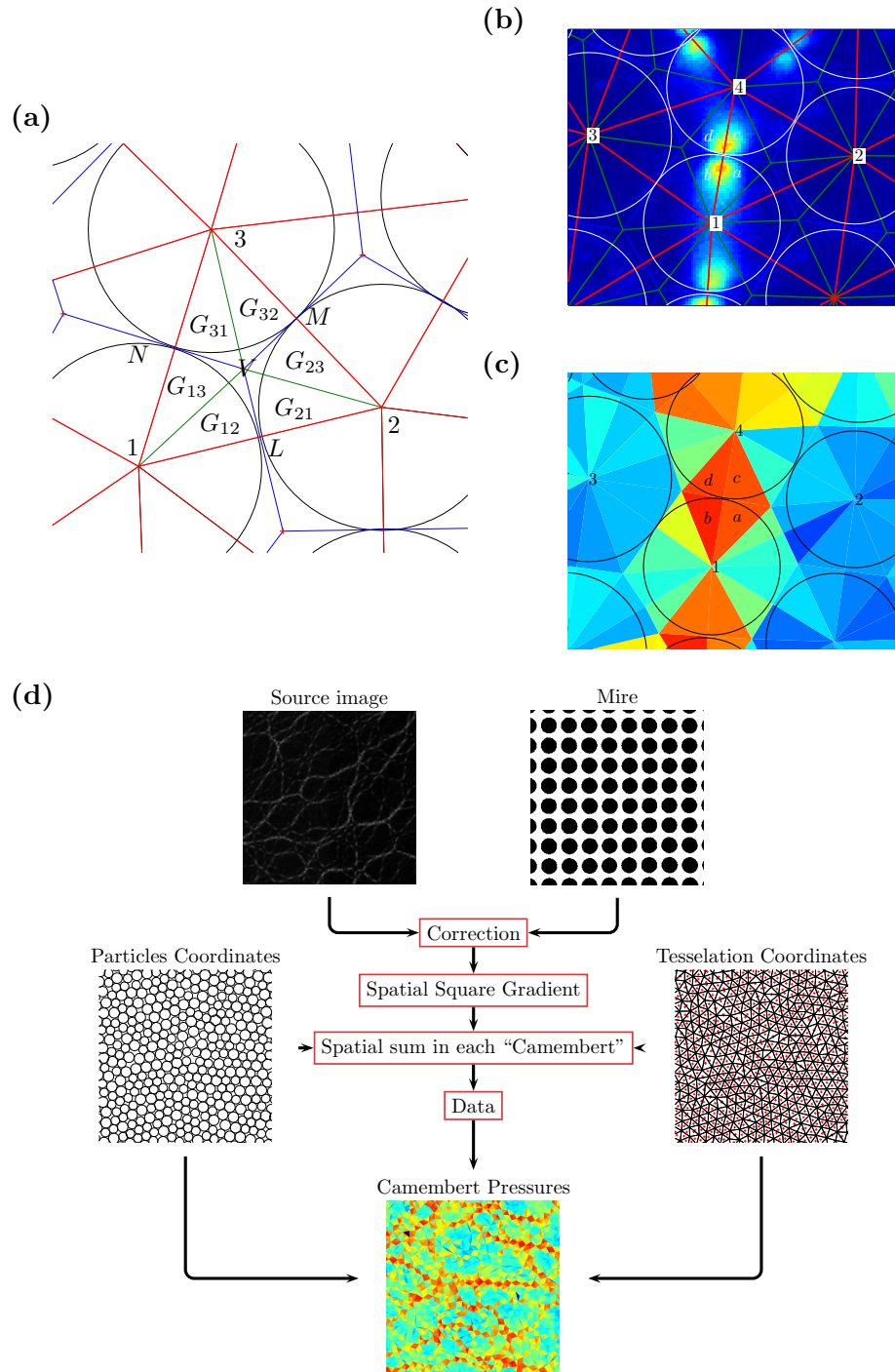


Figure 2.23: G^2 measurement on "Camemberts". (a): Definition of "Camemberts" using tessellation. (b): cross-polarized pictures and Tessellation structure. Grains are drawn in white; Delaunay triangles are sketched in red; Voronoi vertices are linked together by blue lines; Voronoi vertices are linked to grains positions by green lines. (c): "Camemberts" picture: value of the G^2 measurement in each "Camembert". Redder colors correspond to higher forces and bluer colors to lower colors. (d): G^2 measurement on "Camemberts" algorithms.

2.5.3 Summary of the data

Altogether, the data acquisition, treatment and analysis chain allows us to perform numerous experiments. We summarize in table 2.1, the various experiments we have performed, and the amount of data they represent.

Date	Type of experiment	Compaction rate	number of sub-runs	vibration frequency (Hz)	number of images	Size of the images (Go)	Database name	Size of the DB (Go)
Dec, 2010	structure	quenched, $B \sim 45$	26	600	11 000	44	pho_303	0.5
Dec, 2010	structure	quenched, $B \sim 45$	10	600	20 000	80	pho_504	0.9
Jun, 2011	dynamics	annealed, $B \sim 0.02$	13	600	270 000	1080	pho_005 phd_505	7.1 16.0
Dec, 2011	dynamics	annealed, $B \sim 0.02$	14	600	150 000	600	pho_010	22.2
Dec, 2011	dynamics	annealed, $B \sim 0.02$	14	375	150 000	600	pho_110	18.8
Dec, 2011	dynamics	annealed, $B \sim 0.02$	15	600	160 000	640	phd_009	20.9
Dec, 2011	dynamics	annealed, $B \sim 0.02$	15	450	160 000	640	phd_019	21.0
Oct, 2011	structure	annealed, $B \sim 0.02$	30	600	6 000	24	pho_008	0.7
Oct, 2011	structure	annealed, $B \sim 0.02$	30	600	6 000	24	pho_018	0.8
Feb, 2012	dilute		25	200 to 600	10 000	40	pho_021	0.5
Feb, 2012	intruder	annealed, $B \sim 0.02$	22	600	150 000	600	phd_901	22.5

Table 2.1: **All the data.** Summary all the experiments run during the thesis.

Chapter 3

From a stuck liquid to a soft solid

We have shown in the previous chapter that we could measure both particle positions and forces inside the particles as a function of time. In this chapter, we will perform statistical characterizations of particles trajectories and force fluctuations through an “unjamming” transition, *i.e.* the decompression of the packing.

We will first observe the emergence of convection of the packing as it is uncompressed. The convection can reasonably be described by an affine deformation field and can easily be removed from the particle displacements. We study, then, the evolution of the structure by scrutinizing the evolution of the neighborhood network. We observe that the network is frozen at all packing fractions, and we conclude that our system can safely be considered as a “granular glass”.

We thereafter show that this glass has an emergent rigidity when the packing fraction is increased. To do so, we combine measurement of the force at the piston and photo-elastic measurements. Secondly, we study the geometry of the force network and the pressure at the grain level, which happen to be heterogeneous and to have a peculiar spatial organization that differs in the dense and in the loose regimes.

What kind of dynamics is associated to such a rigidity crossover? To address this issue, we turn to the study of the statistical properties of the dynamics of the grains. We here carefully compute the dynamic of the particles. The root mean square displacement and the distributions of displacements strongly change as the packing fraction is tuned.

We dig deeper by defining a dynamical structure factor, similarly to what is done in light scattering. The dynamical structure factor tells us how important the displacement of the particles is as compared to a reference length. While its first moment probes average dynamics on various scales, its second moment provides a measure of dynamical heterogeneities.

We demonstrate here the presence of maximal dynamical correlations at an intermediate packing fraction.

Such a dynamics calls for a look into microscopic force dynamics, which also presents maximally heterogeneous behavior at the same intermediate packing fraction, but of a modest amplitude.

NB: Key to read the plots In order to make the figures caption clear and concise, we will stick to the same color code whenever the family of curves representing all densities are plotted. The code is summarized in table 3.1.














0.8200	0.8178	0.8157	0.8146	0.8136	0.8125	0.8115
						
0.8104	0.8094	0.8083	0.8073	0.8052	0.8032	
						

Table 3.1: **Packing fraction color code.** Summary of the color code used for the various densities throughout the chapter

3.1 Convection

Shaken granular materials often undergo convection. This takes its roots in some asymmetry of the forcing. As a consequence, experiments that aim at measuring large scale currents and collective phenomena are often controversial [Aranson et al., 2008], and ensuring no convection induced currents requires a lot of care [Deseigne et al., 2010, 2012]. Our experiment doesn't escape this rule, and the very first observation we make from dynamics is that there is solid rotation.

3.1.1 Solid Rotation

As pictured in figure 3.1 (top), where trajectories are plotted, we see a solid body rotation. A further indication of solid rotation is given by a plot of ortho-radial displacements $\|\frac{\vec{r}_i(t+\tau)+\vec{r}_i(t)}{2}\|(\theta_i(t+\tau) - \theta_i(t))$ vs. distance to center of the region of interest $\|\frac{\vec{r}_i(t+\tau)+\vec{r}_i(t)}{2}\|$ at one time t for all the particles in 3.1 (bottom). This scatter plot has a finite linear correlation. All the particles thus have the same angle of rotation that is given by the correlation of the scatter plot : this is solid rotation. This is a little bit puzzling because the confining cell is rectangular (see chapter 2). Therefore, there must be some shear localized outside of the camera field and close to the boundary. In this work, our measurements stick to a region of interest

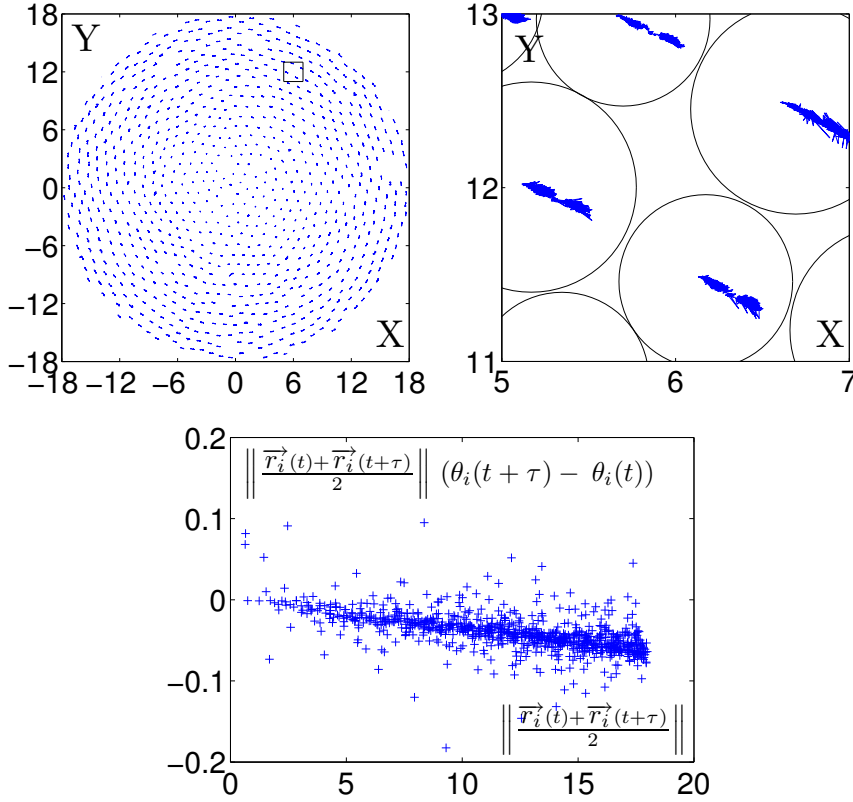


Figure 3.1: **Solid rotation. Top Left:** Trajectories of particles over 10 000 time steps. The frame indicates the zoom for the zoom. **Top Right:** the same with a zoom. **Bottom:** Orthoradial displacements vs. distance to center for a lag time $\tau = 1000$ at $\phi = 0.8125$.

which is located at the center of the confining cell. We will therefore not address the origin of the solid rotation. In order to characterize the rotation, we can do two things that are in principle equivalent: we can either compute an absolute angle of displacement and define a relative rotated reference frame at each time t , or we can compute the rotation angles between two instants t and $t + \tau$. Since we will, in the following, compute statistics on particles displacements, we adopt the second method that directly computes the rotation between the two instants we do statistics on. We could use the first method as well, but this latter approach is more sensitive to small errors that would propagate along time.

We first characterize the solid rotation of displacements. Since a solid rotation field is an affine deformation, it is fairly easy to compute an analytical expression for rotation and to fit it with respect to the trajectories of the grains. To do so, we decompose the trajectories of the particles into

several parts:

$$\vec{r}_i(t + \tau) = \vec{r}_i(t) + \widetilde{\Delta_\tau \vec{r}_i(t)} + \Delta_{\tau, r} \vec{r}_i(t) \quad (3.1)$$

where

$$\Delta_{\tau, r} \vec{r}_i(t) = \begin{pmatrix} 0 & \Delta_\tau \theta \\ -\Delta_\tau \theta & 0 \end{pmatrix} \left(\frac{\vec{r}_i(t) + \vec{r}_i(t + \tau)}{2} - \vec{r}_\tau^0(t) \right), \quad (3.2)$$

is the solid rotation deformation field, and $\widetilde{\Delta_\tau \vec{r}_i(t)}$ is the remaining deformation, that is not encompassed in the solid rotation field.

From the displacements of the particles, we thus directly compute the values of $\Delta_\tau \theta(t)$ and $\vec{r}_\tau^0(t)$ such that

$$\chi(\Delta_\tau \theta(t), \vec{r}_\tau^0(t)) = \frac{1}{N-2} \sum_{i=1}^N \|\vec{r}_i(t + \tau) - \vec{r}_i(t) - \Delta_{\tau, r} \vec{r}_i(t)\|^2 \quad (3.3)$$

is minimal, where N is the number of particle in the field of view. To do so, the derivatives of $\chi(\Delta_\tau \theta(t), \vec{r}_\tau^0(t))$ with respect to $\Delta_\tau \theta(t)$ and $\vec{r}_\tau^0(t)$ have to be zero. This yields

$$\Delta_\tau \theta(t) = - \frac{\sum_{i=1}^N \begin{pmatrix} 0 & 1 \\ -1 & 0 \end{pmatrix} (\vec{r}_i(t + \tau) - \vec{r}_i(t)) \cdot \frac{\vec{r}_i(t) + \vec{r}_i(t + \tau)}{2}}{\sum_{i=1}^N \left\| \frac{\vec{r}_i(t) + \vec{r}_i(t + \tau)}{2} \right\|^2} \quad (3.4)$$

$$\vec{r}_\tau^0(t) = \Delta_\tau \theta(t) \frac{1}{N} \sum_{i=1}^N \begin{pmatrix} 0 & 1 \\ -1 & 0 \end{pmatrix} (\vec{r}_i(t + \tau) - \vec{r}_i(t)) \quad (3.5)$$

We can then remove the solid rotation field from the displacements of the particles. Such a process is illustrated in figure 3.2, where instantaneous

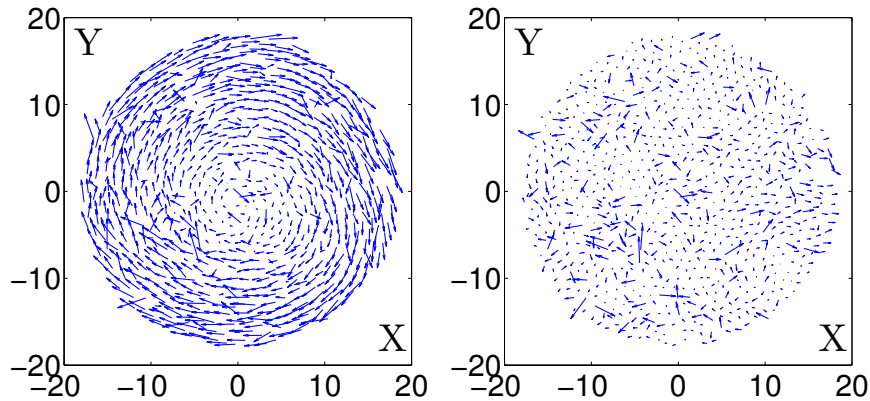


Figure 3.2: **Removing convection. Left:** Displacements of particles (arrows are magnified by a factor of 20) for a lag time $\tau = 500$ at a density $\phi = 0.8125$. **Right:** The same having removed the solid rotation field.

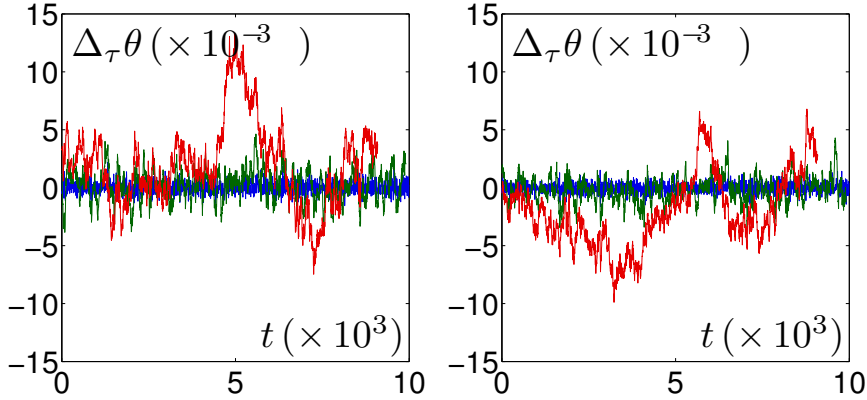


Figure 3.3: **Temporal rotation magnitude** $\Delta_\tau\theta(t)$ vs. t for $\tau = 10$ (blue), $\tau = 100$ (green) and $\tau = 1000$ (red), for $\phi = 0.8125$ (**left**), and $\phi = 0.8136$ (**right**).

displacements fields before (left), and after (right), we have removed the rotation are displayed.

We see that large scale currents have been almost entirely removed. In order to study the magnitude of such an effect, we focus now on $\Delta_\tau\theta(t)$. $\Delta_\tau\theta(t)$ vs. t has been plotted for different lag times τ in figure 3.3. For all lag times, the rotation magnitude is small, on average, but displays large fluctuations which increase significantly with the lag time. We see that the rotation amplitude crosses zero several time. That means that the rotation is rather a fluctuating rotation than a constant rotation in a well defined direction. Besides, the average sense of rotation seems to be random from one run to the other. We illustrate it here by showing $\Delta_\tau\theta(t)$ vs. t for two different runs in figure 3.3: they have a different average rotation sense.

In order to quantify the dependence of the rotation with respect to the lag time τ , we compute respectively the absolute value of the time average and the standard deviation of $\Delta_\tau\theta(t)$, which are respectively displayed for all packing fractions in figure 3.4, top left and top right. For $|\langle\Delta_\tau\theta\rangle|$, we observe a linear behavior with respect to τ at all packing fractions, so that $|\langle\Delta_\tau\theta\rangle|$ can be fitted by $\Omega\tau$, where Ω is an average rotation velocity. We perform such a fit and we plot Ω versus packing fraction ϕ in figure 3.4, bottom-left. We see that Ω undergoes a clear jump from 10^{-6} to 10^{-7} at a packing fraction $\phi = 0.814$. Above this density, Ω is rather constant, around 10^{-7} rad/cycle. Below $\phi \sim 0.814$, Ω lies between 10^{-6} and 10^{-5} rad/cycle and displays a maximum at $\phi \sim 0.807$. The rotation displays a drift, and we have characterized its magnitude.

We now turn toward the study of rotation fluctuations. To do so, we plot in figure 3.4, top right, the standard deviation of the rotation $\text{std}\Delta_\tau\theta$. First, this quantity is much larger than $|\langle\Delta_\tau\theta\rangle|$ for short lag times: the

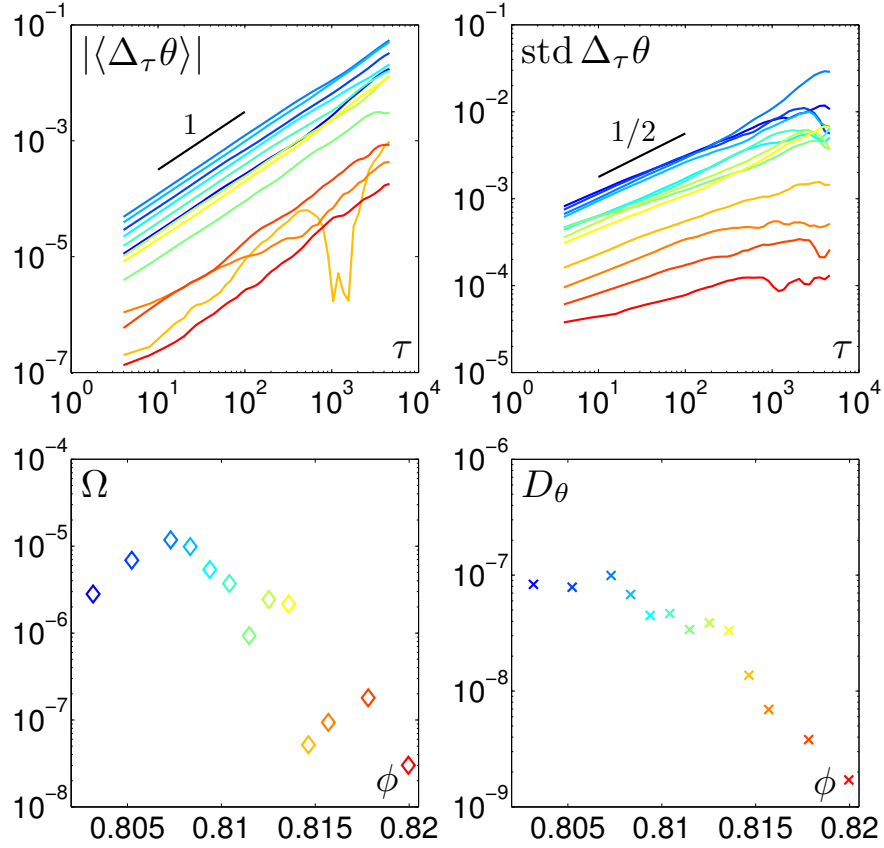


Figure 3.4: **Rotation magnitude.** Absolute value of the average magnitude (**top-left**) and standard deviation (**top-right**) of rotation $\Delta_\tau \theta(t)$ vs. τ . **Bottom-left:** Drift of the rotation Ω (defined in the text) vs. packing fraction ϕ . **Bottom-right:** Diffusion of the rotation D_θ (defined in the text) vs. packing fraction ϕ . Color code spans from blue (low packing fractions) to red (high packing fractions) (See table 3.1).

fluctuations are much larger than the drift. However, for large lag times, they become of the same order of magnitude. Second, all the curves have an exponent close to 1/2. Therefore, we fit $\text{std } \Delta_\tau \theta$ by $\sqrt{D_\theta \tau^{1/2}}$, and we display D_θ with respect to packing fraction in figure 3.4, bottom-right, it decreases with packing fraction, and the curve has a kink at a density $\phi \sim 0.814$ above which the decrease is steeper.

We now turn to the “corrected” displacements fields displayed in figure 3.5, left. For the low densities, we observe that there is shear on top of the solid rotation.

3.1.2 Shear

From the trajectories of the particles, we define

$$\widehat{\Delta_\tau \vec{r}_i(t)} = \widetilde{\Delta_\tau \vec{r}_i(t)} + \Delta_{\tau, s} \vec{r}_i(t), \quad (3.6)$$

where $\widetilde{\Delta_\tau \vec{r}_i(t)}$ was defined in equation 3.1, and

$$\Delta_{\tau, s} \vec{r}_i(t) = \begin{pmatrix} a_\tau & b_\tau \\ b_\tau & -a_\tau \end{pmatrix} \left(\frac{\vec{r}_i(t) + \vec{r}_i(t+\tau)}{2} - \vec{r}_\tau^0(t) \right), \quad (3.7)$$

is the shear deformation field. The same optimizing procedure leads to the following expressions for a_τ and b_τ .

$$a_\tau = \frac{\sum_{i=1}^N \begin{pmatrix} 1 & 0 \\ 0 & -1 \end{pmatrix} \widetilde{\Delta_\tau \vec{r}_i(t)} \cdot \left(\frac{\vec{r}_i(t) + \vec{r}_i(t+\tau)}{2} - \frac{1}{\Delta_\tau \theta} \begin{pmatrix} 0 & 1 \\ -1 & 0 \end{pmatrix} \widetilde{\Delta_\tau \vec{r}_i(t)} \right)}{\sum_{i=1}^N \left\| \frac{\vec{r}_i(t) + \vec{r}_i(t+\tau)}{2} - \frac{1}{\Delta_\tau \theta} \begin{pmatrix} 0 & 1 \\ -1 & 0 \end{pmatrix} \widetilde{\Delta_\tau \vec{r}_i(t)} \right\|^2} \quad (3.8)$$

and

$$b_\tau = \frac{\sum_{i=1}^N \widetilde{\Delta_\tau \vec{r}_i(t)} \cdot \left(\begin{pmatrix} 0 & 1 \\ 1 & 0 \end{pmatrix} \frac{\vec{r}_i(t) + \vec{r}_i(t+\tau)}{2} + \frac{1}{\Delta_\tau \theta} \begin{pmatrix} 1 & 0 \\ 0 & -1 \end{pmatrix} \widetilde{\Delta_\tau \vec{r}_i(t)} \right)}{\sum_{i=1}^N \left\| \frac{\vec{r}_i(t) + \vec{r}_i(t+\tau)}{2} - \frac{1}{\Delta_\tau \theta} \begin{pmatrix} 0 & 1 \\ -1 & 0 \end{pmatrix} \widetilde{\Delta_\tau \vec{r}_i(t)} \right\|^2}, \quad (3.9)$$

where \cdot is the dot product.

Figure 3.5 right displays the displacements where shear has been removed. a_τ and b_τ describe shear the following way: the eigenvalues of the

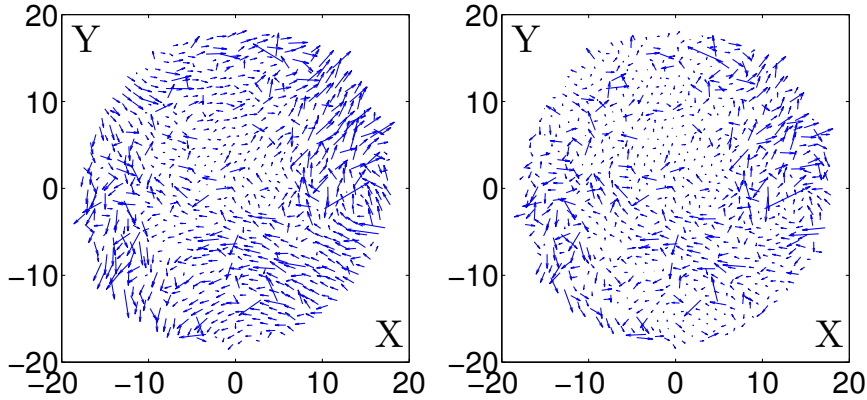


Figure 3.5: **Removing shear. Left:** Displacements of particles (arrows are magnified by a factor of 20) for lag time $\tau = 500$ and at a density $\phi = 0.8073$. **Right:** The same having removed the solid rotation field.

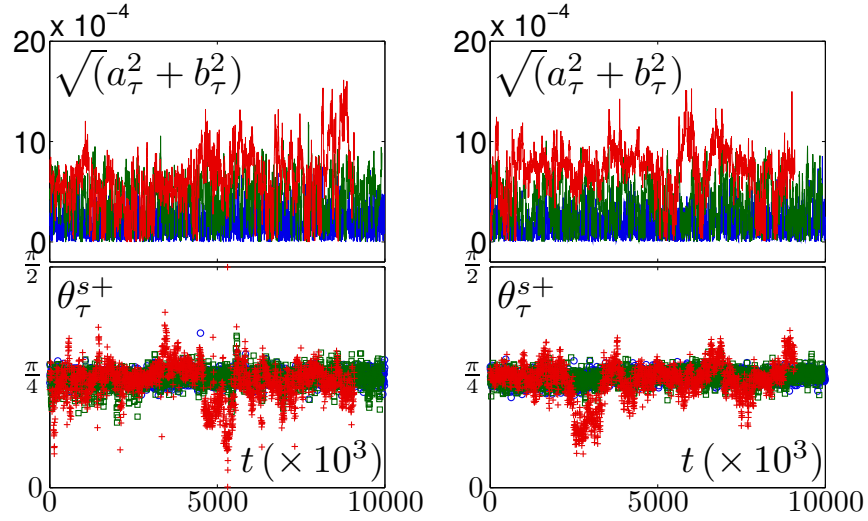


Figure 3.6: **Shear magnitude** $\sqrt{a_\tau^2 + b_\tau^2}$ (**top**) and angle $1/2 \arctan b_\tau/a_\tau$ (**bottom**) vs. t for $\tau = 10$ (blue), $\tau = 100$ (green) and $\tau = 1000$ (red), for $\phi = 0.8125$ (**left**), and $\phi = 0.8136$ (**right**).

shear matrix $\begin{pmatrix} a_\tau & b_\tau \\ -b_\tau & a_\tau \end{pmatrix}$ are $\pm \sqrt{a_\tau^2 + b_\tau^2}$. Therefore, $\sqrt{a_\tau^2 + b_\tau^2}$ quantifies the magnitude of the shear deformation.

$$\theta_\tau^{s\pm} = \arctan \frac{1}{\frac{a_\tau}{b_\tau} \pm \sqrt{1 + \left(\frac{a_\tau}{b_\tau}\right)^2}} \quad (3.10)$$

are the orientation of one eigenvectors (the second is orthogonal to the first) and is related to the principal direction of the shear deformation. Both $\sqrt{a_\tau^2 + b_\tau^2}$ and θ_τ^{s+} are plotted in figure 3.6 for two different packing fractions. For small lag times, the angle of the shear deformation strongly fluctuates and vacillates around $\pi/4$: the shear constantly reverses its direction. For larger lag times, the shear has a more persistent direction. The magnitude of shear displayed in figure 3.6, top, strongly fluctuates as well, and has an average that increases for larger lag times τ .

We now compare shear and rotation magnitudes by plotting $\langle |\Delta_\tau \theta| \rangle$ and $\langle \sqrt{a_\tau^2 + b_\tau^2} \rangle$ versus packing fraction in figure 3.7. First, we see that rotation is more significant than shear at all packing fractions. This is consistent with the very first observation of trajectories we have done above (see figure 3.2). Both shear and rotation have the same dependence on ϕ at all lag time τ . A small kink at $\phi \sim 0.814$ seems to separate high from low packing fractions. For high densities, shear and rotation strongly decrease as the packing fraction is increased. Below $\phi \sim 0.814$, the dependence on density is more modest.

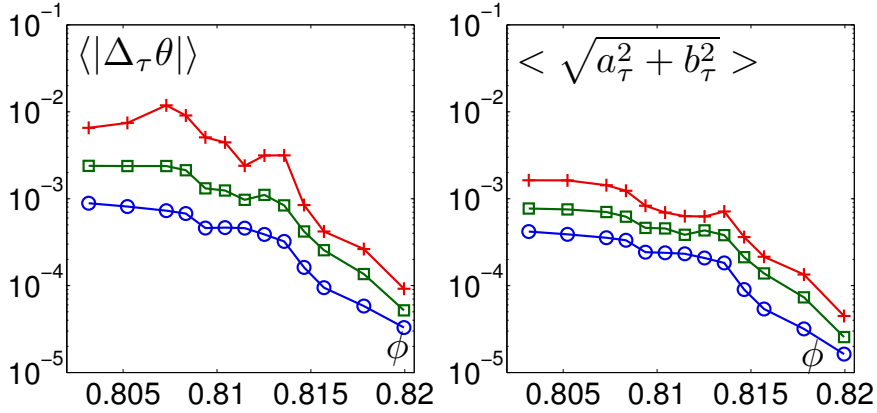


Figure 3.7: **Convection magnitude.** Magnitude (see text for definition) of rotation **left** and shear **right** vs. packing fraction ϕ in radians for $\tau = 10$ (\circ), 100 (\square) and 1000 ($+$).

3.1.3 Aftermath : convection thwarts long time observations

We end this section by a short summary of our observations: we see a convective current that is dominated by solid rotation, the center of which is located around the center of the region of interest. This convection has strong fluctuations and a modest drift in time.

The magnitude of this drift becomes significant at low packing fractions and long lag times. This may thwart the computation of particles displacements, as the remaining motion is tiny compared what has been subtracted. We try here to define a validity criterion for the extraction of the remaining dynamics. We have seen in section 2.5.1 that the resolution on grain position is about $n_g = 5 \cdot 10^{-3}$ grain diameter. We now want to estimate the precision of the convection motion, n_c . To do so, we first stick to the solid rotation measurements since it is always more significant than shear. It is tempting to use the time average of $\chi(\Delta_\tau \theta(t), \vec{r}_\tau^0(t))$ defined in equation 3.3 to estimate the deviation from the solid rotation but this is precisely the mean square displacement that will be investigated in section 3.4: we don't want to use the quantity of interest as a measurement of error. We rather turn toward the average magnitude of convection $|\langle \Delta_\tau \theta \rangle|$, that gives an estimate of the fluctuations of solid rotation. Let's roughly assume that the precision for $|\langle \Delta_\tau \theta \rangle|$ is $|\langle \Delta_\tau \theta \rangle|/\sqrt{N}$, where N is the number of particles.

Altogether,

$$n_c \lesssim r_{max} \frac{|\langle \Delta_\tau \theta \rangle_c|}{\sqrt{N}}, \quad (3.11)$$

where $r_{max} \sim 20$ is the radius of the region of interest. The condition $n_c = n_g$ yields $|\langle \Delta_\tau \theta \rangle_c = 7.5 \cdot 10^{-3}$. Therefore in the following we shall consider all measurements of displacements where $|\langle \Delta_\tau \theta \rangle|$ exceeds $7.5 \cdot 10^{-3}$ as spurious. This criterion is illustrated in figure 3.8, left, where $|\langle \Delta_\tau \theta \rangle|$

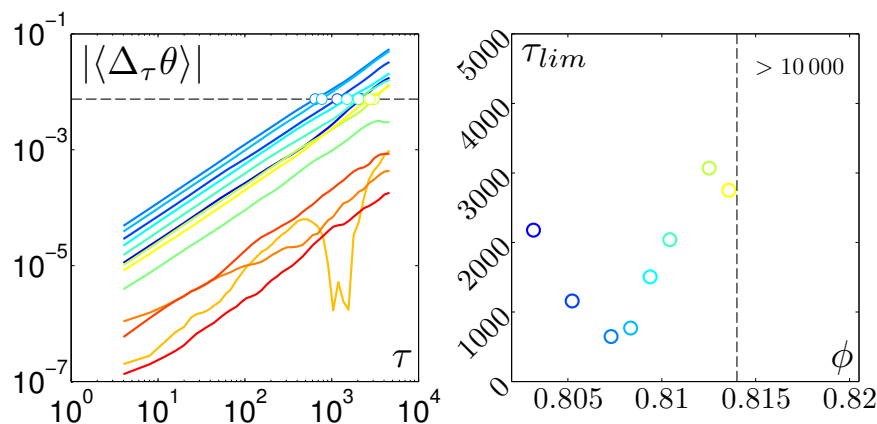


Figure 3.8: **Convection validity criteria.** **Left:** Absolute average magnitude of rotation $\Delta_\tau \theta(t)$ vs. τ . \circ symbols denote their intersection with the constant value $\Delta\theta_s = 7.5 \cdot 10^{-3}$ highlighted by the black dotted line. **Right:** X-value of the intersection τ_{lim} vs. packing fraction. Color code spans from blue (low packing fractions) to red (high packing fractions) (See table 3.1).

is plotted vs. lag time, τ . This defines an upper bound τ_{lim} . τ_{lim} has been plotted vs. packing fraction in figure 3.8, right; we see that it roughly increases with packing fraction, and that it is above the experimental window for high packing fractions. To conclude, we shall consider the measurements of displacements for lag time $\tau > \tau_{lim}$ with care: we wouldn't want to weigh the captain by measuring the difference between the weight of the ship with the captain and its weight without the captain¹.

Besides, although we suspect the mechanical shaking to be responsible for it, the mechanism at the root of such a peculiar convection signal remains unknown in our system.

3.2 Structural Relaxation

3.2.1 About granular glasses

There are several experiments of externally driven dense bi-dimensional granular materials which—using grains as a model system—aim at describing the glass transition, [Abate and Durian, 2006, Reis et al., 2007, Watanabe and Tanaka, 2008, Watanabe et al., 2011]. In particular, despite slight differences in the mechanical shaking and the poly-dispersity, Watanabe and Tanaka [2008], Watanabe et al. [2011], Reis et al. [2007] report that the structural relaxation time, τ_α , is way larger than the experimental time window for densities as low as $\phi \sim 0.75 - 0.79$. The complex

¹The captain is not supposed to leave the ship anyway.

glassy dynamics that occurs in these experiments has to do with a reorganization of the density profile, and in particular Watanabe and Tanaka [2008] establishes a clear link between τ_α and the size of the dynamical heterogeneities occurring within structural relaxation.

On the contrary, we will see in the following section that significant rearrangements of the structure are absent in the present work, at least on the experimental time scale. Hence, we don't address the glass transition, but a complex non-equilibrium dynamics that takes place deep in the glass phase.

3.2.2 Neighbors

The very first observation we can make from the experiment is that the granular packing is very dense. Therefore, neighbor relationships are very well defined. The Delaunay triangulation is a very robust way to establish neighbors relationships: we can perform a Voronoï tessellation out of it. The first thing we can do is to compare the tessellation structures: figure 3.9, left, displays the superimposition of two tessellations separated by a time lag of 5000, for the lowest packing fraction. We see that little has changed between the two time steps. While the overall structure is globally conserved, most zones have barely moved, some have rearranged and have induced displacements of the order of 10^{-1} particle size. Such rearrangements are further

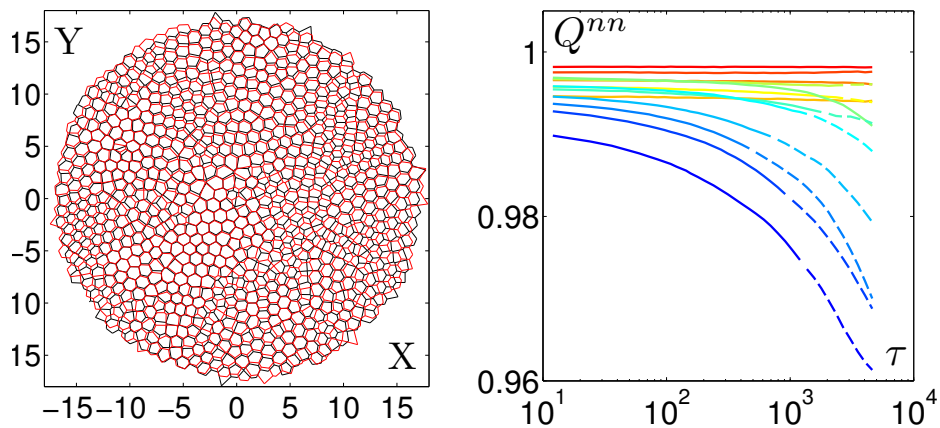


Figure 3.9: **Obtaining a granular glass. Left:** Superposition of the Laguerre cells computed at times $t = 1$ and $t = 5000$ for the loosest packing ($\phi = 0.8031$). **Right:** Average fraction of neighbors $Q_{nn}(\tau)$ which have not changed between two images separated by a time interval τ , for different packing fractions. Dashed lines indicate that τ_{lim} (see section 3.1) has been exceeded. Color code spans from blue (low packing fractions) to red (high packing fractions) (See table 3.1).

quantified by $Q^{nn}(\tau)$, the average fraction of *neighbor* relationships surviving in a time interval τ . Plotted with respect to lag time, τ , in figure 3.9, Q^{nn} remains larger than 95% even for the loosest packing fraction and barely departs from 1 for the densest ones (fig. 3.9 right).

To summarize, in the language of the glass community, “there is no α relaxation”, meaning that the density profile survives *on the experimental time-scale*. Therefore, our system is a glass, the structure of which is essentially frozen. That being said, for the “loose” packing fractions, the structure clearly starts to change on long times: the α relaxation clearly starts to set in, and there is no doubt it would rearrange further if longer experimental windows were investigated. Note that, as stressed by the dashed lines in figure 3.9 right, minor errors in the convection correction might also contribute to this long time behavior.

3.3 Mechanical Rigidity

3.3.1 Wall pressure

As described in chapter 2, the packing undergoes an uni-axial compression. We here present measurements of the piston force coming from the force sensor that is attached to the piston performing the compression. The resulting force we measure can thus be seen as a confining pressure. In the following, we a-dimensionnalize it by the weight of the grains, and we will call it the *Wall-pressure*. In addition, since the grain assembly can be quite stiff, the force sensor can deform quite significantly. Indeed, the Young modulus of PSM-4 and brass are respectively 0.5 MPa [Micro-Measurements, 2010] and 100 GPa (see [MOD]). Assuming Hertz law, the stiffness of two compressed

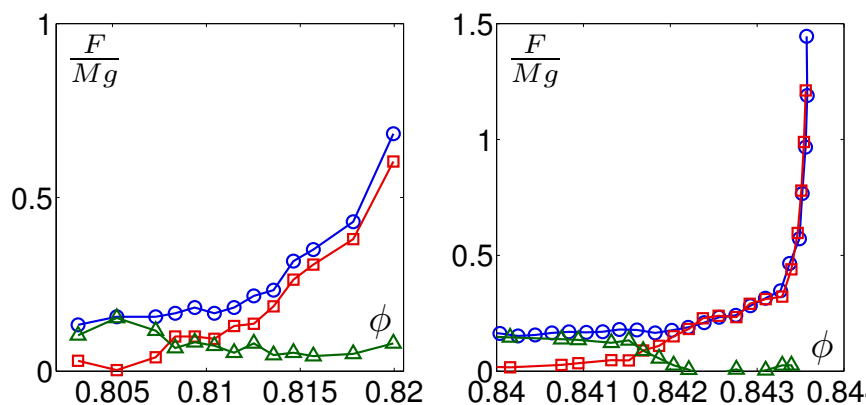


Figure 3.10: **Wall pressure** vs. packing fraction: (\circ): P_{TOT} , (\square): P_{STAT} , (\triangle): P_{DYN} as defined in the text. **Left:** for photo-elastic disks experiment, **right:** for brass disks experiment (see Lechenault’s PhD [Lechenault, 2007]).

4 mm height cylinders is thus respectively 3×10^8 N/m and 1.5×10^3 N/m [Landau and Lifshitz]. Over there weight, this leads to typical grain overlaps of respectively 1×10^{-8} m and 2×10^{-5} m, or equivalently, to respectively 2.5×10^{-6} and 5×10^{-3} grain diameter. In comparison, the stiffness of the force sensor and piston system is 6.10^4 N/m. We recall here that we have to take it into account when we measure the packing fraction (more precisions are given in section 2.1.2).

Wall-pressure vs. packing fraction is represented in figure 3.10 for both photo-elastic (left) and brass (right) disks. P_{TOT} (respectively P_{STAT}) is the pressure measured when the vibration is switched on (respectively off). P_{STAT} is thus the static pressure sustained by the packing in the absence of vibration, whereas $P_{DYN} = P_{TOT} - P_{STAT}$ can be interpreted as the dynamic pressure, induced by the vibration. At low packing fractions, the pressure is constant and is dominated by the dynamic part while at high packing fractions, the pressure increases with packing fraction and is dominated by the static part. P_{STAT} and P_{DYN} cross at an intermediate packing fraction. Let us now compare the results obtained here for the photo-elastic grains in figure 3.10, left, and those obtained by Lechenault et al. [2008a,b], Lechenault [2007] for the brass disks, displayed in figure 3.10, right. The crossover from dynamically to statically dominated pressure is qualitatively similar in the two systems: P_{DYN} and P_{STAT} both cross at an intermediate packing fraction. However, two differences arise;

- the crossover packing fraction is much lower for photo-elastic disks than for brass disks. We interpret this as a signature of the higher friction coefficient between photo-elastic grains than between brass grains. More frictional particles undergoing a similar compaction protocol jam at a lower packing fraction, as suggested by numerical simulations [Silbert et al., 2002, Zhang and Makse, 2005, Shundyak et al., 2007], where a similar effect has been probed.
- The crossover range is five times broader for photo-elastic grains, as illustrated by the range, $\delta\phi$, within which the static pressure increases from 0 to 0.5: $\delta\phi \sim 0.015$ for photo-elastic and $\delta\phi \sim 0.003$ for brass. We interpret this as a signature of the drastically different stiffnesses of these two materials, as suggested by numerical studies of soft a-thermal frictionless disks [van Hecke, 2010]: their mechanical moduli scale trivially with the stiffness of the particles. However, while the stiffness of the photo-elastic and brass grains differ by a factor of 2×10^4 , the range $\delta\phi$ differ by a factor of 5, and thus, does not scale trivially with the stiffness of the grains. We think that this difference relies on the fact that we do not probe truly a-thermal grains, but grains in the presence of vibration.

To conclude, wall pressure measurements yield a first good grasp of the

unjammed to jammed crossover. A further understanding of the mechanical properties across this stiffening crossover requires a closer investigation of the distributions and the spatial organization of microscopic forces. We will thereafter scrutinize the details of the bulk, the geometry and the orientation of the force network.

3.3.2 Bulk force properties

3.3.2.1 Averaging over time?

We ensure here that temporal fluctuations are stationary and gaussian so that statistics can be cumulated over time. The straightforward quantity to consider here is the instantaneous pressure at time t , P_t , defined by

$$P_t = \frac{1}{N} \sum_{i=1}^N G_i(t), \quad (3.12)$$

where $G_i(t)$ is the instantaneous pressure in grain i at time t . A plot of P_t versus t is displayed in figure 3.11 left. We see a signal with rather low fluctuations compared to its average value. This point is also illustrated by 3.11 right, where the distributions of $\frac{P_t - \bar{P}_t}{\text{std}_t P_t}$ have been plotted. Apart from statistical fluctuations, they mostly overlap, close to a gaussian distribution. Therefore, there is no strong intermittency, and it is meaningful to cumulate statistics over time.

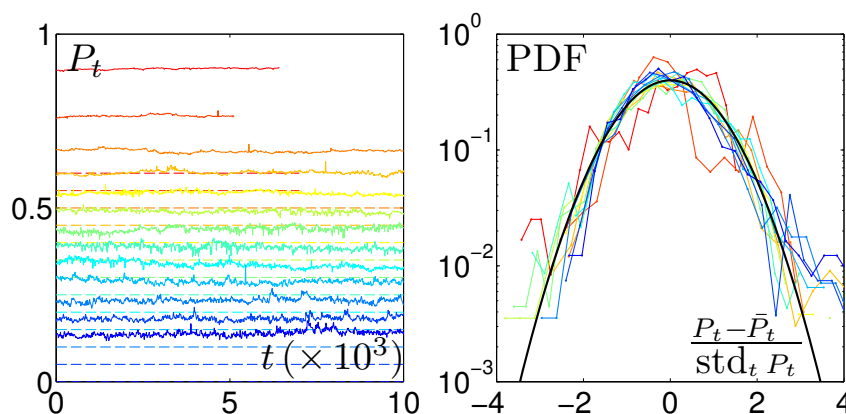


Figure 3.11: **Instantaneous Pressure.** **Left:** P_t vs. t . curves have been shifted for clarity. For each curve, the corresponding dotted lines are drawn using the same color that indicate the shift. **Right:** Distributions of $\frac{P_t - \bar{P}_t}{\text{std}_t P_t}$ for different packing fractions. The black line is a gaussian function of average 0 and of standard deviation 1. Color code spans from blue (low packing fractions) to red (high packing fractions) (See table 3.1).

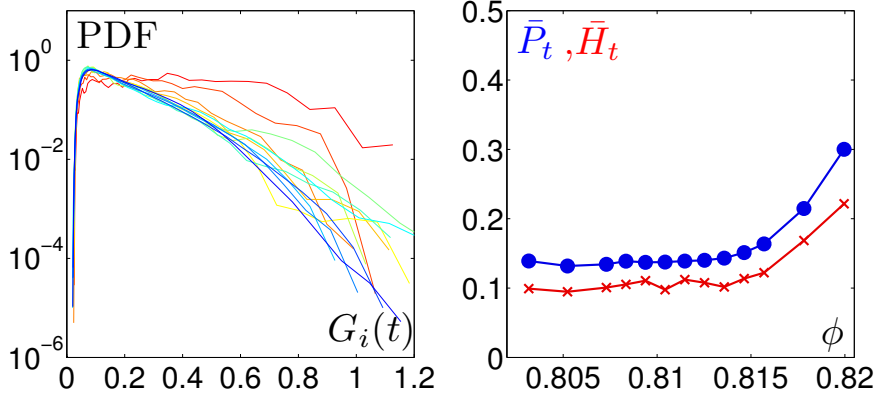


Figure 3.12: **Instantaneous microscopic pressures.** **Left:** Probability density function (Pdf) of $G_i(t)$ sampled over space and cumulated over time. **Right:** Temporal average of P_t (●) and H_t (×) vs packing fractions (see text for definition). Color code spans from blue (low packing fractions) to red (high packing fractions) (See table 3.1).

3.3.2.2 Average and Variance

In this section, we are interested in the spatial distribution of the forces. First, the distributions of $G_i(t)$ sampled over space and cumulated over time are plotted in figure 3.12. For high densities, they are very flat and wide whereas at low densities, the distributions tend to collapse on similar curves, that have exponential tails. In order to quantify their dependence with respect to the packing fraction, we consider both P_t and H_t , where P_t has been defined above, and H_t is the standard deviation of the instantaneous distributions and is defined by

$$H_t = \sqrt{\frac{1}{N} \sum_{i=1}^N G_i(t)^2 - P_t^2}. \quad (3.13)$$

“H” stands for “Heterogeneity”, as H_t quantifies the instantaneous heterogeneity of the packing at time t . Like the wall pressure, \bar{P}_t increases with packing fraction. This has already been described in section 2.4.3. Interestingly, \bar{H}_t behaves similarly to \bar{P}_t : the heterogeneity of the packing is constant for low packing fractions and increases as the forces increase. This similar behavior of average and standard deviation is consistent with the exponential tails of the distributions and basically tells us that a unique parameter, namely the average entirely describes the distribution of the instantaneous pressure field.

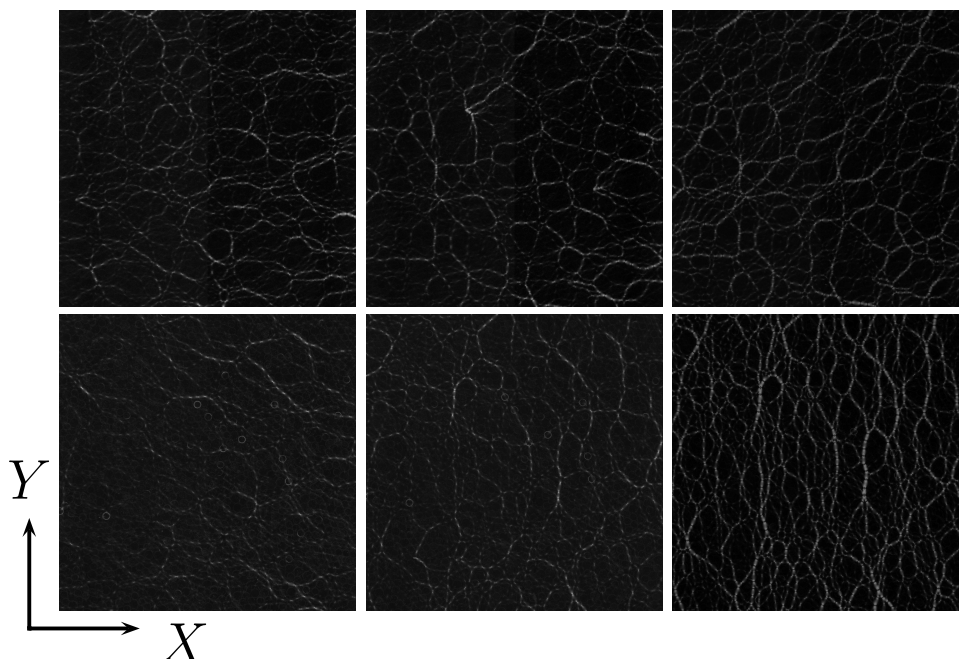


Figure 3.13: **Force chains.** Cross-polarized pictures of (**top left**) a loose packing ($\phi = 0.81$), (**top middle**) an intermediate packing $\phi = 0.82$, and (**top right**) a dense packing rapidly ($\phi = 0.82$). **Bottom:** the same for a quenched packing.

3.3.3 Geometry of the force network

Throughout the remainder of this section, we will investigate the spatial properties of the force network. We will also compare these properties with a packing that has been prepared by compressing it at a larger rate. Therefore, the first packing will be referred to an “annealed” packing and the second one as a “quenched” packing.

First, we present experimental cross-polarized frames in figure 3.13 for both “annealed” (top) and “quenched” (bottom) packings. The gray-scale of the picture contains information on the force. From a caricaturist point of view, black zones correspond to force free zones, while white zones are force bearing zones. We first see that for all packings, the pressure profile is very heterogeneous in space: we very clearly distinguish force chains. These have been observed for quite long in granular media [Wakabayashi, 1950, Liu et al., 1995]. They provide an illustrative picture of the force network geometry implied on both sides of the crossover mentioned above for the “annealed” packing: at low packing fractions (fig. 3.13 left), the forces chains are anisotropic and oriented in the shaking axis, whereas at high packing fractions, the packing is rather isotropic and the force network is

denser (fig. 3.13 top-right). In contrast, a first look at the “quenched” packing at high density (see fig. 3.13 bottom right) reveals a strong anisotropy in the compression direction. No clear difference between “quenched” and “annealed” states appears at low packing fraction. We will, in this section, attempt to describe quantitatively the heterogeneity, the geometry and of the orientation of the force chains for both systems.

3.3.4 Spatial Correlations

Should we desire to go further in the description of the force network, we need to investigate the spatial dependence. To do so, we next investigate spatial correlations in the system. We recall here that the X —axis is the shaking direction and the Y —axis is the compression direction. This computation is performed by transforming instantaneous maps of $G_i(t)$ into interpolated grids $G(X, Y)$, out of which we can compute 2D autocorrelation that are cumulated over time. The 2D autocorrelation C is defined as follows:

$$C(X, Y) = \left\langle \sum_{X'=-L_X}^{L_X} \sum_{Y'=-L_Y}^{L_Y} G(\widetilde{X'+X}, \widetilde{Y'+Y}) G(\widetilde{X'}, \widetilde{Y'}) \right\rangle_t, \quad (3.14)$$

where $\widetilde{G(X, Y)}$ is reduced by its standard deviation and centered by its mean and $\langle \dots \rangle_t$ is time average. This process is summarized in figure 3.14 where an interpolated grid of a G_i map is pictured (top left), as well as its corresponding 2D autocorrelation map (top right). We then extract the decay of the autocorrelation along both the shaking axis (X), $C_X = C(X, Y = 0)$ (bottom left), and the compression axis (Y), $C_Y = C(X = 0, Y)$ (bottom right). In order to measure the decay of the autocorrelations along X and Y , we arbitrarily define respectively ζ_X and ζ_Y the length at which $C_X(\zeta_X) = 0.2$ and $C_Y(\zeta_Y) = 0.2$ (horizontal dotted lines on the figures). This a coarse estimation of the decay, but given that we have not extracted any functional form of C_Y and C_X and that they are not always positive, this remains the best option.

ζ_X and ζ_Y are plotted in figure 3.15 for both the “annealed” (**left**) and their “quenched” (**right**) systems:

The X —decay: both systems have similar X decay length behavior with packing fraction: ζ_X is constant at low packing fractions and falls down at an intermediate packing fraction. The differences here consist of (i) the value of the low density value that is equal to 3 for the annealed system and 2 for the quenched system; (ii) the crossover packing fraction, that is close to 0.810 for the quench and to 0.814 for the annealing.

The Y —decay: while it remains constant and rather small around 1 at all packing fractions for the “annealed” system, ζ_Y departs from 1 and increases significantly at an intermediate packing fraction $\phi \sim 0.810$ for the “quenched” system. This long decay is associated with compression force chains that come from the “quench” protocol, and that we observed above in the experimental picture figure 3.13 right.

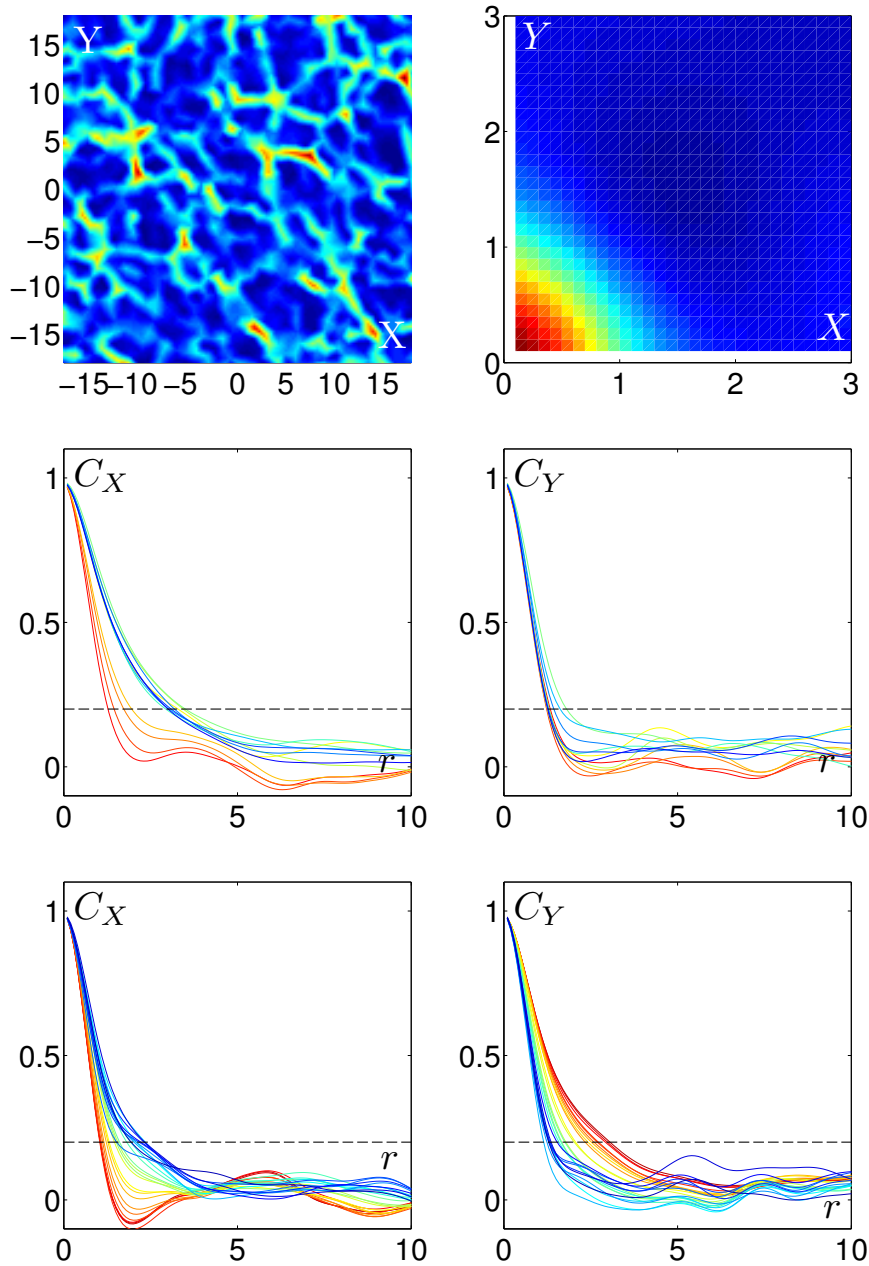


Figure 3.14: **2D autocorrelation for the “annealed” system.** **Top Left:** Force map (see text for definition). **Top Right:** 2D autocorrelation of the Force map. **Middle Left:** Decay of the 2D autocorrelation along the shaking axis for the annealed experiment. **Middle Right:** Decay of the 2D autocorrelation along the compression axis for the annealed experiment. **Bottom Left:** Decay of the 2D autocorrelation along the shaking axis for the quenched experiment. **Bottom Right:** Decay of the 2D autocorrelation along the compression axis for the quenched experiment. Dotted line marks 0.2. Color code spans from blue (low packing fractions) to red (high packing fractions).

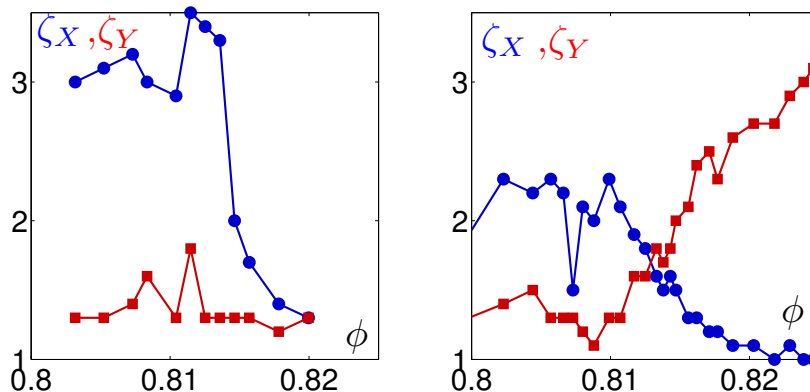


Figure 3.15: **2D autocorrelation decay** ζ_X (●) and ζ_Y (■) vs. packing fraction for an “annealed” (left) and a “quenched” (right) experiment.

To conclude, in the loose regime, the force chains have a typical size of 2 to 3 grain diameter and have spatial correlations in the shaking direction. In the dense regime, the force chains spatial correlations strongly depend on the preparation protocol. In the annealed protocol, which we follow, it is essentially isotropic.

3.3.4.1 Orientation of the contact forces

We here compute the normal forces between particles (they are defined in sections 2.5.2.2 and 4.1.1) and project the forces respectively along the shaking and the compression axis. We then cumulate the statistics over time. The schematic figure 3.16 displays the convention we take for θ , namely the angle with respect to the shaking direction. A possible choice is to perform the projections along shaking and compression axis is for each to compute the products

$$F_X = \frac{\langle F_N \cos^2(\theta) \rangle}{\langle F_N \rangle} \quad \text{and} \quad F_Y = \frac{\langle F_N \sin^2(\theta) \rangle}{\langle F_N \rangle} \quad , \quad (3.15)$$

$\langle . \rangle$ denotes average over links and time. Given that we want here to average either “shaking” or “compression” inter-particle normal forces and not to differentiate between “upwards” and “downwards”, we adopt this particular projection where forces are averaged regardless of their direction. This yields the curves F_X and F_Y vs. packing fraction drawn in figure 3.16 bottom left. First, as a direct consequence of their definition and because F_N and θ are decorrelated, the measurements of F_X and F_Y are symmetric. Second, we see that they are close to 0.50 at high packing fraction, and depart from this value at a packing fraction close to 0.814. Below this density, F_X remains

at a value of 0.52. This means that there is no preferred direction of the forces at high packing fraction while there are more forces that are oriented in the compression direction at low densities. Again, we compare with the “quench” protocol experiment results displayed in figure 3.16 bottom right. We see here that like the annealed protocol, there is a slight anisotropy in the direction of shaking for low densities. In contrast, the forces significantly orient in the compaction direction for high densities. And the crossover packing fraction is close to 0.810. To conclude, in the unjammed regime, the strongly anisotropic mechanical shaking is responsible for anisotropic force chains. In contrast, in the jammed regime, force chains depends on the preparation of the packing and again are essentially isotropic for the “annealed” protocol, which we will use in the following.

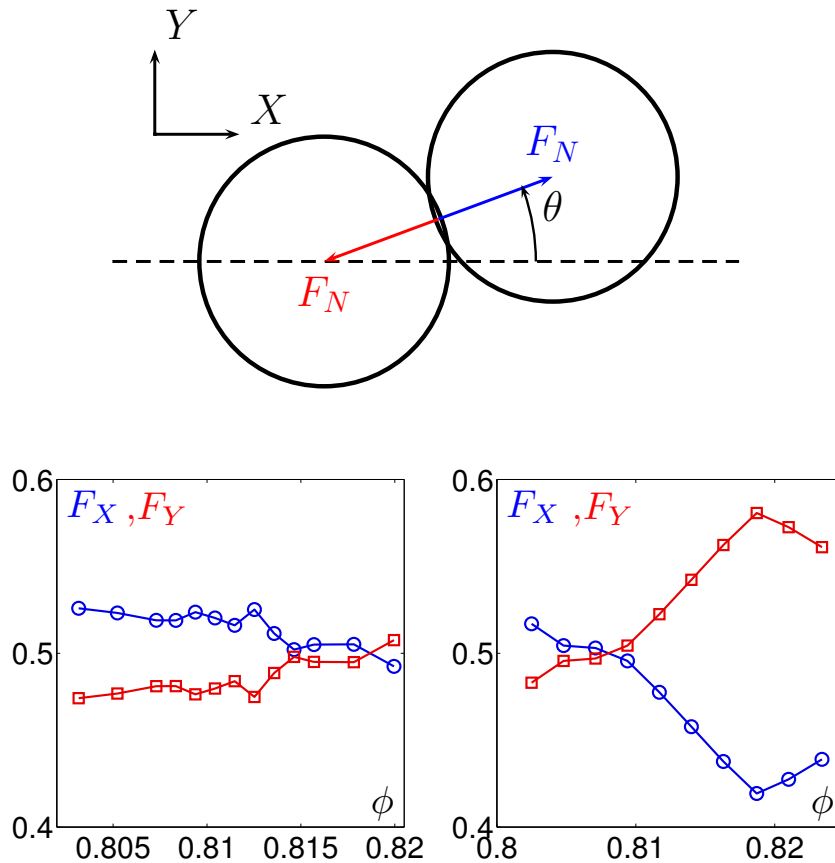


Figure 3.16: **Force chains orientation.** **Top:** Scheme of a contact. **Bottom:** Average of normal inter-particle forces projected along shaking axis F_X (\circ), and compression axis F_Y (\square) vs. packing fraction for (**left**) an annealed packing and (**right**) a quenched packing.

3.3.4.2 Summary

The properties of the force network are summarized on the light of a thermal jamming transition in figure 3.17, where a sketch of pressure versus packing fraction is plotted for no mechanical agitation and for finite mechanical agitation. Without agitation, the specific density ϕ_J marks the limit between mechanical vacuum and elastic response. In the presence of agitation, ϕ_J marks the crossover between dynamically induced forces and statically elastic induced forces. We have seen that the dynamically induced forces are strongly anisotropic, they are made of force chains and are oriented in the direction of the shaking. In contrast, the statically induced forces are made of force chains and depend on the preparation protocol of the packing: they are either anisotropic if the packing has been compressed quickly or isotropic if the packing has been prepared slowly. In the following section, we shall investigate the dynamics of the displacements and try to bridge with the jamming crossover we have just observed.

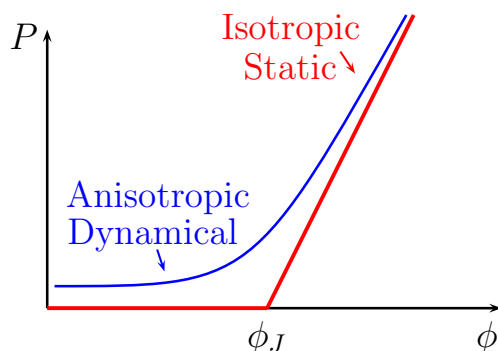


Figure 3.17: **Sketch of pressure vs. density.** Sketch of pressure vs. packing fraction for hard and soft particles, at zero temperature (red) and at finite temperature (blue)

3.4 Dynamics

We then turn to the study the statistical properties of the dynamics of the grains. In this section, we first deal with “rattlers”, that are particles embedded in a cage [Lubachevsky and Stillinger, 1990], and that strongly oscillate, and spoil the statistical measurements of dynamics. We then introduce both root mean square displacements and the dynamical structure factor in order to characterize the dynamics. Both are used in the literature, but we will see that the first provides the information of the average dynamics whereas the latter allows one to choose the length-scale at which we observe the dynamics and to compute a dynamical susceptibility.

3.4.1 Rattlers

We first display the trajectories of one particle in figure 3.18, left. We directly see that this trajectory has a peculiar shape. It is mainly made of back and forth “rattling” moves. Hence, such a particle is called a “rattler”. In order to estimate how significant are the rattling events, we consider

$$D_i(t) = -\overrightarrow{v_i(t)} \cdot \overrightarrow{v_i(t+1)}, \quad (3.16)$$

where $\overrightarrow{v_i(t)}$ is the instantaneous displacement of the grain i at time t . We plot the distribution of D_i sampled over time in figure 3.18, right. We see that this is a bimodal, where there are two maxima. While events that are at the right of the distribution correspond to rattling events, events at the left of the distribution are non-rattling events. The logarithm of the distribution is well fitted by a polynomial of order 3. From this fit, we extract the threshold value th_i between rattling and non-rattling events, that is the local minimum of the fit. We also extract the magnitude of the minimum $h_{\text{th}i}$. Likewise, we extract the maximum position p_{ri} and its magnitude h_{ri} . This allows us to define a criteria. We will take as bimodal all the distributions that satisfy $h_{ri}/h_{\text{th}i} > 2$. This defines particles of type 1. Of course, all the distributions are not bimodal, and in those cases, the parameters th_i , $h_{\text{th}i}$, p_{ri} and h_{ri} are not relevant to describe the rattling events. Two examples of such distributions are given in figure 3.18, bottom left and bottom right. In figure 3.18, bottom left, the figure has an inflection point, that is a good natural threshold between non-rattling and rattling events. Together with the particles with $h_{ri}/h_{\text{th}i} \leq 2$, these particles are labeled type 2. Finally, in figure 3.18 bottom right, no particular characteristic allows us to discriminate between rattling and non-rattling events. However, these particles may be rattlers. These particles are labeled type 3.

We now count the “populations” of grains belonging to each population and represent their fraction in figure 3.19, left. We see that the fraction of bimodal (type 1) particles is almost zero at low packing fractions and increases to 10% for the densest packings. This can be interpreted by the

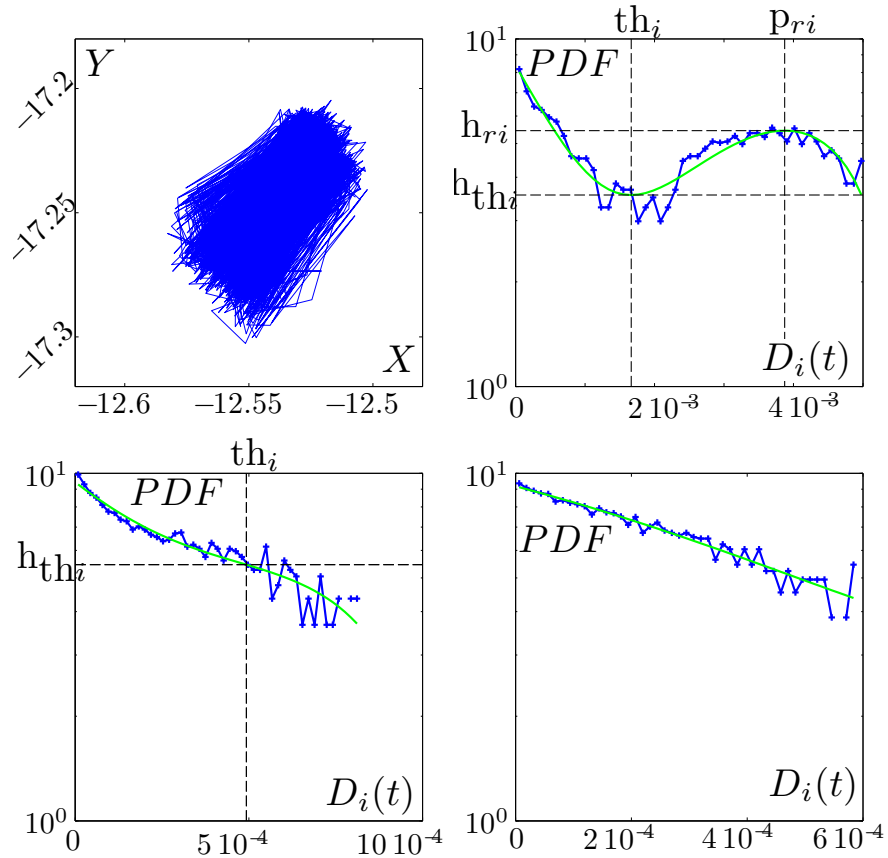


Figure 3.18: **Rattlers.** **Top Left:** Trajectory of a particle. Distribution of $D_i(t)$ for a particle of type 1 (**top right**), for a particle of type 2 (**bottom left**), and for a particle of type 3 (**bottom right**). The green lines are fits of the logarithm of the probability density functions. Dashed lines indicate the coordinates of the roots of the derivative of the polynomial that is plotted.

fact that at high density, the rattling events are well separated from non-rattling events. Particles of type 2 have a rather constant proportion, that is around 70%. Finally, particles of type 3 represent nearly 30% of the particles and are less numerous as the packing becomes dense. This is the same effect, as for the type 1: rattling events are better separated from non rattling events in dense packings, because non-rattling events have smaller displacements. Since thresholds th_i are well defined for particles of type 1 and 2, we directly use them to define rattling events. However, there is no such criteria for particles of type 3, despite the fact that they may be rattling. The fact that there is no bimodal distribution indicates that they have spent most part of the time either rattling or non-rattling; in other words, particles that have very rarely rattled or that have rattled all the time will probably be of type 3. For those particles, we define th_i as the

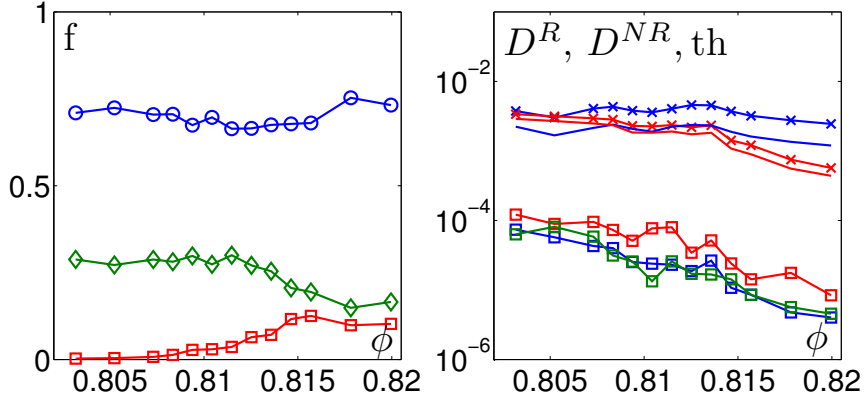


Figure 3.19: **Rattlers properties.** **Left:** population of rattlers: (\square) fraction of type 1 particles, (\circ) fraction of type 2 particles and (\diamond) fraction of type 3 particles. **Right:** $D_{\text{type } 1}^R$ (\times), $D_{\text{type } 1}^{NR}$ (\square), $D_{\text{type } 2}^R$ (\times), $D_{\text{type } 2}^{NR}$ (\square), $D_{\text{type } 3}^{NR}$ (\square), $\text{th}_{\text{type } 1}$ (—) and $\text{th}_{\text{type } 2}$ (—) versus packing fraction ϕ .

average threshold given by type 1 and 2 particles $\text{th}_{\text{type } 1}$ & 2. We then use the values of th_i to define

$$D_i^{NR} = \langle D_i(t) \rangle_{D_i(t) < \text{th}_i} \quad \text{and} \quad (3.17)$$

$$D_i^R = \langle D_i(t) \rangle_{D_i(t) \geq \text{th}_i}, \quad (3.18)$$

where $\langle \cdot \rangle_{D_i(t) < \text{th}_i}$ is the average over time of “non-rattling” events (they satisfy the condition $D_i(t) < \text{th}_i$), and $\langle \cdot \rangle_{D_i(t) \geq \text{th}_i}$ is the average over time on “rattling” events (they satisfy the condition $D_i(t) \geq \text{th}_i$). We then define $D_{\text{type } 1}^R$ (respectively $D_{\text{type } 1}^{NR}$) the average of D_i^R (respectively D_i^{NR}) of particles of type 1. Likewise, we define $D_{\text{type } 2}^R$, $D_{\text{type } 2}^{NR}$, and $D_{\text{type } 3}^{NR}$. Finally, we define $\text{th}_{\text{type } 1}$ (respectively $\text{th}_{\text{type } 2}$) the average of th_i over particles of type 1 (respectively type 2).

We plot in figure 3.19 right $D_{\text{type } 1}^R$, $D_{\text{type } 1}^{NR}$, $D_{\text{type } 2}^R$, $D_{\text{type } 2}^{NR}$, $D_{\text{type } 3}^{NR}$, $\text{th}_{\text{type } 1}$ and $\text{th}_{\text{type } 2}$ versus packing fraction ϕ . First, we see that they all decrease with packing fraction. This shows that we could not have used a constant threshold to define the rattling events. Second, we see that the values of D^{NR} are much below D^R and th for all types all particles. This means that, on average, the dot product D is much larger for rattlers than for non-rattlers. This is good news for us: the definition of $\text{th}_{\text{type } 1}$ & 2 as the threshold for particles of type 3 is consistent with the fact that rattlers have a higher D . Third, $D_{\text{type } 1}^R$ (respectively $D_{\text{type } 2}^R$) is always larger than $\text{th}_{\text{type } 1}$ (respectively $\text{th}_{\text{type } 2}$). This means that the distributions of these quantities are rather narrow.

We now have defined a criteria for defining rattlers. We apply it to particles trajectories and plot on figure 3.20, top left, both the instantaneous fraction of rattlers averaged over time f_R and the fraction of particles having

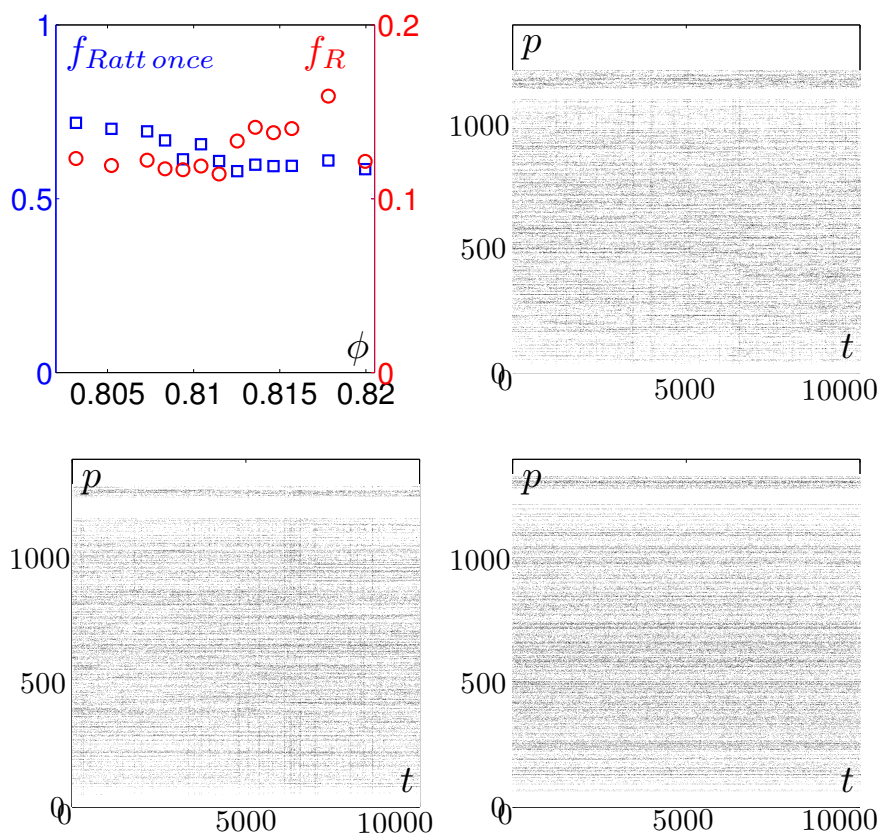


Figure 3.20: **Rattlers properties.** **Top Left:** Instantaneous fraction of rattlers averaged over time f_R (\circ , on right-axis) and fraction of particles having rattled at least once $f_{Ratt\ once}$ (\square , on left-axis) versus packing fraction ϕ . **Rattlerograms:** particle index versus time for $\phi = 0.8083$ (**top-right**), $\phi = 0.8115$ (**bottom-left**) and $\phi = 0.8157$ (**bottom-right**). Each rattling event is marked by a black spot.

rattled at least once $f_{Ratt\ once}$, versus packing fraction. We see that f_R remains between 11% and 17%. Note that, as the packing fraction is increased to high values, we could expect the rattlers population to vanish, as more and more grains touch each other. Meanwhile, at low packing fractions, the population of rattlers is expected to decrease also because all particles start to move a lot, and there is no longer well defined cages in which a few particle would “rattle” strongly. Therefore, it wouldn’t be surprising to observe that f_R has a maximum at an intermediate packing fraction. We see that, apart from the data at $\phi = 0.8178$, f_R seems to have a modest maximum close to $\phi \sim 0.814$. Unfortunately, this tendency is very weak. This has to do with the experimental noise of position detection, that makes some particles be counted as rattlers. Of course, we want these particles to be

discarded for computing statistics on dynamics, but this reduces confident physical interpretation of f_R .

In contrast, $f_{Ratt\ once}$ decreases monotonically from 70% to 55% as the packing fraction is increased. This means that as the packing fraction is increased, particles tend to have a more fixed role. This weak change is illustrated in figures 3.20 where “rattlerograms” (spatio-temporal plot for rattling events) are plotted for three different densities. We discuss further the rattlers issue in appendix C.1.

3.4.2 Root mean square displacement

We now consider the trajectories of the grains, that have been corrected from convection:

$$\widehat{\Delta_\tau \vec{r}_i(t)} = \vec{r}_i(t + \tau) - \vec{r}_i(t) - \Delta_{\tau, r} \vec{r}_i(t) - \Delta_{\tau, s} \vec{r}_i(t), \quad (3.19)$$

where $\Delta_{\tau, r} \vec{r}_i(t)$ (respectively $\Delta_{\tau, s} \vec{r}_i(t)$) has been defined in equation 3.2 (respectively 3.7) and is solid rotation displacement (respectively shear displacement). We compute root mean square displacement defined the following way:

$$RMSD = \left(\frac{1}{N} \sum_{i=1}^N \left\langle \left\| \widehat{\Delta_\tau \vec{r}_i(t)} \right\|^2 \right\rangle_t \right)^{1/2} \quad (3.20)$$

where $\|\cdot\|^2$ is the euclidean norm, and rattling events have been discarded from space and time averages. $RMSD$ vs. lag time τ is displayed in figure 3.21. We see that the data remain constant, with a value that depends on packing fraction for high densities. At low densities, the $RMSD$ increases

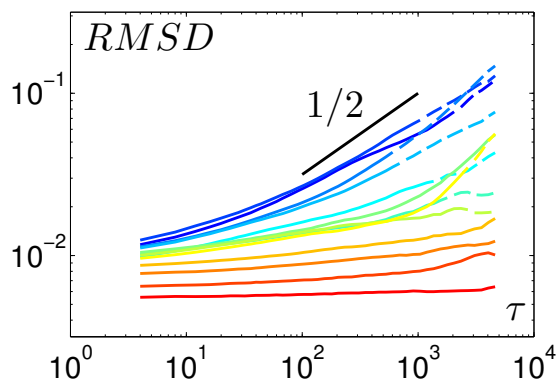


Figure 3.21: **Root mean square displacements ($RMSD$)** vs. lag time τ for different packing fractions. The dotted lines correspond to times larger than the time τ_{lim} defined in section 3.1. Color code spans from blue (low packing fractions) to red (high packing fractions) (See table 3.1).

with lag time for long times τ with a power law dependence with an exponent close to $1/2$. We interpret it as follows: at high densities, the dynamics is only vibrational, no long time correlation builds up. As the packing fraction is decreased on the contrary, a diffusive motion is established up to a tenth of a grain unit.

3.4.2.1 Zoom on big and small displacements

In order to understand better the dynamics, we define a dynamical structure factor:

$$Q^{\vec{r}}(t, \tau, a) = \frac{1}{N} \sum_i Q_i^{\vec{r}}(t, \tau, a), \quad (3.21)$$

where

$$Q_i^{\vec{r}}(t, \tau, a) = \exp \left(- \frac{\left\| \widehat{\Delta_{\tau} \vec{r}_i(t)} \right\|^2}{2a^2} \right), \quad (3.22)$$

where $\|\cdot\|^2$ is the euclidean norm, and we study its average on time $Q(a, \tau)$. We first compute $Q^{\vec{r}}(\tau, a)$, the time average of $Q^{\vec{r}}(t, \tau, a)$, which we plot versus lag time τ for different values of a in figure 3.22, top-left, for a loose packing. $Q^{\vec{r}}(\tau, a)$ decreases with lag time at all values of a , but they decrease faster when a is smaller. This is a direct consequence of the definition of the dynamical structure factor : the more you wait, the more you move. We also see that there no value of a such that its corresponding value of $Q^{\vec{r}}(\tau, a)$ starts from one and decreases down to zero. In this respect, the system is slow. The same family of curves is plotted for a denser packing in figure 3.22, top-right. The dynamical structure factor decay with lag time is even slower. In order to observe more closely the dependence with packing fraction, we choose one particular length-scale $a = 0.5$, and three particular lag times $\tau = 10, 100$ and 1000 , that are the drawn lines in figures 3.22, top. This particular choice of a allows us to study the dynamics that occurs *at the grain scale*.

We then plot the values of $Q^{\vec{r}}(\tau, a)$ versus packing fraction in figure 3.22, bottom-left. First, $Q^{\vec{r}}(\tau, a)$ is always larger than 0.99: the system hasn't relaxed. Still, for low packing fractions the dynamical structure factor departs from 1 with a strong dependence on packing fraction and on lag time. This is further highlighted by the inset of figure 3.22 bottom-left, where $1 - Q^{\vec{r}}(\tau, a)$ is plotted in log-scale versus packing fraction. This means that the system relaxes on tiny length-scales, and that it is not strictly frozen.

Therefore, we now investigate $Q^{\vec{r}}(\tau, a)$ on a much tinier scale, $a = 10^{-2}$, and we plot it for several lag times, τ , versus packing fraction, in figure 3.22, bottom-right. First, as packing fraction decreases, $Q^{\vec{r}}(\tau, a)$ decreases, meaning that the relaxation is more significant. Second, we see two distinct behaviors:

- at high packing fractions (above $\phi \sim 0.814$), $Q(a, \tau)$ depends poorly on τ ;
- at low packing fractions, $Q(a, \tau)$ depends strongly on τ .

Thus, $\phi = 0.814$ seems to be a crossover between a vibrating jammed solid with a short time decorrelation of the displacements and a liquid with a long time decorrelation. Note also that these qualitative differences between these two regimes were already present for $a = 0.5$, in the inset of figure 3.22, bottom-left. Such displacements correspond typically to changes of neighbors network. This suggests a scale invariant phenomena: the decorrelation on small length scales involving rather small time-scales and the decorrelation on large scales share the same properties.

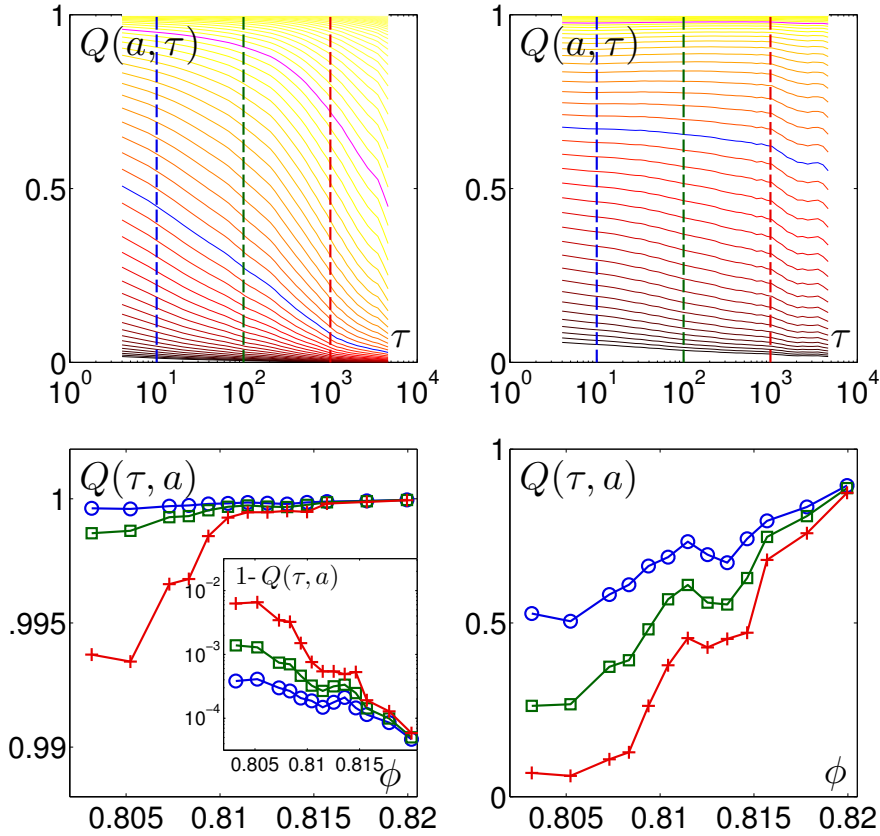


Figure 3.22: **Structure factors.** **Top :** $Q(a, \tau)$ vs. τ and for different a ranging from $a = 0.001$ (red) to $a = 10$ (yellow) at $\phi = 0.8083$ (**left**) and $\phi = 0.8157$ (**right**). The blue (respectively magenta) curve corresponds to $a = 10^{-2}$ (respectively $a = 0.5$). **Bottom :** $Q(a, \tau)$ vs. packing fraction ϕ for (**left**) $a = 0.5$ and (**right**) $a = 10^{-2}$ and for different $\tau = 10$ (\circ), 100 (\square) and 1000 ($+$). **Left - inset:** $1 - Q(\tau, a)$ in log-scale vs. ϕ .

In order to test this hypothesis, we try to rescale the family of curves $Q^r(\tau, a)$, simply by rescaling the lag time τ . To do so, we proceed as follows:

1. we choose a value a_0 of a and we take the curve $Q(\tau, a_0)$ as a reference;
2. we then shift all the other curves with different values of a on this curve, by simply rescaling the time lag by a factor $\tau_0(a)$. Note that $\tau_0(a_0) = 1$. Note also that $\tau_0^{-1}(a)$ the inverse of τ_0 is equivalent to the root mean square displacement versus lag time but on a time range that is extrapolated. We then obtain a rescaled curve $Q(a, \tau/\tau_0(a))$ which we plot versus $\tau/\tau_0(a)$ in figure 3.23, top-left. We see that the curves merge approximately, the decorrelation is not perfectly time-scale invariant. This rescaling procedure works for decaying curves, as represented in figure 3.22 top-left. However, as soon as there is no time decay, as represented in figure 3.22 top-right, the rescaling procedure

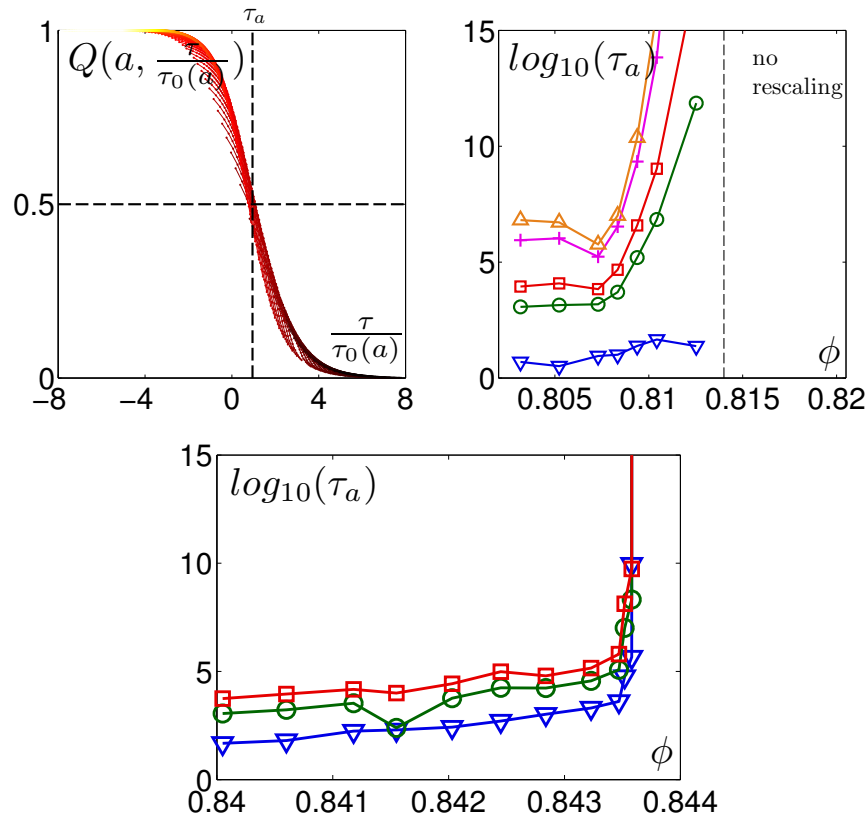


Figure 3.23: **Top-Left:** Rescaled $Q(a, \tau/\tau_0(a))$ vs. $\tau/\tau_0(a)$ for different a ranging from $a = 0.001$ (red) to $a = 10$ (yellow) at $\phi = 0.8083$. **Top-Right:** relaxation-time τ_a vs. density for $a = 10^{-2}$ (∇), $5 \cdot 10^{-2}$ (\circ), 10^{-1} (\square), $5 \cdot 10^{-1}$ ($+$), and 1 (\triangle). **Bottom:** relaxation-time τ_a vs. density for $a = 10^{-2}$ (∇), $5 \cdot 10^{-2}$ (\circ), 10^{-1} (\square) for the brass disks experiment.

doesn't work anymore;

3. the time at which the rescaled curve crosses 0.5 yields the typical relaxation time of the system at scale a , τ_a , represented in figure 3.23, top-left. Owing to a choice of an arbitrary value of a , this allows us to extrapolate τ_a up to huge values that are far larger than the experimental window. Of course, it is not clear that the scale-invariant relaxation would survive on such time scales. τ_a vs. packing fraction is plotted in figure 3.23, top-right. It increases as packing fraction is increased, and seems to diverge at a packing fraction $\phi \sim 0.814$. Above this density, the rescaling doesn't work: we measure no long-time relaxation.

To put it in a nutshell, we would like here to convey two key messages:

- $\phi = \phi_J \sim 0.814$ marks a divergence of the structural relaxation time;
- below $\phi = \phi_J \sim 0.814$, there is always relaxation, no matter how tiny the length-scales and large time scales it involves.

As a comparison, we apply the same procedure on the brass disk experiment data: τ_a vs. packing fraction is plotted in figure 3.23 bottom. As for photo-elastic grains, the relaxation time increases with respect to packing fraction, but one major difference occurs, the rescaling of the data works for all packing fractions, there is no packing fraction at which the time has diverged.

3.4.3 More details on displacements statistics

We check here that the value $a_{1/2}$ defined by

$$Q(a_{1/2}, \tau) = 1/2, \quad (3.23)$$

and $RMSD$ provide related information. Indeed, the physical meaning of equation 3.23 is that on average, particles have moved by a distance $a_{1/2}$ in a time τ . We thus plot in figure 3.24, left, $a_{1/2}$ versus lag time, τ for different packing fractions. For high packing fractions, it increases weakly with lag time. As packing fraction is increased, the curves are shifted towards higher values and increase faster with lag time. At the lowest packing fractions, the curves increase with an exponent which is close to 1/2: grains displacements are nearly diffusive. We see that its behavior is close to the behavior of the $RMSD$ plotted in figure 3.21. It actually can be shown that for gaussian distributions of displacements, $RMSD$ and $a_{1/2}$ are equal. Indeed, the series expansion of the exponential yields:

$$Q(a, \tau) = \left\langle Q_i^{\vec{r}}(t, \tau, a) \right\rangle_{i,t} = \sum_{n=0}^{\infty} \frac{(-2a^2)^{-n}}{n!} \left\langle \left\| \widehat{\Delta_{\tau} \vec{r}_i(t)} \right\|^{2n} \right\rangle_{i,t}, \quad (3.24)$$

where $\langle \cdot \rangle_{i,t}$ is the average over particles and time. For gaussian statistics, moments higher than the second are zero, so that equations 3.23 and 3.24 yield

$$a_{\frac{1}{2}} = \sqrt{\left\langle \left\| \widetilde{\Delta_{\tau} \vec{r}_i(t)} \right\|^2 \right\rangle_{i,t}} = \text{RMSD}. \quad (3.25)$$

However, non gaussian distributions have non-zero higher moments, and $a_{1/2}$ is different from *RMSD*. (See Candelier [2009], Lechenault [2007], Lechenault et al. [2010] for more details). This provides a test for the gaussianity of the displacement distributions. Hence, we plot in figure 3.24, right, the ratio $a_{1/2}$ over *RMSD* vs. τ for all the packing fractions. We see that they are nearly the same. The ratio $a_{1/2}$ over *RMSD* is always lower than one, it increases with lag time, meaning that the displacements statistics tends towards gaussianity for large lag times. Also, it decreases with packing fraction, meaning that the distributions are less gaussian for dense packings.

We now directly confirm our observations by plotting in figure 3.25 distributions of displacements along the shaking (X-axis) and the compression (Y-axis) directions for different densities at different lag times. The shape of the distributions is the same for both axis. In this respect, the system is isotropic. Second, we confirm that the distributions for higher lag times and lower densities are narrower and closer to gaussian shapes.

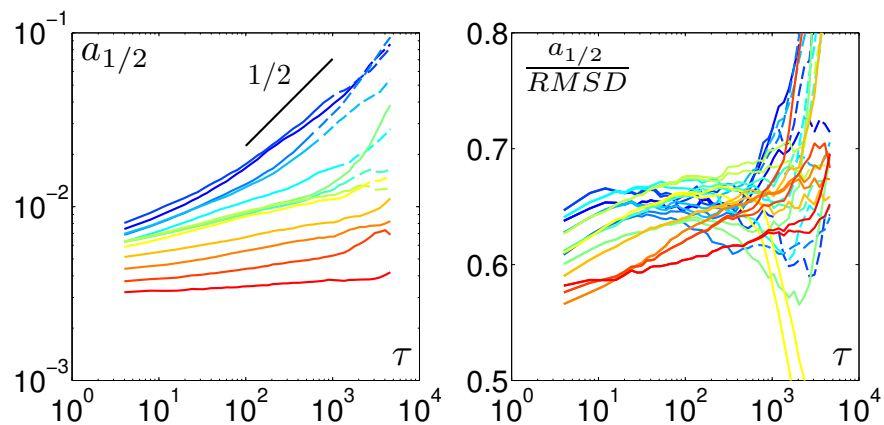


Figure 3.24: **Displacements. Left:** $a_{1/2}$ vs. lag time τ . **Bottom:** Ratio $a_{1/2}$ over *RMSD* vs. lag time τ . Color code spans from blue (low packing fractions) to red (high packing fractions) (See table 3.1).

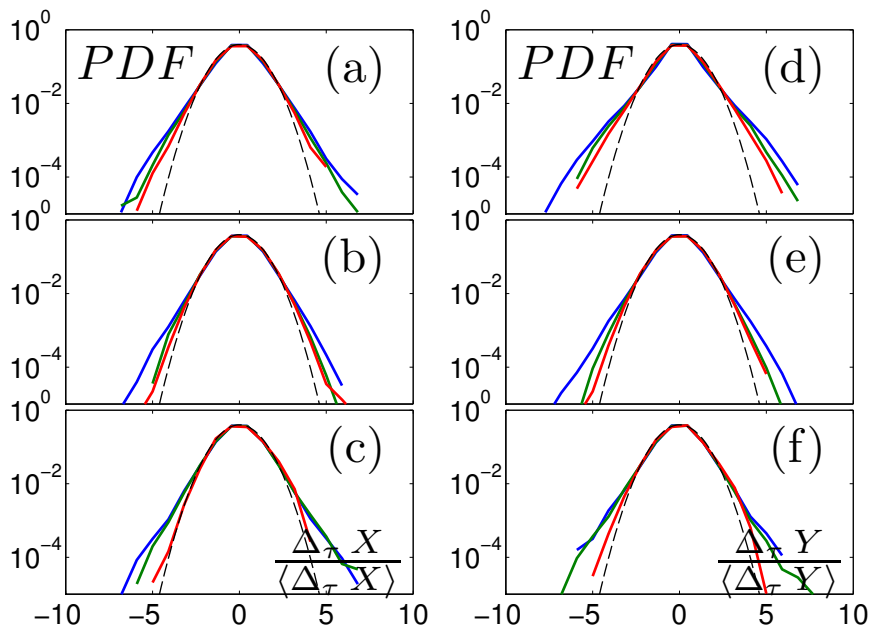


Figure 3.25: **Distribution of displacements** along shaking axis (X -axis) for $\phi = 0.8157$ (a), $\phi = 0.8125$ (b) and $\phi = 0.8083$ (c). along compression axis (Y -axis) for $\phi = 0.8157$ (d), $\phi = 0.8125$ (e) and $\phi = 0.8083$ (f). The different colors corresponds to different lag times $\tau = 10$ (blue), $\tau = 100$ (green) and $\tau = 1000$ (red).

3.4.4 Dynamical Heterogeneities

The dynamical structure factor allows us to compute the details of the dynamics, and in particular, it can be used to study the spatial correlations of particles displacements, namely the *dynamical heterogeneities*. The methods that have been introduced by Lechenault [2007], Candelier [2009], Lechenault et al. [2010] to quantify *dynamical heterogeneities* have been briefly discussed in section 1.2.3 and are introduced in appendix B.1. Similarly, we define the *dynamical susceptibility of the displacements*

$$\chi_4^{\vec{r}} = N \left(\overline{\text{var}_t Q_i^{\vec{r}}(t, \tau, a)} \right)^{-1} \text{var}_t Q^{\vec{r}}(t, \tau, a), \quad (3.26)$$

where $Q_i^{\vec{r}}(t, \tau, a)$ and $Q^{\vec{r}}(t, \tau, a)$ have been defined in equations 3.21 and 3.22, and where $\overline{\cdots}$ and var_t respectively denote the average of particles and the temporal variance.

We plot in figure 3.26, top-left, the dynamical susceptibility versus lag time, τ , for different densities. We plot it for $a = a_{1/2}$, where $a_{1/2}$ is defined in equation 3.23. $\chi_4^{\vec{r}}$ is non-monotonic with lag time. This can be interpreted as follows:

- for small time lags, as pictured in figure 3.24, left, $a_{1/2}$ is rather small, typical grains displacements occur on small length scale, and are not spatially correlated. Hence, according to appendix B.1, $\chi_4^{\vec{r}}$ remains small.
- At intermediate time scales (where $\chi_4^{\vec{r}}$ is maximum), typical grains displacements occur on a slightly larger length scale, and are maximally spatially correlated. In other words, within the lag time τ , a significant number of particles have had a similar dynamics.
- At large time scales, typical grains displacements occur on a larger length scale (up to a tenth of a grain unit) and are not spatially correlated: the lag time is so long that the different particles have experienced different dynamics.

We define the maximum of the dynamical susceptibility $\chi_4^{\vec{r}*}$, occurring at time $\tau^{\vec{r}*}$. From figure 3.26, top-left, we extract $\chi_4^{\vec{r}*}$ (respectively $\tau^{\vec{r}*}$), which we plot with respect to packing fraction on figure 3.26, top-right (respectively bottom-left). The error-bars are extracted according to the steepness of the maximum. We see that it is non-monotonic with respect to packing fraction, and that it shows a maximum at a packing fraction, $\phi^* = 0.810$. $\tau^{\vec{r}*}$ increases with packing fraction. Despite the error bars that smooth it, one can distinguish an intermediate maximum close to ϕ^* . Note that the magnitude of $\chi_4^{\vec{r}*}$ close to ϕ^* is close to 100. As $\chi_4^{\vec{r}*}$ is related to a number of particles, and as 100 is about a tenth of the system size,

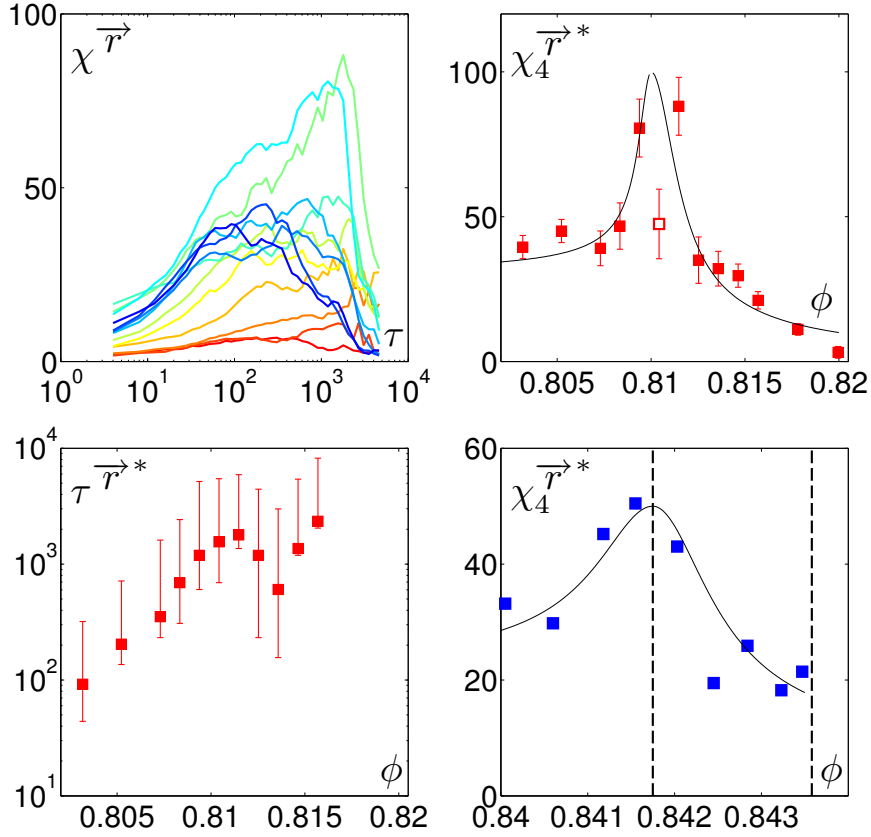


Figure 3.26: **Dynamical Heterogeneities.** **Top-left:** Dynamical susceptibility of the displacements $\chi_4^{\vec{r}}$ versus lag time τ . Color code spans from blue (low packing fractions) to red (high packing fractions) (See table 3.1). **Top-right:** Maximal dynamical susceptibility $\chi_4^{\vec{r}^*}$ vs. packing fraction ϕ . The \square data point has an anomalously low value. **Bottom-left:** Corresponding time τ^* vs. packing fraction. **Bottom-Right:** Maximal dynamical susceptibility $\chi_4^{\vec{r}^*}$ vs. packing fraction ϕ for the brass disks experiments.

this provides an explanation for the \square data point of figure 3.26, that is close to $\phi^* = 0.810$ and that is anomalously low as compared to the trend given by the other data points. We interpret it as the signature of a lack of statistics close to the transition, where the size of the heterogeneities become extremely large. As described in appendix B.1, the four point susceptibility is indeed a time variance of a sum which is poorly sampled, given the number over which the sum is performed. This means that at the packing fraction ϕ^* , the dynamics is maximally collective, indicating a *dynamical crossover*. Indeed, above this density, grains hardly move, and no real dynamics takes place. Below ϕ^* , grains can move without being correlated mutually, and the crossover between these two regimes is marked by maximal dynamical

heterogeneities.

We now can compare with the experiment on brass disks. The same analysis leads to figure 3.26, bottom-right, where $\chi_4^{\vec{r}^*}$ is plotted versus packing fraction. We see that there is a maximum of similar amplitude: the same phenomenon occurs.

3.4.5 Summary

We summarize our observations in figure 3.27, where a scheme of the relaxation time and the maximal dynamical susceptibility versus packing fraction is plotted. We have observed a crossover from a diffusive dynamics to stuck dynamics. The same relaxation process rescales roughly at any length scale for low enough packing fraction, the dynamics is approximately scale invariant. Yet, as the packing fraction is increased, the relaxation time strongly increases and diverges at a packing fraction $\phi_J \sim 0.814$. Above this density, no more scale invariance is observed and the system relaxation time seems to have diverged. Besides, we observe a dynamical crossover that occurs at a distinct and lower packing fraction $\phi^* \sim 0.810$, and that is characterized by maximal dynamic heterogeneities. Similar behavior was observed in the brass experiment, apart from the regime with a stuck dynamics. The brass experiment only probes densities below ϕ_J . We thus observe here two distinct packing fractions ϕ^* and ϕ_J at which the dynamics undergoes strong qualitative changes. In the following section, we shall probe the presence of similar signatures within the dynamics of microscopic forces inside the grains.

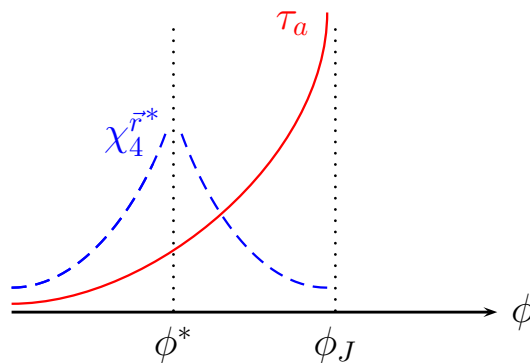


Figure 3.27: **Sketch of dynamics.** Both the behavior of the structural relaxation time of the granular material and the magnitude of the dynamical susceptibility of the displacements have been sketched versus packing fraction.

3.5 Force dynamics

We have observed in section 3.3 that the forces were dynamically induced for low packing fractions whereas they were statically induced at high densities. We also have observed in section 3.4 that some complex dynamics sets in on tiny timescales as the packing fraction is decreased. We now legitimately question the dynamics of the forces itself. Through this entire section, we will define statistical quantities, and quantify their temporal fluctuations by studying the standard deviations sampled over time.

3.5.1 Instantaneous Pressure and Heterogeneity fluctuations

We return here to the instantaneous pressure and to the instantaneous heterogeneity defined above in equations 3.12 and 3.13, and we measure their time standard deviation $\text{std}_t P_t$ and $\text{std}_t H_t$ that are plotted in figure 3.28. At low packing fractions, we observe rather constant values of these quantities. Above $\phi \sim 0.81$, they both decrease significantly. This confirms the previous observations on wall pressure: at high packing fractions, the pressure is mainly static whereas at low packing fractions, the pressure takes its root in dynamics. This calls for a characterization of individual pressures, *i.e.* of each grain, that will be investigated in the following section.

As a side remark, we see that both $\text{std}_t P_t$ and $\text{std}_t H_t$ have a small maximum at $\phi \sim 0.81$, meaning that pressure and heterogeneity fluctuations are maximum at this packing fraction. Despite the small size of the maximum, it is located at the same packing fraction as the maximum of dynamical heterogeneities observed in the previous section.

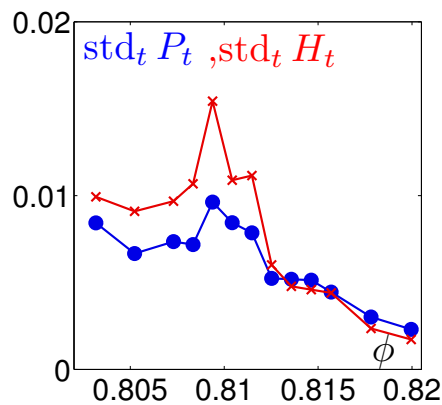


Figure 3.28: **Forces fluctuations.** Temporal standard deviation of P_t value (●) and H_t (×) vs packing fraction (see text for definition).

3.5.2 “Volatility” of the pressure inside grains

We now want to investigate the dynamics of the pressure inside individual grains. To this end, we define the average pressure borne by grain i during the experimental run

$$\bar{G}_i = \frac{1}{T} \sum_{t=1}^T G_i(t). \quad (3.27)$$

The distributions of \bar{G}_i for all packing fractions are plotted in figure 3.29 left. They display exponential tails at all packing fractions. These distributions are reasonably well fitted by a gamma distribution at least for high values of \bar{G}_i :

$$f(X, k, c) = \frac{1}{c^k \Gamma(k)} X^{k-1} \exp -\frac{X}{c}. \quad (3.28)$$

The width of the tails is quantified by c . In the inset of figure 3.29 left, c and k have been plotted vs. packing fraction. We see that c is constant for low fractions and starts to increase at high packing fractions. Despite the questionable accuracy of the fit at low values of \bar{G}_i , we see a clear increase of k as the packing fraction is decreased: the distributions sharpen. Note, that the exponential tails are similar to their instantaneous distribution that we had observed in section 3.3. This confirms that the microscopic forces are frozen in time.

As stressed before in section 3.3.2.1, there is a weak time dependence of the force network. Even though it may be modest, the time evolution of the force network might reveal the dynamics at stake here. To describe it, we

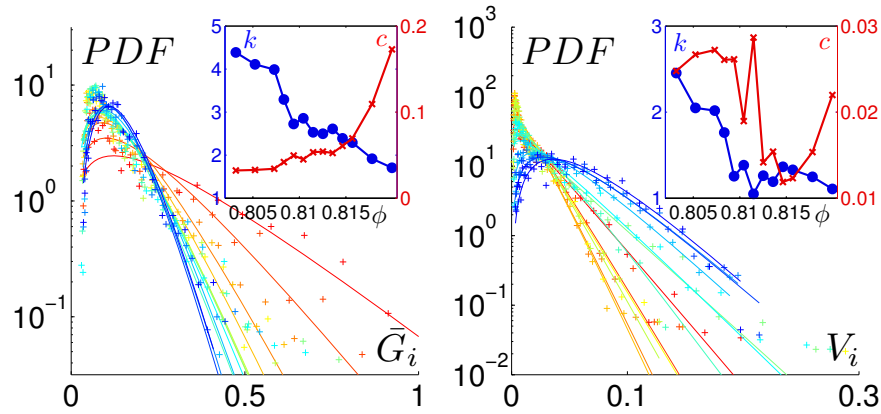


Figure 3.29: **Statics and Dynamics of the microscopic pressures.** Distributions of G_i (left) and V_i (right). The data is denoted by + and fits by gamma functions are the colored lines. The insets respectively represent the dependence of the gamma distribution parameters with respect to packing fraction. Color code spans from blue (low packing fractions) to red (high packing fractions) (See table 3.1).

introduce V_i , the “Volatility” of the pressure inside the grain i , namely, its temporal standard deviation during the entire experimental run:

$$V_i = \sqrt{\frac{1}{T} \sum_{t=1}^T G_i(t)^2 - \bar{G}_i^2}. \quad (3.29)$$

The distributions of V_i are plotted figure 3.29 right. The fit by a gamma distribution yields peculiar dependence of its parameters on packing fraction (see inset of figure 3.29 right): The “cutoff” c is constant and rather high at low packing fractions. Above the density $\phi \sim 0.81$, c suddenly falls to a minimum at $\phi \sim 0.814$, from which c increases again. The density $\phi \sim 0.81$ also corresponds to a change of the shape of the distribution. The factor

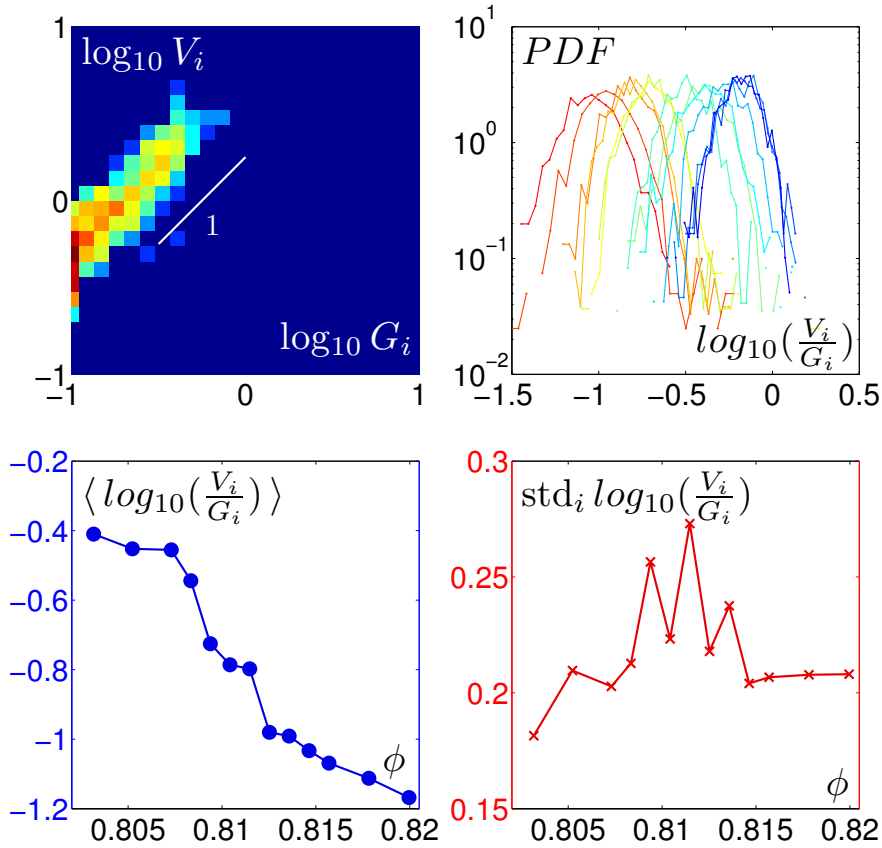


Figure 3.30: **Volatility of grains pressure.** **Top Left:** Joint distribution of $\log_{10} V_i$ and $\log_{10} G_i$ at a density $\phi \sim 0.8125$. A high to low probability is denoted by warm to cool color. **Top Right:** Distributions of $\log_{10} V_i/G_i$ for different packing fractions. Color code spans from blue (low packing fractions) to red (high packing fractions) (See table 3.1). Temporal average and (**bottom left**) standard deviation (**bottom right**) of $\log_{10} V_i/G_i$.

k , indeed, constantly decreases until $\phi \sim 0.81$. Beyond this density, k is constant and remains around 1.2. Thus, the average “Volatility” is constant and high at low packing fractions. What is surprising here is that after this sudden drop, the fluctuations of the grains increase again. This leads us to attempt to describe the fluctuations further and in particular the correlations between the microscopic pressure and the “Volatility”. To do so, we plot in figure 3.30 the joint distribution of V_i and G_i . There is a strong correlation, $V_i \sim G_i$. The higher the force, the higher the “Volatility”, this explains the peculiar shape of the distribution of V_i : the force fluctuations scale with the average force, and that is why c vs. ϕ increases for high packing fraction in the inset of figure 3.29, right.

More interesting to consider is the “relative volatility” V_i/G_i . We thus plot the distribution of $\log_{10} V_i/G_i$ in figure 3.30 top right, that appears to be close to a gaussian distribution. Thus, the distribution of V_i/G_i is close to a log-normal distribution, that is, a wide distribution. Therefore, despite the fact that the differences among the particles have been renormalized, they still have heterogeneous force fluctuations. We quantify the average force fluctuations by computing the average of $\log_{10} V_i/G_i$ versus packing fraction and we plot it figure 3.30 bottom left. This average constantly decreases as packing fraction increases: the system is less and less “volatile” as it gets denser. The spatial heterogeneity of such volatilities can be quantified by the spatial standard deviation of $\log_{10} V_i/G_i$ that is plotted vs. packing fraction in figure 3.30 bottom right. This curve is clearly non monotonic and has a blurred maximum between $\phi \sim 0.810$ and $\phi \sim 0.814$: between these two packing fractions, the relative volatility is the most widely distributed .

3.5.3 Summary

In this section, we have characterized the dynamics of the microscopic pressures; we summarize our observations in figure 3.31. Previously described by forces statics, the crossover between a dynamically induced to a statically induced pressure has been characterized by force dynamics: there is a regime of small forces and large fluctuations at low packing fractions and a regime of large forces and small fluctuations at high packing fractions. The crossover between these two regimes is characterized by maximal temporal fluctuations of the pressures inside the grains. Nevertheless, these signatures are rather weak: no clear signature emerges in the dynamics of forces. Still, we have seen that when force volatilities are renormalized, the crossover is more strongly marked. The fact that we have to consider relative fluctuations to observe more significant fluctuations means that peculiar force dynamics occur over of wide range of forces and suggests to look at a finer quantity. Therefore, in the next chapter we shall abandon the forces and focus instead on the contact network that is a trickier but more eloquent quantity to consider.

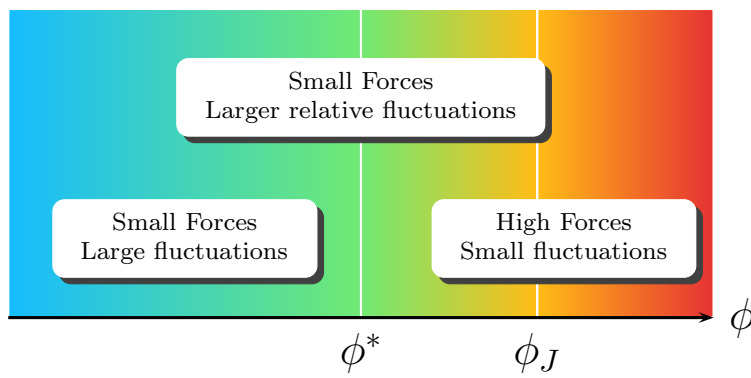


Figure 3.31: **Forces Dynamics.** Sketch of force dynamics behavior versus packing fraction.

3.6 Conclusion and open questions

Altogether, we have extensively characterized the properties of various quantities across the jamming transition. The various quantities we have considered point to two distinct fractions.

at $\phi_J \sim 0.814$ average quantities undergo a change:

- the convection stalls
- the force geometry nature changes
- the relaxation time diverges

at $\phi^* \sim 0.810$ fluctuating quantities undergo a change

- the dynamical heterogeneities of the displacements are maximum;
- the temporal fluctuations of the forces and the heterogeneity of the fluctuations are maximum, but the magnitude of the maximum is modest.

As for the dynamics, similar investigations close to the jamming point [Berthier, Otsuki and Hayakawa, 2011] were done using numerical simulations of thermal soft spheres. We aim here at comparing the root mean square displacements of the simulations and our root mean square displacements plotted in figure 3.21. The authors performed temperature quenches and annealing from high to low temperatures at constant packing fraction. The resulting dynamics have been studied through mean square displacements versus lag time curves in Otsuki and Hayakawa [2011], which we plot in figure 3.32 left:

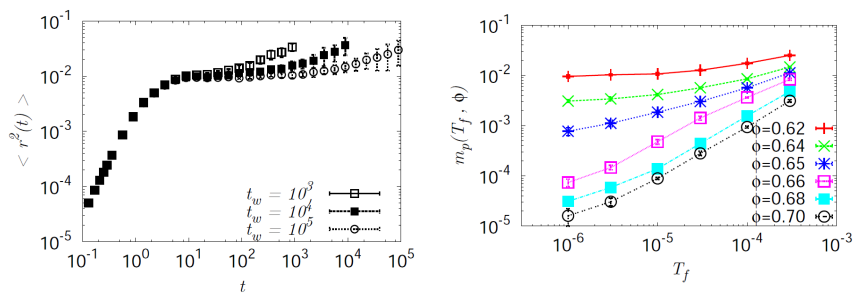


Figure 3.32: **Left : Quench dependence.** Mean square displacements vs. lag time at density $\phi = 0.7$ for different preparation protocols for harmonic spheres in 3 dimensions at finite temperature. Larger t_w is equivalent to slower preparation protocol. **Right : Plateau value** value of the plateau of the Mean square displacements vs. temperature for different densities. Extracted from Otsuki and Hayakawa [2011].

1. the mean square displacement has a plateau, which is reminiscent of a frozen structure;
2. the duration of the plateau seems to be finite but increases significantly as the quenching rate is diminished, or equivalently, as the waiting time after the quench is increased;
3. carefully annealed simulations for higher values of parameter t_w in Otsuki and Hayakawa [2011] have a plateau, whose duration exceeds the investigated “experimental” time scales. The value of this plateau with respect to temperature and density is plotted in figure 3.32 right. As theoretically predicted and numerically observed in Berthier et al. [2011c], the scaling of the plateau with temperature is different below and above the jamming point.

In comparison, in our experiment (plotted in figure 3.21):

1. we see a plateau of the root mean square displacements only for jammed packings;
2. as soon as the density is below ϕ_J , the plateau vanishes as packing fraction is decreased, we cannot compare with the results of Otsuki and Hayakawa [2011] and Berthier et al. [2011c].

Despite this last point, we see that the phenomenology is close. The comparison with Otsuki and Hayakawa [2011] suggests that the packings that we have created have been annealed too fast. In this case, why does the plateau disappear precisely at the jamming packing fraction? Or, —in contradiction with what we have claimed above— since a structural relaxation starts to occur on very tiny length-scales: is the packing really in a glassy state?

Let’s briefly try to compare further with numerics and theory [Berthier et al., 2011c]: in these works, the value of the mean square displacement and the value of the pressure scale the same way with temperature and packing fraction, and their scaling properties are different above and below jamming. In order to check that our shaken grains share the same properties and are also in a deep glass phase, we can investigate the behavior of these two quantities in our experiment. But, as stressed above, there is no plateau for small densities in our experiment. Therefore, we choose a poor man’s measurement of this quantity: we estimate the value of the plateau m by taking the square of the value of the root mean square displacement at short time, displayed in figure 3.21. We plot m and the inverse of the pressure \bar{P}_t —which is the time average of P_t defined in equation 3.12— in figure 3.33, left. Despite the poor precision of our measurement of m , we see that these two quantities follow the same trend. As a comparison, we plot in figure 3.33, right, the inverse pressure for theory and simulations of

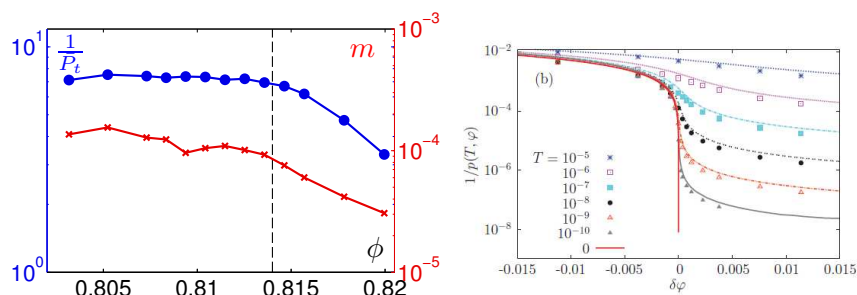


Figure 3.33: **Pressure and mean square plateau. Left: in our experiment** Inverse of the pressure (left axis) and mean square displacement plateau (right axis) vs. packing fraction. The dotted line indicates the structural transition ϕ_J . **Right : in theory and numerics** Inverse pressure vs. reduced packing fraction $\delta\phi = \phi - \phi_J$ for different temperatures in 3 dimensions. The plot is extracted from Berthier et al. [2011c]. $\phi_J = 0.683$ is the glass close packing which is reported in the paper.

Berthier et al. [2011c] for different temperatures. Of course, there are many fewer decades in our experiment, but the trend of the curves are consistent with our observations. Therefore, we suggest that, as in the simulations of Berthier et al. [2011c], the system lies in a deep glass phase. Still, we are not able to reach low enough annealing rates, so that the plateau of the root mean square displacements vanishes at low packing fractions. Furthermore, remember that the packing fractions at which we have observed strong dynamical heterogeneities have increasing *RMSD*. What is the link between the dynamical heterogeneities and the evolving *RMSD*? Would Berthier et al. [2011c] and Otsuki and Hayakawa [2011] observe dynamical heterogeneities despite the fact they have constant *RMSD*? We cannot really address these questions further here, but we will attempt to tackle the problem differently in the next chapter.

To the best of our knowledge, investigations of the other quantities we have studied in this chapter are not reported in the literature, so we cannot perform further comparison.

We recall that we have also seen a complex dynamics of the displacements, and modest signatures among force fluctuations. Therefore, it seems that something is responsible for a complex dynamics at the level of both tiny displacements and forces. No need to be Nestor Burma (or Philip Marlowe) to naturally bring suspicion over the contact network. These surmises also rely on previous studies of the jamming transition [Wyart et al., 2005a, Wyart, 2008], where the contact network guilt has been clearly singled out in the so called *jamming case*. In the following chapter, we shall study the mechanisms at stake in this jamming under vibration experiment by scrutinizing the statics and the dynamics of the contact network.

Chapter 4

“Glassy” Dynamics of Contacts

In this chapter, we aim at describing the statics and the dynamics of the contact network. To do so, we first explain how we achieve measurements of inter-particle forces and gap. We thereby end up with an experimental definition of “contact”, which is used in the rest of the chapter.

- We then describe the statics of the contact network by first studying the behavior of the average number of contacts, z , and then the spatial correlation of contacts.
- We then turn towards the description of the dynamics of the contact network. To this end, we introduce a contact structure factor, that quantifies the relaxation of the contact network. It is a similar quantity to the one that we had introduced when studying the dynamics of the displacements. We describe it in detail and interesting features come out of this analysis.
- We thereafter investigate the details of the dynamics by deriving a dynamical susceptibility using the contact overlap function, like the one that already had been introduced for the dynamics.
- We finally discuss how the dynamical susceptibility of the contact network is related to the dynamical heterogeneities of the displacements and with the dynamics of the forces studied in the previous chapter.
- At the end of this chapter, we will see that the contact network is the relevant object to scrutinize. Hopefully, it will provide the reader with a clearer comprehension of the jamming scenario in the present vibrated system.

4.1 Extracting the contacts

After briefly explaining how we measure normal forces and inter-particle distance, we present here how we extract contacts out of these quantities.

4.1.1 Normal force

As explained in section 2.5.2.2, the Delaunay triangulation and the Voronoï tessellation allow one to cut the grains into “camemberts”. These triangles

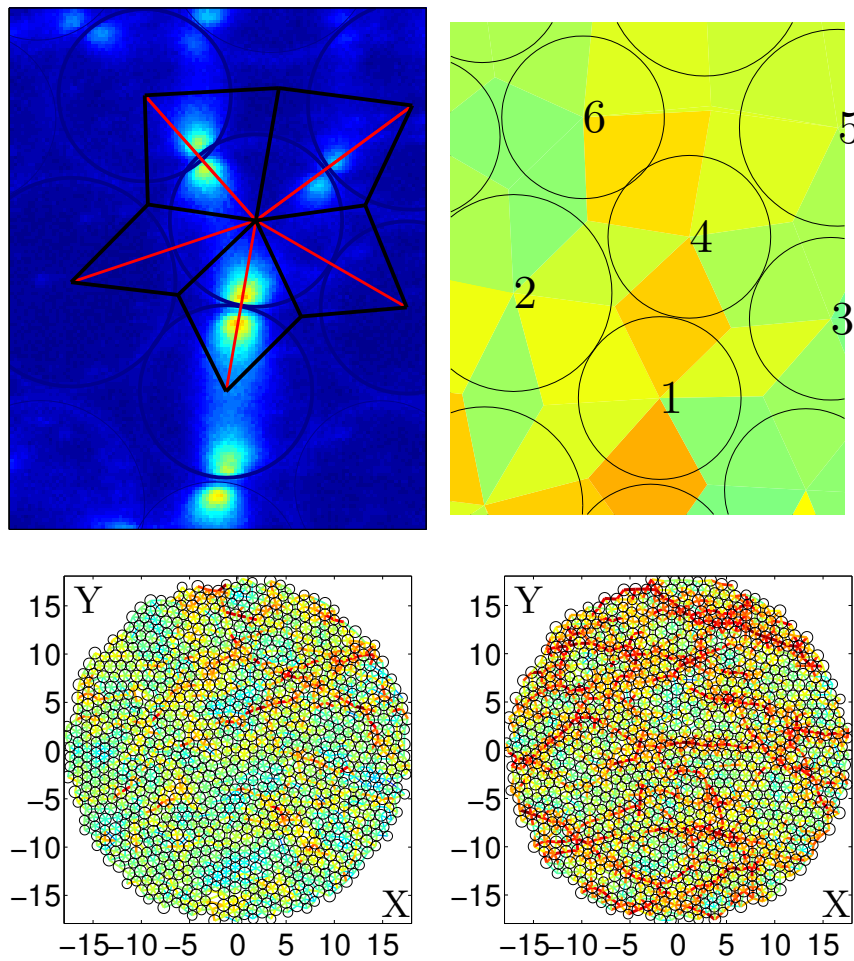


Figure 4.1: **Measuring contact forces.** **Top :** **Contact forces.** **Left:** photoelastic image (color scale) and result of voronoi tessellation (black and red lines). **Right:** Normal force computed from the integration of the square spatial gradient of the photoelastic image into the lozenges. **Bottom:** **Contact forces Maps.** Links are represented by lines, whose thickness and color is encoded by the value of the normal force of the links. **Left:** $\phi = 0.8119$. **Right:** $\phi = 0.8236$.

are represented in figure 4.1, top left. They are defined by the line through two centers of neighboring grains (red lines) and from the Voronoï vertex to the grain centers (black lines). A neighborhood relationship is associated to two Voronoï vertices, hence to two “camemberts”. The normal force is estimated by the sum of the square gradient over these two “camemberts”, which association forms a diamond shaped lozenge. The associated image of lozenges is depicted in figure 4.1, top right. We end up with an estimate of the contact force for each neighbor link. As an illustration, maps of contact forces are drawn in figure 4.1, bottom, for two different densities. As already highlighted in the previous chapter, we clearly see a difference between loose (left) and jammed packings (right). This is further illustrated by the distributions of normal forces that are plotted in figures 4.2. While the right side of these distributions display exponential tails (see right figure), the left side increases sharply. Unfortunately, there is no zero normal forces: even non-contact links particles have a finite normal force. This discrepancy originates in the experimental noise that hides within the pixels values. For a more detailed discussion about noise in photo-elastic pictures, the reader may refer to the experimental setup chapter 2. Hence, no straightforward criteria to define contacts emerges from these distributions, and we are left with the tedious job of defining a threshold between forces and what is supposed to be noise. As a first remark, we will first assume that the experimental noise does not depend on the packing fraction. This seems reasonable, all the more as the left tail of distribution has a constant shape for all the investigated distributions (see figure 4.2, left). Second, we will investigate the inter-particle distance (gap) properties. Both gaps and forces are complementary and will thus leads towards a criteria to define the

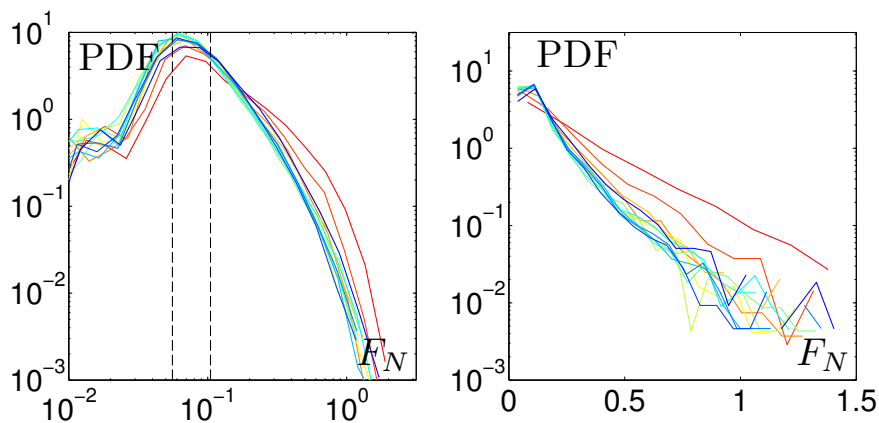


Figure 4.2: **Normal forces distributions** for different packing fractions. The dotted lines represent the two extremal threshold value that are applied to the normal force to extract the contacts. Color code spans from blue (low packing fractions) to red (high packing fractions) (See table 3.1).

contacts.

4.1.2 Inter-particle distance

A neighborhood relationship is also defined by the inter-particle distance defined in figure 4.3, top. This measurement is illustrated in maps in figure 4.3, bottom, where both the size and the color of the edges code for the inter-particle distance. In contrast with a normal force map, there is little difference between jammed and loose packings on this map. We thereafter turn to the distribution of inter-particle distances represented in figure 4.4. A first look at the left tail of the distributions in the right figure betrays the presence of noise on position detection. Indeed, some particles have a negative gap as large as 0.1 grain diameter. We have been arguing above (in sections 2.1.2 and 3.3) that the packing is made of soft grains, but such deformations are unphysical here since it would require forces as high as 400 N (~ 40 kg !). Above this value, we can claim with certainty that the

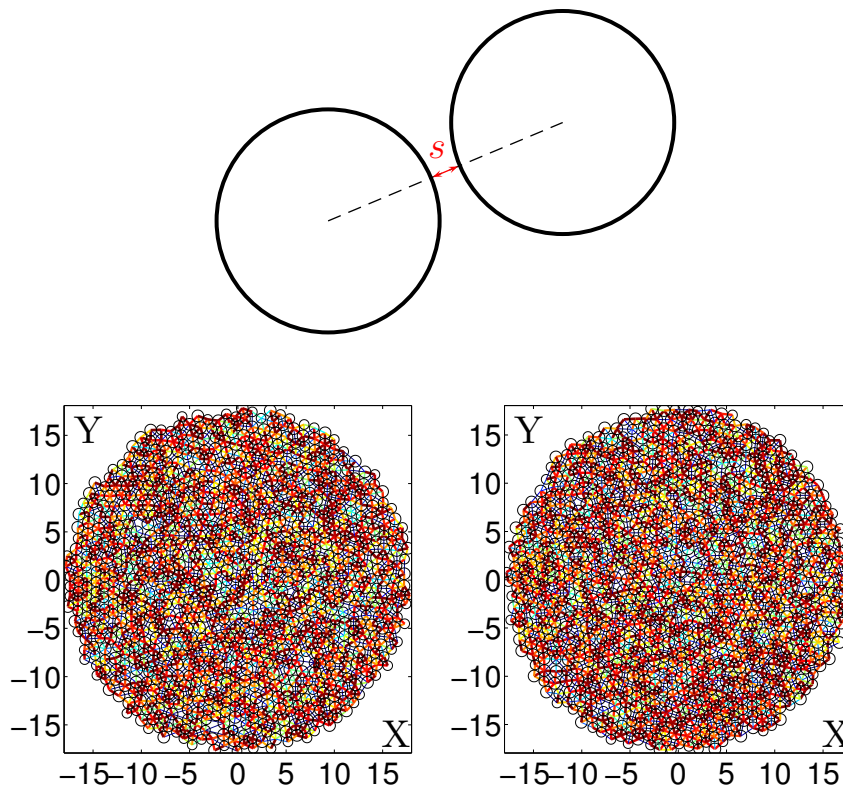


Figure 4.3: **Interparticle distance.** **Top:** Scheme of two particles separated by an interparticle distance s . **Bottom : Maps.** Links are represented by lines, whose thickness and color is encoded by the value of the value of s . **Left:** $\phi = 0.8119$. **Right:** $\phi = 0.8236$.

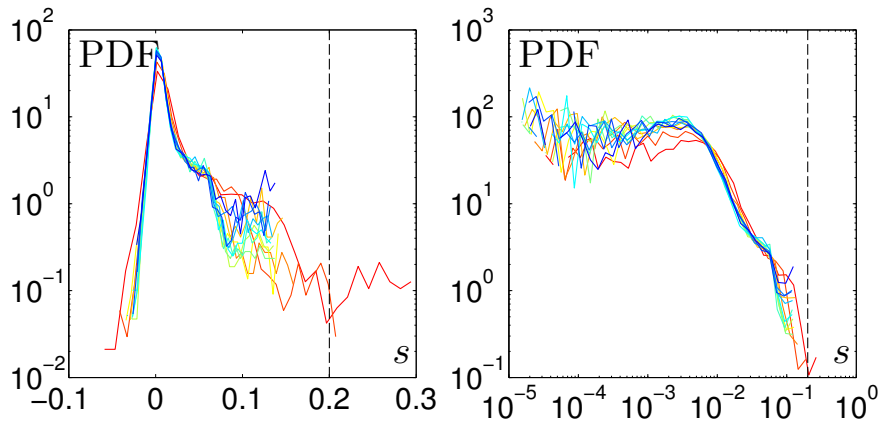


Figure 4.4: **Inter-particle gap distributions** for different packing fractions. The dotted line represent the threshold value s_t that is applied to the inter-particle distance to extract the contacts. s unit corresponds to the diameter of a small grain. Color code spans from blue (low packing fractions) to red (high packing fractions) (See table 3.1).

link is not a contact.

4.1.3 Contact criteria

It is time now to combine the two criteria we have been discussing. To do so, we look at the joint distribution of both normal force and inter-particle distance, plotted in figure 4.5 for a low (left) and a high (right) packing fractions. As stressed above, there is no clear criteria between contacts and non-contacts. Still, joint distributions give a good indication of what we should do: we take as contacts links that have a normal force above the force threshold and that have an inter-particle distance below the distance threshold. A clear threshold can be defined for gaps: while the population with low gaps can either be contact or not, the population with large gaps is entirely made of non-contacts. We thus plot the distribution of normal force conditioned to gaps higher than $s_t = 2 \times 10^{-1}$ grain diameter. Unfortunately, the distributions are widely distributed. Any hope of defining a sharp threshold is now gone! We are doomed to study a range of thresholds. The distribution maxima are located between $F_{N*1} = 5.6 \times 10^{-2}$ and $F_{N*2} = 10.5 \times 10^{-2}$. We use these two extremal values to define the threshold range. The limits of this range are pictured on the joint distributions plotted in figure 4.5, top, and on the distribution of normal force conditioned to the link with $s < s_t$ plotted in figure 4.5, bottom. We discuss the different populations that we have just identified.

1. Links belonging to the top-left panel (low gap, large force) are defined as contacts.

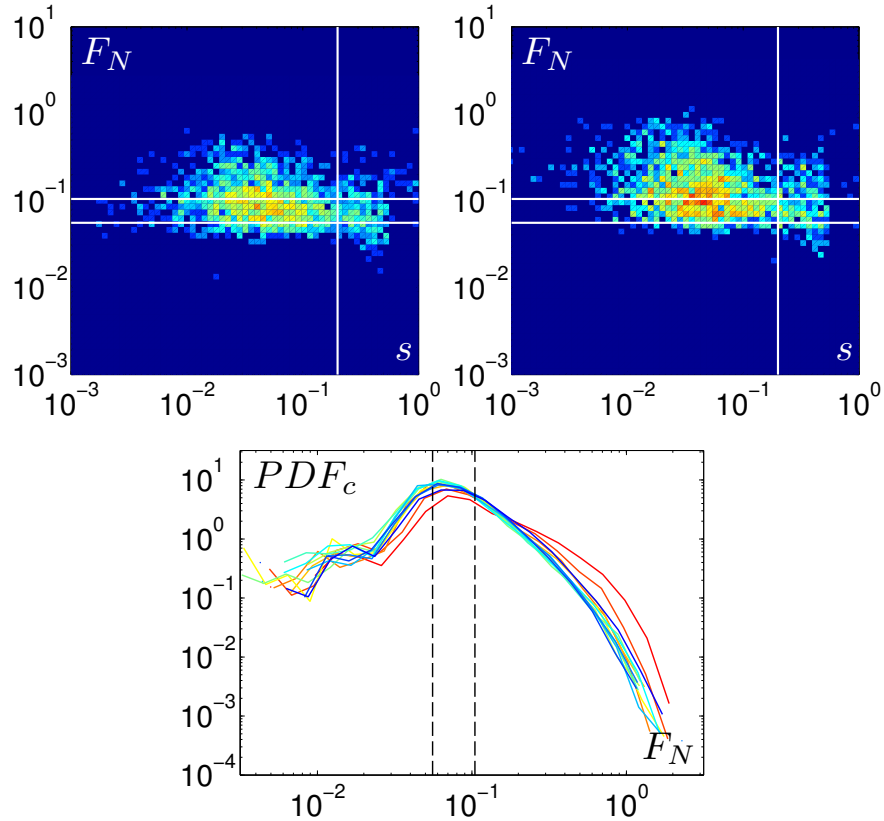


Figure 4.5: **Joint distributions on inter-particle gaps and forces.** **Top:** Normal forces and interparticle distance distributions for $\phi = 0.8125$ (**left**) and $\phi = 0.8178$ (**right**). The white vertical line represents the threshold value s_t that is applied to the inter-particle distance. The horizontal white lines represent the two extremal threshold values F_{N*1} and F_{N*2} applied to the normal force. **Bottom:** Normal forces distributions conditioned to links with an inter-particle distance s smaller than s_t for different packing fractions. The dotted lines represent the two extremal threshold value that are applied to the normal force to extract the contacts. Color code spans from blue (low packing fractions) to red (high packing fractions) (See table 3.1).

2. the bottom-left panel represents low forces and low inter-particle distance and clearly is one of the most populated panels because lots of inter-grains links have a small distance but don't touch each other.
3. the top-right panel is unphysical: non touching particles cannot have a normal force. The normal force we measure comes from neighboring contacts, whose photo-elastic pattern overlap the “camemberts”. This effect is illustrated between grains 1 and 3 in figure 4.1, top right: from inter-particle distance, we clearly see that it is not a contact.

Yet, it has a hotter color – *i.e.* a larger normal force – than the link between grains 4 and 5 that, as we see in figure 4.1, top left, is clearly a contact. When we compare figures 4.5, left and right, we see that the top-right panel is more populated for denser packings. This illustrates the fact that for denser packing, grains undergo stronger forces and photo-elastic patterns spread over larger areas.

4. the bottom-right panel represents low forces and high inter-particle distance links. Its population has not changed much from non dense to dense packing.

This means that the noise on the normal force blurs the whole thing. Choosing to select particles by using a constant threshold is arbitrary, and has the following consequence: we may select as contacts neighboring particles that are close together but that don't touch. On the contrary, we may exclude links that are real contacts with a very weak force. In the following, we shall use the word “contact” to refer to the links that come from this thresholding procedure but the reader has to be aware it does not match the rigorous definition of contact. We will, in the next section, test this procedure for the whole range of force thresholds that we have defined previously.

4.1.4 Test: average number of contacts

In order to check the thresholding procedure, we count the average number of contacts and plot it vs. packing fraction in figure 4.6, top-left, for a range of thresholds F_{N^*} spanning the two limits that we have defined above. Although the number of contacts, z , drastically decreases with increasing force threshold, the dependence with packing fraction remains unchanged. The main effect of varying the threshold is a shift of the curves. At low packing fractions, $z = z_J$ is constant and undergoes a well defined kink at an intermediate packing fraction $\phi_J = 0.814$, from which it starts to increase. We call it ϕ_J because it indicates the packing from which the packing starts to be compressed. We interpret it as a signature of the a-thermal jamming transition. Above ϕ_J , z is compatible with a fit :

$$z = z_J + A(\phi - \phi_J)^\beta \quad (4.1)$$

We perform such a fit and display the value of ϕ_J and β as a function of F_{N^*} in figure 4.6 top-right. We see that β strongly increases with F_{N^*} : for low force thresholds, β is close to the value 0.5 that is reported for a-thermal soft spheres [van Hecke, 2010] while for high force thresholds, β is closer to 1. This evolution of the exponent directly relies on the fact that when the system is denser, weak forces are less significant, and the value of z depends less dramatically on F_{N^*} . ϕ_J weakly decreases with F_{N^*} and we

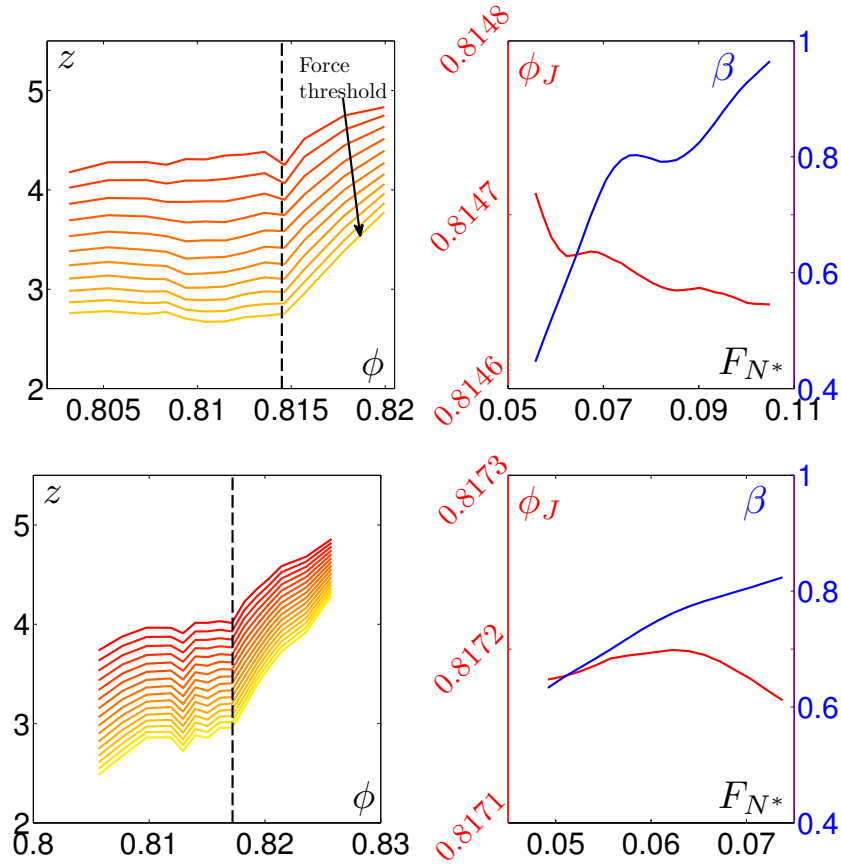


Figure 4.6: **Average number of contact.** **Top Left:** Average number of contacts vs. packing fraction for different force thresholds, ranging from 0.0557 (red) to 0.1047 (yellow). **Top Right:** β (right axis) and ϕ_J (left axis) (see text for definition) vs. force threshold F_{N^*} . **Bottom :** Same as above but for an other similar experiment.

are not able to interpret this dependence. Note that ϕ_J changes by a factor of 5×10^{-5} over the entire range of F_{N^*} . We can therefore consider that the measurement of ϕ_J is performed with an accuracy of 5×10^{-5} . Note additionally, that Maxwell arguments (see section 1.1.1.1) implies that z_J is between 3 and 4. For most thresholds, we find that z_J is between 3 and 4.

In order to ensure the reproducibility of such a result, we reproduce the experiment and the contact analysis on a similar experiment. Thus, we plot in figure 4.6 bottom-left the average number of contacts versus packing fraction for different F_{N^*} . Apart from the kink packing fraction which occurs at $\phi_J = 0.8172$, similar behavior roughly arises. Again, more details are given by the fit above ϕ_J , which we summarize by plotting ϕ_J and β vs. force threshold F_{N^*} in figure 4.6 bottom-right. Again β increases with respect to F_{N^*} and ϕ_J changes by a factor of 5×10^{-5} . Note, also, that

β is between 0.6 and 0.8. To ensure the reproducibility of the experiment, two additional experiments have been done and provide two more values of $\phi_J = 0.8208$ and 0.8145 . Altogether, this yields an average $\hat{\phi}_J = 0.817$ with a dispersion $\delta\hat{\phi} = 0.003$. The jamming packing fraction depends on the history of the packing and is thus slightly different at each attempt. This effect is already present in simulations of frictionless spheres because of the finite size of the system [O’Hern et al., 2002, Chaudhuri et al., 2010] and is even expected for large frictional systems.

The associated values of ϕ_J for the different experiment we have carried out are reported in table 4.1.

4.1.5 Robustness vs. quench and vibration phase of the picture trigger

We would like now to compare these results with the “quenched” packings, whose force geometric properties have been studied in the last chapter. We recall here that as opposed to “annealed” packings that we have been analyzing up to now in this chapter, the quenched packings differ by the fact that they have been prepared at much larger compaction rates. The average contact number is plotted vs. packing fraction for two “quenched” experiments in figure 4.7 (a) and (b). Note that the curves of (a) are noisier. This is due to the fact that there is less time averaging because this experiment was shorter. We see that the global behavior of curves is similar to the previous ones and we find $\phi_J = 0.8117$ and 0.8079 . These values are lower than for the annealed packings. As already mentioned in the last chapter, this difference is consistent with previous studies about compaction rate and final jammed state [Silbert et al., 2002, Zhang and Makse, 2005, Shundyak et al., 2007]. Moreover, we fit the excess of contacts versus the distance to the kink packing fraction by expression 4.1, and we plot the parameter β versus thresholds, F_{N^*} , in figure 4.7 (e). β increases with respect to F_{N^*} and is between 0.3 and 0.5. We attribute the fact that β is lower for “annealed” packings than for “quenched” packings to the quench protocol. Note, nonetheless, that in this experiment, the image contrast was slightly better because of hardware issues. That is why the values of F_{N^*} are lower. Yet, we cannot exclude the contrast issue to be responsible for the difference of β .

We now want to discuss the role of the phase of the vibration that we have chosen to trigger the camera (see section 2.1.2), which we will call the “usual” phase in the following. In order to maximize the contrast, we chose the phase at which grains move the least. At this phase of the vibration, the grains are stopped by one of the walls. As a matter of fact, a shock wave is triggered by this wall. This is precisely what gives rise to a non-zero number of contacts for packing fractions lower than ϕ_J . In order to prove this assumption, we ran a complementary experiment where pictures were taken at a different phase

of vibration (“flying”), namely the moment at which they “fly” between the two walls. But in order to be able to compare with the previous results, we had to perform simultaneous experiments with pictures taken both at the “usual” and the “flying” phases. To do so, we performed one compaction, and then at each decompaction step, we alternatively switched the phase between the “usual” and the “flying” phases. This protocol ensures a direct comparison of the different phases. Unfortunately, for time reasons, we performed this experiment for only a small amount of pictures, and there is less time averaging. This comparison is done by investigating the average number of contacts that is plotted vs. packing fraction in figure 4.7 for the “usual” phase **(c)** and for the “flying” phase **(d)**. First, although it is less pronounced because of lack of statistics, the “usual” phase displays the usual shape: it is constant at low packing fractions and starts to increase at an intermediate packing fraction $\phi_J = 0.8145$. In contrast, the “flying” phase has no kink. But, thanks to the specific protocol we used, the jamming packing fraction is the same as for the “usual” phase. Therefore, we fit both curves above $\phi_J = 0.8145$ with equation 4.1 and we plot β versus F_{N^*} in figure 4.7 **(e)**. β increases with increasing F_{N^*} for both phases, but while the usual phase β is between 0.7 and 1, the flying phase β is between 0.9 and 1.2. As a comparison, a linear increase of the average number of contacts without any kink with packing fraction has been reported in recent theoretical and numerical studies of thermal soft spheres [Berthier et al., 2011c]. Thus, the “flying” phase experimental results are more consistent with this work than the “usual” phase experiments.

4.1.6 Conclusion on contacts

We have defined the notion of “contact” in our experiment and observed its robustness amongst various realizations of the experiment by investigating the average number of contacts. We summarize in table 4.1 the various experiments we have performed and report the different values of ϕ_J in each

number	compaction	ϕ_J	time window	statistics
1	quenched	0.8079	300	60
2	quenched	0.8117	20000	300
3	annealed	0.8147	10000	2500
4	annealed	0.8172	10000	5000
5	annealed	0.8208	10000	5000
6	annealed	0.8145	200	100

Table 4.1: **Experimental Jamming packing fractions.** Summary of the experiments, their “jamming” packing fractions, the width of the time window and the number of time-steps contributing to the average.

case. Hence, in order to compare the different experiments. We define

$$\epsilon = \frac{\phi - \phi_J}{\phi_J}, \quad (4.2)$$

the reduced packing fraction.

Moreover, we have seen that the shape of the average number of contacts versus packing fraction is very specific to the experimental details and in particular to the phase at which pictures are triggered. Still, we have seen that a different phase leads to a behavior that more closely resembles thermal soft colloids.

In the following, we will attempt to use the contacts in order to study

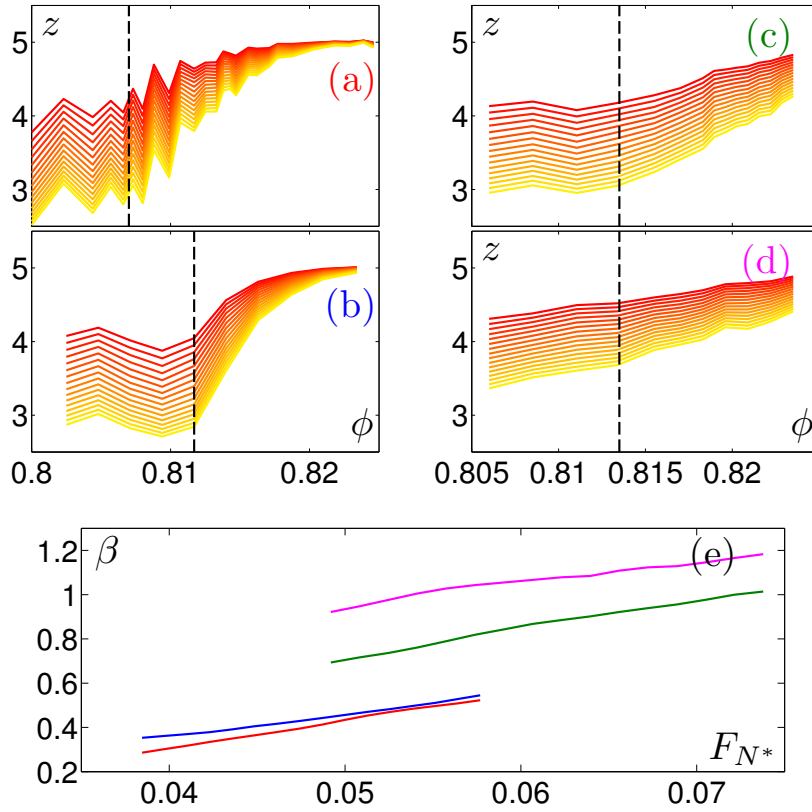


Figure 4.7: **Robustness of contact number.** (a), (b), (c) and (d): Average number of contacts vs. packing fraction, for different force thresholds, ranging from low thresholds (red) to high thresholds (yellow). (a) and (b) corresponds to two distinct “quench experiments” and (c) and (d) correspond to two simultaneous experiments performed at two different phases of the vibration cycle. (c) represents the “usual” phase and (d) the “flying” phase (see text for definition). (e): exponent β (see text for definition) vs. force threshold F_{N^*} . The colors correspond to the colors of the labels (a), (b), (c) and (d).

spatial and time correlations. To do so, we define the number of contact of grain i at time t , $z_i(t)$, by choosing arbitrarily one unique threshold, such that $z_J \sim 3.5$. All the results that we will present in the following use come from this choice. Still, we have checked that the results are qualitatively similar if we choose another threshold. We shall, in the remainder of the chapter, focus on the statistical properties of $z_i(t)$.

4.2 Spatial Correlations of the contacts

4.2.1 Direct Spatial Correlations

First, we describe the spatial correlations of the number of contacts. We display in figure 4.8, top, maps of the instantaneous contact number. We compute a spatial correlation length out of such maps. As was done in the last chapter to describe the force chains 3.3.4, we interpolate the contact number on a grid, out of which we compute spatial autocorrelation. We then extract its radial dependence G_2^z vs. r , that is plotted in figure 4.8, bottom left. It decays quickly towards zero. We estimate a typical decay

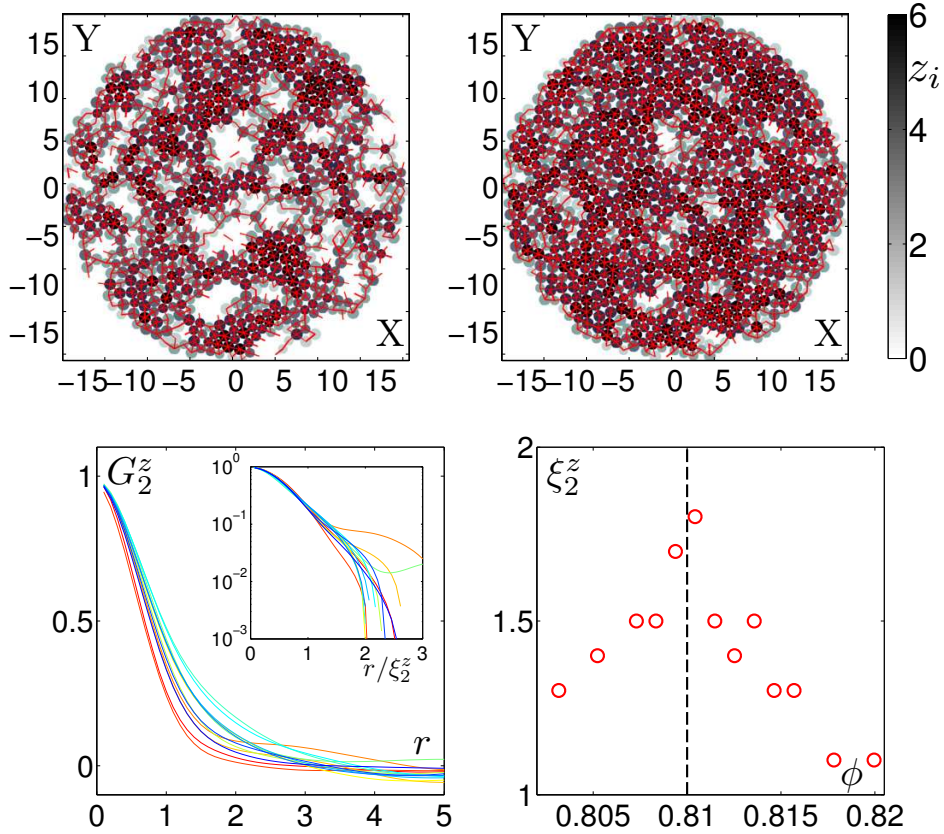


Figure 4.8: **Spatial correlations of the contacts.** **Top :** Instantaneous map of contact number, for $\phi = 0.8172$ (**left**) and $\phi = 0.8214$ (**right**). The color map spans from white ($z_i(t) = 0$) to black ($z_i(t) \geq 6$). Contacts links are indicated in red. **Bottom-Left:** Spatial correlations of the contacts G_2^z vs. r . **Inset:** G_2^z vs. r/ξ_2^z . Color code spans from blue (low packing fractions) to red (high packing fractions) (See table 3.1). **Bottom-Right:** Spatial correlation length of the contacts ξ_2^z vs. packing fraction ϕ .

length ξ_2^z defined as $G_2^z(\xi_2^z) = 0.2$. We then plot G_2^z vs. r/ξ_2^z in figure 4.8, bottom left-inset.

We see that the decay is roughly exponential and that the curves merge approximately. Therefore, ξ_2^z is good estimate of the decay of the spatial correlation of the contacts. We plot it in figure 4.8, bottom right. It has a small maximum at an intermediate packing fraction that coincides with the previously defined $\phi^* = 0.810$. The presence of this maximum thus reveals maximal spatial correlations of the contacts at an intermediate packing fraction.

We will try in the following section to confirm the presence of spatial correlations by studying the temporal variance of the number of contacts.

4.2.2 Gaussian temporal distribution

We here study the time distribution of the instantaneous number of contacts \bar{z}_t defined the following way:

$$\bar{z}_t = \frac{1}{N} \sum_{i=1}^N z_i(t) \quad (4.3)$$

We plot in figure 4.9, left, the reduced instantaneous number of contacts

$$\bar{z}_t^r = \frac{\bar{z}_t - \langle \bar{z}_t \rangle}{\text{std}_t \bar{z}_t}, \quad (4.4)$$

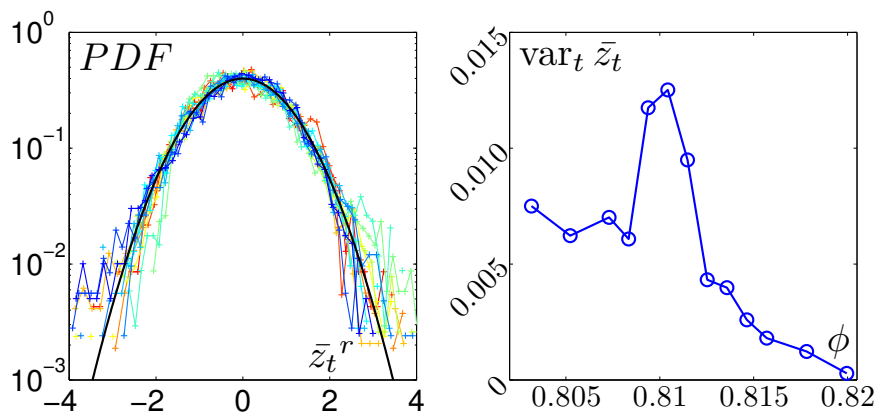


Figure 4.9: **Temporal fluctuations of contact number. Left:** Distribution of \bar{z}_t^r for different packing fractions. The black line is a gaussian function of average 0 and standard deviation 1. Color code spans from blue (low packing fractions) to red (high packing fractions) (See table 3.1). **Right:** Temporal variance of instantaneous contact number $\text{var}_t \bar{z}_t$ vs. packing fraction ϕ .

where $\langle \bar{z}_t \rangle$ and $\text{std}_t \bar{z}_t$ are respectively the time average and standard deviation of \bar{z}_t . We see that the distributions rescale well at all packing fractions and resemble gaussian distributions. It is then straightforward to look at the time variance of \bar{z}_t , which is plotted in figure 4.9, right. This curve shows a maximum at an intermediate packing fraction, $\phi^* = 0.810$. The fluctuations are maximum at this packing fraction! It seems rather peculiar that the fluctuations do not grow monotonically as the packing fraction is reduced as expected for a system that is more and more free to evolve. In order to understand these points, we shall, in the following section, look more closely at these fluctuations.

4.2.3 Spatial correlations through temporal fluctuations

As stressed in appendix B.1, the temporal variance of $z(t)$ can be used to estimate the magnitude of collective fluctuations. To do so, we define a dynamical susceptibility for the number of contacts:

$$\chi_z \equiv \frac{N}{\overline{\text{var}_t z_i(t)}} \text{var}_t \bar{z}_t. \quad (4.5)$$

Along the way, we investigate the “intrinsic” fluctuations quantified by $\overline{\text{var}_t z_i(t)}$, which is the average over the system of individual time fluctuations. $\overline{\text{var}_t z_i(t)}$ is plotted vs. packing fraction in figure 4.10 left. $\overline{\text{var}_t z_i(t)}$ is around 0.6 for the lowest densities and decreases down to 0.1 for the highest packing fractions. Still, the contact number fluctuates at all packing fractions. We now precisely study the collective behavior by plotting χ_z vs. packing fraction in figure 4.10 right. This curve has a maximum at an intermediate packing fraction $\phi^* = 0.810$. Surprisingly, this packing fraction

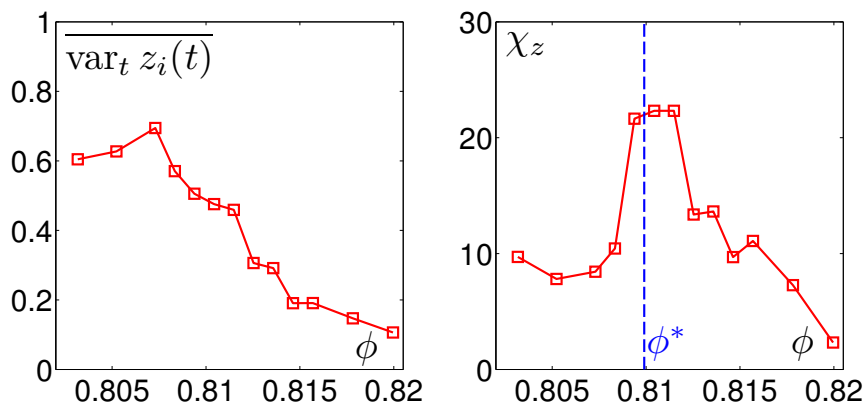


Figure 4.10: **Contacts temporal fluctuations** “intrinsic” fluctuations $\overline{\text{var}_t z_i(t)}$ (**left**) and contact susceptibility χ_z (**right**) vs. packing fraction ϕ .

coincides with the maximal dynamical heterogeneities of the displacements investigated in the previous chapter. The present result confirms that these dynamical heterogeneities are associated with a spatial correlation of contacts (see appendix B.1).

In the following, we shall describe in further detail the dynamics of the contacts. In particular, we shall also study the dynamical heterogeneities of the contacts.

4.2.4 Loops

Another complementary way to estimate spatial correlations of the contacts is to consider force loops. The force loops are indeed connected clusters of neighboring particles without contacts between them. These objects are closely linked to force chains, and their sizes tend to span the packing as the packing is close to jamming [DeGiuli]. In addition, one can expect significant correlations between the loops and the heterogeneity of the dynamics. The force loops involve particles that are not constrained by contacts, and that are therefore free to move. We will here stick to a statistical description of the size of the loops. This work is an on going project with Eric DeGiuli (Department of Mathematics, University of British Columbia, Vancouver, Canada). We gratefully acknowledge Eric DeGiuli for providing the code to extract the “loops” and for fruitful discussions. The loops are extracted from Delaunay triangles, Voronoï vertices and contacts (see DeGiuli and McElwaine [2011] for details); by construction, all the loops tile the entire plane. Figure 4.11, top, displays a snapshot of the loops for a dense state with $z = 4.46$ (left) and a loose state with $z = 3.78$ (right). We see that the size of the loops is larger for the looser packing. We also see that there are a poor statistics. We therefore compute the distribution of cluster size ℓ , *i.e.* the number of grains involved in each loop over the packing and we cumulate it over time. We plot the distributions for several packing fractions in figure 4.11, bottom left. We see that the distributions have exponential tails and widen as packing fraction is decreased. Likewise, we can also study the distribution of the loops areas A_ℓ , that is plotted in figure 4.11. We see that the distributions have even larger tails than exponential and that they widen as the packing fraction is decreased. For these two distributions, we see that the statistics are dominated by a few rare big loops, so that the distributions are ill-defined and noisy for large values of ℓ and A_ℓ . Further work is in progress to study the correlation between the loops and the dynamics.

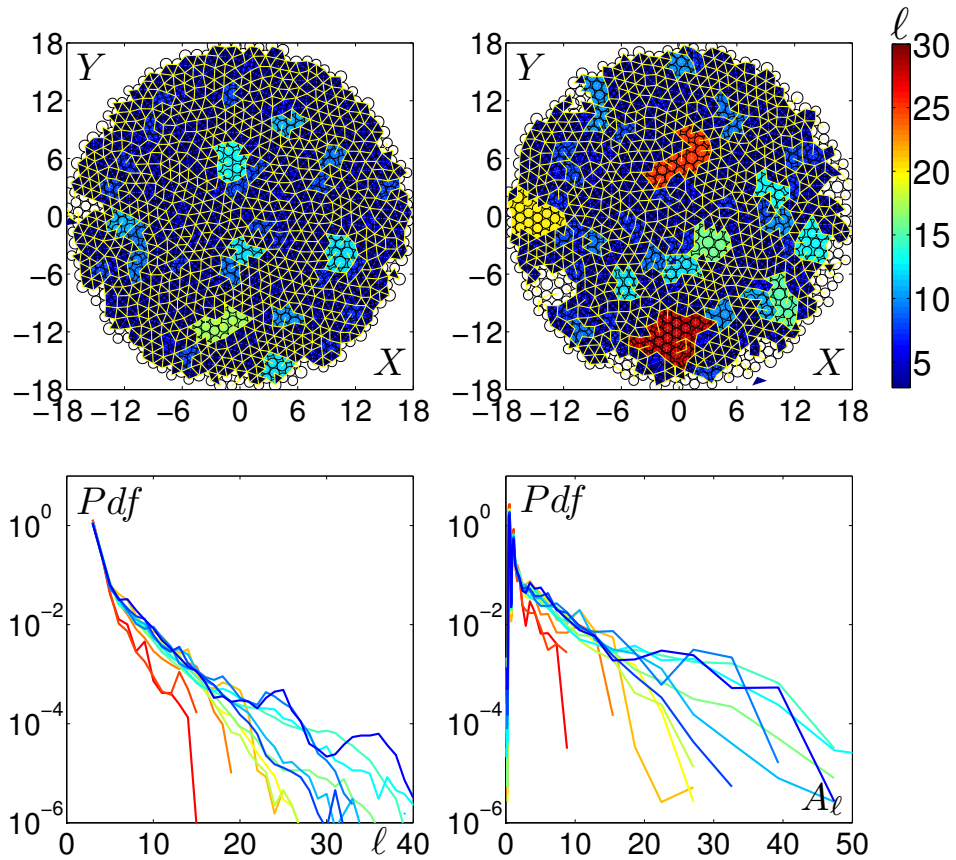


Figure 4.11: **Force loops.** **Top Left:** Snapshot of the loops for a dense packing ($\phi = 0.8214$, $z = 4.46$). **Top Right:** Snapshot of the loops for a loose packing ($\phi = 0.8117$, $z = 3.78$). Color code represents the number of grains, ℓ , involved in a cluster. The yellow lines represent the contacts. **Bottom Left:** Distribution of loops size ℓ (number of grains involved in a loop) for different packing fractions. **Bottom Right:** Distribution of loops area A_ℓ for different packing fractions. Color code spans from blue (low packing fractions) to red (high packing fractions) (See table 3.1).

4.3 Dynamics of the contacts

4.3.1 State of the art

Very few attempts to characterize the dynamics of the contact network in thermal systems close to jamming have been reported so far. From a statistical physics point of view, Brito and Wyart [2006] have attempted to define the contact number in a hard spheres glass system, by counting as contacts the particles that shock each other a certain amount of time. By contrast, Berthier et al. [2011c] probably define the contacts in thermal system by averaging all the particles which overlap instantaneously. Above in this

chapter, in section 4.1, we have defined an effective contact number, that is also an average of the instantaneous number of particles that overlap. The issue here is that “instantaneous” in our experiment is very specific to the external shaking; pictures are taken at one specific phase of the vibration that coincides to a time at which the grains are shaken quite violently against a wall, shock waves propagate through an unjammed packing. Therefore, we would like to stress that some differences with the results of the works cited above may originate here.

4.3.2 The Contact overlap function

In order to quantify the dynamics of the contact network, we need a quantity that tells us when a contact is broken, and that we can follow dynamically in time. One possible approach might be to consider neighbor links, and to assign 1 when there is a contact and -1 when there is not, just like in a spin system. However, the database is constructed using a particle index instead of links. Using links instead of particles index require to build another tables in the database to be efficient, which augment to the existing tables quite significant amount of data. Nonetheless, as displayed in appendix C.2, the results we will obtain in the remainder of the manuscript are qualitatively similar. Therefore, in the following, we will focus on the instantaneous number of contact, $z_i(t)$, of particle i at time t .

In order to quantify the change of the contact network within a lag time τ , let’s define

$$Q^z(t, \tau) = \frac{1}{N} \sum_i Q_i^z(t, \tau), \quad (4.6)$$

where

$$Q_i^z(t, \tau) = \begin{cases} 1 & \text{if } |z_i(t + \tau) - z_i(t)| \leq 1 \\ 0 & \text{if } |z_i(t + \tau) - z_i(t)| > 1 \end{cases} . \quad (4.7)$$

4.3.3 Average

Let’s first compute the time average of the contact overlap function

$$Q^z(\tau) = \langle Q^z(t, \tau) \rangle_t, \quad (4.8)$$

that reveals how much the contact network has relaxed, on average, in a lag time τ . We plot Q^z vs. lag time τ for the different densities in figure 4.12, left. We distinguish two distinct behaviors below and above the density $\phi_J = 0.814$.

- for dense packings, Q^z is constant and lower than 1. The fact that it is different from 1 reveals a short time decorrelation, that occurs on a time that is shorter than the sampling time. We also see that the short time decorrelation decreases with decreasing packing fraction.

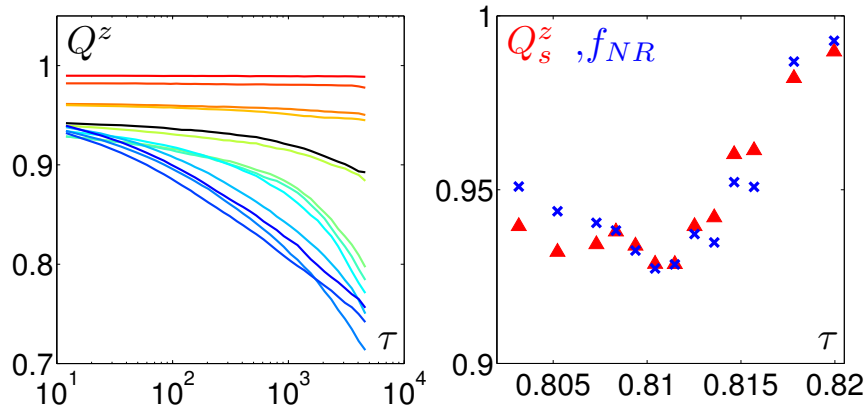


Figure 4.12: **Contact dynamics. Left:** Average contact overlap function $Q^z(\tau)$ vs. lag time τ for different packing fractions. Color code spans from blue (low packing fractions) to red (high packing fractions) (See table 3.1), except for the curve corresponding to $\phi = 0.814$, which is plotted in black. **Right:** Fraction of particles having more than 1 contacts, f_{NR} (\times) and short time value of the average contact overlap function Q_s^z (\blacktriangle) vs. packing fraction.

These two facts indicate that the short time decorrelation is related to rattling particles. In order to ensure it, we estimate the value of the short time decorrelation Q_s^z by taking the value Q^z at $\tau = 4$ and we estimate the fraction of non-rattling particles f_{NR} by measuring the fraction of particles that have more than 1 contact (see Bi et al. [2011] where f_{NR} has been introduced). We plot both Q_s^z and f_{NR} vs. packing fraction in figure 4.12 right. We first see that they are nearly the same at all packing fractions. For dense packing fractions they are close to 0.995, from which they depart with decreasing packing fraction to fall to a minimal value of 0.94 at an intermediate packing fraction 0.811. For smaller densities, they then slightly increase so that f_{NR} and Q_s^z depend weakly on packing fraction.

- at low densities (below $\phi_J = 0.814$), as pointed out before, the dependence of Q_s^z with packing fraction is less significant. However, we can clearly see in figure 4.12 left that Q^z decreases significantly with lag time τ , and all the more quickly as packing fraction is reduced. This indicates that a long time relaxation of the contact network sets in.

The present result is one of the key messages of this chapter. We saw at the beginning of the chapter that $\phi_J = 0.814$ corresponds to the density at which the systems jams when the contact number starts to increase. The very same density also corresponds to the limit between an evolving

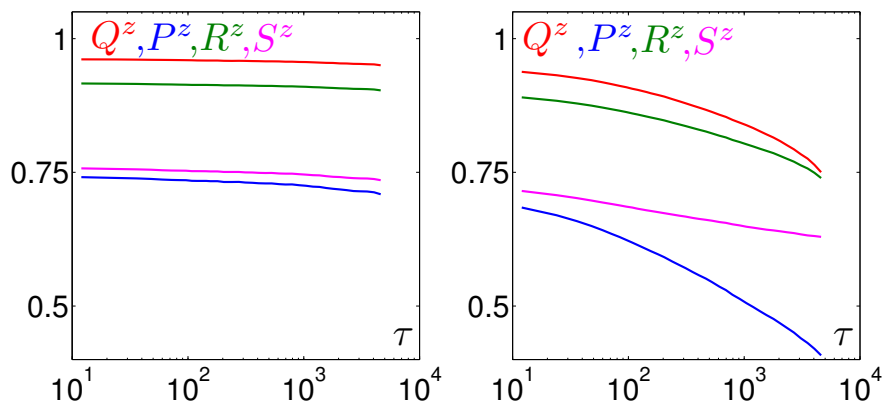


Figure 4.13: **Comparing the overlap functions.** Average contact overlap functions $Q^z(\tau)$ (red), $P^z(\tau)$ (blue), $R^z(\tau)$ (green) and $S^z(\tau)$ (magenta) vs. lag time τ for $\phi = 0.8157$ (left) $\phi = 0.8083$ (right).

and a frozen contact network. Apart from the fact that here it is the contact network and not the structure that is at stake, this is reminiscent of glasses (see Berthier and Biroli [2011], Debenedetti and Stillinger [2001]): the relaxation timescale exceeds the experimental time window.

The reader might be concerned that the choice of the contact function may impact the analysis. We also have tried several alternative definitions to $Q_i^z(t, \tau)$ defined below:

$$P_i^z(t, \tau) = \begin{cases} 1 & \text{if } |z_i(t + \tau) - z_i(t)| < 1 \\ 0 & \text{if } |z_i(t + \tau) - z_i(t)| \geq 1 \end{cases}, \quad (4.9)$$

$$R_i^z(t, \tau) = \begin{cases} 1 & \text{if } |z_i(t + \tau) - z_i(t)| = 0 \\ 3/4 & \text{if } |z_i(t + \tau) - z_i(t)| = 1 \\ 1/2 & \text{if } |z_i(t + \tau) - z_i(t)| = 2 \\ 0 & \text{if } |z_i(t + \tau) - z_i(t)| \geq 3 \end{cases} \quad \text{and} \quad (4.10)$$

$$S_i^z(t, \tau) = \exp\left(-\frac{|z_i(t + \tau) - z_i(t)|^2}{\langle |z_i(t + \tau) - z_i(t)|^2 \rangle}\right), \quad (4.11)$$

where $\bar{\cdot}$ and $\langle \cdot \rangle$ are respectively average over particles and time.

We then average these quantities over particles as was done in equation 4.6, and in addition to $Q^z(t, \tau)$, we obtain $P^z(t, \tau)$, $R^z(t, \tau)$ and $S^z(t, \tau)$. Their time averages $Q^z(\tau)$, $P^z(\tau)$, $R^z(\tau)$ and $S^z(\tau)$ are plotted in figure 4.13, left and right, for two different densities. They all have similar qualitative behaviors: (i) At high packing fraction, all the average overlap function are constant with respect to lag time. (ii) at low packing fraction, there is a slow decay with respect to lag time. All quantities display the short and long time decorrelations. The choice of one quantity in particular does not

significantly affect the description of how network relaxes. Therefore, we choose in the following to use $Q^z(t, \tau)$ as the contact overlap function.

4.3.4 Details of the contact dynamics

Since contact dynamics seems to undergo a glassy scenario, it is then legitimate to look for the details of the relaxation which is associated with dynamic heterogeneities close to the glass transition [Berthier and Biroli, 2011]. As stressed in the last chapter for the dynamic heterogeneities of the displacements, the contact overlap function also provides a straightforward measure of heterogeneity and intermittency via measurements of the dynamic susceptibility. We illustrate this point by plotting $Q^z(t, \tau)$ vs. t in figures 4.14 (a), (b) and (c) for different lag times. These time series have significant fluctuations at rather low densities and high time lags. This is further quantified by the computation of its temporal variance which is plotted vs. packing fraction for different time lags in figure 4.15 (d). $\text{var}_t Q^z(t, \tau)$ increases for decreasing lag times and for decreasing packing fractions and a small maximum seems to occur at an intermediate packing fraction $\phi \sim \phi^*$, and all the more significant as time lag is large. As stressed in the previous section, this variance quantifies the magnitude of the fluctuations and its collectivity at the same time. We can then separately quantify the fluctuations by computing the quantity $\text{var}_t Q_i^z(t, \tau)$. We plot in figure 4.15 (e) $\text{var}_t Q_i^z(t, \tau)$ vs. packing fraction for different lag times τ . We observe that it decreases with packing fraction, all the more quickly as the lag time is large.

The next step is to quantify only the magnitude of temporal cross-correlation defined by:

$$\chi_4^z(\tau) = \frac{N}{\text{var}_t Q_i^z(t, \tau)} \overline{\text{var}_t Q^z(t, \tau)}, \quad (4.12)$$

which is plotted vs. packing fraction for different time lags in figure 4.15 (f). We see that there is a clear maximum at an intermediate packing fraction $\phi^* = 0.810$ at all lag times. However, the τ dependence is not as clear.

Therefore we plot in figure 4.16, left, the contact dynamical susceptibility χ_4^z vs. lag time τ for different packing fractions. We see that it is clearly non-monotonic at all packing fractions. For packing fraction below ϕ_J , the maximum is well defined and corresponds to a time τ^* at which the fluctuations of the contact network is maximally collective (see appendix B.1). The magnitude of this maximum χ_4^{z*} is related to the number of involved particles. Note here that the maximum is broad and there is a lot of noise, so that the localization of the maximum with confidence is difficult. τ^* is plotted vs. packing fraction in figure 4.16 bottom left. It increases with packing fraction with a local maximum located at $\phi^* = 0.810$, and tends to

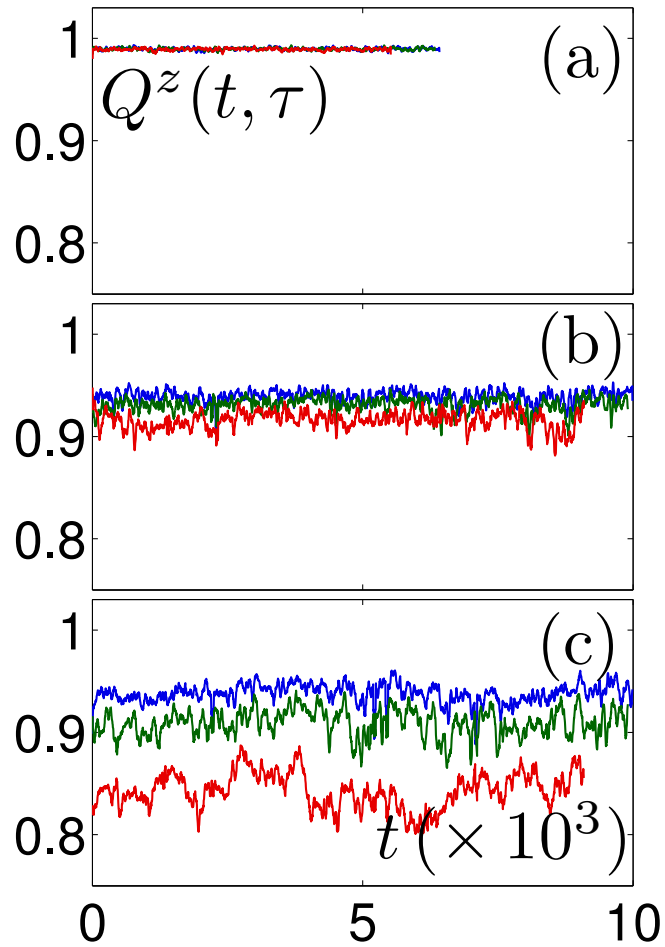


Figure 4.14: **Contact overlap function vs. time.** Contact overlap function $Q^z(t, \tau)$ versus *time* for lag times 10 (blue), 100 (green) and 1000 (red) at $\phi = 0.8083$ (a), $\phi = 0.8125$ (b), and $\phi = 0.8200$ (c).

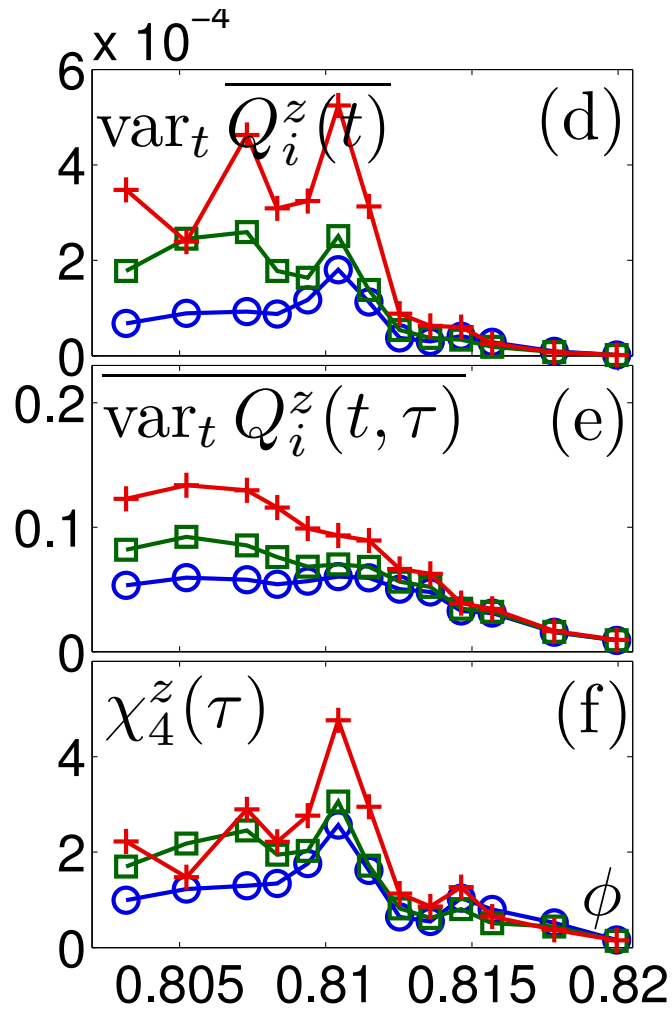


Figure 4.15: **Variations:** Variance of the contact overlap function $\text{var}_t \overline{Q_i^z(t, \tau)}$ (d), contact overlap intrinsic time variance $\text{var}_t Q_i^z(t, \tau)$ (e) and dynamical susceptibility $\chi_4^z(\tau)$ (f) versus packing fraction for lag times τ (\circ), 100 (\square) and 1000 (+).

diverge as the packing fraction reaches ϕ_J . χ_4^{z*} is plotted vs. packing fraction in figure 4.16, bottom right. This displays a maximum of amplitude of 5 at packing fraction $\phi^* = 0.810$. Thus, ϕ^* corresponds to a packing fraction at which the relaxation of the contact network is maximally collective. It also corresponds to a packing fraction at which the time of this collective relaxation tends to be locally maximal. Note, that there are significant error bars and dispersion of the data point. In order to gain confidence in this trend, we ran two similar runs. We plot χ_4^{z*} vs. reduced packing fraction, as defined in equation 4.2, for all the experimental runs in figure 4.17, top. We see that the three data sets tend to have a maximum of amplitude between 4 and 8, located at $\epsilon = -0.6 \times 10^{-2}$. We thus confidently associate the presence of this maximum to a dynamical signature of the jamming transition. This is the second key message of this chapter: a dynamical crossover as-

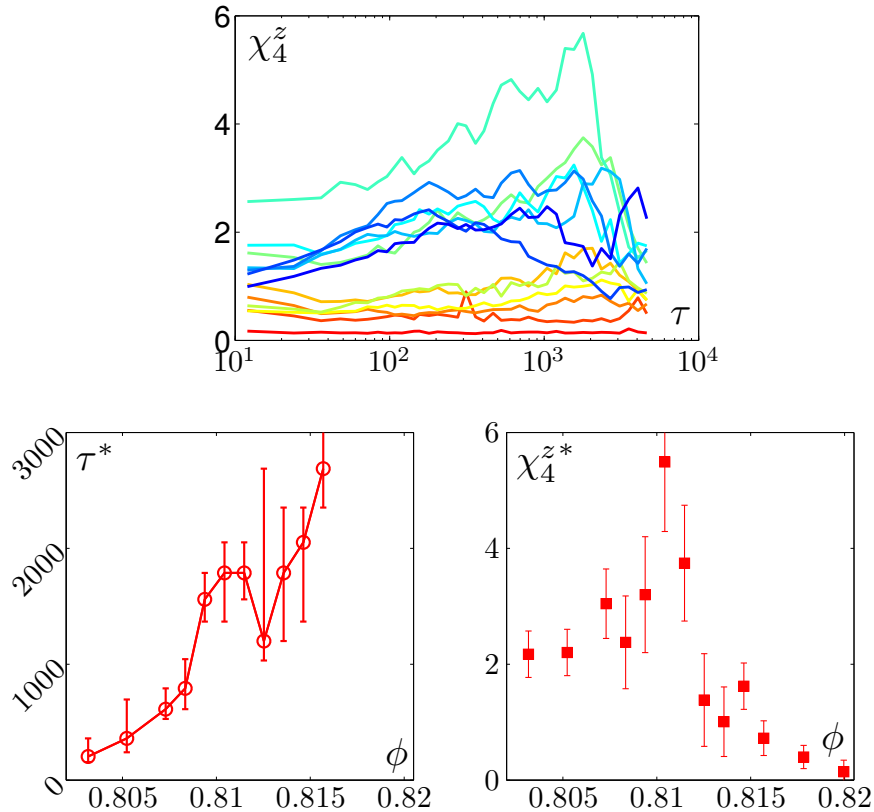


Figure 4.16: **Contact overlap susceptibility.** **Top:** Contact overlap susceptibility χ_4^z versus lag time τ . Color code spans from blue (low packing fractions) to red (high packing fractions) (See table 3.1). **Bottom left:** τ^* versus packing fraction ϕ . **Bottom right:** Maximum dynamical susceptibility χ_4^{z*} versus packing fraction ϕ

sociated to the jamming transition systematically occurs at a lower packing fraction than the structural crossover that has been observed above in this chapter, when studying the contact number.

Let's recall here that we had seen in the previous chapter maximal dynamical heterogeneities *of the displacements* at the same packing fraction ϕ^* . We plot in figure 4.17, bottom left, the maximum dynamical susceptibility *of the contacts* vs. dynamical susceptibility *of the displacements*. We see that they are nearly proportional, and, that the maximum dynamical susceptibility *of the displacements* is about twenty time larger than the maximum dynamical susceptibility *of the contacts*. Remember that the \square

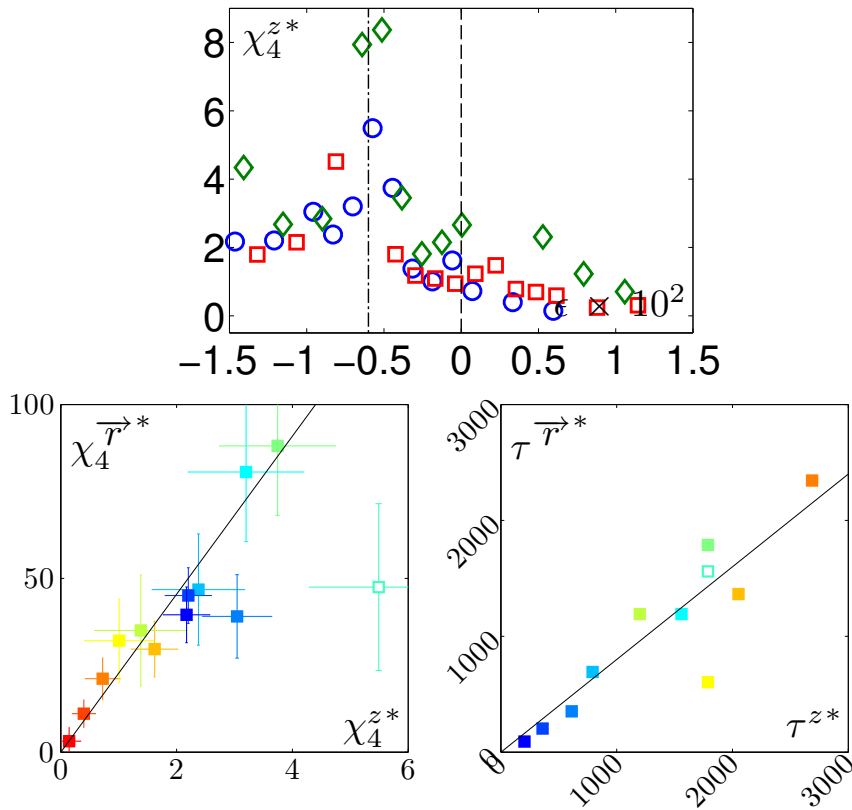


Figure 4.17: **Maximal dynamical contact susceptibility.** **Top:** χ_4^{z*} vs. reduced packing fraction ϵ for three distinct experiments. Each label is a different experiment. **Bottom left:** χ_4^{z*} vs. Maximal dynamical susceptibility *of the displacements* $\chi_4^{\vec{r}^*}$. The solid black line has a slope 23. **Bottom right:** time τ^{z*} of the maximal dynamical *contact* susceptibility vs. time $\tau^{\vec{r}^*}$ of the maximal dynamical susceptibility *of the displacements*. The solid black line has a slope 0.8. Color code spans from blue (low packing fractions) to red (high packing fractions) (See table 3.1).

data point has an anomalously low value of $\chi_4^{\bar{r}^*}$. We interpreted it as the signature of a lack of statistics close to the transition, where the size of the heterogeneities become extremely large. What is astonishing here is that this effect is not present in $\chi_4^{z^*}$. Still, $\chi_4^{z^*}$ is much smaller: hence, it does not suffer from the finite size effect we have described in section 3.4.4 for $\chi_4^{\bar{r}^*}$. We also plot the lag time at which the contact dynamical susceptibility *of the contacts* is maximum $\tau^{\bar{r}^*}$ vs. the time at which the contact dynamical susceptibility *of the displacements* is maximum τ^{z^*} on figure 4.17 bottom right. Despite the fluctuations, we see that $\tau^{\bar{r}^*}$ is proportional to τ^{z^*} with a coefficient close to 1.

4.4 Conclusion and comparison with the brass disks experiment

Having defined and measured the number of contacts per grains in this vibrated experiment, we have extensively studied the properties of the contact network. This part has revealed interesting features that we associate to signatures of jamming, but also that strongly resemble the phenomenology of the glass transition. We summarize them in figure 4.18 and recall them below:

- the study of the statics of the contact network reveals two geometric signatures of the Jamming Transition:
 - at ϕ_J :** the average number of contacts z strongly increases;
 - at ϕ^* :** the spatial correlation length of the contacts ξ_2^z is maximum

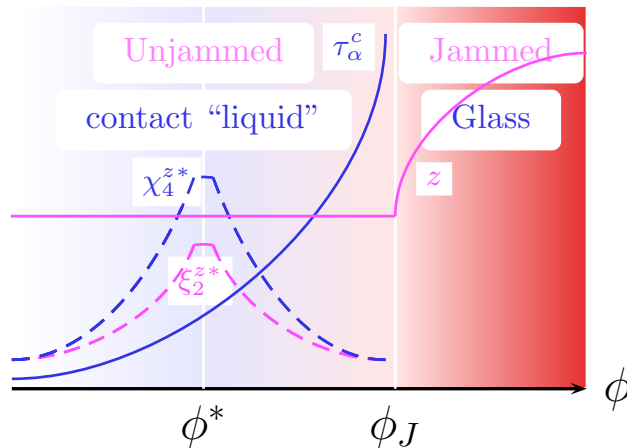


Figure 4.18: **Glassy dynamic of the contacts.** Scheme suggested by the results of this chapter. Contact statics observations are drawn in pink and Contact dynamic observations are drawn in blue.

- the dynamics of the contact network exhibits a glassy scenario that we interpret as two dynamical signatures of the jamming transition:
 - at ϕ_J :** The contact network relaxation time τ_α^c diverges;
 - at ϕ^* :** The relaxation of the contact network is maximally collective.

Remember that at the end of the previous chapter, we had recovered the results obtained during F. Léchenault’s PhD [Lechenault, 2007]: a dynamical crossover characterized by maximal dynamical heterogeneities of the displacements *on the contact scale* but no clear link with the force dynamics. In contrast, we have seen in this chapter that they were profoundly associated with both spatial correlations and dynamical heterogeneities of *the contact network*. The dynamical heterogeneities thus have their roots in an already existing spatial correlation which is amplified as time goes by, and such that they are maximum at an intermediate lag time. Furthermore, the system of photo-elastic disks differs from the brass disks also because it undergoes a geometric signature of jamming at a higher packing fraction. By contrast with the brass disks experiment, that could only access the region $\phi < \phi_J$, a packing of photo-elastic disks can actually cross the Jamming transition.

Nevertheless, some issues remain unresolved, and some questions remain to be addressed. In particular, the fact that dynamical heterogeneities of the displacements magnitude is about 20 times bigger than the dynamical heterogeneities of the contact is puzzling. Also, the fact that there are two signatures of the jamming transition appears as a stumbling block to a straightforward understanding of the interplay of these signatures with the critical a-thermal jamming transition. Two paths forwards seem possible:

- We saw in the previous chapter that the dynamical crossover at ϕ^* also coincides with the point at which static and dynamic pressures cross. Yet, the point at which they cross strongly depends on friction. What specific role does friction play in this case?
- We have seen that mechanical vibration gives rise to a complex dynamics. But what about its precise role? Is it reasonable to compare it with a true thermal agitation?

The glooming perspective of covering the edges of 10 000 disks, one by one with teflon to reduce inter-particle friction glides over the desperate Coërentin.

No! We claim here that both questions could be tackled by changing the vibration. Indeed, two scenarios can be imagined, and are represented in figure 4.19, where “temperature-density” phase space schemes are plotted.

figure 4.19 left: Friction is at stake: The split between the two crossovers has nothing to do with the agitation. As the vibration is reduced, the

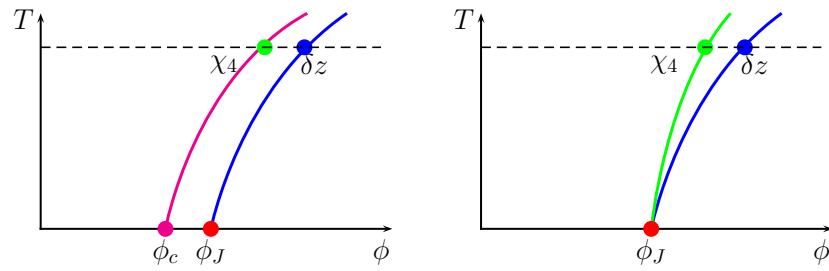


Figure 4.19: **Two possible scenarios when decreasing the “Temperature”.**

dynamical crossover would then tend towards a frictional transition point ϕ_c , that has nothing to do with the a-thermal jamming point.

figure 4.19 right: Vibration is at stake: The two crossovers converges toward the a-thermal jamming point.

In order to tackle this issue, we will, in the following chapter, investigate contacts statics and dynamics at various vibration magnitudes.

Chapter 5

Route towards zero temperature Jamming

In this chapter, we investigate the route to the zero vibration jamming transition by looking at the dependence of the properties of contact statics and dynamics on the vibration amplitude that control the jamming transition in the presence of vibration.

To this end, we first describe in detail the experimental protocol. In particular, we present a preliminary calibrating experiment in which we study the effect of the acceleration, Γ , of the bottom driving plate on the dynamics of a dilute system. We identify a clear threshold value of vibration magnitude Γ_0 below which no motion of the grains occurs, and which is due to static friction between grains and the bottom shaking plate. Above this threshold, we observe a random super-diffusive motion of the grains. We thereby define a reduced vibration magnitude γ , which falls to 0 when grains motion stalls. In addition, by using a minimal model for friction, we show that dynamic friction is likely to induce a random particle motion.

We then present results that are obtained in one experiment where we observe a shift of both geometrical and dynamical crossovers.

Finally, we compile the results of all the experiments and find that the two signatures tend to merge toward, and that the dynamical heterogeneities of the contacts tend to increase. We show that this effect is not present in the dynamic heterogeneities *of the displacements* because of finite size effects. We end this chapter by discussing recent observations of structural vestiges of a-thermal Jamming in numerical simulations of thermal colloids [Zhang et al., 2009, Wang and Xu, 2011].

5.1 Measuring the “zero temperature”

5.1.1 Experiment

Because of friction between the grains and the underneath vibrating glass board, there is a threshold acceleration at which grains move. We propose here to estimate experimentally the threshold value at which energy is injected to the grains. In other words, we would like to measure the “zero-temperature” of this system.

The very first thing we can easily do is to check the role of the vibration in the dilute regime. We perform an experiment at constant density $\phi = 0.05$, and we vary the frequency of the bottom plate oscillation. From image analysis and tracking procedures, we obtain particle trajectories. We first define the dimensionless acceleration magnitude

$$\Gamma = \frac{A\omega^2}{g}, \quad (5.1)$$

where $A = 5.10^{-3}$ m is the oscillation amplitude, ω the oscillation angular frequency and g the acceleration of gravity. We will, in this section, study different values of Γ by varying ω . From grains trajectories, we compute the temporal variance of their displacement in a lag time τ along shaking axis, $\text{var}_t \Delta X_i(\tau)$, and along transverse axis, $\text{var}_t \Delta Y_i(\tau)$. We then obtain

$$\Delta_X(\tau) = \frac{1}{N} \sum_{i=1}^N \text{var}_t \Delta X_i(\tau) \quad \text{and} \quad \Delta_Y(\tau) = \frac{1}{N} \sum_{i=1}^N \text{var}_t \Delta Y_i(\tau), \quad (5.2)$$

where N is the number of particles. We plot Δ_X (respectively Δ_Y) versus lag time τ for different accelerations Γ respectively in figure 5.1, top left (respectively top right). At low values of Γ , both Δ_X and Δ_Y are basically a plateau, which depends on the vibration amplitude. At higher values of Γ , the plateau duration becomes finite and the Δ_X and Δ_Y increase with lag time. Note that the motion is different in X and Y axis: particles move more and the plateau duration is shorter along the shaking axis (X). We report the crossover time τ_D for each direction in figures 5.1, top left and top right. Above, τ_D , we fit both the Δ_X and Δ_Y by

$$\Delta_X^f = D_X \tau^{H_X} \quad \text{and} \quad \Delta_Y^f = D_Y \tau^{H_Y}. \quad (5.3)$$

We plot in figure 5.1 top right H_X and H_Y vs. Γ . We see that the vibration $\Gamma_0 = 0.35$ marks the limit between a “vibrating” regime where $H_X = 0$ and $H_Y = 0$, and a super-diffusive regime where $H_X > 1$ and $H_Y > 1$. Note, that the value of Γ_0 is the same for both axis. The “vibrating” regime is actually due to noise in positions, and the value of the plateau is actually a measure of the noise. We see that it depends slightly on vibration frequency,

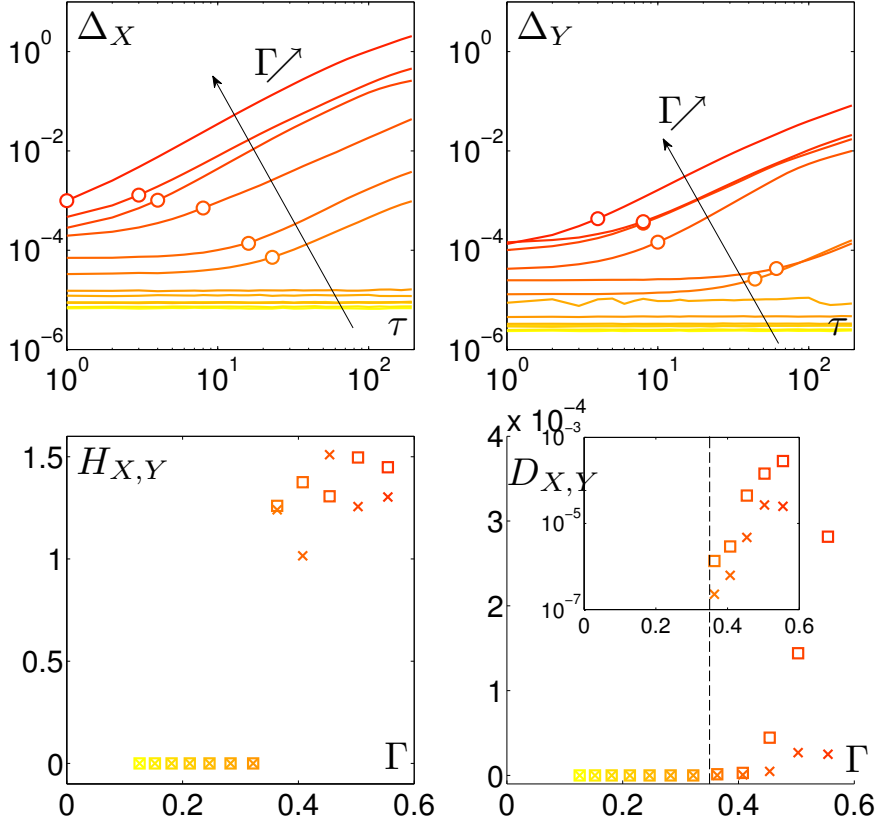


Figure 5.1: **Grain Diffusion properties.** **Top Left:** average variances of grains displacements Δ_X vs. lag time τ for different values of Γ . The \circ points denote the time above which the Δ_X are considered as linear with τ . **Top Right:** idem for Δ_Y . **Bottom Left:** Exponents H_X (\square) and H_Y (\times) vs. vibration magnitude Γ . **Bottom Right:** Diffusion coefficients D_X (\square) and D_Y (\times) vs. vibration magnitude Γ . **Bottom Right - Inset:** the same with the vertical axis on semi-log scales.

and that it is higher for the shaking axis. This must be due to blur that is more significant in the shaking direction and that increases as the speed of the grains increases, whereas the shutter speed of the camera remains constant. In contrast, in the super-diffusive regime, grains slip on the bottom plate because the acceleration overcomes the grain-plate friction force. Note, as $H_X \sim H_Y > 1$, that the “walk” is super diffusive in both axis. However, D_X is significantly higher than D_Y : this means that the grains move significantly more in the shaking than in the transverse axis.

The acceleration provided by the bottom plate is $\Gamma g \cos(\omega t)$. Yet, slip motion will be triggered as soon as the acceleration reaches $\mu_s g$, where μ_s is the grain-plate friction coefficient and g is the acceleration of gravity. We

thus have a measurement of $\mu_s = 0.35$ for the glass-PSM4 friction coefficient. What happens as soon as the grains slip on the plate is more complex, probably due to the fact that the friction coefficient changes as soon as there is slip. This may induce a super-diffusive random walk.

5.1.2 Simulation

Instead of making coarse assumptions, let's try to model simply and to simulate the motion of one grain in one dimension. To do so, we first a-dimensionnalize the accelerations $a/g \mapsto a$. We consider (see figure 5.2) a grain laying on an oscillating board that has an acceleration $a_{ie} = \Gamma \sin \omega t$. In the oscillating board frame, the grain has an acceleration a . The mechanical equilibrium for the grains on the horizontal axis thus is

$$a = \frac{F_T}{mg} - \Gamma \sin \omega t. \quad (5.4)$$

In order to describe the tangential force F_T , we simply use the Coulomb criteria :

$$\frac{F_T}{mg} \begin{cases} = -\mu_d & \text{if } v > 0 \\ < \mu_s & \text{if } v = 0 \\ = \mu_d & \text{if } v < 0 \end{cases}, \quad (5.5)$$

where v is the velocity of the grain in the board frame, μ_s and μ_d are respectively the static and dynamic friction coefficients, and $\mu_s > \mu_d$. We then implement equations 5.4 and 5.5 within an incremental loop, with $\Gamma = 0.7$, $\mu_s = 0.6$ and $\mu_d = 0.5$ (see appendix B.2 for details). We plot the acceleration of the board in figure 5.3 (a), the grain and of the board in figures 5.3 (b) and (c). A periodic acceleration made of stick and slip events sets in. This can be also seen in the time plot of velocity and position in figures 5.3 (d) and (e). Such motions have been observed in experiments in a similar system [Aumaitre et al., 2007]. The position of the grain is

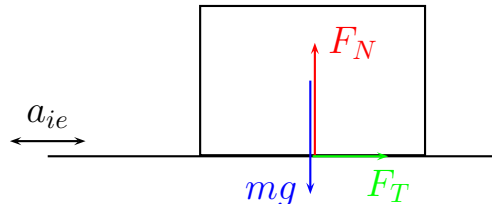


Figure 5.2: **Forces on a grain.** Scheme of a grain of mass m laying on a horizontally oscillating surface.

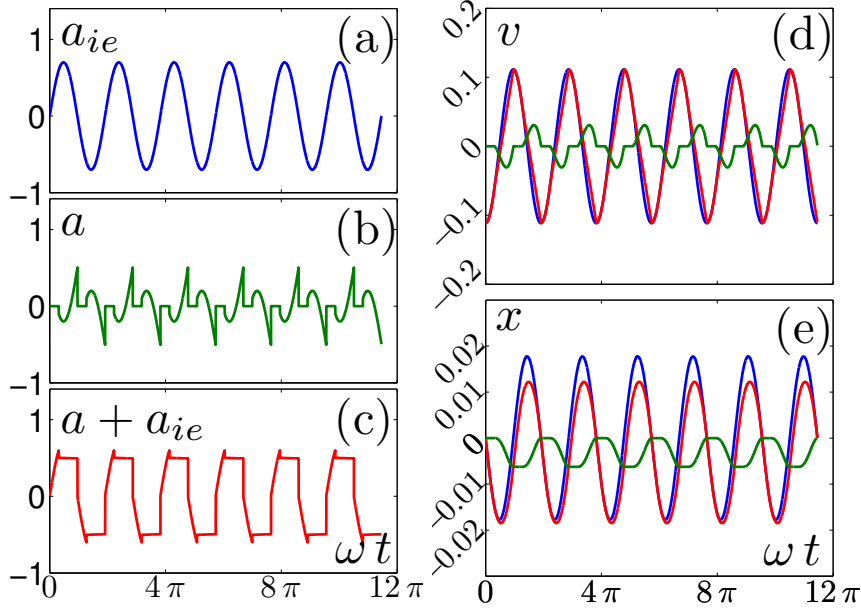


Figure 5.3: **Motion of a simulated grain.** (a) : Acceleration of the board. (b) : Acceleration of a grain in the board frame (c) : Acceleration of a grain in the laboratory frame. (d) : Velocity of the board (blue), Velocity of a grain in the board frame (green), and Velocity of a grain in the laboratory frame (red). (e) : Position of the board (blue), Position of a grain in the board frame (green), and Position of a grain in the laboratory frame (red).

therefore periodic. This is not what we observe in our experiment. On the contrary, we observe a clear drift of the positions. This drift may originate in some inhomogeneities of the dynamic friction coefficient, that drives the “braking” time of the grains, and can only be triggered as soon as the grains start to slip.

In order to ensure this, we add a gaussian noise of standard deviation 0.02 on μ_d and perform the simulation for Γ ranging between 0.1 and 1. We record the position of the grains at one phase of the vibration X . In order to mimic noise detection on grain position, we also add a gaussian noise of standard deviation 5.10^{-5} on grain position X . From these trajectories, we compute the temporal variance $\text{var}_t \Delta X(\tau)$ of the grain displacement in a lag time τ . We perform the simulation 50 times and we compute

$$\Delta(\tau) = \frac{1}{N_s} \sum_{s=1}^{N_s} \text{var}_t \Delta X(\tau), \quad (5.6)$$

where $N_s = 50$ is the number of simulations. We then plot Δ vs. lag time in figure 5.4, left. We see two families of curves:

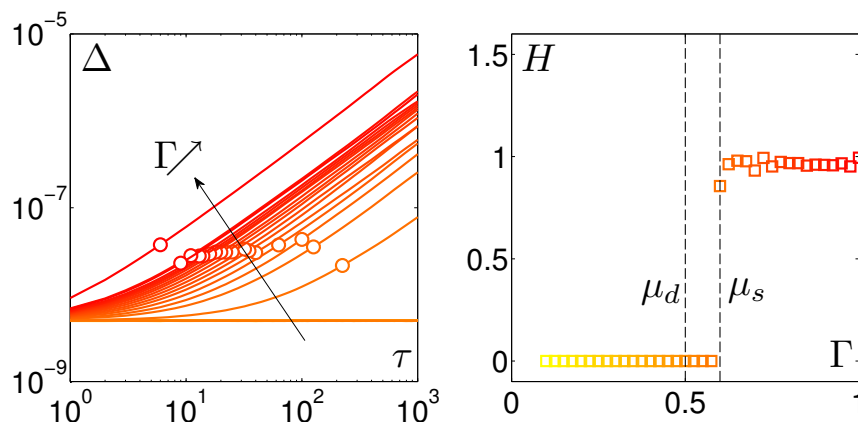


Figure 5.4: **Simulated grain diffusion properties.** **Left:** Mean square displacements vs. lag time τ for different values of Γ . The \circ points denote the time above which the Δ are considered as linear with τ^H . **Right:** Value of the exponent H vs. vibration magnitude Γ .

- Those that have a constant Δ with lag time. The value of this plateau is due to the detection noise we have added. Their corresponding Γ is lower than μ_s .
- Those that have a linear increase of the Δ with lag time. The position of the grain diffuses.

We thus see that the noise on the friction coefficient systematically leads to a drift of particles. This drift resembles a diffusive process with an exponent H that is reported versus Γ in figure 5.4, right. We see that for $\Gamma > \mu_s$, H jumps to 1. The drift is a diffusive walk. We do not find the same exponent as in our experiment. This may have to do either with our choice of the very simplified noise model for the dynamic friction coefficient, or with some asymmetry of the external forcing. Despite this difference, we see the same two regimes, and we can claim that a “zero temperature” is associated with the slipping criteria.

To conclude, we have observed a clear threshold value of the acceleration vibration above which there is a super-diffusive dynamics of the grains. We won’t dwell on the peculiar dependence on vibration acceleration because it is strongly dependent on the density, and, we will consider in the following much higher densities. On the contrary, we don’t expect that the slip threshold is changed by density. Hence, the key message of this section is the measurement of the minimum acceleration at which grains slip: $\Gamma_0 = 0.35$, that is associated to the threshold pulsation $\omega_0 = \sqrt{\Gamma_0 g / A} = 26.2$ rad/s, corresponding to a frequency $f_0 = 4.17$ Hz. In the following, we shall consider the reduced vibration frequency

$$\gamma = \frac{\omega - \omega_0}{\omega_0} \quad (5.7)$$

as a measure of the vibration in our system.

5.1.3 Protocol

We chose to perform *two experiments in one* as represented in figure 5.5; we investigate two magnitudes of vibration at the same time. We systematically take $\gamma_1 = 1.4$ and we will try to vary γ_2 as much as possible. All the investigated values of the parameter space are represented in figure 5.5. This allows us to compare directly the effect of vibration on statics and dynamics of the contact in the first section. We then compile all the experimental results.

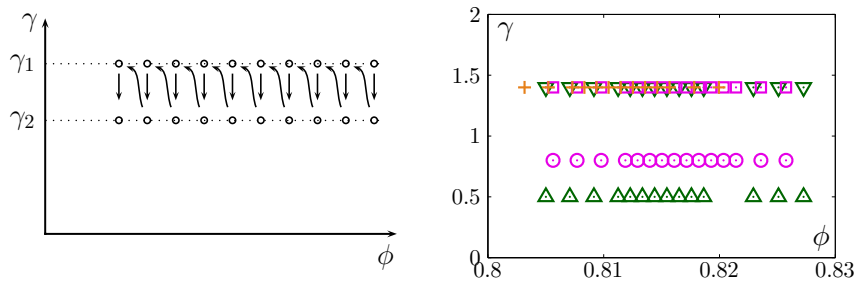


Figure 5.5: **Experimental Protocol.** **Left: principle of the protocol:** Each circle represents a measurement of about 10 000 cycles and is a data point, and the arrows represent the “path” we follow. **Right: all the data points** Parameters in $\gamma - \phi$ space. Same color labels correspond to one experimental run. Each label correspond to a single experiment within these runs.

5.2 The effect of vibration on the absolute values of ϕ_J and ϕ^*

In order to study the dependence of ϕ_J with respect to γ , we plot in figure 5.6 (a) the average number of contact vs. packing fraction for two vibrations $\gamma = 1.4$ and $\gamma = 0.8$ in the same run. The kinks in the curve occur at two different packing fractions, and ϕ_J is higher for higher vibration, γ . In addition, we plot in figure 5.6 (c) the average number of contact vs. packing fraction for two vibrations $\gamma = 1.4$ and $\gamma = 0.5$ in the same run. This time, the two values of ϕ_J are nearly the same, and no clear effect of vibration is seen. Altogether, there is no clear trend of a systematic shift of ϕ_J with vibration. We now turn to the study of the dependence of ϕ^* on γ . To this end, we plot ϕ^* versus packing fraction for two vibrations $\gamma = 1.4$ and $\gamma = 0.8$ in the same run. We first see that the magnitude of the maximum is higher for $\gamma = 0.8$ than for $\gamma = 1.4$. The location of ϕ^* is associated with the same experimental data point so that no clear shift of ϕ^* occurs. Again, we compare with the second experimental run for two vibrations $\gamma = 1.4$ and $\gamma = 0.5$, and again we see that the magnitude of the maximum is higher for

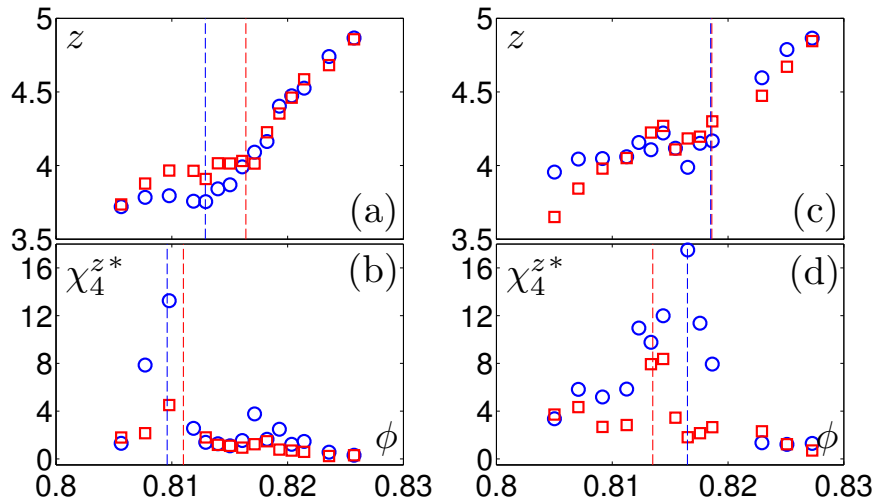


Figure 5.6: **Shift of ϕ_J and ϕ^* .** **Top: Shift of ϕ_J with vibration.** (a): Average number of contacts vs. packing fraction for $\gamma = 1.4$ (\square), and for $\gamma = 0.8$ (\circ). (c): Average number of contacts vs. packing fraction for $\gamma = 1.4$ (\square), and for $\gamma = 0.5$ (\circ). The vertical lines with the same color codes indicate the respective locations of $\phi_J(\gamma)$. **Bottom: Shift of ϕ^* with vibration.** (b): Maximal contact dynamical susceptibility vs. packing fraction for $\gamma = 1.4$ (\square), and for $\gamma = 0.8$ (\circ). (d): Maximal contact dynamical susceptibility vs. packing fraction for $\gamma = 1.4$ (\square), and for $\gamma = 0.5$ (\circ). The vertical lines with the same color codes indicate the respective locations of $\phi^*(\gamma)$.

5.2. THE EFFECT OF VIBRATION ON THE ABSOLUTE VALUES OF ϕ_J AND ϕ^* 153

lower γ . However, the location of ϕ^* has increased with increasing vibration.

To conclude this section, the magnitude of the dynamical heterogeneities of the contact increases significantly as the vibration is reduced. However, we see here that no systematic effect on the location of ϕ_J and ϕ^* appears when the vibration is changed. We actually observe opposite effects for the two different experimental runs we have performed. It is also difficult to directly compare the values of ϕ_J and ϕ^* between the different experimental runs.

5.3 Merging crossovers and the Increasing fluctuations

We use here the reduced packing fraction

$$\epsilon = \frac{\phi - \phi_J}{\phi_J}, \quad (5.8)$$

introduced in the previous chapter, and we plot both the average number of contacts z and the maximum dynamical susceptibility of the contact χ_4^{z*} in figure 5.7, for the different values of γ . We see very clearly that amplitudes of the maximum increase as the vibration is reduced, and that their location $\epsilon^* = \frac{\phi_J - \phi^*}{\phi_J}$ tends towards zero.

We then report $|\epsilon^*|$ vs. vibration magnitude γ in figure 5.8, left. We see an increase: the crossovers tend to merge. Of course, the data spans over less

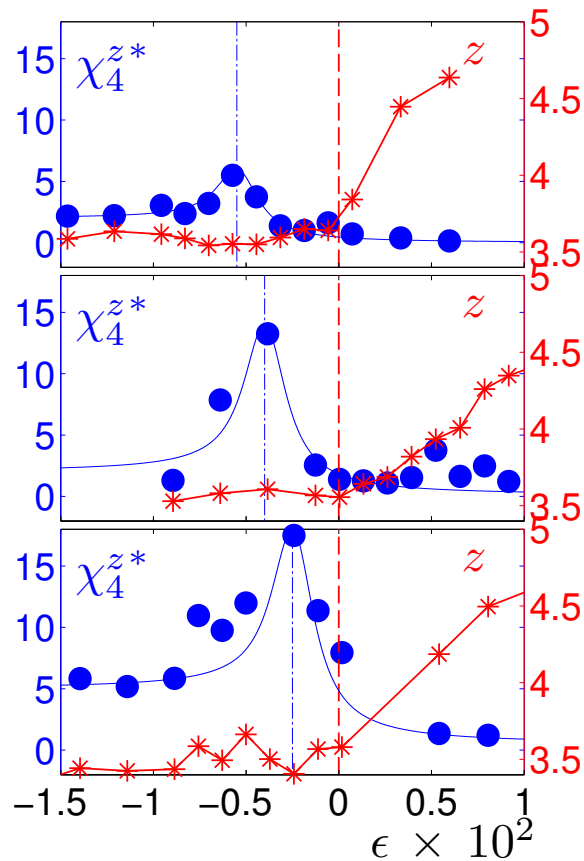


Figure 5.7: **Approaching the zero vibration.** Maximum dynamical susceptibility of the contacts χ_4^{z*} (left axis) and average number of contacts z (right axis) versus reduced packing fraction ϵ for $\gamma = 1.4$ (**top**), $\gamma = 0.8$ (**middle**) and $\gamma = 0.5$ (**bottom**).

than a decade, so a fit is a little bit provocative. Yet, the simplest functional dependence we observe is consistent with a linear increase. We now turn to the study of the amplitude of the maximum $\max \chi_4^{z*}$ with respect to vibration magnitude γ . It significantly increases as vibration is reduced and is consistent with an inverse power law. This is the key result of this chapter: as the vibration is reduced, the two crossovers tend to merge and the fluctuations tend to diverge. The data points in the parameter space $\gamma - \epsilon$ are summarized in figure 5.8, bottom.

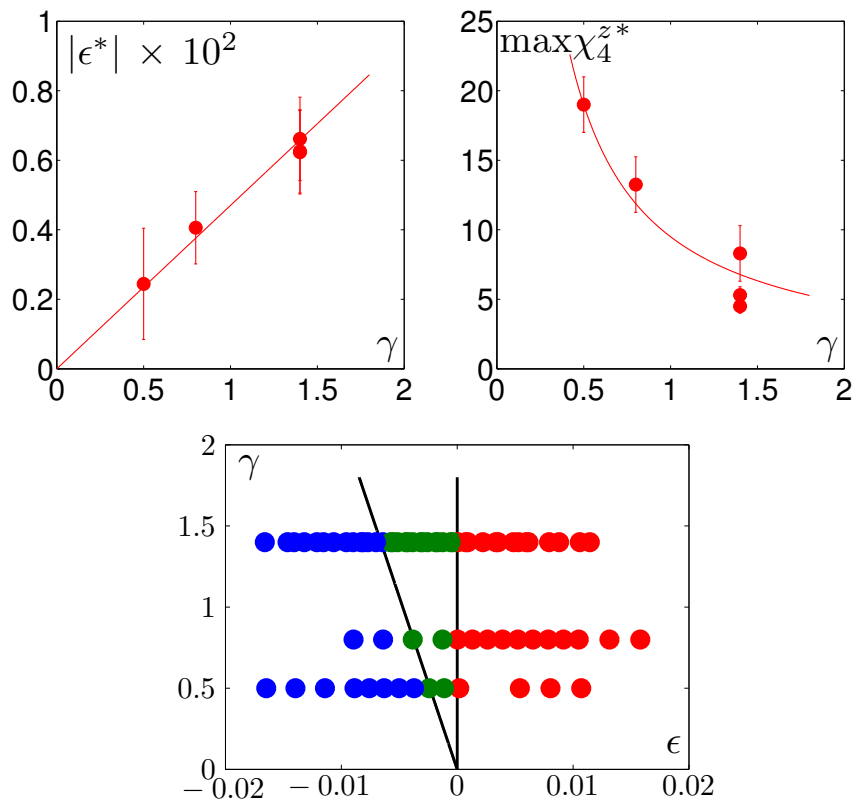


Figure 5.8: **Approaching the zero vibration.** **Top Left:** Split $|\epsilon^*|$ vibration magnitude γ . The solid line is a linear fit. **Top Right:** Peak of the maximum dynamical susceptibility of the contacts $\max \chi_4^{z*}$ vs. vibration magnitude γ . The solid line is an inverse function fit. **Bottom:** Parameters space $\gamma - \epsilon$, each point is a data point, they are represented in red for $\epsilon > 0$, in green for $\epsilon^* < \epsilon < 0$, and in blue for $\epsilon < \epsilon^*$.

5.3.1 Finite size effects

We now can address the question of the difference between the dynamical susceptibility of the contacts and the dynamical susceptibility of the displacements. We have indeed already seen in the previous chapter that the maximal dynamical susceptibility of the contacts has a much lower magnitude than the maximal dynamical susceptibility of the displacements for $\gamma = 1.4$. What about different magnitudes of vibration? We plot the maximum dynamical susceptibility of the displacements $\chi_4^{\vec{r}^*}$ versus the maximum dynamical susceptibility of the contacts $\chi_4^{z^*}$ for different vibration magnitudes in figure 5.9, top. We see that experiments at $\gamma = 1.4$ already displayed in the previous chapter lie on a line. The results at $\gamma = 0.8$ still increase, but are not linear anymore and more scattered. Finally, the results at $\gamma = 0.5$ do not even decrease. We report in figure 5.9, bottom, the maximum of $\max \chi_4^{z^*}$ versus γ and the value of $\chi_4^{\vec{r}^*}$ at ϕ^* , the density at which $\chi_4^{z^*}$ is maximum versus γ . $\chi_4^{\vec{r}^*}(\phi^*)$ does not increase as the vibration magnitude is decreased. For the two highest values of γ , it follows the same trend as $\chi_4^{\vec{r}^*}$. However, it seems to saturate at the lowest γ value. We interpret it as a finite size effect due to limitation of the statistical estimator. The maximal magnitude of dynamical heterogeneities of the displacements is indeed approximately 70, *i.e.* 8% of the system size. If the size of dynamical het-

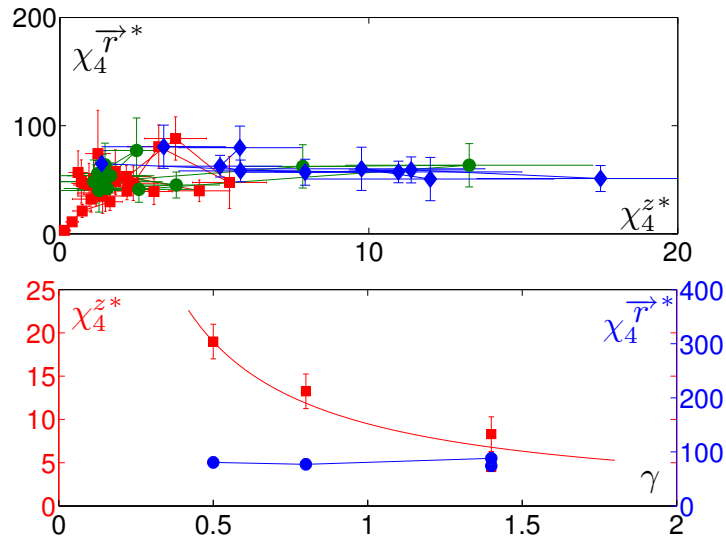


Figure 5.9: **Finite size effects.** **Top:** Maximum dynamical susceptibility of the displacements $\chi_4^{\vec{r}^*}$ vs. maximum dynamical susceptibility of the contacts $\chi_4^{z^*}$ for different vibration amplitudes $\gamma = 1.4$ (■), $\gamma = 0.8$ (●) and $\gamma = 0.5$ (◆). **Bottom:** Peak of the maximum dynamical susceptibility of the displacements $\max \chi_4^{\vec{r}^*}$ (●) and peak of the maximum dynamical susceptibility of the contacts $\max \chi_4^{z^*}$ (■) vs. vibration magnitude γ . The solid line is an inverse power law fit with exponent 1.

erogeneities gets bigger, the statistical estimation of these heterogeneities is doomed to failure because of a lack of statistics. Therefore, the increase of dynamical heterogeneities of the contacts will not be accompanied by a similar increase of the dynamical heterogeneities of the contacts. Finally, the use of the dynamical heterogeneities of the contact has allowed us to observe the merging crossovers and the increasing fluctuations as the vibration is reduced.

5.4 The Widom lines for Jamming

5.4.1 Widom lines for the liquid gas critical point

Our present observations are reminiscent of the so-called *Widom lines* observed in the super critical gas phase, close to the liquid gas critical point. Such lines are the loci of the maximum of the thermodynamic susceptibilities. As the critical point is approached, these lines tend to merge and the susceptibilities tend to diverge at the critical point. A recent extensive numerical study of a Lennard-Jones liquid close to liquid gas critical point has been performed by Brazhkin et al. [2011]. We plot in figure 5.10 (a-b)

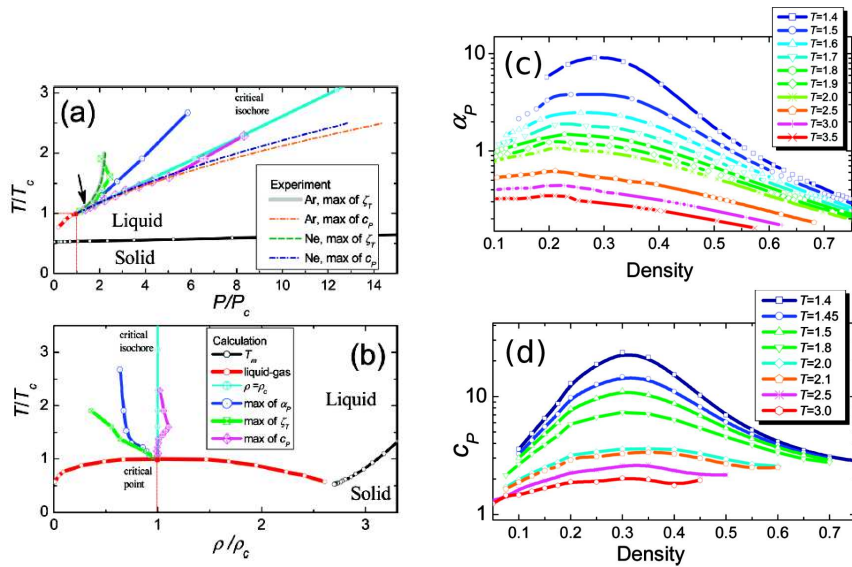


Figure 5.10: **Widom lines for Liquid-gas critical point.** (a) and (b): Phase diagrams (temperature-pressure), on (a), and (temperature-density), on (b) for simulations of a Lennard-Jones liquid. The lines represent loci of maximum thermal expansion α_P (\odot), density fluctuations ζ_T (\boxtimes) and isobaric thermal capacity c_P (\diamond). Extracted from Brazhkin et al. [2011]. (c) and (d): thermal expansion coefficient α_P (c) and isobaric heat capacity c_P (d) versus density for different temperatures. $\rho_c = 0.314$ and $T_c = 1.31$ are the values of the density and of the temperature at the critical point.

the *Widom lines* the authors have obtained both in Temperature—Pressure (a) and in Temperature—Density (b) phase spaces. We see that these lines tend to merge as the critical point is approached. Furthermore, we plot in figures 5.10 (c-d) the density dependence of the thermal expansion coefficient α_P (c) and isobaric heat capacity c_P (d) versus density for different temperatures. We see that the maximum of these susceptibilities increase as the temperature, is reduced towards the critical temperature $T_c = 1.31$. This is a clear illustration of Widom lines in the supercritical phase. Note that recent experiments [McMillan and Stanley, 2010, Simeoni et al., 2010] probing the dispersion of nanometric acoustic waves induced by inelastic X-Ray scattering report a crossover of the acoustic dispersion at one of the Widom lines, namely the one defined by the maximum of the isobaric heat capacity c_P . This work demonstrates the existence of a dynamical crossover involving subtle mechanisms at the particle scale in the supercritical region of the liquid gas critical point, which can be foreseen by thermodynamics, since the Widom lines can be computed from renormalization group theory [Callen, 1985, Goldenfeld, 1992].

5.5 Conclusion and comparison with related work

As explained in the introduction, the thermodynamics of the Jamming transition has been investigated recently [Berthier et al., 2011c] and yielded a theoretical prescription for the scalings of the peak of the pair correlation function and the pressure. We stress here that the jamming transition is not indicated by a divergence of the same thermodynamic susceptibilities but by a maximum of the first peak of the pair-correlation function.

We present in figure 5.11, the phase space suggested by the experimental results. This scenario is similar to what is observed in critical phase

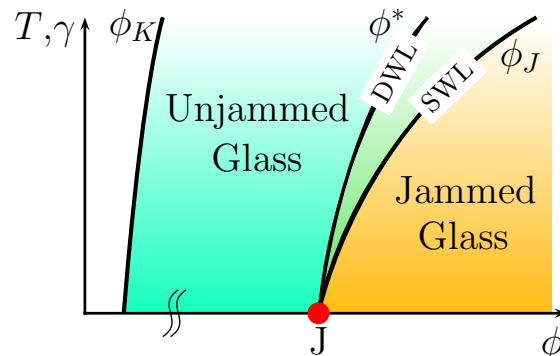


Figure 5.11: **Approaching the zero vibration.** SWL stands for Static Widom Line and depicts the static crossover ϕ_J . DWL stands for Dynamic Widom Line and depicts the dynamic crossover ϕ^*

transitions. In the vicinity of a critical point, the various susceptibilities divergences turn into finite maxima, whose locations tend to split on different lines as the system is moved into the super-critical region. Of course, there is no evidence that the quantity we consider can be matched to thermodynamic susceptibilities, and that the crossovers we observe match the *Widom lines*. But the fact that the fluctuations increase is very reminiscent of what is observed in Brazhkin et al. [2011]. Note that different lines have been observed recently in simulations of colloids [Wang and Xu] in the presence of temperature. These authors claim that the lines correspond to different signatures of Jamming. We plot them in figure 5.12. In particular, the black line of the plot has several signatures: (i) the variance of the instantaneous average of the contacts, $z(\bar{t})$, is maximal, (ii) the first peak of the pair correlation function is maximum, (iii) the scaling $p/\phi^2 \sim \phi - \phi_c$ sets in. The red line is signed by two signatures: (i) the average number of contacts is equal to its isostatic value 6, (ii) the density of states becomes flat. Apart from the temporal variance of the instantaneous average number of contacts, the quantities that have been investigated are different from our experiment. Still, there is a common phenomenology.

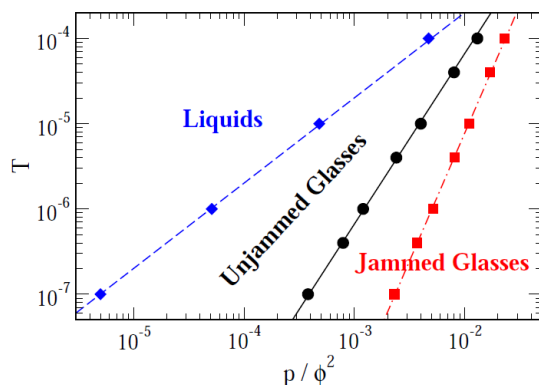


Figure 5.12: **Different lines.** Phase space observed of thermal colloids: Temperature vs. pressure over density. Note that $p/\phi^2 \sim \phi - \phi_c$, where ϕ_c is the jamming packing fraction. Extracted from Wang and Xu.

Chapter 6

Conclusion and perspectives

We have studied the Jamming transition of a vibrated two-dimensional dense packing of soft grains. To do so, we have adapted an existing setup to shake a 2D layer of photo-elastic disks at different densities, and to measure particle positions and contact forces.

By measuring the average number of contacts, which undergoes a kink at a packing fraction ϕ_J , we have identified two regions: a jammed region at packing fractions $\phi > \phi_J$ and an unjammed region at packing fractions $\phi < \phi_J$. While the properties of the contact network of the Jammed region are consistent with the results of the literature, we observe non-trivial dynamics in the unjammed region. First, maximum dynamical heterogeneities are observed at a packing fraction ϕ^* , that is distinct and lower than ϕ_J . These dynamical heterogeneities are observed when probing the dynamics at a length scale 100 times smaller than grain size. Second, contacts dynamics also exhibit a maximum heterogeneity at ϕ^* on long time scales. Therefore, dynamical heterogeneities of the displacements and dynamical heterogeneities of the contacts are closely related. We have further shown that when the mechanical agitation $\gamma \rightarrow 0$, the gap $\phi_J - \phi^* \rightarrow 0$ and $\chi_z^* \rightarrow \infty$, thus suggesting that the two crossovers are two distinct vestiges of the a-thermal Jamming transition.

6.1 A dynamical transition of contacts at ϕ^*

Previous work by the group [Lechenault, 2007] had seen a maximum of dynamical heterogeneities at an intermediate packing fraction ϕ^* , but they couldn't fully appreciate the fact there were two crossovers associated with Jamming. Experiments in hard colloids also report a non-monotonic behavior of dynamic heterogeneities [Ballesta et al., 2008]. Both observations can be understood in the light of what we have observed in the photo-elastic soft grains: there are actually two distinct crossovers related to the zero temperature Jamming, and we believe that what has been reported

in these works is the dynamical one occurring at ϕ^* . Along the way, we have seen that studying a system made of soft particles allows one to understand better hard particles systems. As a similar approach has been used by Berthier and Witten [2009a,b] to study the glass transition of hard and soft grains. It seems that doing soft to understand hard is a seminal approach.

We now discuss a number of open issues and the possible paths to follow to address them.

6.1.1 Spatial origin of dynamical heterogeneities

The microscopic correspondence between the dynamical susceptibility of the contacts and that for the displacements remains to be addressed. We have seen that, although weak, maximal spatial static correlations of the contacts are also observed at ϕ^* . This suggests that the long time dynamical correlations of the contacts originates in the statics. How the dynamical correlations build themselves and amplify from the statics is an open question. As a first step, we have attempted to study forces loops, and to see if there is any correlation with the dynamics, but this work is still in progress.

6.1.2 Link with the vibrational modes

An other path to explore would be to question any possible link between the dynamical heterogeneities and the vibrational modes of the network. Vibrational modes of a-thermal jammed packings are indeed directly linked to the structure and we have seen in section 1.1.3.1 that a diverging length can be constructed out of them. However, the dynamical heterogeneities are seen in the unjammed phase, in the presence of mechanical agitation. Therefore, it is conceptually difficult to directly match them to the vibrational properties of a-thermal soft spheres. This difficulty has been overcome by Brito and Wyart [2006] in a study of the vibrational properties of weakly thermal hard disks system. From the collisions of the grains, the authors defined an effective number of contacts and an effective inter-particle potential. They thus could study the vibrational properties of this effective solid. Studying the vibrational properties and studying its relationship with the dynamical heterogeneities has actually been attempted by Henkes et al. [2012] on the brass disk experimental data. The idea can be summarized as follows: from the fluctuations of the particles, under the assumption that the packing is a linear elastic solid, *i.e.* that the particles fluctuate in a gaussian manner around well defined positions, the displacement cross correlation matrix eigenvalues and eigenvectors give the vibrational modes of the solid. Yet, they found that, as the packing density was decreased toward ϕ^* , the fluctuations depart from gaussian on long timescales. Therefore, in the brass disks system, the dynamical crossover at ϕ^* cannot be related to

the vibrational modes of the system. Nevertheless, preliminary tests on displacement distributions seems to indicate that in the case of photo-elastic disks, the vibrations are more gaussian. Hence, trying to compute the modes in the soft grains packing could be an encouraging perspective.

6.1.3 Exploring the glass phase

Let's recall here that below ϕ_J , there is a significant relaxation of the dynamics on tiny length scale (10^{-2} grain diameter). Yet, these relaxations share similar properties and can be rescaled to a master curve: we can use the relaxation at a tiny length to extrapolate to the relaxation at the grain scale. This leads to a typical relaxation time which is huge, but not infinite. Therefore, in this experiment, there is a dynamics for $\phi < \phi_J$: the Jamming onset and the divergence of the relaxation timescale seem to coincide. This is in disagreement with the replica theory of the glass transition proposed by Parisi and Zamponi [2010], where the Jamming transition occurring at ϕ_J is distinct from the glass transition at ϕ_0 . Where does the discrepancy originate from?

- Is it because ϕ_0 and ϕ_J are so close, as displayed in table 1.1, that we cannot separate them experimentally?
- Is it a finite size effect? In other words, because the system size is finite, it cannot remain forever trapped in one glassy state?

In order to tackle those questions, further experiments/numerics on agitated soft particles would be necessary. And only a non mean-field dynamical theory would give answers to such questions.

6.2 A spin glass transition of contacts at ϕ_J ?

6.2.1 Our observations

We summarize our key observation on the dynamics of the contacts: the features of the contact overlap structure factor defined in equation 4.8 are represented in figure 4.12. For $\phi > \phi_J$, it remains constant, at a certain height, which decreases with packing fraction, there is a short time relaxation, whose magnitude depends on packing fraction. For $\phi < \phi_J$, a long time relaxation sets in, with a typical decay time that decreases as the packing fraction is reduced.

6.2.2 Spin-glasses phenomenology

A similar scenario has been reported in spin glasses [Binder and Young, 1986, Castellani and Cavagna, 2005]. Spin glasses are dilute metallic alloys with a structural disorder and with strong short range magnetic in-

teractions. It is the interplay of disorder with the interactions that creates random interactions, and that gives rise to frustration: all the magnetic interactions cannot be satisfied at the same time. Frustration and disorder are the two key ingredients of spin glasses. Originally introduced by Edwards and Anderson [1975] (EA model), models of spins glasses were extensively studied in the late 70's and in the 80's. A simpler version of the EA model—the SK model—was proposed by Kirkpatrick and Sherrington [1978]. Still too complicated to solve, it was generalized by Derrida [1980] to give the p -spin model. Of course, the details of the dynamics are specific to each model, but a common phenomenology is often observed: as the temperature is decreased, spin-glasses go from a paramagnetic phase to a spin-glass phase with an increasing relaxation time. Both these phases have a zero magnetization. Therefore, unlike non-random Ising Ferromagnets, the magnetization is not an appropriate order parameter. A proper order parameter is the so-called Edwards-Anderson order parameter q_{EA} . Besides its thermodynamic definition, it can be defined in terms of dynamics by the infinite time limit of the spin-spin self-correlation. However, the finiteness of experiments or numerical simulations precludes a straightforward measurement of q_{EA} as a *infinite time limit* and dooms us to measure a *large time limit*. As an illustration, we plot in figure 6.1 left the spin spin self-correlation, a two dimensional nearest-neighbor Gaussian Ising spin glass. It decreases all the more quick as temperature is increased. We represent in figure 6.1, right, q_{EA} from a similar simulation performed at various densities. We see that, in the paramagnetic phase, at high temperatures, $q_{EA} = 0$, and in the spin glass phase, at lower temperatures, $q_{EA} > 0$.

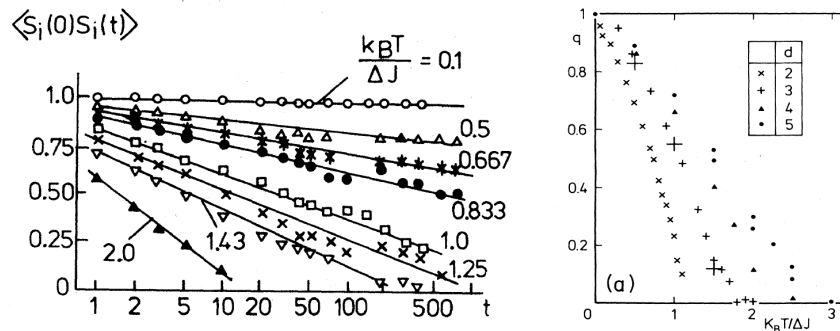


Figure 6.1: **Spin glass order parameter.** **Left:** Spin-spin self-correlation function vs. time for a two dimensional nearest-neighbor Gaussian Ising spin glass on a square lattice of size 24×24 . **Right:** Edwards-Anderson order parameter after an observation time of $t_{obs} = 2000$ Monte Carlo steps plotted vs. temperature for nearest-neighbor Gaussian Ising spin glass with symmetric Gaussian interaction at various dimensions d . Adapted from Binder and Young [1986].

6.2.3 The analogy

Strikingly, the spin-spin self-correlation of spin glasses and the dynamical overlap function of the contacts share similar features (see appendix C.2). It is therefore tempting to propose an analogy between our system, where the positions or the particles remain frozen, and a system of spins.

We represent in figure 6.2 an experimental snapshot of grains: each neighbor relationship can be seen as a spin variable represented by an open circle, which can have either a value 1 if there is a contact or -1 if there is no contact. Each grain links several contacts and can be seen as a constraint, represented by a solid square. This constraint must be imagined as a coarse-grained scalar version of the mechanical equilibrium of each grain. Within this analogy, each variable is linked to two constraints and each constraint is linked to several variables, which depend on the number of neighbors. As for dilute metallic alloys, the quenched disorder comes from the structural disorder of particle positions and the neighborhood network is fixed. However, instead of modeling it by random couplings, what is random in the present analogy is the connectivity around each constraint. If this analogy yields consistent results, our experiments could be seen as an experimental realization of a macroscopic spin-glass: a *granulo-spin glass*.

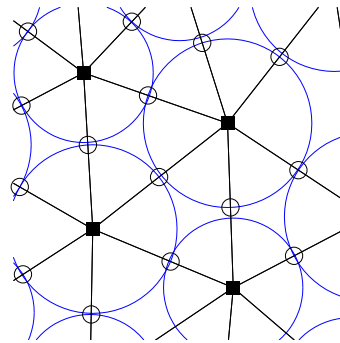


Figure 6.2: **Mapping granular packing with a spin system.** Blue circles are grains, black open circles are neighborhood relationship and

6.3 The route towards a-thermal Jamming

As the mechanical agitation is reduced, we have observed that the dynamic and the static crossover merge, *i.e.* $\phi_J - \phi^* \rightarrow 0$, and that the dynamical heterogeneities of the contacts diverge, *i.e.* $\chi_4^{z*} \rightarrow \infty$. The unjamming a-thermal point is defined by the number of contacts, which drops from z_J to zero, and is associated with a diverging length. We have observed here, how the presence of agitation blurs the singular nature of the Jamming point, and how it gives rise to a complex dynamics of the contact network, which is governed by the proximity of the Jamming point. We not only have observed a structural “vestige” of the Jamming transition; we have also awakened a “sleeping vestige” by agitation, namely the heterogeneities of the contact dynamics, which in essence are absent for a-thermal systems.

Numerical and theoretical [Zhang et al., 2009, Jacquin et al., 2011],

[Berthier et al., 2011c] works have addressed soft spheres close to Jamming in the presence of thermal agitation. These works have reported a static crossover related to the Jamming transition: the pair correlation function has a delta peak at Jamming; adding temperature transforms the delta peak into a maximum whose height decreases with temperature and whose location increases above the Jamming density. In addition, there also have been experimental works on colloids [Zhang et al., 2009] and grains [Cheng, 2010] addressing the structural vestige of the Jamming transition. Should the mechanical agitation not be a true thermal agitation, our work is nevertheless the first experimental work where a structural signature is observed for various agitation magnitudes, that merge toward a dynamical signature at the zero agitation limit.

This calls for a numerical characterization of such a dynamical signature in the contact network, for instance in a soft spheres with temperature. This is indeed a commonly studied system [Berthier et al., 2011c, Otsuki and Hayakawa, 2011, Wang and Xu, 2011, Zhang et al., 2009].

6.4 Active matter

As a matter of fact, one might think of a different way to inject energy in systems close to Jamming. Imagine that each grain has its own engine, such that it develops its own motion, instead of converting it from the bottom plate. This way of driving the system only changes the way grains receive energy, but would probably not drastically affect their global behavior. However, imagine now that we go one step away from the thermal system by imposing some directed motion to the grains. This can be done for instance by breaking the symmetry of each individual grain as done by Kudrolli et al. [2008] and Deseigne et al. [2010, 2012]. One then enters the so-called field of active matter with its own debates and issues: there are a few experiments and most theoretical results tackle point particles. More relevant to our Jamming concerns are the work of Deseigne et al. [2010, 2012]— who addressed the role of hard core repulsion— and Henkes et al. [2011]—who addressed the interplay of the onset of collective motion with the Jamming transition. All of these debates call for further experiments, and a possible perspective would be to design anisotropic self-propelled soft grains.

6.5 Towards rheology

So far, we have discussed the structural properties and the “spontaneous” dynamics of our system where contacts happened to be crucial. It would also be interesting to consider response functions. In particular, what about response to shear and flow properties of such systems?

The flows of a-thermal disordered materials close to Jamming have shown to exhibit complex behavior and have motivated active theoretical research [Cates et al., 1998], [Sollich et al., 1997], [Hébraud and Lequeux, 1998], [Bocquet et al., 2009]. Above the Jamming point, Tighe et al. [2010] established a complex flow curve characterized by various scaling regimes that crucially depend on the microscopic details, and in particular, how energy is dissipated. Below the Jamming threshold, Lerner et al. [2012] performed recent simulations of sheared viscously damped 2D disks and have understood and characterized the flow properties in terms of contact network elasticity that recover recent results on sheared immersed grains [Boyer et al., 2011].

In addition, recent experiments performed by Nichol et al. [2010] and Reddy et al. [2011] addressed the effect of an external perturbation on the flow properties. These experiments can be described as follows: in a sheared granular system rotating at an angular velocity Ω , either regular or split-bottom Couette cell, the flow is localized close to the location of the shear. This is the so-called *shear band* effect: the grains which are further apart, say, 100 grain diameter away, don't move at all. If a constant load is then applied with a probe, far away from the shearing zone, one observes motion of the probe when $\Omega \neq 0$, which strongly depends on Ω while no motion occurs for $\Omega = 0$. What is astonishing here is that the Couette shear does not provoke detectable displacements of the grains at the location of the probe: the shear zone triggers tiny amplitude waves that propagate over a very long distance. The motion of the probe suggests that the waves are able to create or break contacts.

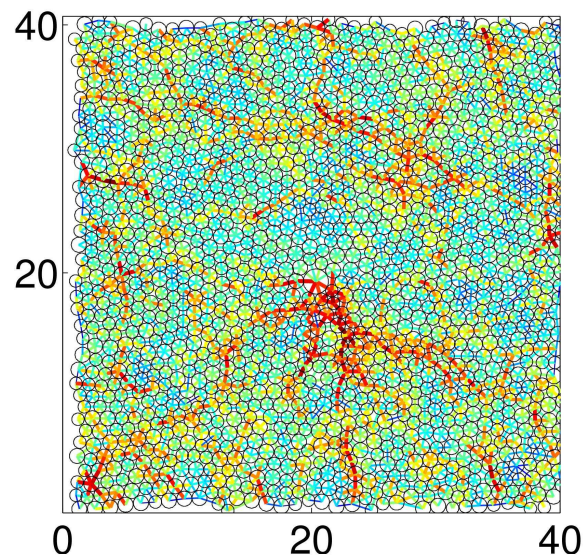


Figure 6.3: **Snapshot of a pulling intruder.** Edges colors code for contact force. The intruder is pulled downwards at constant force.

Finally, the Jamming transition has been shown to exhibit strong non-affine displacements on response to point force [Ellenbroek et al., 2009b].

Together with our own observations, these results suggest that contacts dynamics could also play an crucial role in the rheological properties of dense granular flows. To tackle this point experimentally, a nice program would be to perform an experiment consisting of pulling an intruder through a granular packing, where we can measure the contacts. We have actually started to perform such experiments, which are in the process of being analyzed. A snapshot of an experimental realization of intruder pulling is displayed in figure 6.3. An other complementary experiment we would like to perform is to inflate a particle and to study its influence over contacts dynamics.



Appendix A

Letter on the Widom lines

In the next pages the reader will find a Letter about the route to Jamming when decreasing the mechanical vibration. This is the short version of what has been presented in chapter 4 and 5. Due to the short format letter, only the key results are presented in the letter.

This Letter has been published in Europhysics Letters.

Dynamics of the contacts reveals Widom lines for jamming

C. COULAIS¹, R. P. BEHRINGER² and O. DAUCHOT³

¹ SPHYNX/SPEC, CEA-Saclay, URA 2464 CNRS - 91191 Gif-sur-Yvette, France, EU

² Department of Physics and Center for Nonlinear and Complex Systems, Duke University
Durham, NC 27708-0305, USA

³ EC2M, ESPCI-ParisTech, UMR Gulliver 7083 CNRS - 75005 Paris, France, EU

received 28 August 2012; accepted in final form 9 November 2012

published online 3 December 2012

PACS 45.70.Vn – Granular models of complex systems; traffic flow

PACS 45.70.Cc – Granular systems: Static sandpiles; granular compaction

PACS 64.60.Ht – Dynamic critical phenomena

Abstract – We experimentally study the vicinity of the jamming transition by investigating the statics and the dynamics of the contact network of a horizontally shaken bi-disperse packing of photo-elastic discs. Compressing the packing very slowly, while maintaining a mechanical excitation, yields a granular glass, namely a frozen structure of vibrating grains. In this glass phase, we observe a remarkable dynamics of the *contact network*, which exhibits strong dynamical heterogeneities. Such heterogeneities are maximum at a packing fraction ϕ^* , *distinct* and smaller than the structural packing fraction ϕ^\dagger , which is indicated by an abrupt variation of the average number of contacts per particle. We demonstrate that the two crossovers, one for the maximum dynamical heterogeneity, and the other for static jamming, converge at point J in the zero mechanical-excitation limit, a behavior reminiscent of the Widom lines in the supercritical phase of a second-order critical point. Our findings are discussed in the light of recent numerical and theoretical studies of thermal soft spheres.

Copyright © EPLA, 2012

At large packing fraction, disordered packings of particles with repulsive contact interactions jam into a rigid state. For frictionless and athermal particles, the jamming transition coincides with the onset of isostaticity and a number of geometrical and mechanical quantities exhibit clear scaling laws with the distance to jamming [1]. One prominent signature of jamming is the singular behavior of the average number of contacts per particle $z - z_J \propto (\phi - \phi_J)^{0.5}$, where $z_J = 2d$, d being the space dimension [2,3]. The distribution of the gaps between particles displays a delta function at zero and a square-root decay for increasing gaps, which is key to the singular behavior of the average contact number [4–7].

Although the average coordination number singularity is the hallmark of jamming at zero temperature, its behavior is less clear at finite temperature. Both experimentally [8] and numerically [6,8–11], it has been observed that the first peak of the partial pair correlation function has a finite maximum at a packing fraction $\phi_j(T) > \phi_j(0) = \phi_J$. This maximum has been interpreted as a vestige of the divergence of the pair correlation function at point J , the $T=0$ jamming transition (fig. 1). However, it was later argued [12] that this structural anomaly can be accounted

for using equilibrium liquid-state theory, and is therefore not specific to jamming. The vicinity of point J has also been explored in a mean-field-like replica description of thermal soft and hard spheres [13]. This description recovers all the observed scalings in temperature and packing fraction *but* the square-root singularity of the pair correlation function when $T=0^+$ and $\phi = \phi_J^\dagger$. This discrepancy, together with the onset of a diverging length in the vibrational properties of the jammed state [14], suggests that larger-scale correlations must be taken into account, and calls for a better characterization of the vicinity of point J .

In the present letter, we focus on the *dynamics* of the contact network, a natural quantity of interest as soon as dynamics is present, which, to our knowledge, has never been explored so far. To this end, we experimentally investigate a vibrated two-dimensional bi-disperse packing of photo-elastic grains, close to its jamming transition. We control both the packing fraction, ϕ , and the mechanical excitation, γ , to be defined precisely below. This mechanically driven and dissipative system is far from equilibrium and the mechanical excitation is different from a temperature in

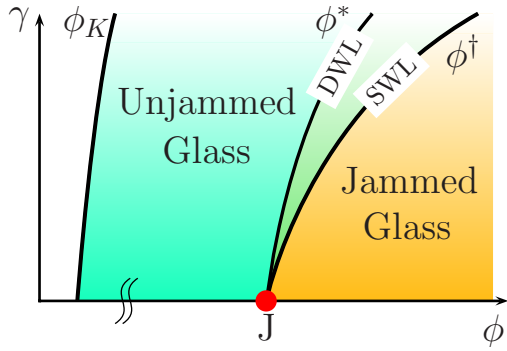
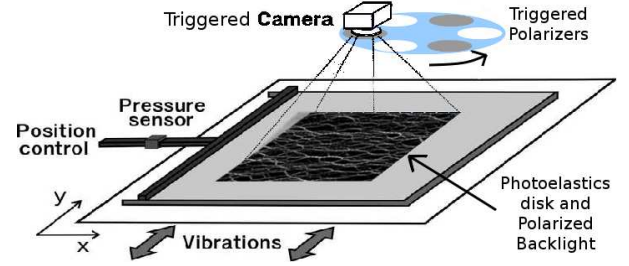


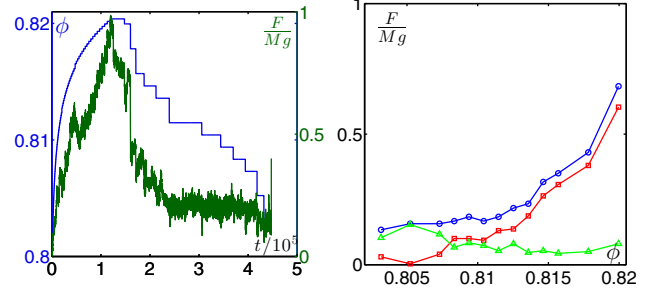
Fig. 1: (Color online) Sketch of phase space. In the glass phase, two Widom lines, a structural one (SWL) and a dynamical one (DWL), emerge from point J and separate the jammed glass (frozen structure and frozen contacts) from the unjammed one (frozen structure but “liquid” contacts).

many aspects. However, by analogy, one can reasonably consider that both temperature and mechanical excitation provide agitation to the particles. The structure, in terms of particle neighborhoods, is completely frozen on the experimental time scales: the system can safely be considered as a granular glass. The structural signature of jamming $\phi^\dagger(\gamma)$ is given by an abrupt variation of the average number of contacts. Above $\phi^\dagger(\gamma)$, the contacts are also frozen. On the contrary below $\phi^\dagger(\gamma)$, they exhibit a rich dynamics with strong heterogeneities. For any finite mechanical excitation γ , these heterogeneities are maximum at a packing fraction $\phi^*(\gamma)$ smaller than $\phi^\dagger(\gamma)$. The relative shift $|\epsilon^*| = |\phi^* - \phi^\dagger|/\phi^\dagger$ decreases linearly towards zero and the characteristic length of the dynamical heterogeneities eventually diverges as the mechanical excitation approaches zero. Our results suggest the phase space diagram sketched in fig. 1, where the structural and the dynamical crossovers are reminiscent of Widom lines [15,16] for point J , namely the locus of the maxima of the second derivatives of the free energy, introduced in the context of critical phenomena.

Our experimental set up (fig. 2(a)) is adapted from [17,18], and allows us to shake photoelastic discs between two cross-polarizers, thereby accessing the contact and force network [3,19]. A bi-disperse mixture of 4964 and 3216 polyurethane (PSM-4) discs, of, respectively, 4 mm and 5 mm diameter, lies on a flat transparent surface, which oscillates with an amplitude of 1 cm at different frequencies of 6.25, 7.5 or 10 Hz. For frequencies smaller than $f_0 = 4.17$ Hz, the grains do not slip on the plate and the mechanical excitation is effectively null. In the following we shall use the reduced frequency $\gamma = (f - f_0)/f_0$ as a measure of the mechanical excitation. The grains are confined in a static rectangular cell, for which the position of one horizontal boundary is tuned using a micro-metric piston attached to a force sensor. A LED back-light and a circular polarizing sheet are



(a)



(b)

(c)

Fig. 2: (Color online) Experimental setup and protocol. (a) The vibrating cell. (b) Logarithmic increase followed by a stepwise decrease of the packing fraction, and pressure at the wall. (c) Average pressure *vs.* packing fraction, $\gamma = 1.4$: P_{TOT} (\circ), P_{STAT} (\square), P_{DYN} (\triangle) as defined in the text.

inserted in the vibrating surface, so that the grains are lighted by transmission of circularly polarized light. A monochromatic high-resolution CCD camera records two types of images in phase with the vibration. Every odd period, a circular analyzer is inserted by a rotating wheel in the camera field to visualize the photoelastic pattern. From the direct-light images acquired every even period, we obtain the grain positions with a resolution of 0.5% of the mean grain diameter. We then use standard tracking and tessellation techniques to obtain the dynamics and structure of the packings. From the cross-polarized images, we estimate the normal force between two neighbors by integrating the square spatial gradient of the light intensity over the area defined by the two Delaunay triangles sharing a common edge. Henceforth, all lengths are expressed in units of the small grain diameter, and time is expressed in units of vibration cycles.

In order to ensure the highest and most reproducible jammed packings, the packing fraction, which we control with a relative resolution of 5×10^{-6} is increased by steps of $\delta\phi = 3 \times 10^{-4}$ to some maximum value, using exponentially increasing time steps (fig. 3(b)). All images are then acquired during stepwise decompression. For each decompression step we carefully check that the system reaches a steady state, and all data presented here have been computed in this steady regime. Figure 3(c) displays the pressure with respect to the packing fraction. P_{TOT}

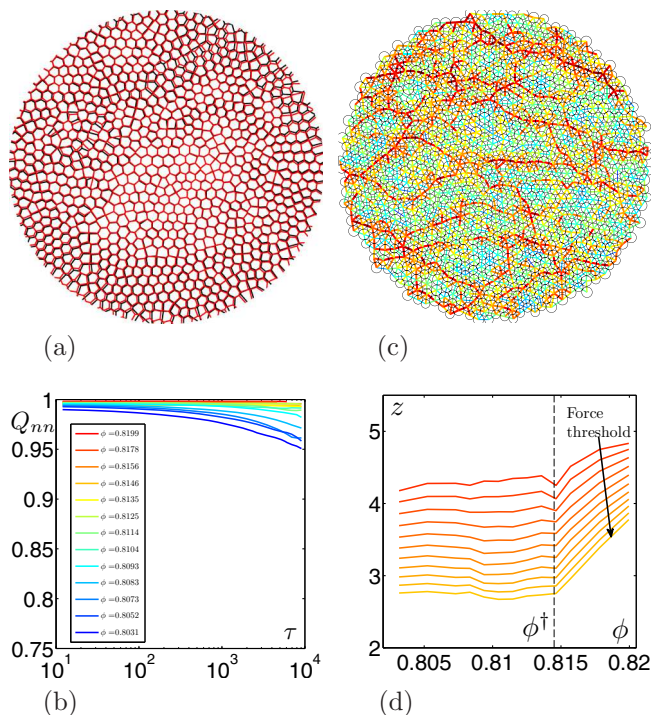


Fig. 3: (Color online) Structure of the granular glass, $\gamma = 1.4$. (a) Superposition of the Laguerre cells computed at times $t = 1$ and $t = 5000$ for the loosest packing ($\phi = 0.8031$). (b) Average fraction of neighbors $Q_{nn}(\tau)$ which have not changed between two images separated by a time interval τ , for different packing fractions, as indicated in the legend. (c) Map of contact forces. Color code spans from blue (low forces) to red (high forces). (d) Average coordination number z vs. packing fraction ϕ , determined according to various force thresholds

(respectively, P_{STAT}) is the pressure measured when the vibration is switched on (respectively, off). P_{STAT} is thus the static pressure sustained by the packing in the absence of vibration, whereas $P_{DYN} = P_{TOT} - P_{STAT}$ can be interpreted as the additional dynamic pressure, induced by the vibration. At high packing fraction, the pressure is dominated by its static part, whereas at low packing fraction, it is mostly dynamic. A crossover occurs at some intermediate packing fraction, which in [17] was shown to coincide with a maximum in the heterogeneity of the dynamics, as probed at scales of the order of 10^{-2} grain diameter. Here, the transition is shifted to lower values of ϕ , a fact which we attribute to the higher interparticle friction of the photoelastic discs [1]. Also the transitional range is wider, which is likely due to the relative softness of the photoelastic discs as compared to the brass discs used in earlier experiments. (Young modulus of 0.5 GPa, as compared to 100 GPa).

We first focus on the largest mechanical-excitation level, $\gamma = 1.4$. Altogether, the above compression protocol produces a structure in terms of nearest-neighbor relationships, which is completely frozen on experimental timescales. The Laguerre tessellation of

two different packings separated by a time lag 5000 can be superimposed almost perfectly, even at the loosest packing fraction (fig. 3(a)). This is further quantified by $Q_{nn}(\tau)$, the average fraction of *neighbor* relationships surviving in a time interval τ . Q_{nn} remains larger than 95% even for the loosest packing fraction, and is barely less than 100% for the denser ones (fig. 3(b)). The contact network within this frozen structure is provided by an analysis of the photoelastic images. A threshold is applied to both the gap between neighboring particles and the contact force (see map of contact forces in fig. 3(c)), to decide what particles are in contact. Figure 3(d) displays the average number of contacts, z , as a function of the packing fraction for different thresholds. While the absolute value of z depends on the threshold, the dependence on ϕ is very robust: z is constant at low packing fractions, displays a kink at some intermediate packing fraction, and thereafter, increases. The kink occurs at a packing fraction which is independent of the threshold. We interpret this packing fraction as the signature of a structural crossover to jamming in the presence of vibration and find $\phi^\dagger = 0.8143 \pm 0.0005$. Above ϕ^\dagger , the system is jammed and, $z \sim a(\phi - \phi^\dagger)^\beta + z_c$, where $\beta \in [0.4, 1]$ and $z_c \in [2.7, 4.3]$ depend on the threshold. Since counting arguments for frictional packings [1] constrain z_c between 3 and 4 for two-dimensional systems, it is fair to say that the transition indicated by the kink is robust to the thresholding procedure. We now come to the innovative part of this work, which consists of studying the *dynamics* of the contact network and its dependence on the mechanical excitation.

Analyzing the force network, we recover existing results on the force distributions [20] and observe that its dynamics is slaved to that of the contacts. We thus concentrate on the description of the dynamics of the contact network. It is naturally quantified by an estimator of the contact overlap between t and $t + \tau$:

$$Q^z(t, \tau) = \frac{1}{N} \sum_i Q_i^z(t, \tau), \quad (1)$$

where $Q_i^z(t, \tau) = \Theta(2 - |\delta z_i(t, \tau)|)$, with $\Theta(\cdot)$, the Heaviside function and $\delta z_i(t, \tau)$, the change in number of contacts of grain i , between t and $t + \tau$. Alternative definitions, *e.g.*, requiring smaller or larger local contact fluctuations, do not change the following conclusions. Figure 4(a) displays $Q_z(\tau) = \langle Q^z(t, \tau) \rangle_t$ for the various packing fractions, where $\langle \cdot \rangle_t$ denotes the time average. The black curve corresponds to the packing fraction of the jamming crossover ϕ^\dagger . For $\phi > \phi^\dagger$, $Q^z(\tau)$ remains constant at values ranging between 0.7 and 0.9, indicating that there is no long-time decorrelation of the contact network: the contacts are established permanently, once they are formed. The sole decorrelation observed above ϕ^\dagger occurs at short times and is induced by the fast dynamics of the rattlers, the number of which increases when ϕ approaches ϕ^\dagger . For $\phi < \phi^\dagger$, long-time relaxation clearly

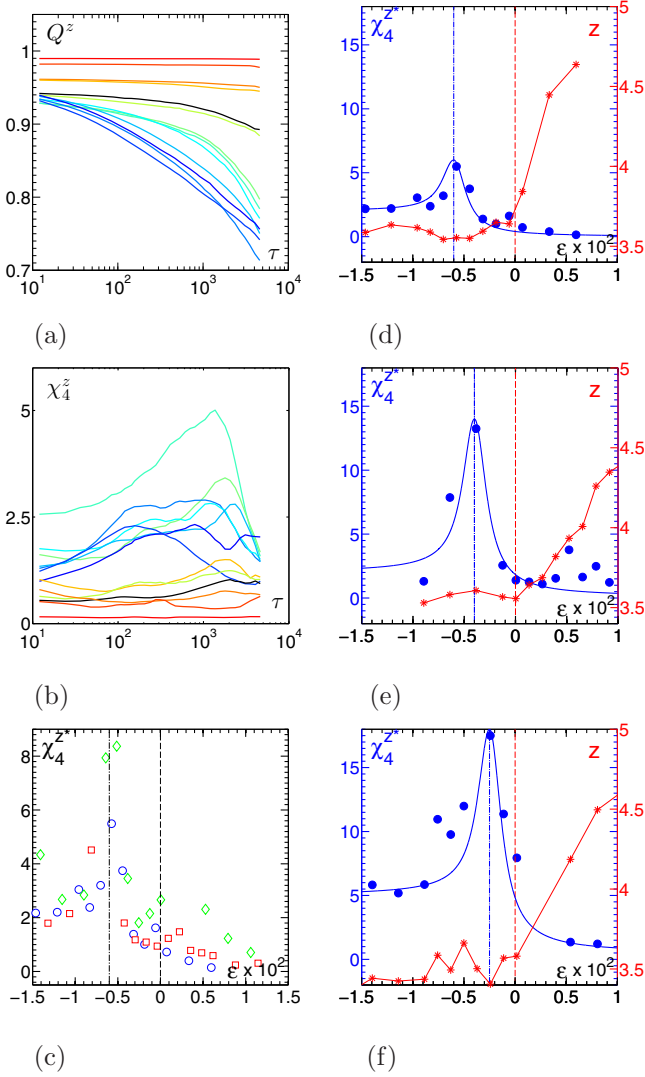


Fig. 4: (Color online) Contact Dynamics. (a) Average contact overlap $Q_z(\tau)$ for different packing fractions, $\gamma = 1.4$ (same color code as in fig. 3(a) with the curve corresponding to ϕ_J plotted in black). (b) Contact overlap dynamical susceptibility $\chi_4^z(\tau)$, $\gamma = 1.4$ (same color code). (c) Contact overlap dynamical susceptibility χ_4^{z*} , chosen for the delay time, τ , that maximizes its value, as a function of $\epsilon = (\phi^* - \phi^\dagger)/\phi^\dagger$ for three realizations (\bullet , \square , \diamond) of the same experiment, $\gamma = 1.4$. (d)–(f) Maximal contact overlap dynamical susceptibility χ_4^{z*} (\bullet) and average contact number z (\star) vs. ϵ for three different amplitudes of the vibration: (d) $\gamma = 1.4$; (e) $\gamma = 0.8$; (f) $\gamma = 0.5$. The red, respectively blue, dashed line indicates the location of ϕ^* , respectively ϕ^\dagger . The continuous blue curve is a guide to the eye.

sets in, indicating that contacts now rearrange. One can thus think about this structural crossover as a glass transition for the binary degrees of freedom (*e.g.*, yes/no) which indicate whether neighboring particles are in contact or not. Accordingly, one would like to further investigate this long-term dynamics, in order to see whether it shares other similarities with glassy dynamics in spin systems.

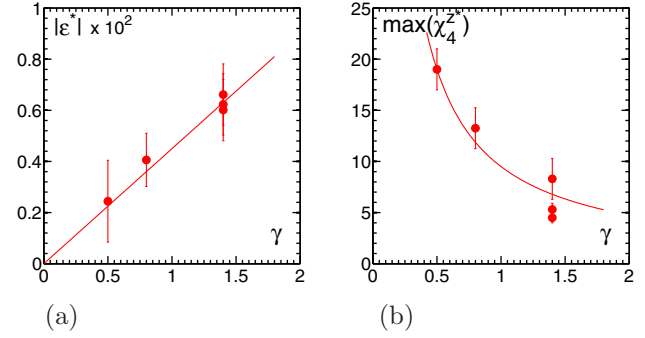


Fig. 5: (Color online) Dependence on the vibration amplitude of (a) $|\epsilon^*|$, the relative shift between ϕ^* and ϕ^\dagger and (b) the maximal dynamical susceptibility as a function of the vibration amplitude γ . The continuous lines indicate, respectively, a linear and a $1/\gamma$ dependence on γ .

We compute the dynamical susceptibility (see [21] for an introduction to dynamical heterogeneities):

$$\chi_4^z(\tau) = N \frac{\text{Var}(Q^z(t, \tau))}{\langle \text{Var}(Q_i^z(t, \tau)) \rangle_i}, \quad (2)$$

where $\text{Var}(\cdot)$ denotes the variances sampled over time and $\langle \cdot \rangle_i$ denotes the average over the grains. This dynamic susceptibility estimates the range of the spatial correlation in the dynamics of the contact network. One sees in fig. 4(b) that $\chi_4^z(\tau)$ becomes significant for $\phi < \phi^\dagger$ and then exhibits a maximum χ_4^{z*} in time, which in turn displays a clear maximum at a packing fraction ϕ^* . Performing three independent experimental runs, with the same vibration $\gamma = 1.4$, we observe in fig. 4(c) that ϕ^* is systematically smaller than ϕ^\dagger , with a relative shift $\epsilon^* = (\phi^* - \phi^\dagger)/\phi^\dagger = -5 \times 10^{-3}$: the reorganization of the contacts is maximally collective, indicating a dynamical crossover *below* ϕ^\dagger . Since it is well known that the jamming transition and its related crossovers, *a priori* depend on the initial conditions and the preparation protocol [22], we shall now use the reduced packing fraction $\epsilon = (\phi - \phi^\dagger)/\phi^\dagger$, in order to compare different experimental runs.

The robustness of our finding is further reinforced by the fact that we could demonstrate a systematic dependence on the excitation γ . Figures 4(d)–(f) display the dynamical susceptibility together with the average contact number as a function of the packing fraction for respectively $\gamma = 1.4, 0.8, 0.5$. On decreasing γ , one observes that i) the dynamical crossover ϕ^* moves closer to the structural signature of jamming and ii) the maximum of the dynamical susceptibility χ_4^{z*} , hence the correlation length, increases when γ decreases. Figure 5 summarizes these dependencies. Our data are compatible with a linear variation $|\epsilon^*| \propto \gamma$ and $\max(\chi_4^{z*}) \propto 1/\gamma$ suggesting a divergence of the correlation length at zero excitation.

Let us now summarize and discuss our observations. Having prepared a granular glass, with a frozen neighborhood structure, we have observed three salient features

of the contact network: i) the evolution of the averaged number of contacts with packing fraction, $z(\phi)$, points to a first transitional packing fraction ϕ^\dagger ; ii) the dynamics of the contact network, together with the fluctuation of the coordination number are maximally heterogeneous at a packing fraction $\phi^* < \phi^\dagger$. The shift in packing fraction decreases linearly with the amplitude of the mechanical excitation, while the dynamical heterogeneities increase sharply. This phenomenology, summarized in fig. 1, is reminiscent of the so-called Widom lines observed in the supercritical region close to a critical point [15,16]. To our knowledge, the present study is the first experimental characterization of these crossovers, including their dependence on the mechanical excitation. Obviously one would like to extend the range of dependence towards even lower excitation, but the required precision then calls for numerical investigations.

Along the way, our results address a long-standing conundrum left from earlier experiments using the same apparatus, but with hard (brass) discs [17]. The authors observed a maximum in the heterogeneities of the dynamics for the packing fraction, where $P_{DYN}(\phi)$ and $P_{STAT}(\phi)$ intersect. The existence of this maximum suggests that the experiment probed both sides of the jamming transition, a puzzling conclusion given the very strong stiffness of the brass discs. Using soft discs, we demonstrate here that there are several signatures of point J at finite mechanical excitation, γ , and that the one associated with the dynamical heterogeneities occurs at a lower packing fraction, $\phi^*(\gamma)$, than the one at which the average number of contact increases, $\phi^\dagger(\gamma)$. The previous experiment using brass discs [17] was actually probing the dynamical crossover, ϕ^* , both sides of which lie below the structural signature of the jamming transition. This is further confirmed by the observation that, here also, $P_{DYN} \simeq P_{STAT}$ at ϕ^* .

Unlike thermal systems, our system is in an out-of-equilibrium, mechanically driven state. Still, recent numerical simulations [6,9,11,23] suggest that for the kind of physics we are interested in, the similarities with thermal systems are much stronger than one may have expected at first sight. For instance, the structural crossover reported here might be related to the finite-temperature first-peak pair correlation maxima near the jamming point reported in [6,8,9]. More specifically, in [23] the authors report an extensive study of the dynamics close to point J , in the temperature-density space, which they conclude by comparing with existing colloidal experiments. To do so they essentially use the Debye-Waller factor, namely the size of the cage surrounding the particles, as a sensitive thermometer. In the present case, the cage size at the largest packing fraction and largest magnitude of excitation is of the order of 5×10^{-3} . This would correspond in fig. 1 of their work to a rescaled kinetic energy of 10^{-6} . For lower excitation, it is even smaller. In all cases, we conclude that the present experiments, together with those of [17,18] are for the moment the only

ones, which have probed the dynamical criticality related to the jamming transition (see the discussion part and fig. 12 in [23]). Whether the same scenario as the one described here holds for thermal soft spheres, such as emulsions, is an open issue for further experimental investigation.

Finally, one cannot exclude the possible effect of friction. Here the friction coefficient amongst the grains is typically $\mu = 0.7$ and one indeed notes that the packing fractions of interest reported here have a lower value than those obtained for the brass discs ($\mu = 0.4$) and for frictionless particles. However, our results demonstrate that at the qualitative level and in the dynamical regime probed by our setup, friction does not seem to be a relevant parameter. Whether it impacts the quantitative scaling properties close to points J requires further studies, presumably numerical ones.

We thank L. BERTHIER and F. ZAMPONI for illuminating discussions and are grateful to CÉCILE WIERTEL-GASQUET and VINCENT PADILLA for their skillful technical assistance.

REFERENCES

- [1] VAN HECKE M., *J. Phys.: Condens. Matter*, **22** (2010) 033101.
- [2] O'HERN C. S., LANGER S. A., LIU A. J. and NAGEL S. R., *Phys. Rev. Lett.*, **88** (2002) 075507.
- [3] MAJMUDAR T. S., SPERL M., LUDING S. and BEHRINGER R. P., *Phys. Rev. Lett.*, **98** (2007) 058001.
- [4] SILBERT L. E., ERTAŞ D., GREST G. S., HALSEY T. C. and LEVINE D., *Phys. Rev. E*, **65** (2002) 031304.
- [5] PARISI G. and ZAMPONI F., *Rev. Mod. Phys.*, **82** (2010) 789.
- [6] JACQUIN H., BERTHIER L. and ZAMPONI F., *Phys. Rev. Lett.*, **106** (2011) 135702.
- [7] DONEV A., TORQUATO S. and STILLINGER F. H., *Phys. Rev. E*, **71** (2005) 011105.
- [8] ZHANG Z., XU N., CHEN D. T. N., YUNKER P., ALSAYED A. M., APTOWICZ K. B., HADBAS P., LIU A. J., NAGEL S. R. and YODH A. G., *Nature*, **459** (2009) 230.
- [9] WANG L. and XU N., arXiv:1112.2429 [cond-mat.soft] (2011).
- [10] CHENG X., *Phys. Rev. E*, **81** (2010) 031301.
- [11] OTSUKI M. and HAYAKAWA H., *Phys. Rev. E*, **86** (2012) 031505.
- [12] JACQUIN H. and BERTHIER L., *Soft Matter*, **6** (2010) 2970.
- [13] BERTHIER L., JACQUIN H. and ZAMPONI F., *Phys. Rev. E*, **84** (2011) 051103.
- [14] WYART M., NAGEL S. R. and WITTEN T. A., *Europhys. Lett.*, **72** (2005) 486.
- [15] STANLEY H. E., *Introduction to Phase Transitions and Critical Phenomena*. (Oxford University Press) 1971.
- [16] BRAZHKIN V. V., FOMIN Y. D., LYAPIN A. G., RYZHOV V. N. and TSIOK E. N., *J. Phys. Chem. B*, **115** (2011) 14112-14115.

- [17] LECHENAULT F., DAUCHOT O., BIROLI G. and BOUCHAUD J. P., *EPL*, **83** (2008) 46003.
- [18] LECHENAULT F., DAUCHOT O., BIROLI G. and BOUCHAUD J. P., *EPL*, **83** (2008) 46002.
- [19] MAJMUDAR T. S. and BEHRINGER R. P., *Nature*, **435** (2005) 1079.
- [20] O'HERN C. S., LANGER S. A., LIU A. J. and NAGEL S. R., *Phys. Rev. Lett.*, **86** (2001) 111.
- [21] BERTHIER L., BIROLI G., BOUCHAUD J.-P., CIPOLLETTI L. and SAARLOOS W. V. (Editors), *Dynamical Heterogeneities in Glasses, Colloids, and Granular Media* (Oxford University Press) 2011.
- [22] CHAUDHURI P., BERTHIER L. and SASTRY S., *Phys. Rev. Lett.*, **104** (2010) 165701.
- [23] IKEDA A., BERTHIER L. and BIROLI G., arXiv:1209.2814 [cond-mat.stat-mech] (2012).

Appendix B

Recipes

B.1 Dynamical Recipes

B.1.1 Indirect method : temporal variance

We show here that the computation of temporal variance of a spatial average is a way to quantify spatial correlations. We demonstrate here that the variance can actually be used to estimate of the size of the correlated zones. The quantity of interest is here $q_i(t)$, where i denotes space and t denotes time. $\langle \dots \rangle$ denotes time average, and $\overline{\dots}$ denotes spatial average. Indeed,

$$\text{var}_t q_t = \left\langle \left(\frac{1}{N} \sum_{i=1}^N q_i(t) - \left\langle \frac{1}{N} \sum_{i=1}^N q_i(t) \right\rangle \right)^2 \right\rangle, \quad (\text{B.1})$$

which can also be written in the form

$$\text{var}_t q_t = \frac{1}{N^2} \left(\left\langle \left(\sum_{i=1}^N q_i(t) \right)^2 \right\rangle - \left\langle \sum_{i=1}^N q_i(t) \right\rangle^2 \right), \quad (\text{B.2})$$

where by separating diagonal and off-diagonal terms in both first and second term,

$$\left\langle \left(\sum_{i=1}^N q_i(t) \right)^2 \right\rangle = \sum_{i=1}^N \langle q_i(t)^2 \rangle + \sum_{i=1}^N \sum_{j \neq i} \langle q_i(t) q_j(t) \rangle, \quad (\text{B.3})$$

$$\left\langle \sum_{i=1}^N q_i(t) \right\rangle^2 = \sum_{i=1}^N \langle q_i(t) \rangle^2 + \sum_{i=1}^N \sum_{j \neq i} \langle q_i(t) \rangle \langle q_j(t) \rangle, \quad (\text{B.4})$$

One then obtains

$$\text{var}_t q_t = \frac{1}{N^2} \sum_{i=1}^N \left(\langle q_i(t)^2 \rangle - \langle q_i(t) \rangle^2 \right) \quad (\text{B.5})$$

$$+ \frac{1}{N^2} \left(\sum_{i=1}^N \sum_{j \neq i} \langle q_i(t) q_j(t) \rangle - \langle q_i(t) \rangle \langle q_j(t) \rangle \right). \quad (\text{B.6})$$

We see that the second term is the temporal covariance of the system and contains spatial correlation. From it we can then directly define the quantity

$$\chi_q \equiv \frac{N}{\overline{\text{var}_t q_i(t)}} \text{var}_t q_t \quad (\text{B.7})$$

$$= 1 + \frac{\frac{1}{N} \left(\sum_{i=1}^N \sum_{j \neq i} \langle q_i(t) q_j(t) \rangle - \langle q_i(t) \rangle \langle q_j(t) \rangle \right)}{\overline{\text{var}_t q_i(t)}}, \quad (\text{B.8})$$

where

$$\overline{\text{var}_t q_i(t)} = \frac{1}{N} \sum_{i=1}^N \left(\langle q_i(t)^2 \rangle - \langle q_i(t) \rangle^2 \right). \quad (\text{B.9})$$

We see that $\chi_q - 1$ is the temporal cross correlation of the system. For a spatially uncorrelated system, this term falls down to zero. We stress here that this term is built up by temporal fluctuations: *This estimator quantifies the spatial correlations by using time fluctuations.*

B.1.2 Link with dynamical heterogeneities

We present an argument which has been proposed by Dauchot et al. [2011], and which is useful to explain constraints on the measurements of dynamical heterogeneities, when using χ_q . To do so, we consider a simple system made of N particles with a fluctuating number, M_t , of mobile regions of size n . The mobile regions have $q = q_0$, and the slow regions have $q = q_1$. Thus,

$$q_t = \frac{nM_t}{N} q_0 + \left(1 - \frac{nM_t}{N} \right) q_1. \quad (\text{B.10})$$

The temporal average of q_t is then

$$q = \langle q_t \rangle_t = \langle M_t \rangle_t \frac{n}{N} (q_0 - q_1) + q_1, \quad (\text{B.11})$$

As the value of $q_i(t)$ changes, it fluctuates between q_0 and q_1 . Therefore, the typical average heterogeneity is

$$\overline{\text{var}_t q_i(t)} = (q_0 - q_1)^2. \quad (\text{B.12})$$

Finally, from equation B.7, we compute the dynamical susceptibility,

$$\chi_q = \frac{N}{(q_0 - q_1)^2} \text{var}_t \left(\frac{n}{N} M_t (q_0 - q_1) + q_1 \right). \quad (\text{B.13})$$

Since the different mobile regions are uncorrelated, they fluctuate randomly, and

$$\text{var}_t \left(\frac{n}{N} \langle M_t \rangle_t (q_0 - q_1) + q_1 \right) \sim \langle M_t \rangle_t \left(\frac{n}{N} (q_0 - q_1) \right)^2. \quad (\text{B.14})$$

Finally,

$$\chi_q = \frac{n^2 \langle M_t \rangle_t}{N} = n \frac{q - q_1}{q_0 - q_1} \sim n. \quad (\text{B.15})$$

Thus, we have a measurement of the number of dynamically correlated particles number. The key assumption here is that the number of regions M_t is large and that they are decorrelated. Therefore, in practice, it is necessary to have a sufficiently large system as well as sufficiently long time acquisition to perform statistics on.

B.2 Modelling the motion of one grain

This is the MATLAB code that is used to compute the dynamics of the grain on the board. We here acknowledge Brice Saint-Michel. The code has been written together with him and he actually wrote the most part.

```

Gamma=0.7;mud=0.5;mus=0.6:Dt=1000;tmax=6;
%Board acceleration
aie = Gamma*sin((1:Dt*tmax)*2*pi/Dt);
%Board velocity
Bv = -1/(2*pi)*Gamma*cos((1:Dt*tmax)*2*pi/Dt);
%Board position
Bx = -1/(2*pi)^2*Gamma*sin((1:Dt*tmax)*2*pi/Dt);

%Initialize time acceleration and velocity
time = 1:Dt*tmax;
acc = zeros(size(aie));
vit = zeros(size(aie));

%Initial condition no stick
stick = true;

for t = time(1:end-1);
    % Test on stick
    if stick
        % Slip condition
        stick = abs(aie(t)) < mus;
        if ~stick
            vit(t) = eps*sign(-aie(t));
        end
    else
        % Stick if the velocity has changed position
        vit_p_dt(vit(t)+1/Dt*(- aie(t)-sign(vit(t))*mud))
        stick = sign(vit(t)*vit_p_dt)~=1;
    end

    % Consequence of slip
    if ~stick
        acc(t+1) = - aie(t) - sign(vit(t))*mud;
        vit(t+1) = vit(t) + (acc(t) + acc(t+1))/2/Dt;
    end
end
%Rescaling of the time.
time = time/Dt;

```

```
%Computation of the position  
x = cumtrapz(time, vit);
```


Appendix C

Side studies

C.1 More on rattlers

Despite the fact they are always present in numerical simulations [Lubachevsky and Stillinger, 1990] ,[O’Hern et al., 2003] ,[Shundyak et al., 2007] ,[van Hecke, 2010], and experiments [Bi et al., 2011, Candelier, 2009, Lechenault, 2007], there is rather poor literature about rattling particles in jammed packings. In addition, no real theory encompasses a description of rattlers [Biazzo et al., 2009, Parisi and Zamponi, 2010]. Rather, they are considered as an annoying issue, and are still matters of debate, when discussing the geometrical properties of packings close to jamming [Parisi and Zamponi, 2010, Donev et al., 2005, van Hecke, 2010]. Still, they are characterized by two key features:

1. They do not contribute to the mechanical rigidity of the packing, they have less than d contacts, d being the space dimension. We call them “non force-bearing” particles in the following.
2. They occupy a volume in which they are free to “rattle”, accordingly to the external energy injection, or the compaction algorithm. We call them “rattling” particles in the following.

We have discussed separately these points above in the manuscript —point 1 was briefly mentioned in section 4.3.3 and point 2 was more extensively discussed in section 3.4.1. We would like, in this short appendix, to discuss and compare more closely these two points.

C.1.1 “Non force-bearing” particles

In this section, we determine the rattlers from the contact number measurement, and we call them “non force bearing” particles. Are considered as rattlers, the particles having less than 2 contacts. We plot in figure C.1, left, the instantaneous fraction of “non force-bearing” particles averaged over time, f_R^{Nfb} , vs. packing fraction. At high packing fraction, the average fraction of rattling particles is close to $\sim 1\%$, and it increases to $\sim 7\%$ as packing fraction is decreased to 0.81. For lower packing fractions, it then decreases again to $\sim 5\%$. Since the average number of contacts is constant below $\phi \sim 0.814$ (see fig. 4.6), this indicates that, spatially, particles have more uniform contact number at low packing fraction ($\phi \sim 0.802$), than at intermediate packing fraction ($\phi \sim 0.810$). At high packing fractions ($\phi > 0.814$), the decrease of f_R^{Nfb} is consistent with the increase of the average number of contacts.

We plot in figure C.1, right, the fraction of particles having rattled at least once, *i.e.* having being “non force-bearing” at least once during the experimental run, vs. packing fraction. It monotonically decreases from $\sim 50\%$ to $\sim 10\%$ as packing fraction is increased. As the packing is compressed,

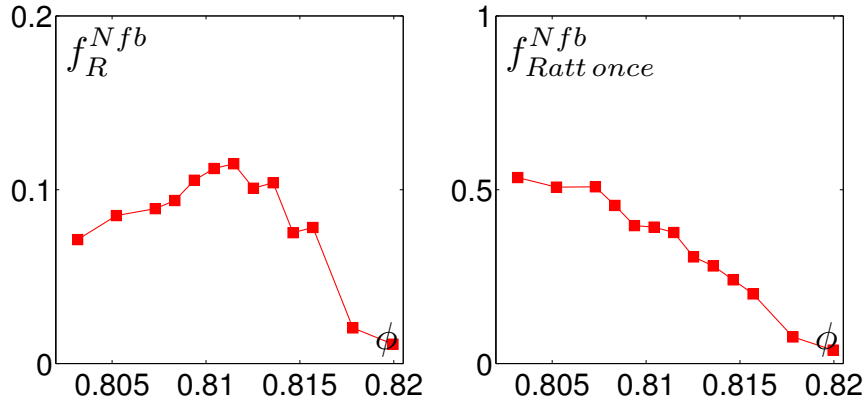


Figure C.1: **Rattlers: Left:** instantaneous fraction of “non force-bearing” particles averaged over time f_R^{Nfb} vs. packing fraction. **Right:** Fraction of particles being “non force-bearing” at least once during the experimental run $f_{Ratt once}^{Nfb}$ versus packing fraction.

the “non force-bearing” particles tend to be always the same, whereas at low packing fractions, they change role.

To conclude, “non force-bearing” particles seems to be consistent with intuition, and so big surprise comes out here. In the following, we compare them more closely with “rattling” particles.

C.1.2 Comparison with “rattling” particles

“Rattling” particles have been extensively studied in section 3.4.1, and their population has already been plotted in figure 3.20, top left, where both the instantaneous fraction “rattling” particles, f_R , and the fraction of particles having rattled at least once, $f_{Ratt once}$, are plotted. Those results contrast, with what is showed in figures C.1, left and right. Indeed, there are always twice as much “rattling” than “non force-bearing” particles.

This discrepancy might originate in the experimental noise on particle displacements, that could induce errors on particle displacements. Thereby, the population of “rattling” particles would be systematically overestimated. In order to check this, we compute the instantaneous fraction of particles, which have been “rattling” and “non force-bearing” at the same time, averaged over time, f_R^j . We plot f_R^j vs. packing fraction, ϕ , in figure C.2, left. f_R^j is always five time smaller than f_R^{Nfb} : the overlap between the two populations is about a fifth of the population of “non force-bearing” particles.

As a further, check, we display in figure C.2, right, a snapshot of particle instantaneous displacement, where both “non force-bearing” and “rattling” particles have been pointed out. The populations are completely different:

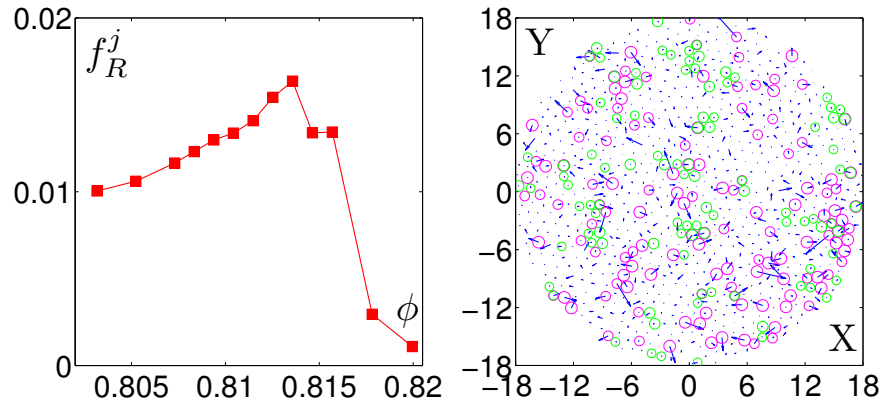


Figure C.2: **Rattlers: Top Left:** f_R^j vs. ϕ (see text for definition). **Right:** Snapshot of instantaneous displacement (magnified by 20). “non force-bearing” particles (having less than two contacts) are drawn in green, and “rattling” particles (identified in section 3.4.1) are drawn in magenta, at $\phi = 0.8157$.

the particles that have a “rattling” motion are not the particles that are “non force-bearing”. This is a rather puzzling issue, and we don’t have any convincing explanation to provide for such a fact.

C.2 Another contact overlap function

As briefly mentioned in the conclusion of this manuscript, the phenomenology of the contact overlap function is very close to the phenomenology of spin glasses. Inspired by the literature on spin glasses [Binder and Young, 1986], it is then tempting to make the analogy more precise.

As we have seen in section 3.2.1, we can consider the neighborhood structure as frozen on the experimental timescale. Therefore, we consider here each neighborhood link p , which, at time t , can either be a contact, $S_p(t) = 1$ or not $S_p(t) = -1$. This allows to map our system or grains like a spin system.

C.2.1 The average magnetization

Then, we define an average magnetization

$$M = \left\langle \frac{1}{N_p} \sum_{p=1}^{N_p} S_p(t) \right\rangle_t, \quad (\text{C.1})$$

where N_p is the number of links, and $\langle \cdot \rangle_t$ the time average. We plot M vs. packing fraction ϕ in figure C.3. For low packing fractions, it is constant. At a packing fraction $\phi_J = 0.814$, there is a kink and M increases with packing fraction.

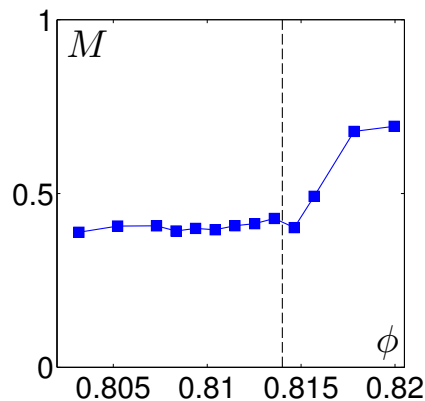


Figure C.3: **Spin magnetization.** Left : Average magnetization vs. packing fraction ϕ . The dashed line corresponds to $\phi_J = 0.814$.

C.2.2 The contact overlap function

In order to study the dynamics, we also define the contact overlap function,

$$Q^S = \left\langle \frac{1}{N_p} \sum_{p=1}^{N_p} S_p(t) S_p(t + \tau) \right\rangle_t, \quad (\text{C.2})$$

where τ is the lag time. We plot in figure C.4, top, the contact overlap function Q^S vs lag time τ . We see that for high packing fractions, Q^S is constant and slightly lower than 1. However, for low packing fractions, Q^S decreases on long times. This is very similar to what we have observed in

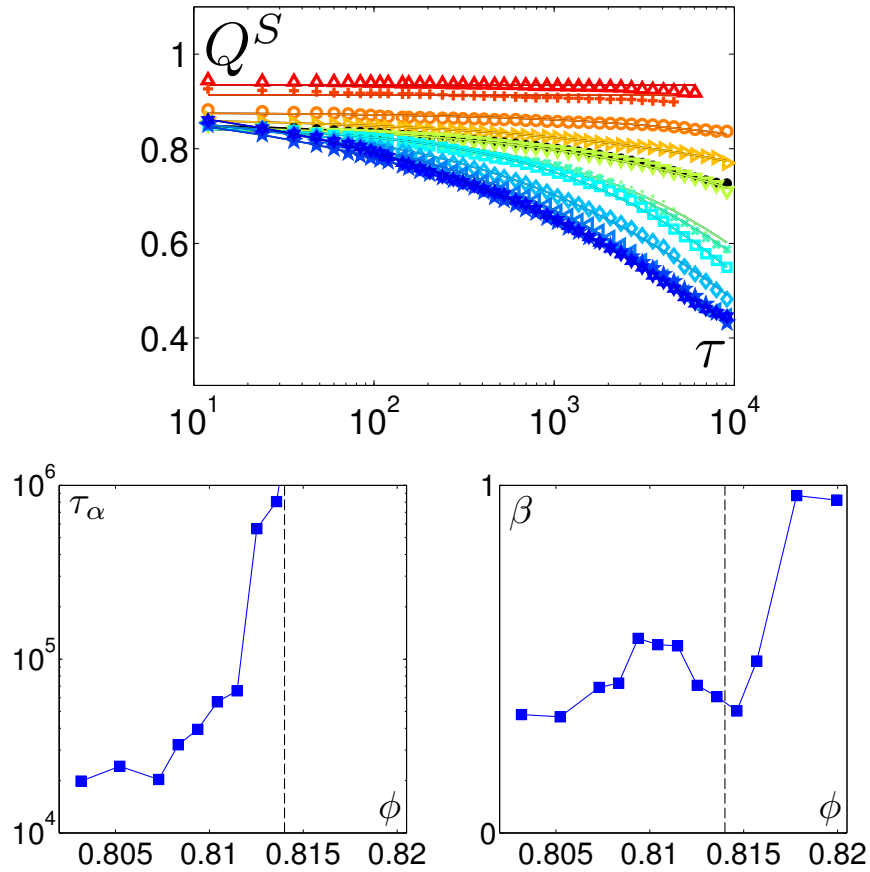


Figure C.4: **Spin overlap function.** **Top:** Average contact overlap functions Q^S vs. lag time τ for different densities. Color code spans from blue (low packing fractions) to red (high packing fractions) (See table 3.1). Markers indicate data points and lines fits by stretched exponentials. **Bottom:** Fit parameters τ_α (left) and β (left) vs. packing fraction ϕ . The dashed line corresponds to $\phi_J = 0.814$.

section 4.12. Here, we fit Q^S by a stretched exponential function,

$$Q_f^S = A \exp \left(- \left(\frac{\tau}{\tau_\alpha} \right)^\beta \right). \quad (\text{C.3})$$

We plot τ_α vs. packing fraction in figure C.4, bottom left. We see that it increases significantly as packing fraction is increased, and that it exceeds 10^6 for densities above ϕ_J . We plot in figure C.4, bottom right, the exponent β vs. packing fraction. It is close to 0.3 at low densities; at ~ 0.81 there is a maximum up to 0.5. Above ϕ_J , it increases significantly, but we see on figure C.4, top, that the fit is rather bad for the two highest packing fractions.

C.2.3 The dynamical susceptibility

As we have done in section 4.3.4, in order to quantify dynamic heterogeneities of the contacts, we compute a dynamical susceptibility, defined as follows:

$$\chi_4^S(\tau) = N \left(\overline{\text{var}_t S_p(t) S_p(t + \tau)} \right)^{-1} \text{var}_t \left(\overline{S_p(t) S_p(t + \tau)} \right), \quad (\text{C.4})$$

where $\overline{\dots}$ is the average over links, and var_t is the temporal variance. Thus, we plot χ_4^S vs. τ in figure C.5, left. We see that it is non-monotonous with respect to lag time, τ . This indicates an intermediate time, at which the contact network relaxation is the most heterogeneous. We report the

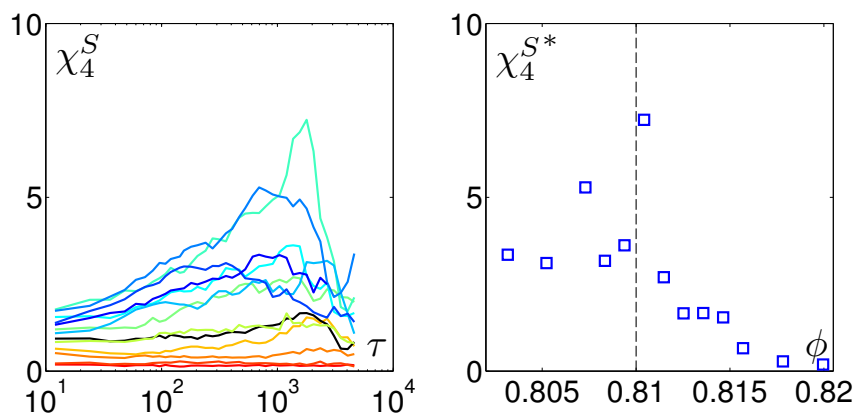


Figure C.5: **Spin overlap dynamical susceptibility.** **Left:** Spin contact susceptibility χ_4^S vs. lag time τ for different densities. Color code spans from blue (low packing fractions) to red (high packing fractions) (See table 3.1). **Right:** Maximum spin contact susceptibility χ_4^{S*} vs. packing fraction ϕ . The dashed line corresponds to $\phi_J = 0.81$.

maximum of the spin dynamical susceptibility $\chi_4^{S^*}$ vs. packing fraction in figure C.5, right. Like $\chi_4^{z^*}$ in section 4.3.4, $\chi_4^{S^*}$ has a maximum at ϕ^* , thus pointing a maximum collective relaxation of the contact network on long time.

To conclude, we have investigated the statics and the dynamics of the contact network in a similar fashion to what has been done in chapter 4. However, we have mapped our problem to a spin problem, *i.e.* with binary variable, as it is discussed in the conclusion of this manuscript.

Bibliography

URL http://www.engineeringtoolbox.com/linear-expansion-coefficients-d_95.html.

URL http://en.wikipedia.org/wiki/Young%27s_modulus#cite_note-etb20120106-2.

URL <http://www.woodrow.org/teachers/chemistry/institutes/1992/Graham.html>.

A. R. Abate and D. J. Durian. Approach to jamming in an air-fluidized granular bed. *Phys. Rev. E*, 74:031308, Sep 2006. doi: 10.1103/PhysRevE.74.031308. URL <http://link.aps.org/doi/10.1103/PhysRevE.74.031308>.

A. R. Abate and D. J. Durian. Topological persistence and dynamical heterogeneities near jamming. *Phys. Rev. E*, 76:021306, Aug 2007. doi: 10.1103/PhysRevE.76.021306. URL <http://link.aps.org/doi/10.1103/PhysRevE.76.021306>.

I. S. Aranson, A. Snezhko, J. S. Olafsen, and J. S. Urbach. Comment on "long-lived giant number fluctuations in a swarming granular nematic". *Science*, 320(5876):612, 2008. doi: 10.1126/science.1153456. URL <http://www.sciencemag.org/content/320/5876/612.3.abstract>.

S. Aumaitre, C. Puls, J. N. McElwaine, and J. P. Gollub. Comparing flow thresholds and dynamics for oscillating and inclined granular layers. *Phys. Rev. E*, 75:061307, Jun 2007. doi: 10.1103/PhysRevE.75.061307. URL <http://link.aps.org/doi/10.1103/PhysRevE.75.061307>.

Pierre Ballesta, Agnes Duri, and Luca Cipelletti. Unexpected drop of dynamical heterogeneities in colloidal suspensions approaching the jamming transition. *Nat Phys*, 4(7):550–554, Jul 2008. ISSN 1745-2473. doi: 10.1038/nphys1000. URL <http://dx.doi.org/10.1038/nphys1000>.

J. D. Bernal. Bakerian lecture 1962 - structure of liquids. *Proceedings of the Royal Society of London series A-Mathematical and Physical Sciences*, 280(1380):299+, 1964. ISSN 0080-4630. doi: {10.1098/rspa.1964.0147}.

J. D. Bernal and J. Mason. Packing of spheres: Co-ordination of randomly packed spheres. *Nature*, 188(4754):910–911, Dec 1960. doi: 10.1038/188910a0. URL <http://dx.doi.org/10.1038/188910a0>.

- J. D. Bernal, J. Mason, and K. R. Knight. Radial distribution of the random close packing of equal spheres. *Nature*, 194(4832):957–958, Jun 1962. doi: 10.1038/194957a0. URL <http://dx.doi.org/10.1038/194957a0>.
- L. Berthier and T. A. Witten. Compressing nearly hard sphere fluids increases glass fragility. *EPL (Europhysics Letters)*, 86(1):10001, 2009a. URL <http://stacks.iop.org/0295-5075/86/i=1/a=10001>.
- Ludovic Berthier. Private communication.
- Ludovic Berthier and Giulio Biroli. Theoretical perspective on the glass transition and amorphous materials. *Rev. Mod. Phys.*, 83: 587–645, Jun 2011. doi: 10.1103/RevModPhys.83.587. URL <http://link.aps.org/doi/10.1103/RevModPhys.83.587>.
- Ludovic Berthier and Gilles Tarjus. Nonperturbative effect of attractive forces in viscous liquids. *Phys. Rev. Lett.*, 103: 170601, Oct 2009. doi: 10.1103/PhysRevLett.103.170601. URL <http://link.aps.org/doi/10.1103/PhysRevLett.103.170601>.
- Ludovic Berthier and Thomas A. Witten. Glass transition of dense fluids of hard and compressible spheres. *Phys. Rev. E*, 80: 021502, Aug 2009b. doi: 10.1103/PhysRevE.80.021502. URL <http://link.aps.org/doi/10.1103/PhysRevE.80.021502>.
- Ludovic Berthier, Giulio Biroli, Jean-Philippe Bouchaud, Luca Cipelletti, and Wim Van Saarloos, editors. *Dynamical Heterogeneities in Glasses, Colloids, and Granular Media*. Oxford University Press, 2011a.
- Ludovic Berthier, Giulio Biroli, Jean-Philippe Bouchaud, and Robert L. Jack. *Overview of different characterizations of dynamic heterogeneity*, chapter 3, pages 68–109. Oxford University Press, 2011b.
- Ludovic Berthier, Hugo Jacquin, and Francesco Zamponi. Microscopic theory of the jamming transition of harmonic spheres. *Phys. Rev. E*, 84:051103, Nov 2011c. doi: 10.1103/PhysRevE.84.051103. URL <http://link.aps.org/doi/10.1103/PhysRevE.84.051103>.
- Dapeng Bi, Jie Zhang, Bulbul Chakraborty, and R. P. Behringer. Jamming by shear. *Nature*, 480(7377):355–358, Dec 2011. doi: 10.1038/nature10667. URL <http://dx.doi.org/10.1038/nature10667>.
- Indaco Biazzo, Francesco Caltagirone, Giorgio Parisi, and Francesco Zamponi. Theory of amorphous packings of binary mixtures of hard spheres. *Phys. Rev. Lett.*, 102:195701, May 2009. doi: 10.1103/PhysRevLett.102.195701. URL <http://link.aps.org/doi/10.1103/PhysRevLett.102.195701>.

- K. Binder and A. P. Young. Spin glasses: Experimental facts, theoretical concepts, and open questions. *Rev. Mod. Phys.*, 58: 801–976, Oct 1986. doi: 10.1103/RevModPhys.58.801. URL <http://link.aps.org/doi/10.1103/RevModPhys.58.801>.
- Giulio Biroli, Jean-Philippe Bouchaud, Kunimasa Miyazaki, and David R. Reichman. Inhomogeneous mode-coupling theory and growing dynamic length in supercooled liquids. *Phys. Rev. Lett.*, 97: 195701, Nov 2006. doi: 10.1103/PhysRevLett.97.195701. URL <http://link.aps.org/doi/10.1103/PhysRevLett.97.195701>.
- Lydéric Bocquet, Annie Colin, and Armand Ajdari. Kinetic theory of plastic flow in soft glassy materials. *Phys. Rev. Lett.*, 103: 036001, Jul 2009. doi: 10.1103/PhysRevLett.103.036001. URL <http://link.aps.org/doi/10.1103/PhysRevLett.103.036001>.
- F. Bolton and D. Weaire. Rigidity loss transition in a disordered 2d froth. *Phys. Rev. Lett.*, 65:3449–3451, Dec 1990. doi: 10.1103/PhysRevLett.65.3449. URL <http://link.aps.org/doi/10.1103/PhysRevLett.65.3449>.
- Francois Boyer, Élisabeth Guazzelli, and Olivier Pouliquen. Unifying suspension and granular rheology. *Phys. Rev. Lett.*, 107: 188301, Oct 2011. doi: 10.1103/PhysRevLett.107.188301. URL <http://link.aps.org/doi/10.1103/PhysRevLett.107.188301>.
- G. Brambilla, D. El Masri, M. Pierno, L. Berthier, L. Cipelletti, G. Petekidis, and A. B. Schofield. Probing the equilibrium dynamics of colloidal hard spheres above the mode-coupling glass transition. *Phys. Rev. Lett.*, 102:085703, Feb 2009. doi: 10.1103/PhysRevLett.102.085703. URL <http://link.aps.org/doi/10.1103/PhysRevLett.102.085703>.
- V. V. Brazhkin, Yu. D. Fomin, A. G. Lyapun, V. N. Ryzhov, and E. N. Tsiok. Widom line for the liquid-gas transition in lennard-jones system. *J. Phys. Chem. B*, 115:14112–14115, 2011.
- C. Brito and M. Wyart. On the rigidity of a hard-sphere glass near random close packing. *EPL (Europhysics Letters)*, 76(1):149, 2006. URL <http://stacks.iop.org/0295-5075/76/i=1/a=149>.
- Carolina Brito, Olivier Dauchot, Giulio Biroli, and Jean-Philippe Bouchaud. Elementary excitation modes in a granular glass above jamming. *Soft Matter*, 6:3013–3022, 2010. doi: 10.1039/C001360A. URL <http://dx.doi.org/10.1039/C001360A>.
- Herbert B. Callen. *Thermodynamics and an introduction to thermostatistics*. 1985.

- R. Candelier. *Dynamics and Structure close to the Glass and Jamming transitions ; Experiments and Simulations*. PhD thesis, UPMC, 2009. URL <http://tel.archives-ouvertes.fr/tel-00440848>.
- Tommaso Castellani and Andrea Cavagna. Spin-glass theory for pedestrians. *Journal of Statistical Mechanics: Theory and Experiment*, 2005(05):P05012, 2005. URL <http://stacks.iop.org/1742-5468/2005/i=05/a=P05012>.
- M. E. Cates, J. P. Wittmer, J.-P. Bouchaud, and P. Claudin. Jamming, force chains, and fragile matter. *Phys. Rev. Lett.*, 81:1841–1844, Aug 1998. doi: 10.1103/PhysRevLett.81.1841. URL <http://link.aps.org/doi/10.1103/PhysRevLett.81.1841>.
- Andrea Cavagna. Supercooled liquids for pedestrians. *Physics Reports*, 476(4–6):51 – 124, 2009. ISSN 0370-1573. doi: 10.1016/j.physrep.2009.03.003. URL <http://www.sciencedirect.com/science/article/pii/S0370157309001112>.
- David Chandler and Juan P. Garrahan. Dynamics on the way to forming glass: Bubbles in space-time. *Annual Review of Physical Chemistry*, 61(1):191–217, 2010. doi: 10.1146/annurev.physchem.040808.090405. URL <http://www.annualreviews.org/doi/abs/10.1146/annurev.physchem.040808.090405>.
- David Chandler, John D. Weeks, and Hans C. Andersen. Van der waals picture of liquids, solids, and phase transformations. *Science*, 220(4599):787–794, 1983. doi: 10.1126/science.220.4599.787. URL <http://www.sciencemag.org/content/220/4599/787.abstract>.
- Pinaki Chaudhuri, Ludovic Berthier, and Srikanth Sastry. Jamming transitions in amorphous packings of frictionless spheres occur over a continuous range of volume fractions. *Phys. Rev. Lett.*, 104:165701, Apr 2010. doi: 10.1103/PhysRevLett.104.165701. URL <http://link.aps.org/doi/10.1103/PhysRevLett.104.165701>.
- Ke Chen, Wouter G. Ellenbroek, Zexin Zhang, Daniel T. N. Chen, Peter J. Yunker, Silke Henkes, Carolina Brito, Olivier Dauchot, Wim van Saarloos, Andrea J. Liu, and A. G. Yodh. Low-frequency vibrations of soft colloidal glasses. *Phys. Rev. Lett.*, 105:025501, Jul 2010. doi: 10.1103/PhysRevLett.105.025501. URL <http://link.aps.org/doi/10.1103/PhysRevLett.105.025501>.
- Xiang Cheng. Experimental study of the jamming transition at zero temperature. *Phys. Rev. E*, 81:031301, Mar 2010. doi: 10.1103/PhysRevE.81.031301. URL <http://link.aps.org/doi/10.1103/PhysRevE.81.031301>.

- Luca Cipelletti and Eric R. Weeks. *Glassy dynamics and dynamical heterogeneity in colloids*, chapter 4, pages 110–151. Oxford University Press, 2011.
- Maxime Clusel, Eric I. Corwin, Alexander O. N. Siemens, and Jasna Brujic. A /‘granocentric/’ model for random packing of jammed emulsions. *Nature*, 460(7255):611–615, Jul 2009. ISSN 0028-0836. doi: 10.1038/nature08158. URL <http://dx.doi.org/10.1038/nature08158>.
- G. D’Anna and G. Gremaud. The jamming route to the glass state in weakly perturbed granular media. *Nature*, 413(6854):407–409, Sep 2001. ISSN 0028-0836. doi: 10.1038/35096540. URL <http://dx.doi.org/10.1038/35096540>.
- O. Dauchot, G. Marty, and G. Biroli. Dynamical heterogeneity close to the jamming transition in a sheared granular material. *Phys. Rev. Lett.*, 95:265701, Dec 2005. doi: 10.1103/PhysRevLett.95.265701. URL <http://link.aps.org/doi/10.1103/PhysRevLett.95.265701>.
- Olivier Dauchot, Douglas J. Durian, and Martin van Hecke. *Dynamical Heterogeneities in Grains and Foams*, chapter 6, pages 203–224. Oxford University Press, 2011.
- Pablo G. Debenedetti and Frank H. Stillinger. Supercooled liquids and the glass transition. *Nature*, 410:8, 2001.
- Eric DeGiuli. Private communication. 2012.
- Eric DeGiuli and Jim McElwaine. Laws of granular solids: Geometry and topology. *Phys. Rev. E*, 84:041310, Oct 2011. doi: 10.1103/PhysRevE.84.041310. URL <http://link.aps.org/doi/10.1103/PhysRevE.84.041310>.
- B. Derrida. Random-energy model: Limit of a family of disordered models. *Phys. Rev. Lett.*, 45:79–82, Jul 1980. doi: 10.1103/PhysRevLett.45.79. URL <http://link.aps.org/doi/10.1103/PhysRevLett.45.79>.
- Julien Deseigne, Olivier Dauchot, and Hugues Chaté. Collective motion of vibrated polar disks. *Phys. Rev. Lett.*, 105:098001, Aug 2010. doi: 10.1103/PhysRevLett.105.098001. URL <http://link.aps.org/doi/10.1103/PhysRevLett.105.098001>.
- Julien Deseigne, Sebastien Leonard, Olivier Dauchot, and Hugues Chate. Vibrated polar disks: spontaneous motion, binary collisions, and collective dynamics. *Soft Matter*, 8:5629–5639, 2012. doi: 10.1039/C2SM25186H. URL <http://dx.doi.org/10.1039/C2SM25186H>.

- Thibaut Divoux, Hervé Gayvallet, and Jean-Christophe G eminard. Creep motion of a granular pile induced by thermal cycling. *Phys. Rev. Lett.*, 101:148303, Oct 2008. doi: 10.1103/PhysRevLett.101.148303. URL <http://link.aps.org/doi/10.1103/PhysRevLett.101.148303>.
- Aleksandar Donev, Ibrahim Cisse, David Sachs, Evan A. Variano, Frank H. Stillinger, Robert Connelly, Salvatore Torquato, and P. M. Chaikin. Improving the density of jammed disordered packings using ellipsoids. *Science*, 303(5660):990–993, 2004. doi: 10.1126/science.1093010. URL <http://www.sciencemag.org/content/303/5660/990.abstract>.
- Aleksandar Donev, Salvatore Torquato, and Frank H. Stillinger. Pair correlation function characteristics of nearly jammed disordered and ordered hard-sphere packings. *Phys. Rev. E*, 71: 011105, Jan 2005. doi: 10.1103/PhysRevE.71.011105. URL <http://link.aps.org/doi/10.1103/PhysRevE.71.011105>.
- Aleksandar Donev, Frank H. Stillinger, and Salvatore Torquato. Do binary hard disks exhibit an ideal glass transition? *Phys. Rev. Lett.*, 96:225502, Jun 2006. doi: 10.1103/PhysRevLett.96.225502. URL <http://link.aps.org/doi/10.1103/PhysRevLett.96.225502>.
- Aleksandar Donev, Robert Connelly, Frank H. Stillinger, and Salvatore Torquato. Underconstrained jammed packings of nonspherical hard particles: Ellipses and ellipsoids. *Phys. Rev. E*, 75: 051304, May 2007. doi: 10.1103/PhysRevE.75.051304. URL <http://link.aps.org/doi/10.1103/PhysRevE.75.051304>.
- D. J. Durian. Foam mechanics at the bubble scale. *Phys. Rev. Lett.*, 75:4780–4783, Dec 1995. doi: 10.1103/PhysRevLett.75.4780. URL <http://link.aps.org/doi/10.1103/PhysRevLett.75.4780>.
- S F Edwards and P W Anderson. Theory of spin glasses. *Journal of Physics F: Metal Physics*, 5(5):965, 1975. URL <http://stacks.iop.org/0305-4608/5/i=5/a=017>.
- W. G. Ellenbroek, Z. Zeravcic, W. van Saarloos, and M. van Hecke. Non-affine response: Jammed packings vs. spring networks. *EPL (Europhysics Letters)*, 87(3):34004, 2009a. URL <http://stacks.iop.org/0295-5075/87/i=3/a=34004>.
- Wouter G. Ellenbroek, Martin van Hecke, and Wim van Saarloos. Jammed frictionless disks: Connecting local and global response. *Phys. Rev. E*, 80: 061307, 2009b.
- Nigel Goldenfeld. *Lectures On Phase Transitions And The Renormalization Group*. Westview Press, 1992.

- Thomas Graham. Xxxv.-on the properties of silicic acid and other analogous colloidal substances. *J. Chem. Soc.*, 17:318–327, 1864. doi: 10.1039/JS8641700318. URL <http://dx.doi.org/10.1039/JS8641700318>.
- Stephen Hales. *VEGETABLE STATICKS: Or, An ACCOUNT of fome Statical Experiments ON THE SAP in VEGETABLES: Being an ESSAY towards a Natural Hiftory of Vegetation.*, chapter CHAP. I. Experiments, fhewing the quantities moifture imbibed and ferfired by Plants and Trees. Experiment XXXII., pages 94–96. 1727.
- Thomas C. Hales. A proof of the kepler conjecture. *Annals of Mathematics*, 162:1065–1085, 2005.
- T. K. Haxton and A. J. Liu. Kinetic heterogeneities at dynamical crossovers. *EPL*, 90(6):66004, 2010. doi: 10.1209/0295-5075/90/66004. URL <http://dx.doi.org/10.1209/0295-5075/90/66004>.
- P. Hébraud and F. Lequeux. Mode-coupling theory for the pasty rheology of soft glassy materials. *Phys. Rev. Lett.*, 81:2934–2937, Oct 1998. doi: 10.1103/PhysRevLett.81.2934. URL <http://link.aps.org/doi/10.1103/PhysRevLett.81.2934>.
- Eugene Hecht. *Optics*. 2005.
- Silke Henkes, Yaouen Fily, and M. Cristina Marchetti. Active jamming: Self-propelled soft particles at high density. *Phys. Rev. E*, 84:040301, Oct 2011. doi: 10.1103/PhysRevE.84.040301. URL <http://link.aps.org/doi/10.1103/PhysRevE.84.040301>.
- Silke Henkes, Carolina Brito, and Olivier Dauchot. Extracting vibrational modes from fluctuations: a pedagogical discussion. *Soft Matter*, 8:6092–6109, 2012. doi: 10.1039/C2SM07445A. URL <http://dx.doi.org/10.1039/C2SM07445A>.
- Hugo Jacquin, Ludovic Berthier, and Francesco Zamponi. Microscopic mean-field theory of the jamming transition. *Phys. Rev. Lett.*, 106:135702, Mar 2011. doi: 10.1103/PhysRevLett.106.135702. URL <http://link.aps.org/doi/10.1103/PhysRevLett.106.135702>.
- H. M. Jaeger, Chu-heng Liu, and Sidney R. Nagel. Relaxation at the angle of repose. *Phys. Rev. Lett.*, 62:40–43, Jan 1989. doi: 10.1103/PhysRevLett.62.40. URL <http://link.aps.org/doi/10.1103/PhysRevLett.62.40>.
- Ivane Jorjadze, Lea-Laetitia Pontani, Katherine A. Newhall, and Jasna Brujić. Attractive emulsion droplets probe the phase diagram of jammed granular matter. *Proceedings of the National Academy of Sciences*, 108(11):4286–4291, 2011. doi: 10.1073/pnas.1017716108. URL <http://www.pnas.org/content/108/11/4286.abstract>.

- Aaron S. Keys, Adam R. Abate, Sharon C. Glotzer, and Douglas J. Durian. Measurement of growing dynamical length scales and prediction of the jamming transition in a granular material. *Nat Phys*, 3(4): 260–264, Apr 2007. ISSN 1745-2473. doi: 10.1038/nphys572. URL <http://dx.doi.org/10.1038/nphys572>.
- Scott Kirkpatrick and David Sherrington. Infinite-ranged models of spin-glasses. *Phys. Rev. B*, 17:4384–4403, Jun 1978. doi: 10.1103/PhysRevB.17.4384. URL <http://link.aps.org/doi/10.1103/PhysRevB.17.4384>.
- James B. Knight, Christopher G. Fandrich, Chun Ning Lau, Heinrich M. Jaeger, and Sidney R. Nagel. Density relaxation in a vibrated granular material. *Phys. Rev. E*, 51:3957–3963, May 1995. doi: 10.1103/PhysRevE.51.3957. URL <http://link.aps.org/doi/10.1103/PhysRevE.51.3957>.
- Florent Krzakala and Jorge Kurchan. Landscape analysis of constraint satisfaction problems. *Phys. Rev. E*, 76: 021122, Aug 2007. doi: 10.1103/PhysRevE.76.021122. URL <http://link.aps.org/doi/10.1103/PhysRevE.76.021122>.
- Florent Krzakala, Andrea Montanari, Federico Ricci-Tersenghi, Guilhem Semerjian, and Lenka Zdeborová. Gibbs states and the set of solutions of random constraint satisfaction problems. *Proceedings of the National Academy of Sciences*, 104(25):10318–10323, 2007. doi: 10.1073/pnas.0703685104. URL <http://www.pnas.org/content/104/25/10318.abstract>.
- Arshad Kudrolli, Geoffroy Lumay, Dmitri Volfson, and Lev S. Tsimring. Swarming and swirling in self-propelled polar granular rods. *Phys. Rev. Lett.*, 100:058001, Feb 2008. doi: 10.1103/PhysRevLett.100.058001. URL <http://link.aps.org/doi/10.1103/PhysRevLett.100.058001>.
- L.D. Landau and E.M. Lifshitz. *Theory of elasticity*. Pergamon, Oxford, UK.
- F. Lechenault. *The "Jamming" transition in a bidimensional granular medium: Statics and dynamics of a model athermal system*. PhD thesis, Paris 11, 2007. URL <http://tel.archives-ouvertes.fr/tel-00200902>.
- F. Lechenault, O. Dauchot, G. Biroli, and J. P. Bouchaud. Critical scaling and heterogeneous superdiffusion across the jamming/rigidity transition of a granular glass. *EPL (Europhysics Letters)*, 83(4):46003, 2008a. URL <http://stacks.iop.org/0295-5075/83/i=4/a=46003>.
- F. Lechenault, O. Dauchot, G. Biroli, and J. P. Bouchaud. Lower bound on the four-point dynamical susceptibility: Direct experimental test on a

- granular packing. *EPL (Europhysics Letters)*, 83(4):46002, 2008b. URL <http://stacks.iop.org/0295-5075/83/i=4/a=46002>.
- F. Lechenault, R. Candelier, O. Dauchot, J.-P. Bouchaud, and G. Biroli. Super-diffusion around the rigidity transition: Levy and the lilliputians. *Soft Matter*, 6(13):3059–3064, 2010. doi: 10.1039/c000802h. URL <http://dx.doi.org/10.1039/c000802h>.
- Edan Lerner, Gustavo Düring, and Matthieu Wyart. A unified framework for non-brownian suspension flows and soft amorphous solids. *Proceedings of the National Academy of Sciences*, 109(13):4798–4803, 2012. doi: 10.1073/pnas.1120215109. URL <http://www.pnas.org/content/109/13/4798.abstract>.
- Andrea J. Liu and Sidney R. Nagel. Nonlinear dynamics: Jamming is not just cool any more. *Nature*, 396:21–22, 1998. doi: 10.1038/23819.
- C. h. Liu, S. R. Nagel, D. A. Schecter, S. N. Coppersmith, S. Majumdar, O. Narayan, and T. A. Witten. Force fluctuations in bead packs. *Science*, 269(5223):513–515, 1995. doi: 10.1126/science.269.5223.513. URL <http://www.sciencemag.org/content/269/5223/513.abstract>.
- Jia Liu, Yue Cai, Yonghui Deng, Zhenkun Sun, Dong Gu, Bo Tu, and Dongyuan Zhao. Magnetic 3-d ordered macroporous silica templated from binary colloidal crystals and its application for effective removal of microcystin. *Microporous and Mesoporous Materials*, 130(1–3):26 – 31, 2010. ISSN 1387-1811. doi: 10.1016/j.micromeso.2009.10.008. URL <http://www.sciencedirect.com/science/article/pii/S1387181109004594>.
- Boris D. Lubachevsky and Frank H. Stillinger. Geometric properties of random disk packings. *Journal of Statistical Physics*, 60:561–583, 1990. ISSN 0022-4715. URL <http://dx.doi.org/10.1007/BF01025983>. 10.1007/BF01025983.
- Mitch Mailman, Carl F. Schreck, Corey S. O’Hern, and Bulbul Chakraborty. Jamming in systems composed of frictionless ellipse-shaped particles. *Phys. Rev. Lett.*, 102:255501, Jun 2009. doi: 10.1103/PhysRevLett.102.255501. URL <http://link.aps.org/doi/10.1103/PhysRevLett.102.255501>.
- T. S. Majmudar and R. P. Behringer. Contact force measurements and stress-induced anisotropy in granular materials. *Nature*, 435(1079):1079–1082, June 2005. ISSN 0028-0836. URL <http://dx.doi.org/10.1038/nature03805>.
- T. S. Majmudar, M. Sperl, S. Luding, and R. P. Behringer. Jamming transition in granular systems. *Phys. Rev. Lett.*, 98:

- 058001, Jan 2007. doi: 10.1103/PhysRevLett.98.058001. URL <http://link.aps.org/doi/10.1103/PhysRevLett.98.058001>.
- Paul F. McMillan and H. Eugene Stanley. Fluid phases: Going supercritical. *Nat Phys*, 6(7):479–480, Jul 2010. ISSN 1745-2473. doi: 10.1038/nphys1711. URL <http://dx.doi.org/10.1038/nphys1711>.
- Marc Mézard and Giorgio Parisi. A first-principle computation of the thermodynamics of glasses. *The Journal of Chemical Physics*, 111(3):1076–1095, 1999. doi: 10.1063/1.479193. URL <http://link.aip.org/link/?JCP/111/1076/1>.
- Micro-Measurements. Photostress coatings. Technical report, Vishay, 2010. URL <http://www.vishaypg.com/docs/11222/pscoat.pdf>.
- Rémi Monasson. Structural glass transition and the entropy of the metastable states. *Phys. Rev. Lett.*, 75:2847–2850, Oct 1995. doi: 10.1103/PhysRevLett.75.2847. URL <http://link.aps.org/doi/10.1103/PhysRevLett.75.2847>.
- M. Mézard, G. Parisi, and R. Zecchina. Analytic and algorithmic solution of random satisfiability problems. *Science*, 297(5582):812–815, 2002. doi: 10.1126/science.1073287. URL <http://www.sciencemag.org/content/297/5582/812.abstract>.
- Kiri Nichol, Alexey Zanin, Renaud Bastien, Elie Wandersman, and Martin van Hecke. Flow-induced agitations create a granular fluid. *Phys. Rev. Lett.*, 104:078302, Feb 2010. doi: 10.1103/PhysRevLett.104.078302. URL <http://link.aps.org/doi/10.1103/PhysRevLett.104.078302>.
- Corey S. O’Hern, Stephen A. Langer, Andrea J. Liu, and Sidney R. Nagel. Random packings of frictionless particles. *Phys. Rev. Lett.*, 88:075507, Jan 2002. doi: 10.1103/PhysRevLett.88.075507. URL <http://link.aps.org/doi/10.1103/PhysRevLett.88.075507>.
- Corey S. O’Hern, Leonardo E. Silbert, Andrea J. Liu, and Sidney R. Nagel. Jamming at zero temperature and zero applied stress: The epitome of disorder. *Phys. Rev. E*, 68:011306, Jul 2003. doi: 10.1103/PhysRevE.68.011306. URL <http://link.aps.org/doi/10.1103/PhysRevE.68.011306>.
- Michio Otsuki and Hisao Hayakawa. Critical scaling near jamming transition at finite temperature. *arxiv*, 1111.1313, 2011.
- Giorgio Parisi and Francesco Zamponi. Mean-field theory of hard sphere glasses and jamming. *Rev. Mod. Phys.*, 82:789–845, Mar 2010. doi: 10.1103/RevModPhys.82.789. URL <http://link.aps.org/doi/10.1103/RevModPhys.82.789>.

- P. Philippe and D. Bideau. Compaction dynamics of a granular medium under vertical tapping. *Europhys. Lett.*, 60(5):677–683, 2002. doi: 10.1209/epl/i2002-00362-7. URL <http://dx.doi.org/10.1209/epl/i2002-00362-7>.
- P. Philippe and D. Bideau. Granular medium under vertical tapping: Change of compaction and convection dynamics around the liftoff threshold. *Phys. Rev. Lett.*, 91:104302, Sep 2003. doi: 10.1103/PhysRevLett.91.104302. URL <http://link.aps.org/doi/10.1103/PhysRevLett.91.104302>.
- O. Pouliquen, M. Belzons, and M. Nicolas. Fluctuating particle motion during shear induced granular compaction. *Phys. Rev. Lett.*, 91:014301, Jul 2003. doi: 10.1103/PhysRevLett.91.014301. URL <http://link.aps.org/doi/10.1103/PhysRevLett.91.014301>.
- P. Pusey and W. van Meegen. Phase behavior of concentrated suspensions of nearly hard colloidal spheres. *Nature*, 320:340, 1986.
- P. N. Pusey and W. van Meegen. Observation of a glass transition in suspensions of spherical colloidal particles. *Phys. Rev. Lett.*, 59:2083–2086, Nov 1987. doi: 10.1103/PhysRevLett.59.2083. URL <http://link.aps.org/doi/10.1103/PhysRevLett.59.2083>.
- K. A. Reddy, Y. Forterre, and O. Pouliquen. Evidence of mechanically activated processes in slow granular flows. *Phys. Rev. Lett.*, 106:108301, Mar 2011. doi: 10.1103/PhysRevLett.106.108301. URL <http://link.aps.org/doi/10.1103/PhysRevLett.106.108301>.
- David R Reichman and Patrick Charbonneau. Mode-coupling theory. *Journal of Statistical Mechanics: Theory and Experiment*, 2005(05):P05013, 2005. URL <http://stacks.iop.org/1742-5468/2005/i=05/a=P05013>.
- P. M. Reis, R. A. Ingale, and M. D. Shattuck. Caging dynamics in a granular fluid. *Phys. Rev. Lett.*, 98:188301, Apr 2007. doi: 10.1103/PhysRevLett.98.188301. URL <http://link.aps.org/doi/10.1103/PhysRevLett.98.188301>.
- Patrick Richard, Mario Nicodemi, Renaud Delannay, Philippe Ribiere, and Daniel Bideau. Slow relaxation and compaction of granular systems. *Nat Mater*, 4(2):121–128, Feb 2005. ISSN 1476-1122. doi: 10.1038/nmat1300. URL <http://dx.doi.org/10.1038/nmat1300>.
- Ludger Santen and Werner Krauth. Absence of thermodynamic phase transition in a model glass former. *Nature*, 405(6786):550–551, Jun 2000. ISSN 0028-0836. doi: 10.1038/35014561. URL <http://dx.doi.org/10.1038/35014561>.

- Carl F. Schreck, Thibault Bertrand, Corey S. O'Hern, and M. D. Shattuck. Repulsive contact interactions make jammed particulate systems inherently nonharmonic. *Phys. Rev. Lett.*, 107: 078301, Aug 2011. doi: 10.1103/PhysRevLett.107.078301. URL <http://link.aps.org/doi/10.1103/PhysRevLett.107.078301>.
- Carl F. Schreck, Mitch Mailman, Bulbul Chakraborty, and Corey S. O'Hern. Constraints and vibrations in static packings of ellipsoidal particles. *Phys. Rev. E*, 85:061305, Jun 2012. doi: 10.1103/PhysRevE.85.061305. URL <http://link.aps.org/doi/10.1103/PhysRevE.85.061305>.
- Guilhem Semerjian. Glassy aspects of optimization problems. In *Beg Rohu Summer School*, 2012.
- Sextant. *Optique Experimentale*. Hermann.
- Kostya Shundyak, Martin van Hecke, and Wim van Saarloos. Force mobilization and generalized isostaticity in jammed packings of frictional grains. *Phys. Rev. E*, 75:010301, Jan 2007. doi: 10.1103/PhysRevE.75.010301. URL <http://link.aps.org/doi/10.1103/PhysRevE.75.010301>.
- Leonardo E. Silbert, Deniz Ertas, Gary S. Grest, Thomas C. Halsey, and Dov Levine. Geometry of frictionless and frictional sphere packings. *Phys. Rev. E*, 65:031304, Feb 2002. doi: 10.1103/PhysRevE.65.031304. URL <http://link.aps.org/doi/10.1103/PhysRevE.65.031304>.
- Leonardo E. Silbert, Andrea J. Liu, and Sidney R. Nagel. Vibrations and diverging length scales near the unjamming transition. *Phys. Rev. Lett.*, 95:098301, Aug 2005. doi: 10.1103/PhysRevLett.95.098301. URL <http://link.aps.org/doi/10.1103/PhysRevLett.95.098301>.
- G. G. Simeoni, T. Bryk, F. A. Gorelli, M. Krisch, G. Ruocco, M. Santoro, and T. Scopigno. The widom line as the crossover between liquid-like and gas-like behaviour in supercritical fluids. *Nat Phys*, 6(7): 503–507, Jul 2010. ISSN 1745-2473. doi: 10.1038/nphys1683. URL <http://dx.doi.org/10.1038/nphys1683>.
- Peter Sollich, François Lequeux, Pascal Hébraud, and Michael E. Cates. Rheology of soft glassy materials. *Phys. Rev. Lett.*, 78: 2020–2023, Mar 1997. doi: 10.1103/PhysRevLett.78.2020. URL <http://link.aps.org/doi/10.1103/PhysRevLett.78.2020>.
- Ellák Somfai, Martin van Hecke, Wouter G. Ellenbroek, Kostya Shundyak, and Wim van Saarloos. Critical and non-critical jamming of frictional grains. *Phys. Rev. E*, 75: 020301, Feb 2007. doi: 10.1103/PhysRevE.75.020301. URL <http://link.aps.org/doi/10.1103/PhysRevE.75.020301>.

- Grzegorz Szamel. Slow and glassy dynamics. In *Beg Rohu Summer School*, 2012.
- Grzegorz Szamel and Hartmut Löwen. Mode-coupling theory of the glass transition in colloidal systems. *Phys. Rev. A*, 44: 8215–8219, Dec 1991. doi: 10.1103/PhysRevA.44.8215. URL <http://link.aps.org/doi/10.1103/PhysRevA.44.8215>.
- G Tarjus, S A Kivelson, Z Nussinov, and P Viot. The frustration-based approach of supercooled liquids and the glass transition: a review and critical assessment. *Journal of Physics: Condensed Matter*, 17(50):R1143, 2005. URL <http://stacks.iop.org/0953-8984/17/i=50/a=R01>.
- Gilles Tarjus. An overview of the glass transition. In *Beg Rohu Summer School*, 2012.
- Marco Tarzia. On the absence of the glass transition in two dimensional hard disks. *Journal of Statistical Mechanics: Theory and Experiment*, 2007(01):P01010, 2007. URL <http://stacks.iop.org/1742-5468/2007/i=01/a=P01010>.
- Brian P. Tighe. Floppiness, cutting, and freezing: Dynamic critical scaling near isostaticity. *Arxiv*, 1203.3411, March 2012.
- Brian P. Tighe, Erik Woldhuis, Joris J. C. Remmers, Wim van Saarloos, and Martin van Hecke. Model for the scaling of stresses and fluctuations in flows near jamming. *Phys. Rev. Lett.*, 105: 088303, Aug 2010. doi: 10.1103/PhysRevLett.105.088303. URL <http://link.aps.org/doi/10.1103/PhysRevLett.105.088303>.
- Alexei V. Tkachenko and Thomas A. Witten. Stress propagation through frictionless granular material. *Phys. Rev. E*, 60: 687–696, Jul 1999. doi: 10.1103/PhysRevE.60.687. URL <http://link.aps.org/doi/10.1103/PhysRevE.60.687>.
- S. Torquato and F. H. Stillinger. Jammed hard-particle packings: From kepler to bernal and beyond. *Rev. Mod. Phys.*, 82: 2633–2672, Sep 2010. doi: 10.1103/RevModPhys.82.2633. URL <http://link.aps.org/doi/10.1103/RevModPhys.82.2633>.
- S. Torquato, T. M. Truskett, and P. G. Debenedetti. Is random close packing of spheres well defined? *Phys. Rev. Lett.*, 84: 2064–2067, Mar 2000. doi: 10.1103/PhysRevLett.84.2064. URL <http://link.aps.org/doi/10.1103/PhysRevLett.84.2064>.
- M van Hecke. Jamming of soft particles: geometry, mechanics, scaling and isostaticity. *Journal of Physics: Condensed Matter*, 22(3):033101, 2010. URL <http://stacks.iop.org/0953-8984/22/i=3/a=033101>.

- W. van Meegen and S. M. Underwood. Glass transition in colloidal hard spheres: Measurement and mode-coupling-theory analysis of the coherent intermediate scattering function. *Phys. Rev. E*, 49:4206–4220, May 1994. doi: 10.1103/PhysRevE.49.4206. URL <http://link.aps.org/doi/10.1103/PhysRevE.49.4206>.
- Vishay. Photostress®. Technical report, Vishay, 2010.
- Takao Wakabayashi. Photo-elastic method for determination of stress in powdered mass. *Journal of the Physical Society of Japan*, 5(5):383–385, 1950. doi: 10.1143/JPSJ.5.383. URL <http://jpsj.ipap.jp/link?JPSJ/5/383/>.
- Lijin Wang and Ning Xu. Critical scalings and jamming in thermal colloidal systems. ArXiv:1112.2429 (2012).
- Lijin Wang and Ning Xu. Critical scalings and jamming in thermal colloidal systems. *ArXiv e-prints*, page 1112.2429, December 2011.
- Keiji Watanabe and Hajime Tanaka. Direct observation of medium-range crystalline order in granular liquids near the glass transition. *Phys. Rev. Lett.*, 100:158002, Apr 2008. doi: 10.1103/PhysRevLett.100.158002. URL <http://link.aps.org/doi/10.1103/PhysRevLett.100.158002>.
- Keiji Watanabe, Takeshi Kawasaki, and Hajime Tanaka. Structural origin of enhanced slow dynamics near a wall in glass-forming systems. *Nat Mater*, 10(7):512–520, Jul 2011. ISSN 1476-1122. doi: 10.1038/nmat3034. URL <http://dx.doi.org/10.1038/nmat3034>.
- Eric R. Weeks and D. A. Weitz. Properties of cage rearrangements observed near the colloidal glass transition. *Phys. Rev. Lett.*, 89:095704, Aug 2002. doi: 10.1103/PhysRevLett.89.095704. URL <http://link.aps.org/doi/10.1103/PhysRevLett.89.095704>.
- John D. Weeks, David Chandler, and Hans C. Andersen. Role of repulsive forces in determining the equilibrium structure of simple liquids. *The Journal of Chemical Physics*, 54(12):5237–5247, 1971. doi: 10.1063/1.1674820. URL <http://link.aip.org/link/?JCP/54/5237/1>.
- A. W. Williamson. The late professor graham. *Nature*, 1:20–22, Nov 4 1864.
- M. Wyart. *On the rigidity of amorphous solids*. PhD thesis, 2008.
- M. Wyart, S. R. Nagel, and T. A. Witten. Geometric origin of excess low-frequency vibrational modes in weakly connected amorphous solids. *EPL (Europhysics Letters)*, 72(3):486, 2005a. URL <http://stacks.iop.org/0295-5075/72/i=3/a=486>.

- M. Wyart, H. Liang, A. Kabla, and L. Mahadevan. Elasticity of floppy and stiff random networks. *Phys. Rev. Lett.*, 101: 215501, Nov 2008. doi: 10.1103/PhysRevLett.101.215501. URL <http://link.aps.org/doi/10.1103/PhysRevLett.101.215501>.
- Matthieu Wyart, Leonardo E. Silbert, Sidney R. Nagel, and Thomas A. Witten. Effects of compression on the vibrational modes of marginally jammed solids. *Phys. Rev. E*, 72: 051306, Nov 2005b. doi: 10.1103/PhysRevE.72.051306. URL <http://link.aps.org/doi/10.1103/PhysRevE.72.051306>.
- N. Xu, V. Vitelli, A. J. Liu, and S. R. Nagel. Anharmonic and quasi-localized vibrations in jammed solids—modes for mechanical failure. *EPL (Europhysics Letters)*, 90(5):56001, 2010. URL <http://stacks.iop.org/0295-5075/90/i=5/a=56001>.
- Z. Zeravic, N. Xu, A. J. Liu, S. R. Nagel, and W. van Saarloos. Excitations of ellipsoid packings near jamming. *EPL (Europhysics Letters)*, 87(2):26001, 2009. URL <http://stacks.iop.org/0295-5075/87/i=2/a=26001>.
- H. P. Zhang and H. A. Makse. Jamming transition in emulsions and granular materials. *Phys. Rev. E*, 72: 011301, Jul 2005. doi: 10.1103/PhysRevE.72.011301. URL <http://link.aps.org/doi/10.1103/PhysRevE.72.011301>.
- Zexin Zhang, Ning Xu, Daniel T. N. Chen, Peter Yunker, Ahmed M. Alsayed, Kevin B. Aptowicz, Piotr Habdas, Andrea J. Liu, Sidney R. Nagel, and Arjun G. Yodh. Thermal vestige of the zero-temperature jamming transition. *Nature*, 459:230–233, 2009.

Résumé

Un ensemble de particules avec interactions répulsives, dans un empilement dense, se bloquent dans un état rigide: sous cisaillement, ces systèmes ont une contrainte seuil avant de céder. Pour des particules sans friction et à température nulle, l'empilement, à la transition de Jamming, est isostatique. Les propriétés mécaniques et géométriques présentent de nombreuses lois d'échelles avec la distance au Jamming qui peut alors être vu comme un point critique. La généralisation de ce concept en présence de température et son lien avec la transition vitreuse ont fait récemment l'objet de nombreux travaux et laissent encore de nombreuses questions ouvertes.

Nous tentons d'apporter des éléments de réponse à celles-ci en étudiant expérimentalement la dynamique des particules et du réseau de force d'un empilement désordonné de disques bi-disperses photo-élastiques vibrés horizontalement, dont nous varions la fraction surfacique pour plusieurs amplitudes de vibrations γ .

Au delà d'un lent mouvement convectif d'ensemble, la dynamique des grains présente principalement une dynamique complexe —intermittente et hétérogène— à une échelle bien plus petite que la taille typique d'un grain. Ces hétérogénéités dynamiques sont d'amplitude maximale à une densité intermédiaire $\phi^*(\gamma)$.

Au niveau du réseau de contacts, nous observons deux signatures franches et distinctes—statique et dynamique— analogues à la phénoménologie de la transition vitreuse. À l'instar du maximum d'hétérogénéités dynamiques des déplacements, la signature dynamique du réseau de contacts a lieu à $\phi^*(\gamma)$, si bien que dynamiques des déplacements et des contacts sont liées. En revanche, c'est à une densité plus élevée $\phi_J(\gamma)$ que l'on identifie la signature statique de la transition de Jamming.

Lorsque l'on diminue l'amplitude de vibration vers la limite d'excitation mécanique nulle, $\gamma \rightarrow 0$, $\phi^*(\gamma)$ et $\phi_J(\gamma)$ se confondent, et l'échelle de longueur des corrélations dynamiques augmente. Nous comparons ces résultats aux propriétés des sphères molles au voisinage du Jamming.

Abstract

At large packing fraction, disordered packings of particles with repulsive contact interactions jam into a rigid state where they withstand finite shear stresses before yielding. For frictionless particles at zero temperature, the Jamming transition coincides with the onset of iso-staticity. Various geometrical and mechanical properties exhibit critical behavior with the distance to Jamming. What vestiges of Jamming remain at finite temperature and how Jamming impacts the thermodynamics of glasses remain open issues.

We address these questions experimentally by investigating the dynamics of both the density field and the force network of an horizontally shaken bi-disperse packing of photo-elastic disks while varying the packing fraction, ϕ , at several vibration amplitudes γ . Although disks displacements reveal a slow global convective dynamics, strongly collective and intermittent motions take place on length scale much smaller than the grain diameter. These so-called dynamical heterogeneities are maximum at an intermediate packing fraction $\phi^*(\gamma)$.

The statics and dynamics of the contact network display, respectively, two distinct sharp signatures, which are reminiscent of the glass transition phenomenology, albeit occurring at the contact scale. A dynamical signature occurs at $\phi^*(\gamma)$, and we relate it to the dynamical heterogeneities of the displacements. The static signature occurs at a larger packing fraction $\phi_J(\gamma)$.

We show further that $\phi^*(\gamma)$ and $\phi_J(\gamma)$ merge in the $\gamma \rightarrow 0$ limit and that the dynamical signature strongly increases as the vibration amplitude is reduced. These results are discussed in light of thermal soft-sphere properties close to Jamming.